Quasi-Static and Dynamic Crack Initiation and Growth in Soda-lime Glass: Full-field Optical Investigations

by

Sivareddy Dondeti

A dissertation submitted to the Graduate Faculty of
Auburn University
in partial fulfillment of the
requirements for the Degree of
Doctor of Philosophy

Auburn, Alabama
December 10, 2022

Keywords: experimental mechanics, brittle materials, high stiffness transparencies, fracture, crack branching, optical measurements,

Approved by

Hareesh V. Tippur, Chair, McWane Professor of Mechanical Engineering
Jeffrey C. Suhling, Quina Distinguished Professor of Mechanical Engineering
Nima Shamsaei, Philpott-WestPoint Stevens Distinguished Professor of Mechanical Engineering
James S. Davidson, Gottlieb Professor of Civil Engineering

Abstract

Soda-lime glass (SLG) is a widely used structural material with numerous advantages in terms of thermal, physical, and mechanical properties besides sustainability and recyclability. It is widely used for structural facades, in automobile windshields, as transparent military armor, and in medical packaging, as observation ports, in home appliances, etc. Being a highly brittle material with very low-toughness and high-stiffness, understanding its failure behavior in general and fracture mechanics in particular is extremely challenging yet critical for mechanical design and structural performance. In this context, this dissertation deals with characterization of quasi-static and dynamic crack initiation and growth behaviors of SLG using full-field optical methods.

The first part of this dissertation dynamic fracture of SLG using full-field optical methods are assessed. Here the focus is on crack initiation and growth by overcoming spatio-temporal challenges posed by SLG as crack speeds typically exceed mile-a-second accompanied by nanoscale deformations. Yet, it is tacitly assumed that all optical methods are equally capable of dealing with this challenging problem though none are demonstrated to date. Towards this end, three prevalent optical techniques of experimental mechanics - transmission photoelasticity, 2-D Digital Image Correlation (DIC) and transmission Digital Gradient Sensing (DGS) - were concurrently implemented to visualize crack tip fields and quantify fracture characteristics during crack initiation and growth in SLG plates subjected to identical loading. Each method used ultrahigh-speed (1 Mfps) photography, flash/pulse visible light illumination, and a modified-Hopkinson pressure bar for impact loading. The feasibility of measuring fracture parameters along with the pros and cons of each approach for this material were critically examined. The photoelastic recordings allowed precise visualization and quantification of crack length history. The stress intensity factor histories, however, could not be evaluated due to insufficient stress-

optic response of SLG. Hence, photoelasticity was found suitable only to test velocity-based fracture criteria; others based on stress intensity factors and/or energy release rate cannot not be tested. The 2-D DIC approach did not allow direct visualization of the crack tip at different time instants. The identification of the crack tip via dominant displacement fields did not fare any better and resulted in unrealistic instantaneous velocities and stress intensity factors. The DGS method, though relies on principles of 2-D DIC to quantify angular deflections of light rays proportional to stress gradients in the whole field, performed well on both these fronts. That is, visualization and quantification of crack length and crack velocity histories with high precision was possible. Thus, both velocity, stress intensity factor and energy release rate-based criteria could be readily tested.

Based on the comparative investigation on SLG using different optical methods, dynamic mixed-mode fracture was experimentally investigated next using DGS, again in conjunction with ultrahigh-speed photography. Single edge-notched specimens subjected to inertial loading using a modified Hopkinson pressure bar apparatus were examined. A simple, eccentrically loaded specimen geometry was designed to generate a wide range of mode-mixities, from mode-I to nearly mode-II condition, at initiation. Two time-resolved orthogonal angular deflection fields of light rays proportional to the respective full-field stress gradients were measured during experiments. Mode-I and -II stress intensity factor histories spanning pre- and post-initiation behaviors were evaluated using measured full-field data in conjunction with the prevailing crack tip fields. By considering the critical stress intensity factors at crack initiation, a fracture envelope for SLG encompassing various mode-mixities was generated and compared with predictions from prevailing approaches for brittle solids. The measured crack kink angles were compared with two popular fracture criteria; both predicted the kink angles reasonably well. The effective critical stress intensity factors for SLG were found to be independent of mode-mixity over a large range

of values but rapidly decrease as mode-II conditions become dominant; a critical mode-II stress intensity factor of 0.37 MPa√m, approx. one-half of its mode-I counterpart, was estimated.

In the next part of the dissertation, unprovoked crack branching events during dynamic crack growth in SLG was assessed via direct measurement of fracture mechanics-based precursors. Towards this end, time-resolved stress gradients were measured in SLG plates of two different geometries, first one producing a single crack bifurcation event and the second one a two-tier cascading crack bifurcations in dynamic wedge-loaded specimens. The measurements were then used to extract precursors based on crack velocity, stress intensity factors, and higher order coefficients of an asymptotic crack tip field. A significant drop in the macroscale crack velocity was observed consistently when crack branching event is imminent. The cracks bifurcated when the effective stress intensity factor reached twice its value at initiation in both geometries. The fracture surface roughness and other features were also separately quantified via fractography to corroborate them with macroscale measurements. There was a lack correlation between surface roughness (R_a) and crack speed, predicted in the literature. However, a linear variation of $\log(R_a)$ with the effective stress intensity factor was seen.

Hairline cracks in SLG occasionally heal when the structure is unloaded, become optically undetectable and cause catastrophic failure upon reloading during service. This was addressed in the final part of the dissertation by recreating crack initiation and slow crack growth from a self-healed crack in a SLG plate. A wedge-splitting test (WST) geometry was adopted for this study to generate a hairline crack and let it heal without external stimulus. An opto-mechanical study of crack (re-) initiation and growth was carried out by mapping the crack tip stress gradients in the whole field using DGS. An abrupt re-initiation and extension of the self-healed crack, subsequent initiation of the natural crack tip followed by a slow crack growth were all captured both in the

far- and near-fields and the stress intensity factor history for the entire event was extracted. The results indicate a 50% reduction in critical stress intensity factor at re-initiation of the self-healed crack relative to the virgin counterpart. A companion finite element (FE) model was developed; the simulations suggest a contact stiffness of the self-healed crack to be about 60% of virgin SLG.

Acknowledgments

I would like to express my sincere gratitude to my research advisor Dr. Hareesh V. Tippur, for his continuous support, academic and technical guidance, financial support, motivation throughout my PhD journey. I consider my tenure in the Laboratory for Failure Mechanics & Optical Techniques at Auburn University, USA under Dr. Tippur's guidance has inculcated critical thinking, problem solving, collaboration, interpersonal, time management skills. It is a great privilege and honor to have him as advisor for my PhD. I would like to thank Dr. Jeffrey C. Suhling. Dr. James S. Davidson, Dr. Nima Shamsaei for their feedback and reviewing this dissertation. I sincerely thank Dr. Suhasini Gururaja for acting as external reader for my thesis. Special thanks to Dr. Kyle Schulze and Dr. Nima Shamsaei for allowing me to use their microcopy facilities. I acknowledge the support of Mr. Matt Montgomery for his help in machining glass samples at Auburn University Glass Shop. Partial support for this research through Army Research Office grants W911NF-16-1-0093, W911NF-15-1-0357 (DURIP), W911NF-17-1-0355-RI and W911NF-22-1-0015 are gratefully acknowledged.

I would like to thank my fellow lab members Bala, Chengyun, John, Taylor, Azeez, Alex and Jackson for fostering a great learning environment.

Finally, it should not have been possible without the support from my parents, wife and brothers who encouraged and motivated me during the PhD journey and I dedicate this work to all my family members.

Table of Contents

List of Tables

List of Figures

List of Abbreviations

ALON	Aluminum Oxynitride
CGS	Coherent Gradient Sensing
DIC	Digital Image Correlation
DGS	Digital Gradient Sensing
FEA	Finite Element Analysis
FGM	Functionally Graded Material
LEFM	Linear Elastic Fracture Mechanics
MTS	Maximum Tangential Stress
PMMA	poly(methylmethacrylate)
PVB	Polyvinyl Butyral
r-DGS	Reflection-mode Digital Gradient Sensing
SED	Strain Energy Density
SIF	Stress Intensity Factor
SLG	Soda-lime Glass
WST	Wedge Splitting Test

Chapter 1. Introduction

1.1 Motivation

Transparent materials are widely used for transparent armor [1-3], as structural facades [4-6], aircraft and spacecraft windows [7-9], automotive windshields [10], observation ports, laboratory and home appliances [11], electronic and medical devices [12], to name a few (Figure 1.1). In contemporary spacecraft design, observation windows are a major factor in attracting customers to space tourism. In military vehicles, it is critical to provide an ability to watch the surroundings without becoming vulnerable to incoming projectiles and stress waves. Transparent materials are critical and functional part of buildings for aesthetics and capturing natural light.

Soda-lime glass (SLG) is a widely used structural material and it accounts for over 80% of all manufactured glasses [13]. It has excellent optical transparency, high stiffness, hardness, very high compression strength, and superior fire and chemical resistance [14-16] (see Table 1.1). It is also cost effective, recyclable and sustainable. However, structures that use SLG are subjected to a wide loading spectrum, static to dynamic, during service. Due to the extreme brittle nature of SLG, it is critical to understand material failure in general and fracture mechanics in particular for mechanical design and structural integrity.

Despite the vast number of applications of SLG, the previous investigations have all been carried out on brittle polymers such as Homalite-100 and poly(methylmethacrylate) (PMMA) as stand-in materials due to enormous challenges of directly studying SLG using optical methods. Majority of the previous fracture studies on SLG were undertaken without the use of optical

methods and have been generally limited only to far-field measurements. This is largely due to a lack of suitable techniques for capturing crack tip fields as SLG poses unique challenges to such measurements due its high stiffness and low toughness. Crack speeds in this material often exceed 1500 m/s within a couple of microseconds after crack initiation [17-19]. The crack tip opening displacements are extremely small and in the nano- to sub-macroscale resulting in *mile-a-second hairline crack growth* [16] events. Furthermore, the crack initiation leads to growth leading to multiple crack branching events.

Figure 1.1: Commercial and military applications of brittle transparencies - (a) spaceship window (source: Blue Origin), (b) automotive window glass (source: MS Glass outlet), (c) military armored vehicles (source: army-technologies), (d) building elevations (source: ASE Europe), (e) electronic devices (source: Gadget Reviews)

In general, structural materials experience three modes of fracture during service, namely mode-I, mode-II and mode-III, as shown schematically in Figure 1.2. Mode-I is the crack opening mode and the dominant displacements are normal to crack flanks. Mode-II is the crack sliding mode, where the major displacements are along the crack flanks and in crack direction. And, mode-III, or the crack tearing mode, corresponds to where the dominant displacements are sliding

displacement of crack flanks but in the out-of-plane direction. When more than one mode of fracture is involved in the fracture process, it is referred to as the mixed-mode fracture.

Table 1.1 – Some relevant optical, thermal and physical properties of soda-lime glass [18, 20-22]

Property	**Value**
Refractive index, n	1.5234 at 0.5876 μm wave length
Coeffecient of thermal expansion, CTE	8.3×10^{-6} /°C
Transmittance, T	0.91 at 0.750 μm wave length
Density, ρ	2500 kg/m^3
Elastic modulus, E	70 GPa
Poisson's ratio, υ	0.22
Compressive strength, σ_c	330 MPa
Elasto-optic constant, C_σ	-0.027×10^{-10} m^2/N

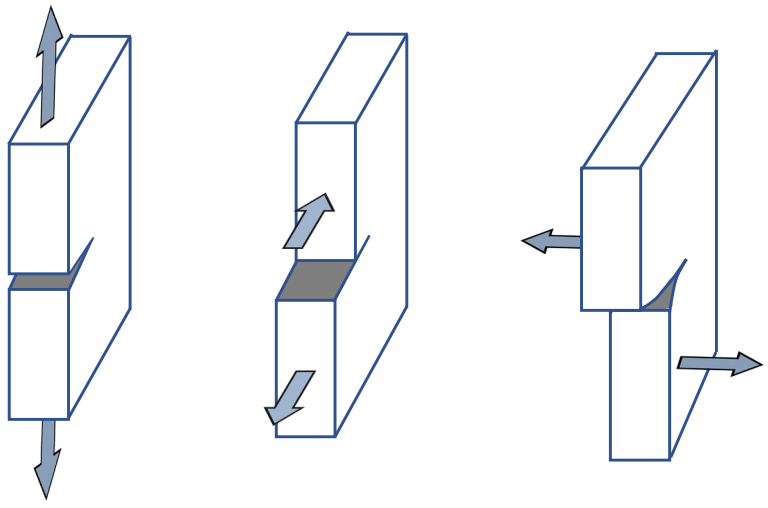

Figure 1.2: Standard fracture modes

1.2 Literature Review

In the following, the background literature relevant to the current research is provided in four parts. In the first part, literature on the full-field optical methods applied to the study of SLG is reviewed. The reported works on brittle mixed-mode dynamic fracture is briefly reviewed in the second part. In the third part, reports on crack branch formations in brittle materials including the ones for SLG are surveyed. In the fourth and the last part, the reported works on slow crack initiation and growth in soda-lime glass is reviewed.

Part-1: As noted earlier in the last section, transparent glasses and ceramics are routinely used in many civilian and military structures. Dynamic fracture characterization of these high-stiffness and low-toughness materials often poses severe challenges to legacy optical methods because: (a) the crack tip opening displacements and deformations are often extremely small, estimated to be < 100 nm, and highly localized, (b) the crack growth is highly transient with speeds exceeding 1500 m/s attained within a couple of microseconds after initiation, and (c) it often involves crack branching. The absence of an easy-to-use, full-field, optical method capable of mapping extremely small deformations over relatively large regions-of-interest (ROI) (say, 75-100 mm square) to examine these issues have also been responsible for the lack of progress towards addressing these basic questions since popular methods such as photoelasticity, Coherent Gradient Sensing (CGS) and Digital Image Correlation (DIC) are tacitly assumed to be capable of quantifying the mechanical fields near growing cracks in transparent glasses and ceramics. However, it is much more challenging than this common perception because (a) soda-lime glass (SLG) has a stress-optic constant 30-50 times lower than birefringent polymers often used in photoelastic investigation, (b) CGS would need a very large diameter coherent laser beam and an unrealistic grating separation distance (of over 20 m when, say, 25 μm pitch Ronchi rulings are used) to

laterally shear the object wave front, (c) DIC would need to be able to measure crack tip displacements of ~100 nm at nominal optical magnifications (say, 0.5X) and at crack speeds of over 1500 m/s. These are indeed severe experimental challenges to the state-of-the-art.

In light of the above, the dynamic fracture mechanics of brittle materials has routinely been studied in the past using loading rate dependent glassy polymers instead. For example, Dally et. al [23, 24] investigated dynamic fracture in Homalite-100 along with a Cranz-Schardin high-speed camera, by relating the instantaneous stress intensity factor with the velocity of a propagating crack. The recorded photoelastic fringes and the resulting stress intensity factor, $K_I(t)$, and crack velocity plot are shown in Figure 1.3 and Figure 1.4, respectively. The crack did not initiate until a minimum value of SIF, K_{Im} = 0.418 MPa√m, which represents arrest toughness. Once the crack initiated, crack velocity reached 200 m/s almost instantaneously. Subsequently, the SIF increased continuously to 1.38 MPa√m in the transition region, where successful crack branching occurred.

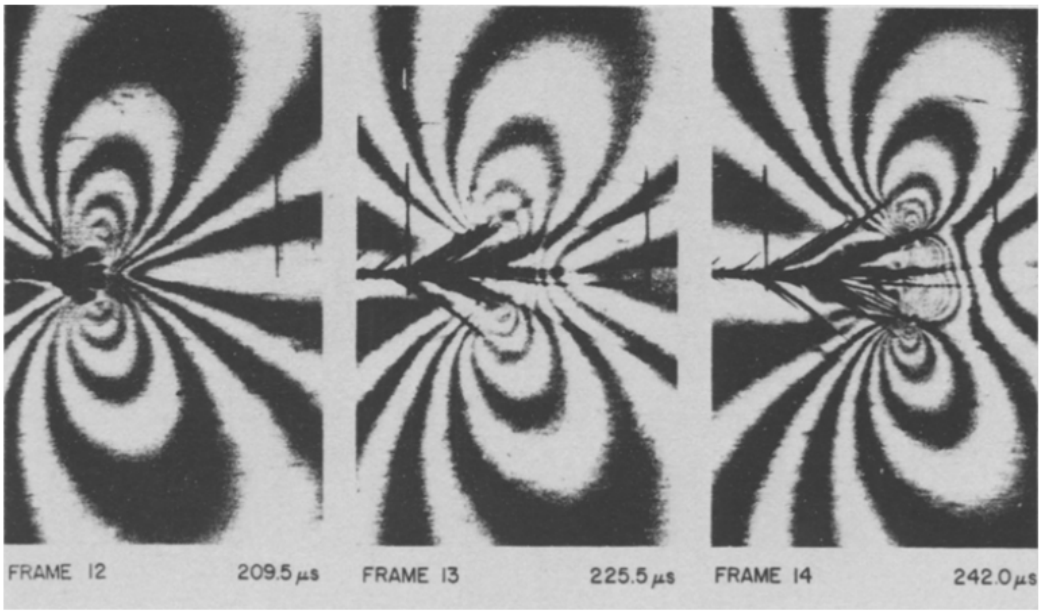

Figure 1.3: Isochromatic fringe pattern during crack propagation, prior to initiation, at initiation and after branching [23].

Bradley et. al [25] also used photoelasticity to investigate propagating cracks in Homalite-100 material. Single edge notched specimens (3/8 in. × 10 in. × 15 in. plates) were subjected to tensile load and the dynamic photoelastic fringes were studied using modified Schardin-type camera with 16-spark gap illuminators. They evaluated both stress intensity factor and crack length histories. Shukla et. al [26] used dynamic reflection photoelasticity to investigate functionally graded materials (FGM) in conjunction with high-speed photography. They employed birefringent coatings due to the opaqueness of FGM specimens to obtain isochromatic fringes around the crack tip. A modified single edge notch specimen was subjected to tensile loading and the $\dot{a} - K(t)$ plots were obtained from optical measurements. The mechanical fields in the vicinity of dynamically propagating crack tip were well represented using higher order terms in the asymptotic series.

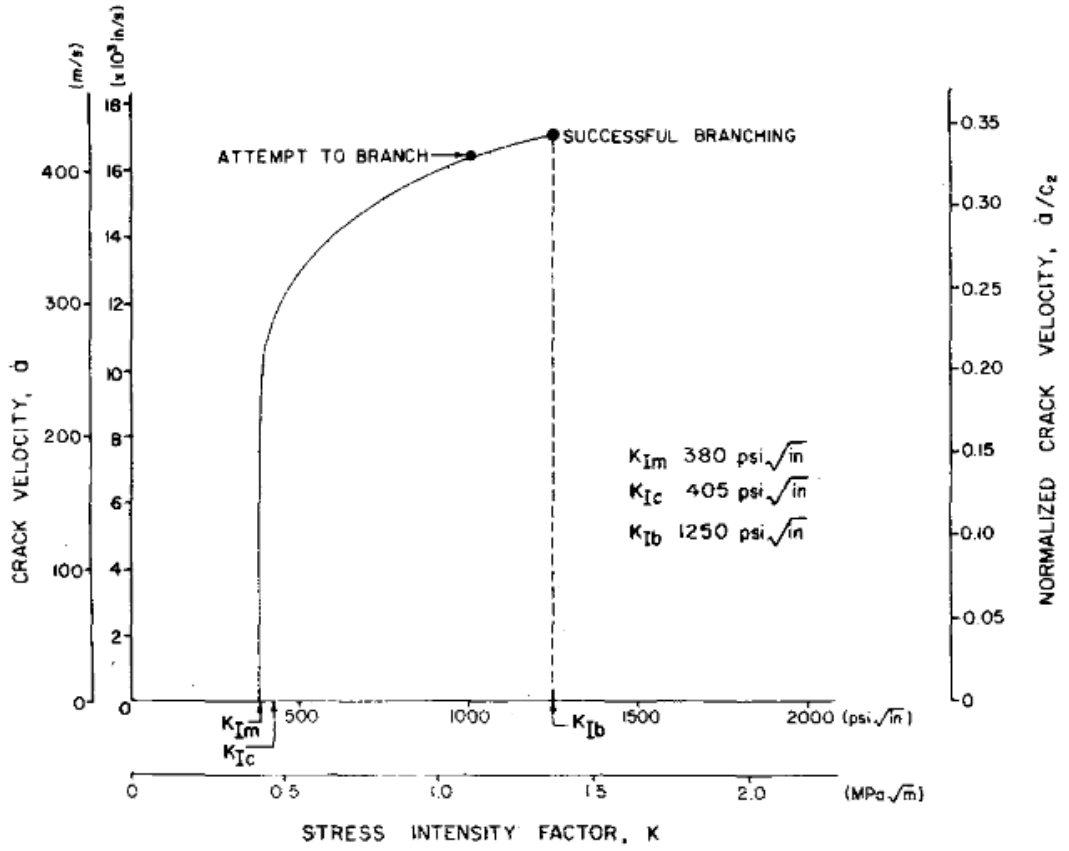

Figure 1.4: Variation crack velocity with stress intensity factor for Homalite-100 [23].

Kobayashi and his associates [27] investigated crack branching using photoelastic experiments, also in Homalite-100 polyester, and proposed a necessary condition based on a critical dynamic stress intensity factor and a sufficient condition of minimum characteristic distance for crack curving. The transmission-mode CGS method was employed by Tippur et al. [28] and Krishnaswamy et al. [29] to investigate dynamic crack growth in edge-cracked PMMA plates subjected to impact loading by mapping crack tip stress gradients near growing cracks. Optical methods have also played a major role in dynamic fracture mechanics study of non-transparent brittle materials. A reflection-mode CGS was introduced by Tippur et al. [30] to study front-coated PMMA mirrors and subsequently used to evaluate notch initiation toughness of bulk metallic glasses [31]. Lately, DIC methods have been popular in the study of dynamic fracture mechanics of polymers [32-37], metals [38, 39], geomaterials [40-42], and composites [43-45] as they are relatively easy-to-implement and provide full-field displacement information [46-48]. Kirugulige and Tippur [49] were the first to use 2-D DIC for characterizing dynamic fracture of epoxy-based syntactic foams along with ultrahigh-speed multi-sensor digital photography. In that work, the crack opening and sliding displacement contours were visualized before crack initiation and during crack propagation as shown in Figure 1.5(A), (B), (C), (D). By performing over-deterministic least-squares analysis on measured crack tip fields, stress intensity factor histories and mode-mixities were obtained and the plots are shown in Figure 1.5(E) and (F). From, the results it was observed that, crack growth in syntactic foam occurs predominantly under mode-I conditions and in agreement with a macroscopically homogeneous and isotropic material behavior. The experimental results compared well with finite element analysis results. Lee and Tippur [50] extended DIC to investigate stress-wave induced fracture of graphite fiber reinforced epoxy laminates. The instantaneous crack tip locations were identified using high-speed photographs to

determine dynamic crack growth behavior in terms of stress intensity factors and energy release rate histories to study fiber orientation effects. Makki et al. [51] employed 3D DIC and investigated the performance of laminated glass due to blast loading to evaluate the structural integrity.

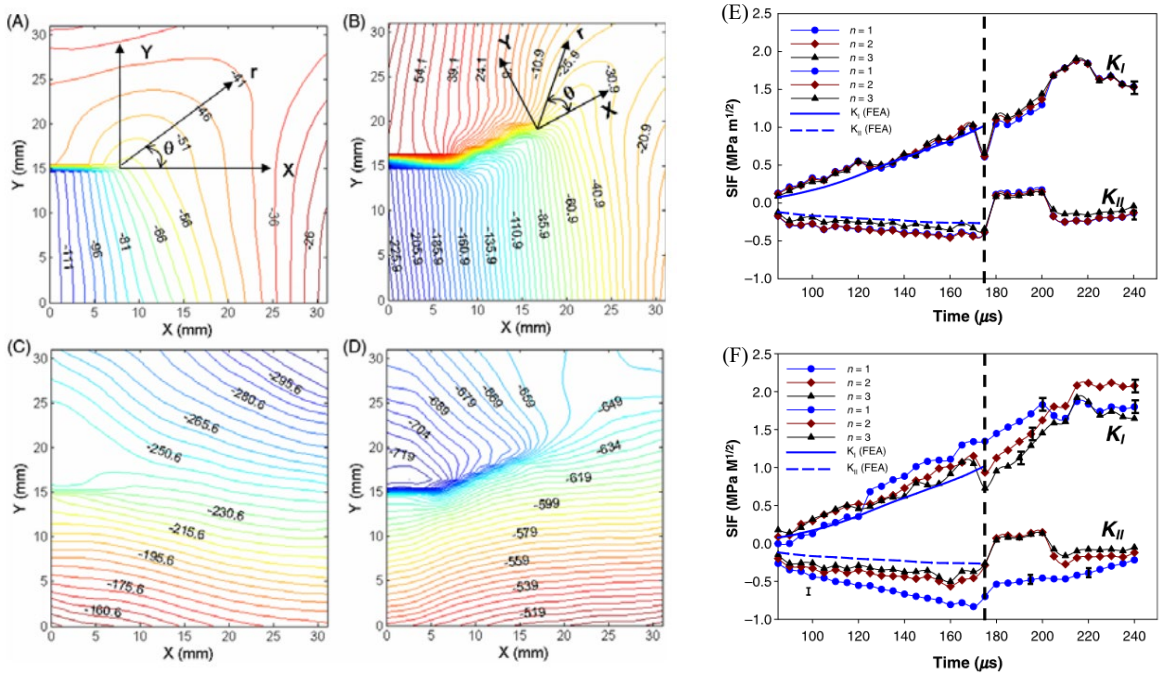

Figure 1.5: (A) Crack opening displacement and (B) sliding displacement prior to crack initiation and (C) crack opening displacement and (D) sliding displacements during mixed-mode crack propagation in syntactic foam sheets, (E) mode-I strss intensity factor histories, and (F) mode-II stress intensity factor histories in syntactic foam sheet. [49]

Recently, material characterization of additively printed materials in polymers and metals have been performed using DIC method. Isaac et. al [33] implemented a hybrid DIC-FEA approach and the effect of loading rate was investigated to study the fracture behavior in additively printed ABS. Using this hybrid approach, the in-plane displacements obtained from image correlation were enforced on the finite element model as boundary conditions. Subsequently, the Abaqus finite element software (v16.1) was run and the *J*-integral, mode-I and mode-II stress intensity factors were determined by inputting crack tip location and its orientation. In another

study conducted by Isaac et. al [35], the fracture behavior of additively manufactured metal Scalmalloy® was performed to investigate the role of build orientation, loading-rate, and heat-treatment on critical energy release rate and crack growth resistance behaviors. DIC was extended to investigate dynamic fracture of 3D printed rock-like materials by Sharafisafa et. al [40]. Disc specimens were prepared with and without flaws and subjected to impact loading using a split Hopkinson pressure bar to visualize and quantify crack initiation and propagation. Aliabadian et. al [52] applied DIC method for experimental and numerical study of crack initiation, propagation and coalescence of new cracks in rocks. Their work focused on the applicability of 3D printing coupled with DIC and bonded particle model (BPM) for simulating the behavior of natural rocks with pre-existing flaws. More recently, Miao et. al [46] employed DIC to perform mechanical characterization of cellulose nano-paper (CNP) under stress wave loading producing crack speeds of 600-700 m/s.

In addition to the above popular optical methods applied to investigate fracture, a full-field optical method called Digital Gradient Sensing (DGS) to measure small angular deflections of light rays proportional to in-plane stress gradients in transparent solids was introduced more recently by Periasamy and Tippur [53]. The authors demonstrated the utility of the method for both static and dynamic investigations [54]. Subsequently, DGS method was extended by Jain and Tippur [55, 56] to evaluate surface slope and out-of-plane displacements to study opaque materials under stress wave loading. Recently, Sundaram and Tippur [57] extended DGS to the problem of dynamic crack-interface interactions in PMMA bilayers. They observed different crack growth behaviors across a discrete interface oriented normally to an incoming mode-I crack. The measured crack tip parameters showed that if the interface experienced tensile stress waves in excess of its tensile strength, a debond nucleation occurred at the interface prior to the arrival of the mode-I

mother crack resulting in branching; otherwise, branching did not occur [19]. More recently, Sundaram and Tippur [19, 58] have used DGS coupled with ultrahigh-speed photography to characterize static and dynamic fracture of SLG material. They were able to quantify fracture parameters including crack velocity, stress intensity factors, and energy release rate from their optical measurements at crack initiation and at crack branching. Miao et. al., extended DGS along with finite difference based least-squares integration (HFLI) scheme to evaluate stress fields using the measured stress gradients. Subsequently, Miao demonstrated the measurement of micro-radian surface slopes over the large (50mm × 75mm) region of interest at micro-second temporal resolution using r-DGS method. Further, they measured sub-micron scale out-of-plane deformations in a [59] carbon fiber reinforced plastic (CFRP) plate subjected to impact loading. Miao et. al., [60] successfully employed r-DGS to study the effect of loading rate and to evaluate instantaneous crack tip velocities and stress intensity factors of CFRP plates.

Part-2: Structures often fail in service due to combined tensile and shear loads resulting in mixed-mode fracture. Therefore, understanding the structural integrity under these conditions is critical. In this dissertation research, the fracture characteristics of SLG plates is investigated under in-plane mixed-mode loading conditions by performing full-field optical measurements during impact loading events. Again, due to the lack of suitable full-field optical technique to investigate SLG, the previous investigations on this topic are generally limited to brittle polymers [49, 55, 61-69] and comparable works on glasses are not reported. For example, Mason et al. [61] studied dynamic mixed-mode, *K*-dominant, crack tip fields in PMMA using the coherent gradient sensing (CGS) method. The ability of that method to quantify dynamic mixed-mode crack tip deformations accurately was tested in their work. Guo et al. [62] studied dynamic mixed-mode fracture in three-

point bend concrete specimens using moiré interferometry along with ultrahigh-speed photography. Kirugulige and Tippur [63] studied mixed-mode dynamic fracture of functionally graded materials (FGM). They tested glass-filled epoxy sheets using reflection-mode CGS and high-speed photography to map instantaneous crack tip deformations. The fractured specimens and mode-I, mode-II stress intensity factor histories are shown in Figure 1.6. Two configurations were studied namely crack on compliant side ($E_1<E_2$) and crack on the stiffer side ($E_1>E_2$). Their experimental results showed crack initiated earlier on the stiffer side in comparison to compliant side. Further, crack paths and velocities were different in each case. Kirugulige and Tippur [49] also measured mixed-mode fracture parameters in syntactic structural foams experiencing stress wave loading.

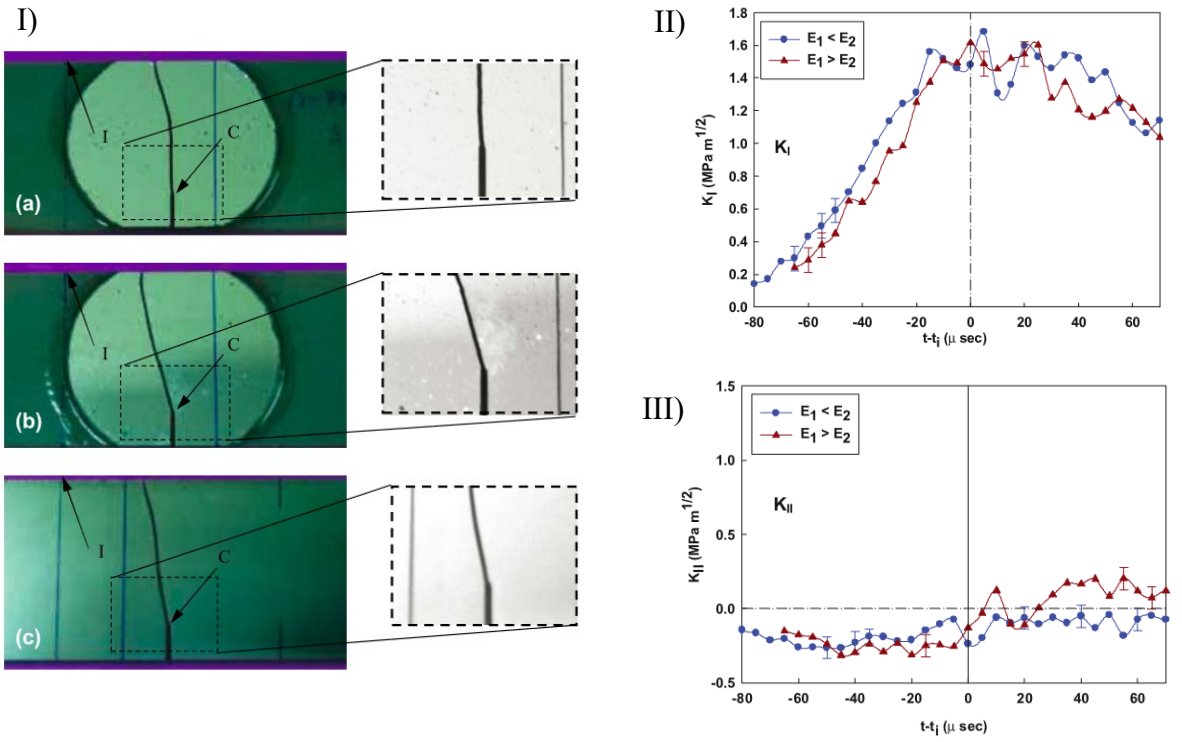

Figure 1.6: I) fractured specimens for FGM with a crack on the (a) compliant side ($E_1<E_2$), (b) stiffer side ($E_1>E_2$) and (c) a homogeneous specimen. (I) is loading point and C is initial notch-tip. (II) mode-I stress intensity factor, K_I histories and (III) mode-I stress intensity factor, K_I histories. Time, t-t_i corresponds to crack initiation time instant. [63]

They mapped crack opening and sliding displacements around a moving crack tip and quantified temporal evolution of fracture parameters. Jain and Tippur [55] successfully investigated dynamic fracture in PMMA by extending reflection-mode digital gradient sensing (r-DGS) method for visualizing and quantifying fracture parameters. The stress intensity factor histories in the mixed-mode cases conformed well with the physical aspects both before and after crack initiation. Recently, Sundaram and Tippur [65] comparatively investigated dynamic fracture of two popular transparent polymers, PMMA and Polycarbonate, under mixed-mode loading conditions using transmission-mode DGS and developed fracture envelopes for each. The crack tip fields were visualized using DGS method and fracture parameters obtained are shown in Figure 1.7.

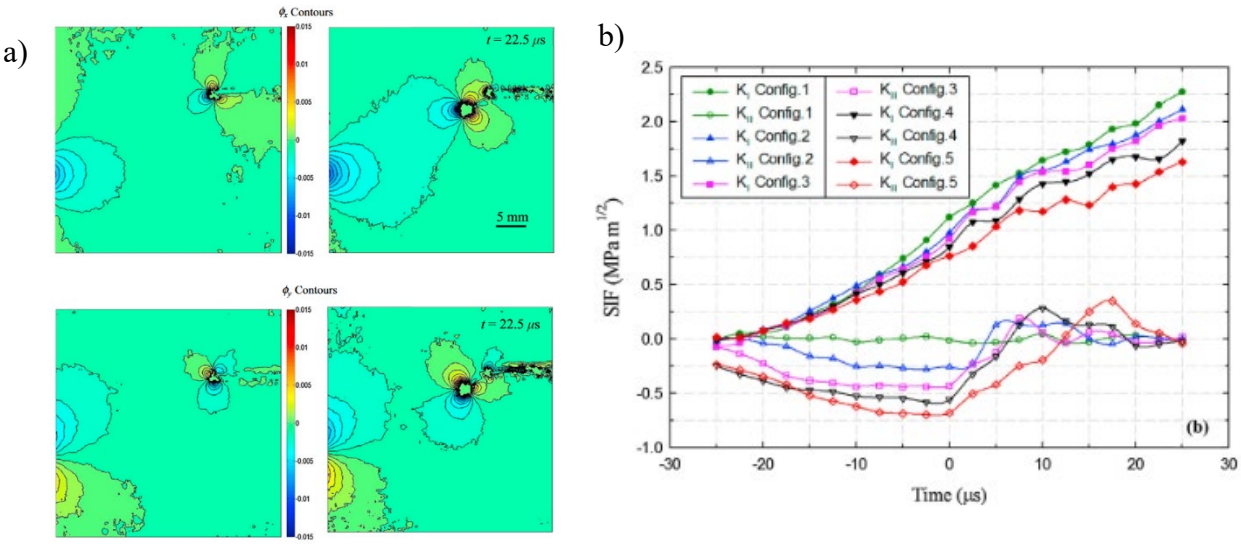

Figure 1.7: a) angular deflection contours proportional to stress gradients in PMMA specimen, with initial notch length, a = 15mm, eccentricity, e = 15 mm, b) mode-I and mode-II stress intensity factor histories for different PMMA configurations. Time equal to zero corresponds to crack initiation time instant at the original notch tip. [65]

Their results suggested that in PMMA, mode-I stress intensity factor continued to increase even after crack initiation, in contrary to the polycarbonate where the increasing trends are at much slower rates (polycarbonate SIF histories plots are not shown here for brevity). Mixed-mode

dynamic fracture studies were also carried out in geomaterials - sandstone and granite by Braunagel and Griffith [66]. They tested notched semi-circular specimens using a split Hopkinson pressure bar; to obtain various mixed-mode configurations, orientation of notch relative to loading direction was altered. Their results showed a decrease in energy release rate with increasing mode-mixity for Berea Sandstone. They also observed that mixed-mode propagation to be energetically favorable than pure opening mode propagation in sandstone, while the opposite to be true for granite. Snow et al. [67] investigated mixed-mode fracture of bovine cortical bone subjected to impact loadings. Aliha et al. [70] studied fracture toughness of Harsin marble under mixed-mode conditions ranging from pure mode-I to pure mode-III using edge-notched disc bend specimens. Their results indicated that the fracture toughness decreased with increase in mode-mixity.

Several numerical studies [64, 71-76] on dynamic mixed-mode fracture mechanics have also been reported. Kirugulige and Tippur [64] studied mixed-mode dynamic crack growth behavior in a compositionally graded glass-filled epoxy using finite element simulations. An intrinsic cohesive element method with a bilinear traction separation law was used to model mixed-mode dynamic crack growth. Their finite element simulations captured the experimental characteristics of crack kinking under mixed-mode dynamic loading conditions. Asareh et al. [71] used a modified extended finite element method (XFEM) to study dynamic mixed-mode fracture. A non-nodal XFEM was developed within an explicit time integration scheme for modeling discontinuities in planar bodies and mimic mixed-mode crack propagation paths in three-point bending experiments. The dynamic mixed-mode fracture has also been studied using peridynamics for two-dimensional elastic cracked solids in Ref. [72]; three types of mixed-mode crack problems were investigated and dynamic stress intensity factors were evaluated. Cheng et al. [73] investigated dynamic fracture in functionally graded materials using peridynamics. The mixed-

mode loading was enforced by applying eccentric impact load relative to the pre-crack, and their results agreed well with the experiments.

Part 3: The intriguing phenomenon of crack branching and fracture mode-transition of a dynamically growing mode-I crack to mixed-mode daughter cracks remain unresolved from fracture mechanics perspective. A range of hypotheses such as the dynamically growing crack tip (i) reaching a critical velocity, (ii) stress intensity factor attaining a critical value, (iii) the hoop stress ahead of it reaching a maximum at an angle other than the self-similar growth direction, (iv) encountering stress wave pile-up ahead of it, (v) exciting of a void and microcrack nucleation at increasingly greater distances ahead of it, have all been alluded to as potential causes for crack branching to occur in various theoretical, numerical and experimental reports [77-85]. Due to the widespread use of SLG where crack branching is a common phenomenon, understanding it becomes highly relevant but lacking. Again, this is primarily due to the fact that investigation of dynamic crack branching in SLG is extremely challenging owing to severe spatial and temporal resolution requirements noted previously. Some earlier studies have reported on crack branching in highly brittle materials such as rocks and glass without using optical methods. For example, Bieniaswki [86] investigated dynamic crack branching in rocks and reported that a crack branched upon reaching a terminal velocity. Using a multiple-spark high-speed camera Schardin [87] studied fracture of glass and observed that the crack propagated with a constant velocity of ~1500 m/s. In addition, in the presence of an imposed far-field tensile stress, the crack propagated for a shorter distance before branching and the number of branches increased with the applied stress. In another study, Doll [17] investigated crack propagation in different glasses - plate glass, FK-52 and Duran 50 - and noted that crack branching depended on (a) the crack attaining a maximum velocity and, (b) the energy release rate exceeding a critical value. Sundaram and Tippur [19, 58] were the first

to quantitatively study crack tip fields in SLG using a full-field optical technique. They were able to quantify not only crack velocities but fracture parameters namely, stress intensity factor and energy release rate histories, from the start to the finish that included crack initiation, mode-I crack growth and mixed-mode crack branching.

Several analytical studies on dynamic crack branching of brittle materials have also been carried out by various researchers. Yoffee [81] investigated a straight crack moving through an elastic medium and described the stress fields around the propagating crack. She observed that the crack tended to curve when propagating at a critical velocity of ~0.6C_s (C_s = shear wave speed) with the maximum hoop stress occurring at 60° relative to the self-similar crack growth direction. Eshelby [88] reviewed some of the energy relations and evaluated the energy required for dynamic crack branching based on elastic energy-momentum tensors.

In addition to the above experimental and analytical contributions, a considerable amount of data on crack branching has been generated over the years from numerical simulations. Needleman et al., [89] studied dynamic crack branching in PMMA using cohesive elements. They found that the crack velocities reached ~45% of the Rayleigh wave speed at branching. Furthermore, their study revealed crack speed oscillations that eventually led to crack branching at an angle of 29° from the initial crack plane. When the crack growth was restricted to the crack plane, the crack accelerated initially and then propagated at a constant velocity. Zhou and Molinari [90] also studied dynamic brittle fracture by introducing cohesive elements into their finite element model to address mesh dependency. Recently, Zeng et al., [91] simulated dynamic crack propagation in brittle and quasi-brittle materials using embedded finite element method (EFEM) and extended finite element method (XFEM). They concluded that the crack growth history from XFEM agreed better with the experimental data than EFEM. The phase-field method was employed by Karma et

al., [92] to simulate dynamic brittle fracture of mode III cracks. Their simulations show occurrence of branching instability at a fraction of the wave speed. Ha and Bobaru [93] employed peridynamics to investigate dynamic crack branching in SLG. They noted that branching patterns correlated well with that of experimental results in addition to crack propagation velocities. Furthermore, they noticed that branching occurred in a region where crack propagation velocities reached higher fraction of the maximum value along with roughening of the fractured surface before crack branching and a detectable reduction in crack velocities after the crack branching event.

Part-4: During service, cracks tend to initiate and grow in regions of high stress concentration in a structure. In high stiffness and low toughness brittle structural materials such as soda-lime glass (SLG), hairline cracks emanating from stress concentrations can occasionally heal naturally [94-96] upon unloading. Such self-healed cracks are optically invisible and can go undetected, making structures highly vulnerable to premature and catastrophic failure during subsequent overload cycles. In this context, crack initiation and crack growth from a self-healed crack in soda-lime glass is important to understand and hence investigated in this work.

The slow crack growth in soda-lime glass is said to occur in three characteristic phases [97-99]. In the first phase, the crack velocity dependence on stress intensity factor is governed by an exponential relationship. In the second phase, the crack velocity is said to be nearly independent of the stress intensity factor. After an increase of stress intensity factor, higher crack velocity occurs in the third phase, followed by an unstable crack propagation. Both first and second phases are considered slow (subcritical) crack growth regimes. Wiederhorn and Townsend [94, 97, 99] were among the early investigators to examine slow crack growth in self-healed soda-lime glass plates. They generated cracks in double cantilever beam specimens and observed crack closures

upon unloading. The closure was attributed to partial reestablishment of chemical bonds between the newly formed surfaces. Their results indicated a lower stress intensity factor and surface energy for self-healed cracks when compared to unhealed cracks. The critical stress intensity factor and fracture surface energy for self-healed crack were reported by them as 0.17 MPa√m and 0.2 ± 0.2 J/m^2, respectively. This was significantly lower relative to the critical stress intensity factor of the virgin material, at ~0.76 MPa√m, indicating substantial diminution of fracture toughness of SLG due to a self-healed crack relative to the virgin material. They also reported that the critical stress intensity factor increased with an increase in relative humidity (RH). Michalske et al., [95] investigated self-healed cracks in soda-lime glass using double cleavage drilled-hole compression (DCDC) specimens. They reported strain energy release rate for crack closure to be 0.15 J/m^2. Their results also showed that the healed cracks required more energy to reopen (at a RH < 50%) when compared to crack closure counterparts. At RH > 50%, the amount of strain energy release rate required for reopening of healed cracks was almost same as that for crack closure. Due to challenges associated with achieving controlled slow crack growth in a highly brittle material such as soda-lime glass, very few works can be found on this topic in the subsequent literature. Recently, To et al. [100] have revisited slow crack growth in SLG. They have successfully created pre-cracks in a beam using a bridge-flexure method and conducted three-point bend experiments on specimens with healed cracks to evaluate the critical stress intensity factors. Similar to prior works, they have employed far-field applied loads to quantify the local fracture parameters.

Despite the availability of a number of sophisticated full-field interferometric and vision-based techniques, very few optical investigations on this topic can be found in the literature due to extreme sensitivity requirements to study SLG. An exception in this regard is a report by Ferretti et al., [101]. These authors examined intriguing questions concerning inelastic (plastic) crack tip

deformations in annealed soda-lime glass. Using electronic speckle pattern interferometry they evaluated the crack opening displacements near a stationary natural crack grown ahead of a notch in a beam. Their measurements suggest the presence of a bulk process zone confined to the crack tip vicinity. A numerical analysis employing the finite element method and Gurson-like material model to account for microvoids and microcracks matched measurements better than LEFM and cohesive zone models. In another study, Singh et al., [102] optically investigated crack growth in glass. They adopted holographic interferometry to monitor crack growth. By using Fourier transform-based fringe analysis and phase-unwrapping methods, the crack location was identified. However, no quantification of fracture parameters is reported in their work. Sundaram and Tippur [103] were the first to demonstrate the feasibility of a relatively new optical method called digital gradient sensing (DGS) to quantitatively visualize two orthogonal stress gradients near a stationary crack and extract fracture parameters in SLG.

A wedge splitting test (WST) geometry has been used by many investigators to achieve slow crack growth in ultra-brittle materials including cementitious and geomaterials [104, 105]. This geometry enables controlled slow crack propagation using a relatively small force applied in a standard testing machine [104]. Bruhwiler et al., [105] and Korte et al., [106] used WST geometry to study stable fracture in concrete and evaluate fracture parameters. Walter et al., [107] investigated steel-concrete interfaces using a WST configuration and determined fracture parameters. Slow crack propagation in commercial refractory materials has also been studied using this method. Varga et al., [108] evaluated fracture parameters using WST geometry and digital image correlation (DIC). Dai et al., [109] used WST configuration to study quasi-brittle magnesia refractories. They evaluated crack lengths in magnesia and magnesia spinel materials during cyclic loading of WST specimens based on the localized strains evaluated using DIC. The

refractory materials that showed reduced brittleness were found to consume a small amount of energy for crack initiation but a large amount of energy for subsequent crack propagation.

1.3 Research objectives

The above literature suggests that there is a need for quantifying fracture parameters from direct crack tip field measurements in soda-lime glass (SLG) to understand its quasi-static and dynamic failure behaviors better. Here, it is hypothesized that vision-based optical methods can contribute greatly towards this goal. In particular, the method of Digital Gradient Sensing (DGS) developed at Auburn University over the past decade is beneficial in terms of meeting the stringent requirements associated with low-toughness and high-stiffness attributes of SLG. Thus, the broad objective of this research effort is to comparatively assess DGS relative to other popular approaches of experimental mechanics to study mode-I fracture of SLG before extending it to advanced topics of mixed-mode fracture, cascading crack branch formation and slow crack growth in self-healed SLG plates. The specific tasks for achieving the above objective are as follows:

- Comparatively evaluate DGS as an optical tool for measuring crack tip fields relative to other popular methods used previously to study similar problems,
- Examine the feasibility of quantifying fracture parameters from measured crack tip fields using DGS,
- Investigate mixed-mode fracture behavior of SLG and establish a fracture envelope and fracture toughness vs. mode-mixity relation for the material,
- Extend DGS to study cascading crack branching phenomenon in SLG and identify potential fracture mechanics-based precursors for the same,
- Extend DGS to study ultraslow crack growth behavior in SLG and assess mechanical performance degradation in the presence of self-healed cracks.

1.4 Organization of the dissertation

This dissertation is organized into seven chapters including the current one. In Chapter 2, three different full-field optical methods - photoelasticity, Digital Image Correlation (DIC), and Digital Gradient Sensing (DGS) - are briefly reviewed. A comparative study of dynamic mode-I crack initiation and growth in soda-lime glass using these three full-field optical methods are presented in Chapter 3. The outcome of the study including the pros and cons of each method for SLG are discussed. In Chapter 4, Investigation of dynamic mixed-mode fracture ranging from mode-I to nearly mode-II in SLG using DGS is described. Experimental details pertaining to specimen geometry and loading configuration besides results from optical measurements and mixed-mode fracture characteristics of SLG are reported in this chapter. In Chapter 5, dynamic cascading crack branching phenomenon is reported. Results on dynamic fracture parameters in single and cascading branch formations from multiple experiments and configurations are described in this chapter before quantifying a few plausible fracture mechanics-based crack branching precursors. In Chapter 6, details on crack initiation and slow crack growth in self-healed SLG plates is included. Both experimental details and supplementary finite element simulations are provided in this chapter to assess fracture parameters for a self-healed crack. Finally, major conclusions of this dissertation along with potential future topics are recorded in Chapter 7. A few miscellaneous and supplementary research perusals during this dissertation research are included in different appendices at the end.

Chapter 2. Experimental methods

In this chapter, three full-field optical methods attempted in the study of SLG fracture under dynamic conditions are briefly reviewed. Each method along with its working principles is described. First, a commonly used full-field optical method, photoelasticity is discussed. Next, another popular full-field optical method, Digital Image Correlation (DIC), is reviewed. Lastly, the full-field optical method, Digital Gradient Sensing (DGS) is described.

2.1 Photoelasticity

Photoelasticity is one of the well-established full-field optical methods used for studying dynamic fracture of birefringent materials in experimental mechanics. Many materials including glasses exhibit stress induced birefringence; that is, the light rays passing through the stressed material get resolved into to two orthogonally polarized components with the phase difference related to the local state of stress in the solid. In this work, a dark-field circular polariscope is used to study photoelastic manifestations due to stresses in the form of optical intensity fringes. The schematic representation of dark-field circular polariscope is shown in Figure 2.1. It consists of a monochromatic expanded light beam passing through a polarizer, a pair of quarter-wave plates, and an analyzer before being recorded by a camera. The expanded light beam propagates first through the linear polarizer, which converts light into a plane polarized beam with oscillations along its polarization axis in the vertical direction. The emergent light passes through the quarter-wave plate, which has its 'fast' and 'slow' axes set at 45° to the plane of polarization. This quarter wave plate resolves the light vector into two, one along each of the axes, and introduces a 90° phase difference between them. This results in a circularly polarized light that exits and propagates through the planar SLG sample of interest. In the unstressed state of the specimen, a constant phase is introduced to the light waves before they enter the second quarter-wave plate. The second

quarter-wave plate with its fast and slow axes opposing that of the first, removes the previously introduced phase difference. The emergent waves are resolved along the polarization axis of the analyzer in the horizontal direction. This results in an infinite dark fringe (fringe spacing infinity under ideal conditions) before being recorded by the camera. When the specimen subjected to non-uniform mechanical stresses, different phase differences are introduced to the light waves departing the specimen at different locations of the solid body, resulting in the formation of light intensity - dark and light - fringes over the entire field.

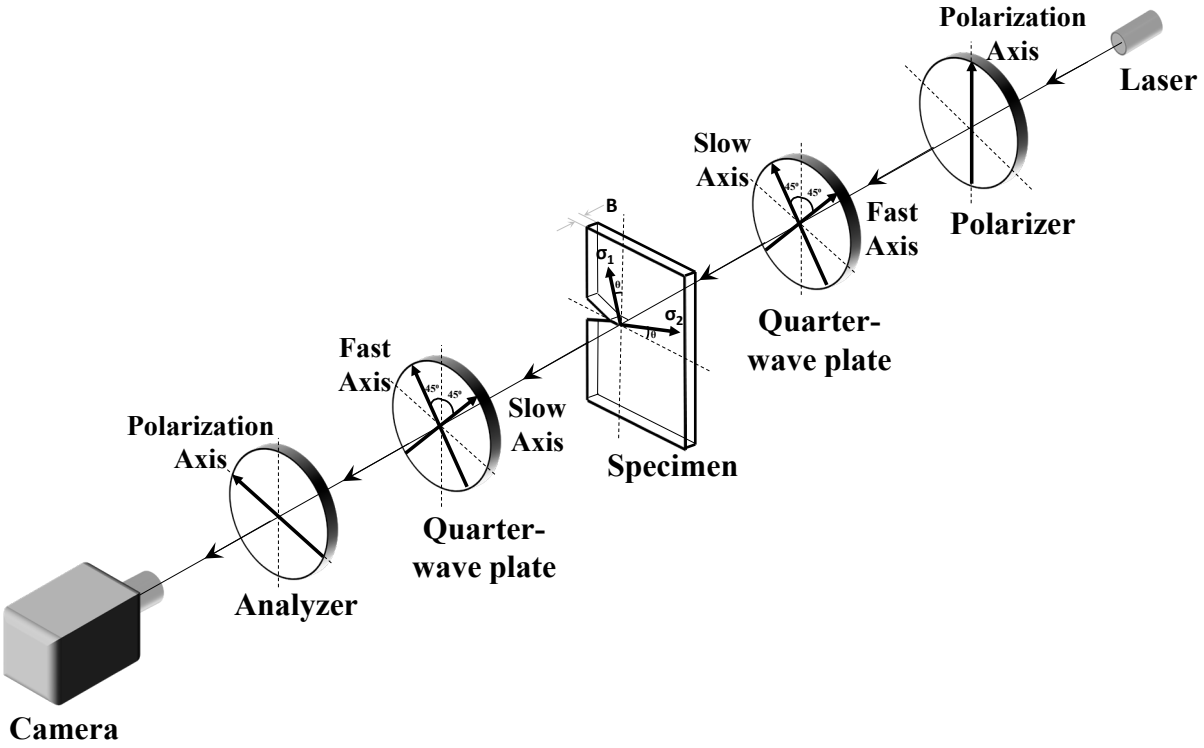

Figure 2.1: Schematic representation of dark-field circular polariscope

These analog fringe patterns can be assigned fringe numbers by the user based on the boundary conditions of the problem. The local stress at a point of interest can be obtained as,

$$\sigma_1 - \sigma_2 = \frac{N f_\sigma}{B} \tag{2.1}$$

where, $\sigma_1 - \sigma_2$ is difference in-plane principal stresses, N is fringe order, f_σ is the stress-optic constant and B is the nominal specimen thickness. In dark-field circular polariscope setup with a monochromatic light source, the dark fringes correspond to integer orders.

2.2 Digital image correlation

2-D digital image correlation has become a popular full-field optical/vision-based method in recent years since its first introduction in the early 1980s. In this method, a random black and white speckle pattern is sprayed onto a specimen to create a trackable texture. Ordinary white light is used to illuminate the pattern during the experiment. The speckle pattern is monitored by recording the gray scales using a digital camera before and after loading the specimen or at different time instants during a dynamic event.

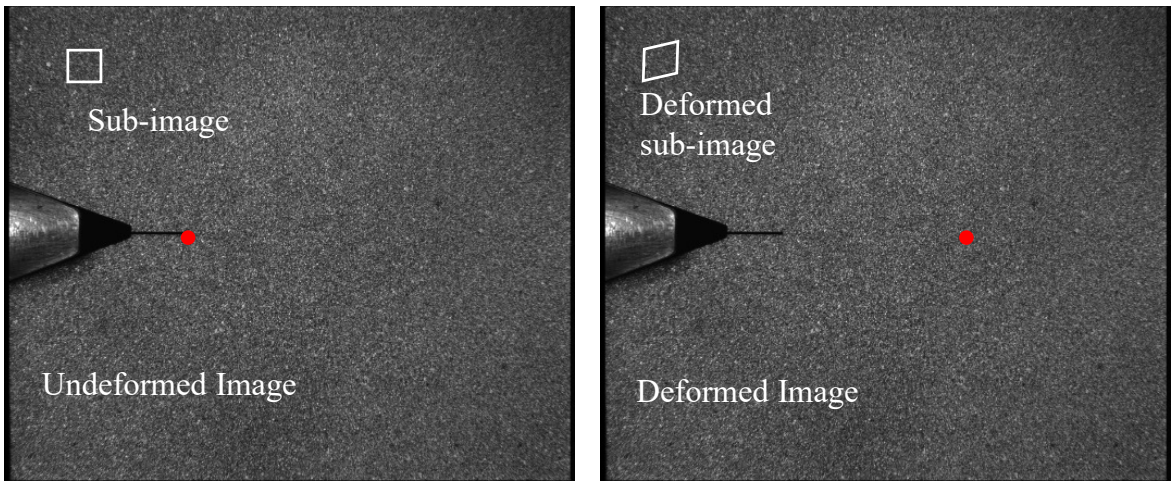

Figure 2.2: Speckle images near a crack tip region in a specimen captured by a digital camera in undeformed and deformed states of specimen.

To evaluate the surface displacements at different load-steps or instants of time, both the reference image in the unloaded state and the one in the deformed state are segmented into sub-images or subsets [15, 110]. The sub-image in reference state or undeformed state of specimen are located in various deformed images via gray scale correlation operation, as shown schematically

in Figure 2.2. During correlation, point *P(x,y)* in the undeformed sub-image is mapped to the corresponding point $P'(\tilde{x},\tilde{y})$ in the deformed sub-image using,

$$\begin{aligned}\tilde{x} &= x + u(x,y)\\ \tilde{y} &= y + v(x,y)\end{aligned} \tag{2.2}$$

where *u* and *v* are displacement components. It is assumed that, these displacement components *u* and *v* can be approximated using a Taylor's series expansion about point $P(x_o, y_o)$. Then, Eq. (2.2) can be expressed as,

$$\begin{aligned}\tilde{x} &= x_o + u_o + \frac{\partial u}{\partial x}\Delta x + \frac{\partial u}{\partial y}\Delta y + \frac{1}{2}\frac{\partial^2 u}{\partial x^2}\Delta x^2 + \frac{1}{2}\frac{\partial^2 u}{\partial y^2}\Delta y^2 + \frac{\partial^2 u}{\partial x \partial y}\Delta x \Delta y\\ \tilde{y} &= y_o + v_o + \frac{\partial v}{\partial x}\Delta x + \frac{\partial v}{\partial y}\Delta y + \frac{1}{2}\frac{\partial^2 v}{\partial x^2}\Delta x^2 + \frac{1}{2}\frac{\partial^2 v}{\partial y^2}\Delta y^2 + \frac{\partial^2 v}{\partial x \partial y}\Delta x \Delta y\end{aligned} \tag{2.3}$$

where $\Delta x = x - x_o$ and $\Delta y = y - y_o$. The Eq. (2.3) gives mapping parameters namely, $u_o, v_o, \frac{\partial u}{\partial x}, \frac{\partial v}{\partial x}, \frac{\partial u}{\partial y}, \frac{\partial v}{\partial y}, \frac{\partial^2 u}{\partial x^2}, \frac{\partial^2 v}{\partial x^2}, \frac{\partial^2 u}{\partial y^2}, \frac{\partial^2 v}{\partial y^2}, \frac{\partial^2 u}{\partial x \partial y}$ and $\frac{\partial^2 v}{\partial x \partial y}$.

The grayscale intensity in digital images in both reference and deformed state change abruptly between pixels. Hence, the data is smoothed over the entire field using smoothing functions. By using a bi-cubic spline interpolation, the gray-scale value of the intensity at any point in the reference images is calculated from,

$$g(x,y) = \sum_{m=0}^{3}\sum_{m=0}^{3} a_m x^m y^n \tag{2.4}$$

where a_m representing the fitting coefficients for the bi-cubic spline. Similarly, for the deformed the image, the bi-cubic spline interpolation function for its gray-scale image is given by,

$$h(\tilde{x},\tilde{y},P) = \sum_{m=0}^{3}\sum_{m=0}^{3} b_m \tilde{x}^m \tilde{y}^n + \alpha \tag{2.5}$$

where b_m are the fitting coefficient for the bi-cubic spline, α is an additional mapping parameter and *P* is a vector with its 13 mapping parameters as components.

In general, the correlation operation maximizes the correlation coefficient expressed as,

$$C = \frac{\sum_{s_p \in s} \left\{ g(S_p) - h(S_p, P) \right\}^2}{\sum_{s_p \in s} g^2(S_p)} \tag{2.6}$$

The correlation coefficient can be expressed in alternative form as,

$$C = 1 - \frac{\sum_{s_p \in s} g(S_p) h(S_p, P)}{\left[\sum_{s_p \in s} g^2(S_p) \sum_{s_p \in s} h^2(S_p, P) \right]^{1/2}} \tag{2.7}$$

The best estimate of the mapping parameters is provided by minimizing the value of C and this expression is computationally easy to implement via optimization methods. Different algorithms including Newton-Raphson [111], coarse-fine and Lavenburgh-Marquardt (L-M) methods [112, 113] are used for this purpose.

2.3 Digital gradient sensing

Transmission-mode Digital Gradient Sensing (DGS) [54] is a relatively new full-field vision-based optical technique. This technique utilizes 2-D DIC described in the previous section to quantify perceived/pseudo speckle shifts due the local state of stress in the specimen. The speckle shifts are evaluated on a planar surface (*not* on the transparent specimen) called the 'target' decorated with sprayed black and white random speckles by photographing them through the region-of-interest (ROI) in specimen, see Figure 2.3. The speckle shifts can be used to evaluate two orthogonal angular deflections of lights rays relative to the reference state. The angular deflections of light rays are shown proportional to two corresponding in-plane stress gradients.

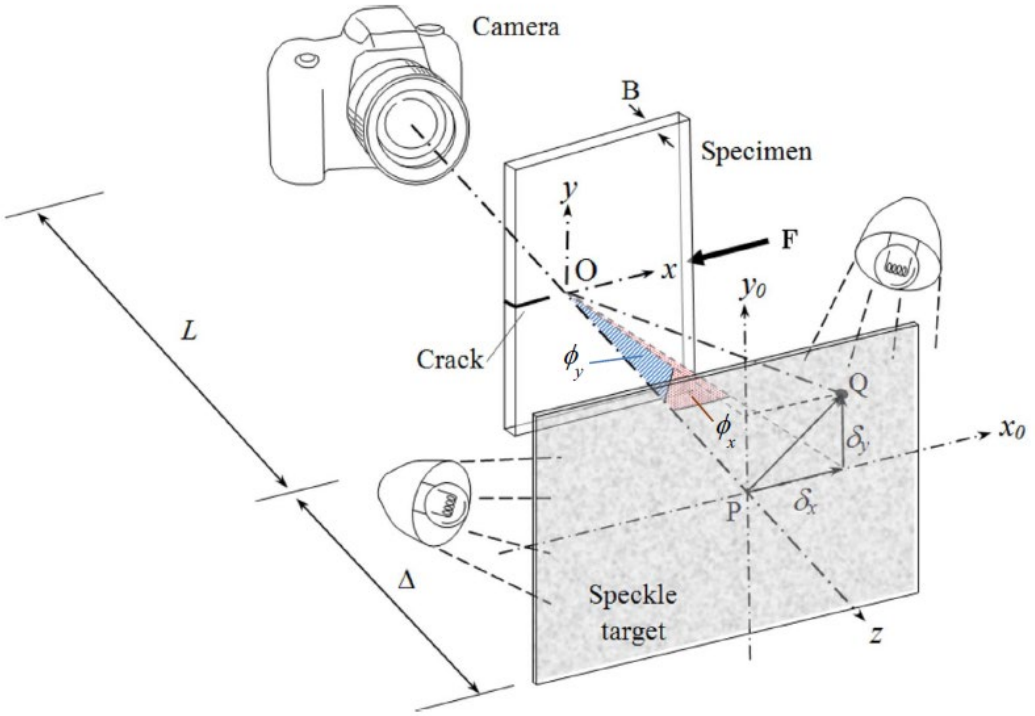

Figure 2.3: The schematic representation of Digital Gradient sensing (DGS) technique to determine planar stress gradients [54].

During the experiment, the gray scales on the target are illuminated using polychromatic lamps. The speckle pattern on the target is photographed first through the unstressed (reference) specimen. That is, the gray scale information at a point P on the target plane (x_0-y_0 plane) through a point O on the specimen plane (x-y plane) is captured by the camera. Upon loading, the non-uniform state-of-stress alters the refractive index of the specimen locally, say, in the crack tip vicinity. In addition, the specimen thickness changes non-uniformly in the ROI due to the Poisson effect. A combination of these two phenomena, commonly referred to as the elasto-optic effect, make the light rays to deviate from their original path as they propagate through the stressed specimen. The speckle pattern is once again photographed through the specimen in the stressed state to record the gray scale at a neighboring point Q on the target through the same point O on the specimen. By correlating the speckle images in the reference and stressed states, local shifts in speckle clusters,

δ_x and δ_y, are quantified using speckle/image correlation algorithms. The resulting optical path change can be expressed as,

$$\delta S(x,y) = 2B(n-1)\int_0^{1/2} \varepsilon_{zz}\, d(z/B) + 2B\int_0^{1/2} \delta n\, d(z/B) \tag{2.8}$$

where B is specimen thickness and n are refractive index of specimen. The two terms represent contribution for optical path change from normal strain, ε_{zz} , and change in refractive index, δn respectively. By using generalized linear elastic principles and Maxwell-Neumann relation, Eq. (2.8) can be written as,

$$\delta n = 2B(D_1 - \frac{\upsilon}{E}(n-1))\int_0^{1/2} \left\{ (\sigma_{xx}+\sigma_{yy}) \left[1 + D_2 (\frac{\sigma_{zz}}{\upsilon\left(\sigma_{xx}+\sigma_{yy}\right)} \right] \right\} d(z/B) \tag{2.9}$$

where D_1 is the stress-optic constant of an optically isotropic solid, υ and E are Possion's ratio and elastic modulus of transparent specimen. $D_2 = \left[\upsilon D_1 + \upsilon(n-1)/E\right] / \left[D_1 - \upsilon(n-1)/E\right]$, the second term, $\delta n = 2BD_2(\frac{\sigma_{zz}}{\upsilon\left(\sigma_{xx}+\sigma_{yy}\right)}$ represents the degree-of-plane strain that can be neglected for plane-stress conditions. σ_{xx}, σ_{yy}, and σ_{zz} are normal stresses in x, y and z directions, respectively. Thus, the above Eq. (2.9) can be reduced to,

$$\delta S(x,y) \approx C_\sigma B(\sigma_{xx}+\sigma_{yy}) \tag{2.10}$$

Where $C_\sigma = D_1 - (\upsilon/E)(n-1)$ is the elasto-optic constant of the specimen material. The stresses σ_{xx} and σ_{yy} denote the thickness-wise averages of Cauchy's normal stress components. Knowing the distance between the specimen and the target planes, Δ, from the experimental setup, the angular deflections of the light rays ϕ_x and ϕ_y in two orthogonal planes (x-z and y-z planes, the z-axis coinciding with the optical axis of the setup and x-y being the specimen plane coordinates) are evaluated:

$$\tan\phi_x = \frac{\delta_x}{\Delta} \text{ and } \tan\phi_y = \frac{\delta_y}{\Delta} \tag{2.11}$$

Due to elasto-optic effect, the angular deflection of a generic light ray will change its optical path. Hence, the propagation vector in relation to the optical path change for small gradients can be given by [30, 53, 114],

$$\hat{d} \approx \frac{\partial(\delta S)}{\partial x}\hat{i} + \frac{\partial(\delta S)}{\partial y}\hat{j} + \hat{k} \tag{2.12}$$

From Eq. (2.10) and Eq. (2.12) direction cosines α and β can be determined as,

$$\alpha = \frac{\partial(\delta S)}{\partial x} = C_\sigma B \frac{\partial(\sigma_{xx} + \sigma_{yy})}{\partial x}, \text{ and } \beta = \frac{\partial(\delta S)}{\partial y} = C_\sigma B \frac{\partial(\sigma_{xx} + \sigma_{yy})}{\partial y} \tag{2.13}$$

For smaller angular deflections ($\delta_x, \delta_y \ll \Delta$), these direction cosines expressions, α and β can be reduced to angular deflections of the light rays ϕ_x and ϕ_y, respectively, as provided in Ref. [53]. The details are not shown here for brevity. That is,

$$\phi_x \approx \alpha, \text{ and } \phi_y \approx \beta \tag{2.14}$$

These angular deflections of the light rays proportional to the gradients of the in-plane normal stresses are expressed as,

$$\phi_{x;y} = \pm C_\sigma B \frac{\partial\left(\sigma_{xx} + \sigma_{yy}\right)}{\partial x; y} \tag{2.15}$$

Chapter 3. Comparative optical study of dynamic crack growth

In this chapter, three different full-field optical methods are comparatively examined to study dynamic fracture of SLG under nominally identical conditions but in separate experiments. Sample preparation, experimental setup, loading configuration and measurement procedures adopted for each method are described and the resulting crack length histories, velocity histories, stress intensity factor histories are presented and analyzed. The contact force histories due to dynamic loading of the specimen are also evaluated. Based on the outcomes, the pros and cons of each method for studying this challenging material system are identified.

3.1 Specimen preparation

Commercially procured transparent SLG plates were used to study dynamic mode-I crack growth leading up to crack branch formation. Specimens were cut using a resin-bonded diamond blade from a single large 5.7 mm thick SLG plate into 150 mm × 100 mm rectangular plates.

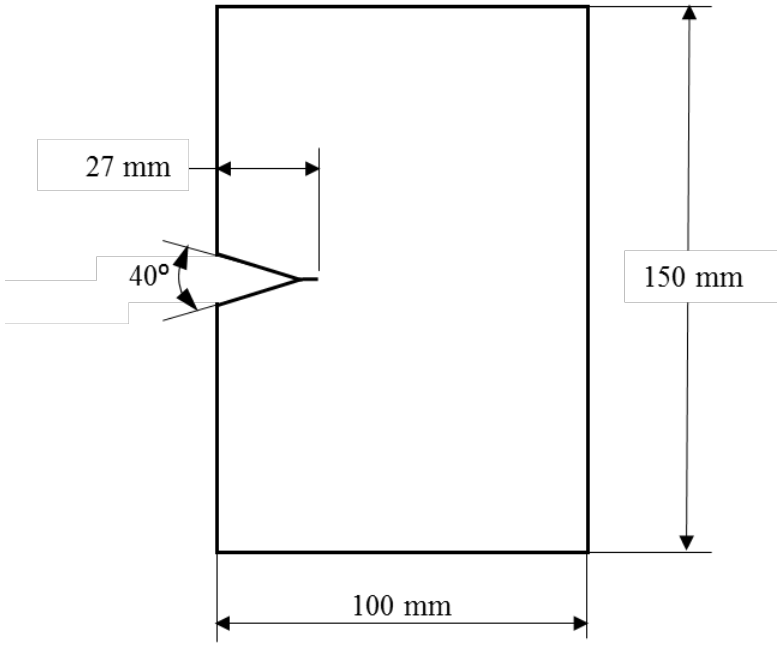

Figure 3.1: V-notched soda-lime glass specimen with an extended notch. (Thickness = 5.7 mm).

A symmetric 40º V-notch was introduced at the mid-span along the long edge of each specimen, as shown in Figure 3.1. The apex of the notch-tip was further extended by 8 mm with a diamond impregnated circular saw of 0.3 mm thickness. A few mechanical and physical properties of SLG relevant to this work are listed in Table 3.1.

Table 3.1 – Some relevant soda-lime glass properties[18]

Property	**Value**
Density, ρ	2500 kg/m^3
Longitudinal wave speed, C_L	5700 m/s
Shear wave speed, C_S	3400 m/s
Rayleigh wave speed, C_R	3100 m/s
Elastic modulus, E	70 GPa
Poisson's ratio, υ	0.22
Tensile strength, σ_t	41 - 180 MPa
Compressive strength, σ_c	330 MPa
Elasto-optic constant, C_σ	-0.027×10^{-10} m^2/N
Stress-optic constant, f_σ	0.22 MPa-m/fringe

3.2 Photoelastic study

3.2.1 Experimental details

As described in the last chapter, photoelasticity is one of the well-established full-field optical methods which can be used to study dynamic fracture of bi-refringent materials. In the past, it has been extensively used to investigate dynamic fracture behavior of glassy polymers such as epoxies, polycarbonate, and polyesters [23, 115]. SLG being a birefringent material, an attempt to investigate crack initiation leading to branching using this popular method was considered first. An incoherent, monochromatic, LED pulse light source was used for illuminating the specimen in

a standard dark field circular polariscope. An ultrahigh-speed digital camera (Kirana model 05M from Specialized Imaging, Inc.) was used to capture the emergent light waves exiting the analyzer as interference fringes proportional to the local principal stress differences.

The dynamic fracture experiments on SLG specimens were performed using a setup shown schematically in Figure 3.2. The stress wave loading of the specimen leading to crack initiation, crack growth, and failure mode transition involving crack branching were all recorded during the experiment. A modified Hopkinson pressure bar (1830 mm long and 25.4 mm diameter C-300 maraging steel rod) with a symmetrically tapered blunt tip matching the V-notch of the specimen was used to impact an unconstrained ('free-free') sample. Approximate free support conditions were created for the specimen by placing it on a ~4 mm thick strip of soft-putty laid down on a height-adjustable translation stage. The opposite edge of the specimen was also pressed-on with an identical putty strip to ensure symmetry in terms of acoustic impedance relative to the loading axis. Other edges, with the exception of the V-notch flanks, were free as well. A 305 mm long, 25.4 mm diameter cylindrical steel striker, held inside a gas-gun barrel and aligned co-axially with the long-bar was used to subject the sample to stress wave loading. Once the striker was launched by the gas-gun, the collision between the striker and the long- bar (impact velocity ~6 m/s) generated a stress pulse which subsequently loaded the upper and lower flanks of the V-notch after propagating along the long-bar. When the striker contacted the long-bar, a trigger pulse was generated by a DC circuit to initiate recording of images by the camera which in turn triggered the laser unit (SI model LUX640) to emit synchronized laser pulses. The illumination source produced a string of 160 ns duration pulses in sync with the camera exposure to capture the photoelastic fringes. An adjustable delay generator was used in series with the trigger pulse unit and the camera,

to account for the time lapse associated with the stress wave propagation along the length of the long-bar before the specimen was loaded. In these experiments, 320 μs delay was used.

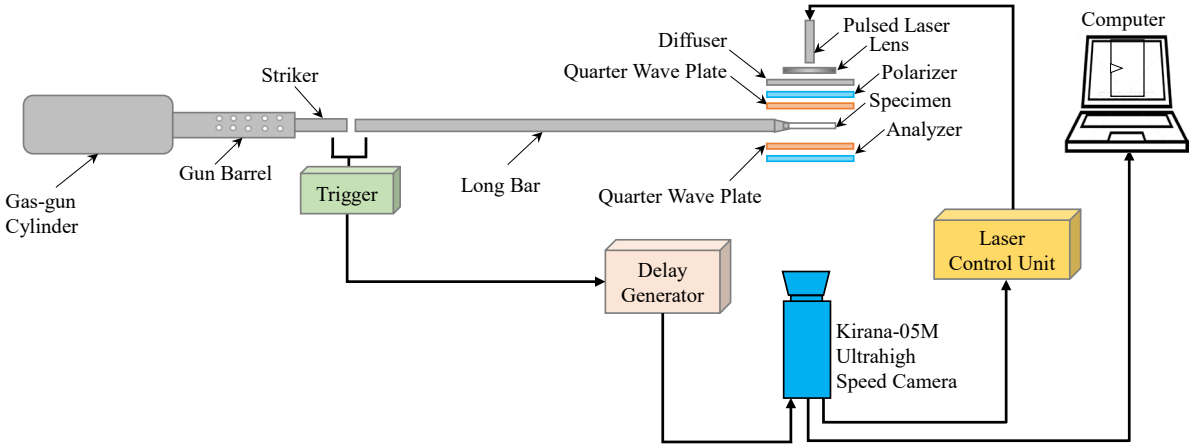

Figure 3.2: The schematic of experimental setup (top-view) for photoelasticity with dark-field circular polariscope.

The single sensor ultrahigh-speed camera with 924 × 768 pixels spatial resolution (10-bit gray scale images) was operated at 1 million frames per second to record 180 full resolution images. The camera was located at a distance of approx. 3.86 m in front of the specimen. A Nikkor 400 mm focal length $F^{\#}2.8$ macro lens along with a Nikon focal length doubler (or 2X tele-converter) and adjustable bellows (Nikon PB6) were used. An aperture setting of $F^{\#}16$ was necessary to achieve good focus and satisfactory exposure. The ROI in this study was such that contact stress evolution, crack initiation, crack propagation, and branching could all be observed successively in a single experiment. Based on a few trials, photographing a rectangular region of 85 × 74 mm^2 on the specimen plane was found necessary to achieve this requirement.

3.2.2 Crack length and velocity histories

The evolution of photoelastic fringes, proportional to principal stress difference at a location, from the instant the V-notch flanks begin to get loaded to the instant mother crack initiation at the notch-tip, its subsequent growth in mode-I condition, mode transition to two

dominant mixed-mode, branched daughter cracks were all recorded. Upon impact, a mode-I crack first initiated and then propagated approximately to the middle of the specimen width (~24 mm from the original notch-tip), then branched into two macroscopic mixed-mode (mode-I + mode-II) daughter cracks[1] globally symmetric relative to the loading axis, as evident from the reassembled fractured specimen shown in Figure 3.3. A few select instantaneous fringes from the optical history are shown in Figure 3.4(a)-(d). Figure 3.4(a) and (b) correspond to mode-I crack initiation and growth, respectively, whereas Figure 3.4(c) and (d) correspond to fracture mode-transition in the early and late stages resulting in two mixed-mode daughter cracks. (For illustration purposes, the brightness of some of these images is enhanced, and therefore the intensity field outside the specimen appears slightly lighter than the original recordings.)

A few qualitative observations can be made from Figure 3.4. As evident from the individual images, the crack tip location at each time instant is rather clear during the entire fracture event. Additionally, two groups of fully-formed fringe lobes immediately adjacent to the two crack flanks represent contours of principal stress differences due to two equal and opposite compressive forces imposed on the specimen during stress wave loading. Under the assumption of negligible friction, these contours could be analyzed to estimate the instantaneous force magnitudes using the optical fringes in conjunction with an available closed-form solution. However, *since the crack tip vicinity experience dominant tensile stresses, it does not show fully-formed fringes required for performing quantitative analysis.* Hence, extracting the crack tip stress intensity factors, as often done with studies using glassy polymers [23], is not feasible for SLG. This stark difference regarding the availability of well-formed fringes at the impact locations and crack tip is attributed to the low tensile failure strain of SLG relative to its compressive counterpart. That is, SLG can support

[1] A hint of an unsuccessful mode-I self-similar crack growth along its original path is evident in the fractured sample though it is not evident in the interferograms.

significantly higher compressive stresses when compared to the tensile counterparts. Additionally, from Figure 3.4, it can be observed that the propagating crack is trailed by gangs/groups of relatively small fringes giving it an appearance of stitch-marks along the crack path. They are attributed to Rayleigh waves propagating along the two crack flanks causing periodic contact between the upper and lower lips as the crack opening displacements are in the sub-micron scale. The spatial interval between these gangs of fringes was estimated from the images. It was 2900 ± 100 m/s, which is close to the reported Rayleigh wave speed for SLG (Table 3.1).

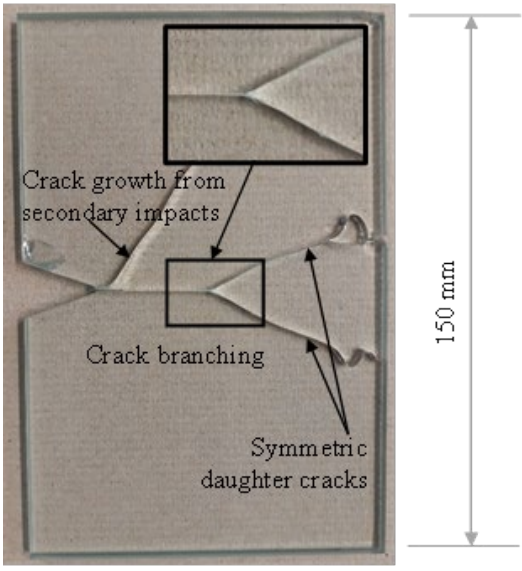

Figure 3.3: Reconstructed fractured specimen used in photoelasticity experiment.

Although well-formed crack tip fringes needed for extracting fracture parameters were absent near the growing crack, the spatial position of the crack tip could be easily detected from the photographed images to obtain crack length history accurately during the entire fracture event. The uncertainty of locating the crack tip was less than 0.2 mm. This could affect the computed crack velocities evaluated via numerical differentiation. To minimize errors in the instantaneous crack speed, a quadratic Bézier curve [57, 116] was fitted to the crack length data at a time instant '*i*' as,

$$a_i(s) = (1-s)^2 \hat{a}_i + 2s(1-s)\hat{a}_{i+1} + s^2 \hat{a}_{i+2},\ 0 \le s \le 1 \tag{3.1}$$

where s, $\hat{a}$ and a are smoothing parameter, measured crack length, and the smoothed crack length, respectively.

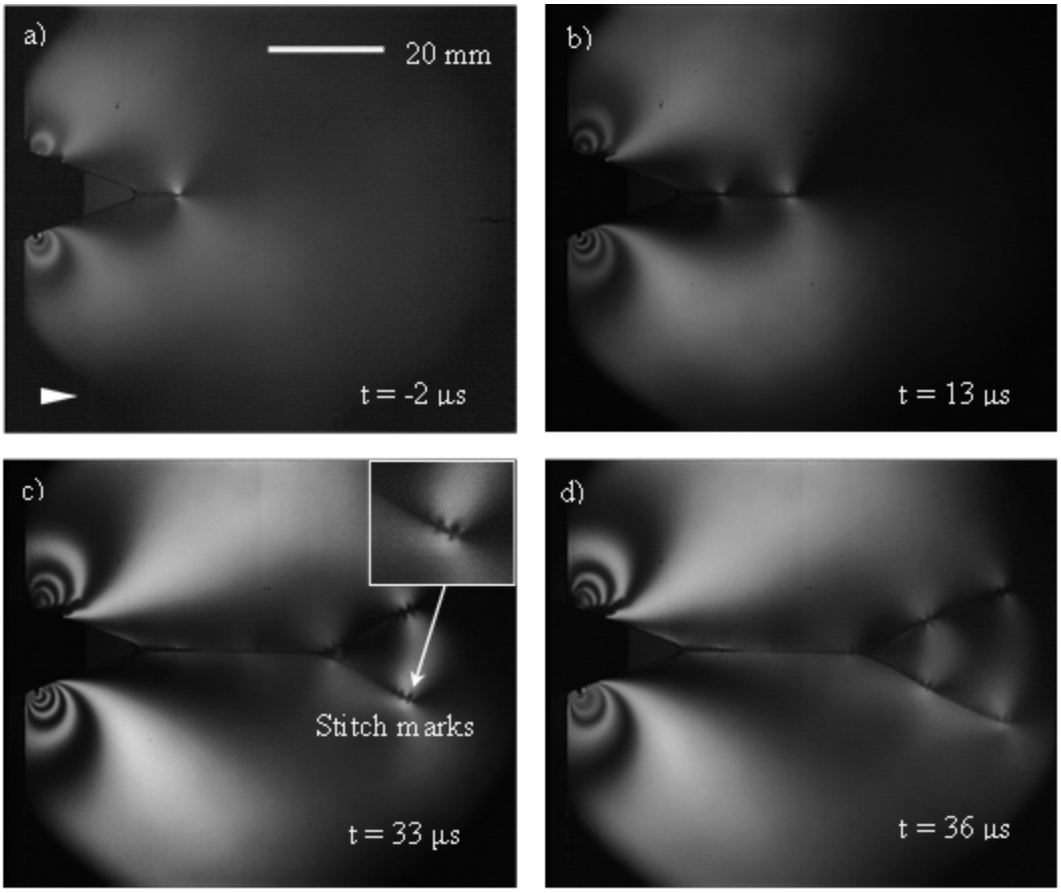

Figure 3.4: Photoelastic fringes in soda-lime glass specimen subjected to dynamic loading. Arrowhead (in the top left image) represents crack growth direction. Time, $t = 0$ corresponds to crack initiation at the original notch-tip. The 'stitch marks' along the crack path are attributed to contact stresses due to Rayleigh waves.

In the above expression $\hat{a}_i, \hat{a}_{i+1}, \hat{a}_{i+2}$ are the control points of $a_i(s)$. The value of s was chosen as 0.5 such that the smoothed data point was at the middle of each interval. Subsequently, the crack velocity (V) was estimated from the smoothed crack length history using backward difference approximation,

$$V_i = \frac{a_i - a_{i-1}}{t_i - t_{i-1}} \tag{3.2}$$

where a and t are crack length and time, respectively. Figure 3.5(a) and (b) represent the apparent crack length and velocity histories, respectively. Here $t = 0$ corresponds to crack initiation at the original notch-tip. The crack length increased monotonically from initiation to the end of the observation window, including branching. A small change in the slope is noticeable before and after the crack branching event that occurred over 16–19 μs after crack initiation. The measured crack tip locations from the two mixed-mode daughter cracks were such that the crack length data essentially overlapped on each other with an excellent symmetry in the overall branching phenomenon observed during this experiment. The crack velocity of the mode-I crack increased steadily to ~1400 m/s rapidly, within the first 2-3 μs after initiation, before attaining a *nearly constant velocity* in the 1400-1600 m/s range until ~12 μs after crack initiation. Furthermore, prior to the mode-I crack entering the branching phase, the apparent crack velocity gradually decreased to ~1250 m/s. Subsequently, the propagating mode-I crack branched to produce two globally symmetric mixed-mode daughter cracks which almost instantaneously (within 1-2 frames) reached ~1600 m/s before settling back to steady values over the next 4 μs. The daughter crack velocities were again in the range of 1400-1600 m/s, same as the steady-state values of the mother crack. These trends are similar to the one observed in experiments in [19], and the drop in crack velocities prior to branching are attributed to the increasing surface roughness in the so-called 'hackle' phase [24] of crack growth. Similary, the rapid increase in crack velocities after branching punctuate the daughter cracks enter the so-called 'mirror' phase [19] corresponding to a steady crack velocity of ~ 155 m/s.

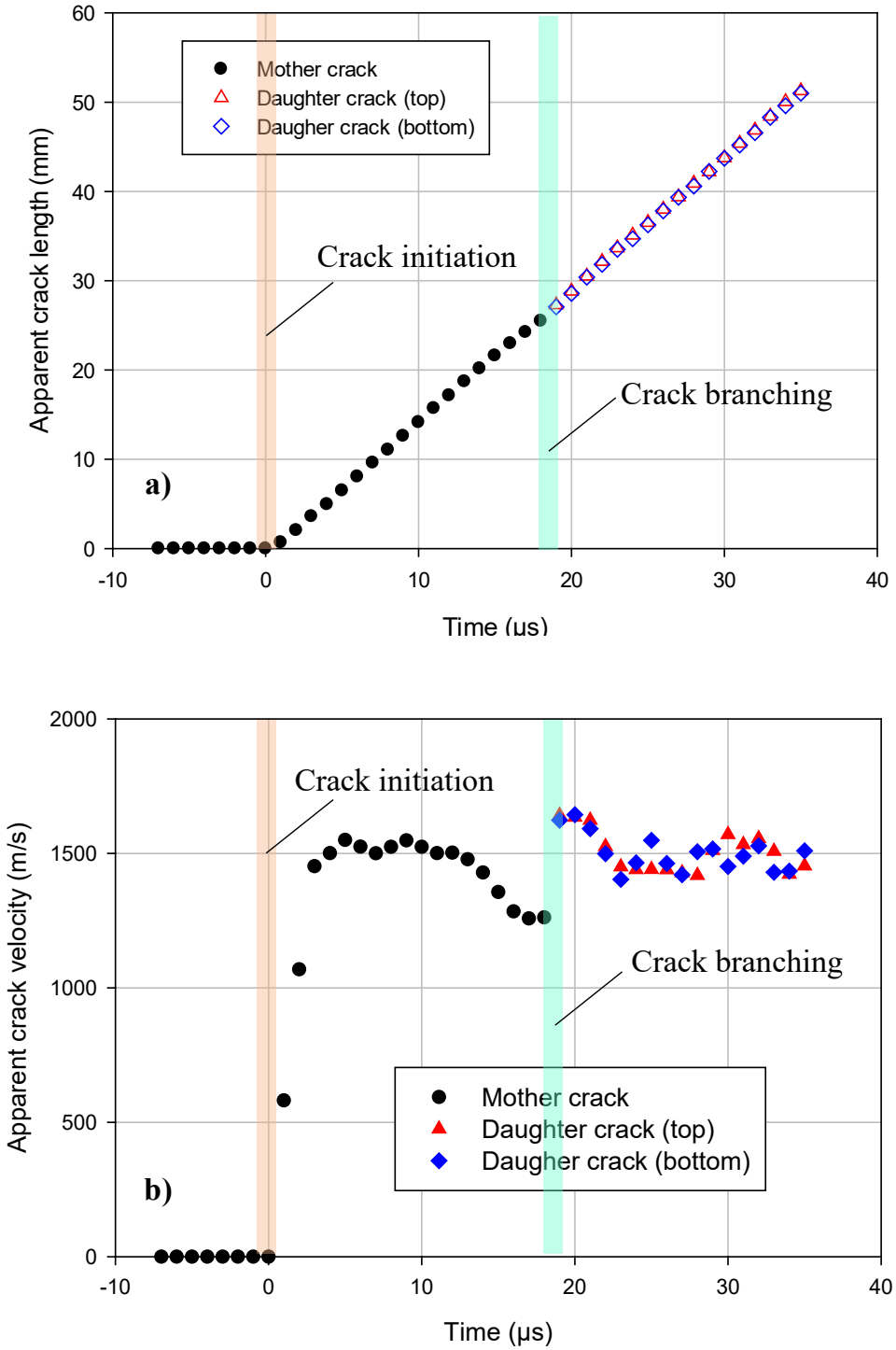

Figure 3.5: Apparent crack length (top) and crack velocity (bottom) histories from photoelasticity. (Time, $t = 0$ corresponds to crack initiation at the original notch-tip.)

3.2.3 Contact force history measurement

The force histories on the V-notch faces of the specimen by the long-bar were evaluated from the photoelastic fringes. The shape of the fringe lobes suggests an approximate line-loading of each of the two flanks of the V-notch. Accordingly, for ease of interpretation, each interferogram was used in conjunction with the Flamant's solution for line-load acting normally on the edge of a planar elastic solid. Using the closed-form solution [117] along with the stress-optic law, the normal force on the specimen flanks were estimated using,

$$\frac{Nf_\sigma}{B} \approx \frac{2F(t)}{\pi r B} \tag{3.3}$$

where N is fringe order, f_σ is the stress-optic constant (= 220 N/m/fringe for SLG), r is the radial distance of the fringes measured from the contact point (origin) and B is the specimen thickness. Both the dark and light fringes were analyzed by assigning integer and half orders, respectively.

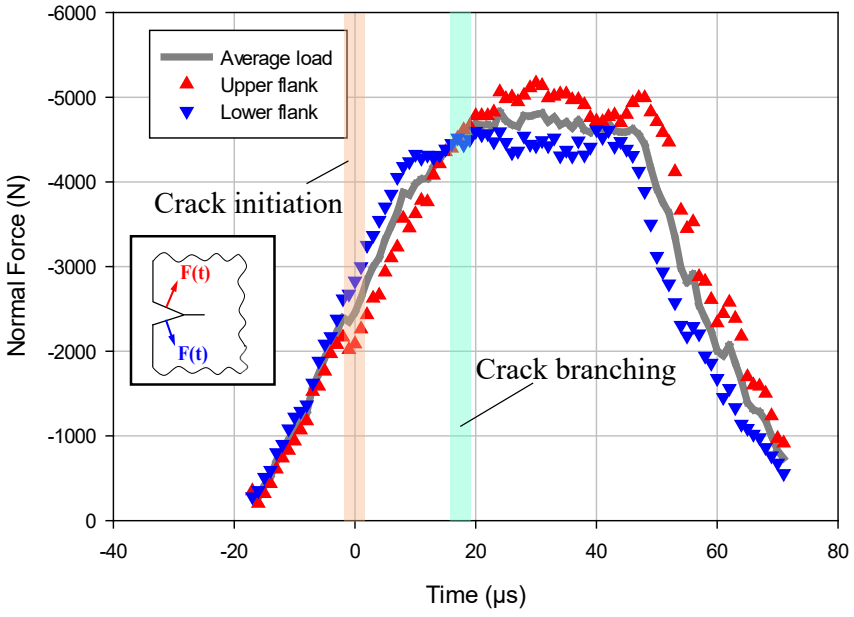

Figure 3.6: Contact force history from photoelasticity (Time, $t = 0$ corresponds to crack initiation at the original notch-tip.)

The contact force was evaluated at each of the fringe locations and averaged at each time instant (t = 0 corresponds to mode-I crack initiation event at the notch-tip). The resulting normal force history is shown in Figure 3.6. The histories for the upper and lower flanks were computed separately (blue and red symbols) and averaged (solid line). Apart from the expected measurement differences, the force histories of the two flanks follow approximately 'ramp-up, plateau, ramp-down' pattern. An estimated loading rate during the ramp-up phase is of approx. 150 MN/s. The overall loading period the analysis could be performed satisfactorily was about 100 μs. A peak load of 4800 ± 150 N in the plateau region was realized during the dynamic loading event.

3.3 Digital image correlation (DIC)

3.3.1 Experimental details

Currently, the digital image correlation or DIC methods are popular for full-field experimental mechanics studies, including dynamic fracture mechanics investigations [49, 118-123]. Previous works have utilized DIC to study many traditional metallic and polymeric materials. To date, however, there are no reports on examining the feasibility of DIC to quantitatively study rapidly growing cracks in glasses and ceramics subjected to stress wave loading. Yet, it is generally assumed that the method would work. However, knowing the unique challenges posed by growing cracks in SLG, an attempt to examine crack initiation, growth and branching phenomena in SLG specimens of geometry and loading configuration described in the previous section was undertaken. That is, a V-notched specimen (Figure 3.1) was spray painted with uniform but random black and white speckle pattern. The ROI on the specimen for imaging purposes was maintained same as in the one in the photoelastic study (85 × 74 mm^2) in order to capture all the three fracture events, crack initiation - growth - branching, in a single specimen. (It should be noted

here that, 2-D DIC being scale independent methodology, nano or microscale speckles created over sub-mm or mm size ROI would not be practical for capturing all the intended phases of fracture behavior targeted in this work.) The specimens were subjected to impact loading using the experimental setup shown schematically in Figure 3.7. It is similar to the one shown in Figure 3.2 but was modified for recording the random speckles directly off the specimen surface. That is, the speckle images were captured in the undeformed/reference and deformed states of the specimen using the same ultrahigh-speed camera, Kirana-05M, operating at the same framing rate of 1 Mfps, as in the photoelasticity experiment. The specimen was illuminated by two broad-spectrum xenon flash lamps. Again, a Nikon 400 mm/F2.8 lens along with a focal length doubler and an adjustable bellows was used to achieve good focus from a distance of 3.86 m from the specimen plane. The lens aperture was stopped-down to $F^{\#}16$ after focusing on the speckles to increase the depth-of-focus. The corresponding angle-of-view was approx. 1.3 deg.

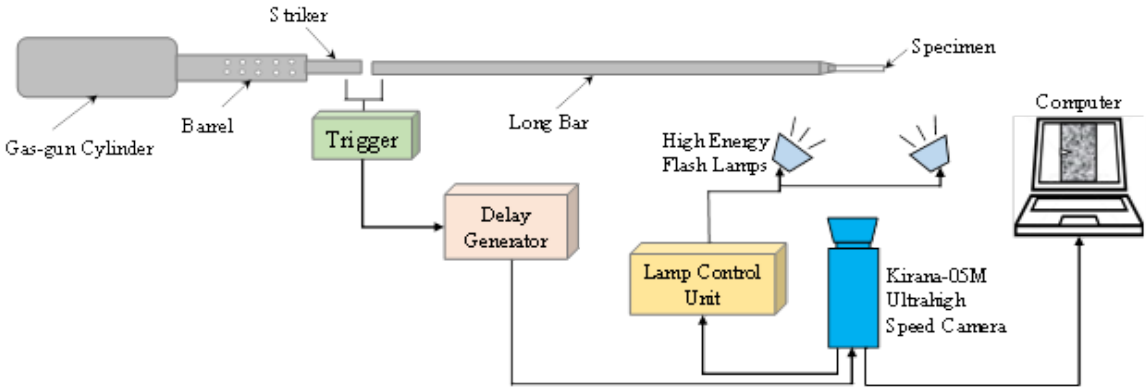

Figure 3.7: Schematic of experimental setup (top-view) for DIC to study dynamic fracture of soda-lime glass.

Two speckle images from the post-impact regime (t = 0 again corresponds to crack initiation at the initial notch-tip) are shown in Figure 3.8, where the direction of crack growth is indicated by the arrowhead. Despite an excellent quality of the recorded speckles images, unlike in the photoelastic counterparts (Figure 3.4), neither the growing hair-line crack nor the instantaneous

crack tip is discernible even after close examination. Accordingly, a *probable* region where the crack tip resides at that time instant is highlighted by a dotted circle in these images. Subsequently, using principles of DIC, sub-images in the reference state were located in various deformed images via gray scale correlation operation [124] using image analysis software ARAMIS® (GOM mbH, Braunschwelg, Germany). This involved segmenting the speckle images into 30×30 pixel sub-images with an overlap of 5 pixels between neighboring sub-images. Once the location of the corresponding sub-image in the deformed state was identified, the local displacements were quantified at the center of each sub-image. This resulted in u and v displacement data arrays, each of 147×178 size in the ROI corresponding to horizontal and vertical directions, respectively. It should be noted that the larger sub-image sizes of 40×40 and 50×50 pixels were tried and they did not improve our ability to locate the crack tip as the displacements are expected to be in the sub-micron level.

As in the photoelastic experiment, the crack initiated at the original notch-tip and propagated under dominant mode-I conditions for a distance of ~25 mm before bifurcating into two globally symmetric mixed-mode daughter cracks. The dynamic crack initiation event produced a hairline crack from the pre-notch-tip but, as noted earlier, could not be discerned directly from the speckle images (see, Figure 3.8). Accordingly, the in-plane displacement fields were plotted from the u and v data arrays as contours in the ROI. The expected jump in the v-displacements across the crack flanks behind the crack tip and convergence of v-displacement contours were considered to locate the instantaneous crack tip at each time step [58]. It should be noted that the strain component fields were also plotted (not shown) and were very noisy despite using different sub-image sizes while performing speckle correlation.

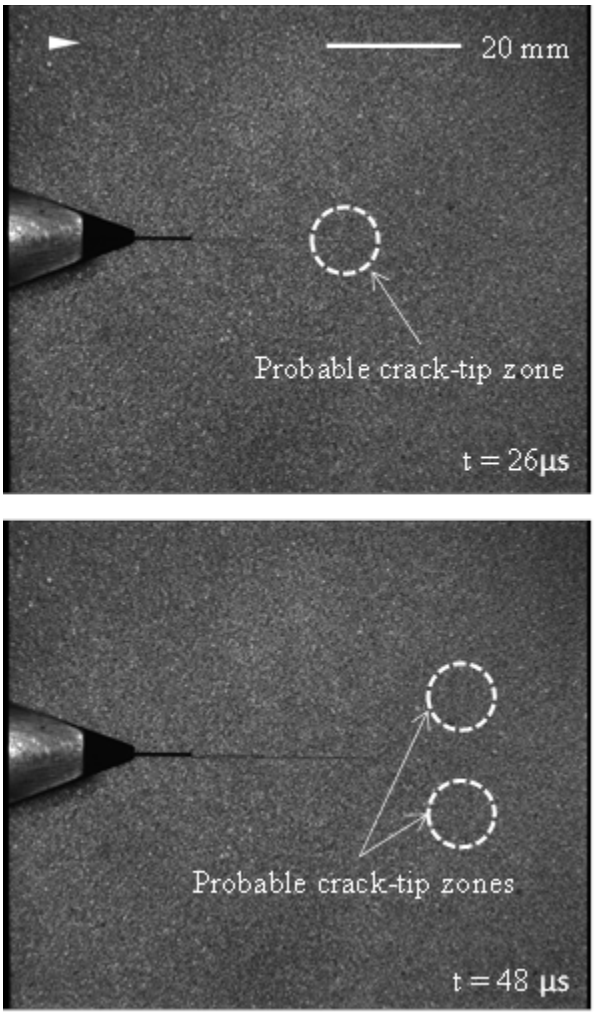

Figure 3.8: DIC speckle images subjected to dynamic loading. Arrowhead represents crack growth direction. (Time, $t = 0$ corresponds to crack initiation at the original notch-tip)

3.3.2 Crack length and velocity histories

The dominant *v*-displacement (in the vertical direction with respect to mode-I propagating mother crack) obtained from image correlation were plotted for all time instants. A few select images, before and after crack branching, are shown in Figure 3.9. The lowest possible contour increment of 2 μm was used for plotting displacement fields based on 2% of the pixel size, close to the limit of DIC method's capability. It should be noted that since displacements are non-singular, locating the crack tip precisely when compared to photoelasticity was indeed a challenge. It is worth pointing out that, to tackle this issue, methods such as nonlinear least-squares regression

with crack tip position as an unknown, genetic algorithms, subset splitting, to name a few, have all been proposed. These approaches, however, are computationally expensive due to additional variables; more importantly, numerical convergence nor accuracy is not assured even for traditional polymers and metal substrates [119], [125-127] where displacements are two orders of magnitude higher than SLG. Furthermore, the feasibility of these methods when crack flank displacements are in the sub-micron scale is unknown and hence was not pursued in this work.

From the probable crack tip locations thus identified, the *apparent* crack length histories were evaluated from displacement field maps, see Figure 3.10(a). As in the photoelastic experiment, the crack length increased with the passage of time (again $t = 0$ corresponds to crack initiation at the original tip) until crack branching (between 16-17 μs) and beyond. The crack length history is rather noisy when compared to the one from the photoelastic experiment (Figure 3.5), with frequent and unexplainable crack length *reductions* at some of the time instants relative to the previous step/s. The crack growth also seems to have stalled before crack branching, inconsistent with Figure 3.11. In addition, the two daughter crack lengths did not match temporally with each other even though the branching was exceptionally symmetric based on the reassembled specimen shown. These anomalies were attributed to large uncertainties in finding the moving crack tip location from DIC. By overlooking these anomalies in the crack length history, the data was smoothed (Eq. (3.1)and (3.2) and crack velocities were determined using backward difference approx. and are as shown in Figure 3.10(b). The outcome was that the crack velocity increased to 1890 m/s instantaneously and fluctuated over a relatively wide range, from 1060 m/s to 2370 m/s, until the crack branched. After branching, the velocity increased instantaneously to an unrealistic ~2400 m/s which subsequently stayed in the range of 800-3000 m/s for ~11 μs. Due to high-stiffness and low-toughness of SLG, crack flank displacements near the crack tip are expected to

be extremely small, estimated to be ~80 nm. Therefore, it was concluded that finding the crack tip location using convergent displacement contours was not just challenging, but resulted in very noisy and unreliable crack velocities in SLG.

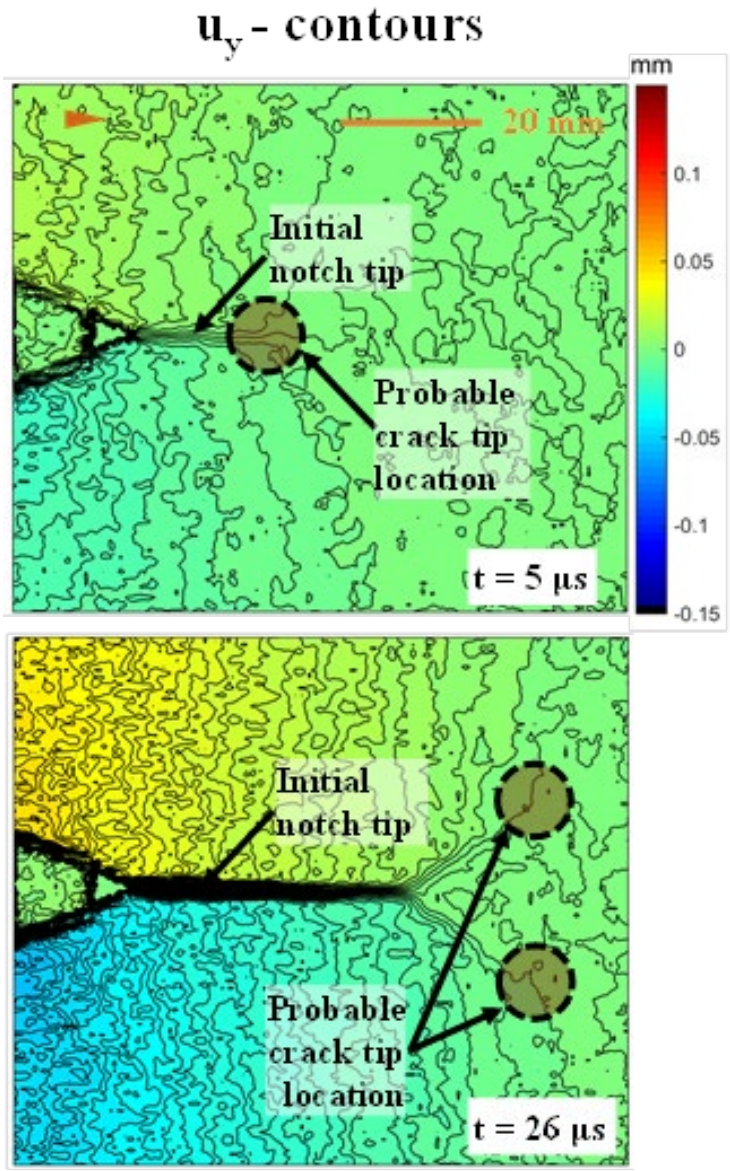

Figure 3.9: Displacement contours on soda-lime glass specimen surface along the vertical direction (normal to the mode-I crack propagation) from DIC at ~5 µs and ~26 µs after crack initiation at the original notch-tip.

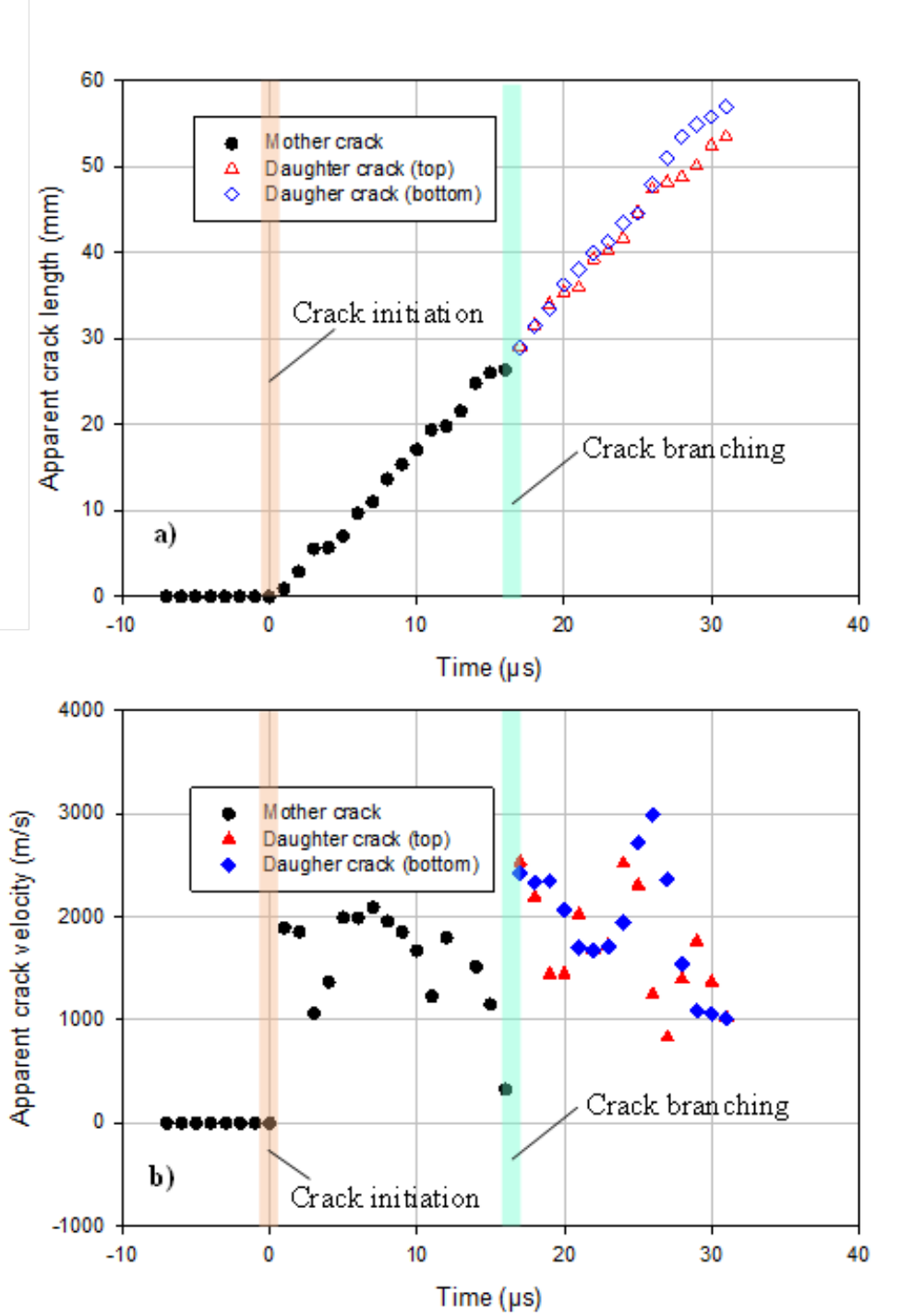

Figure 3.10: Apparent crack length (top) and velocity (bottom) histories from DIC. (Time, t = 0 corresponds to crack initiation at the original notch-tip.)

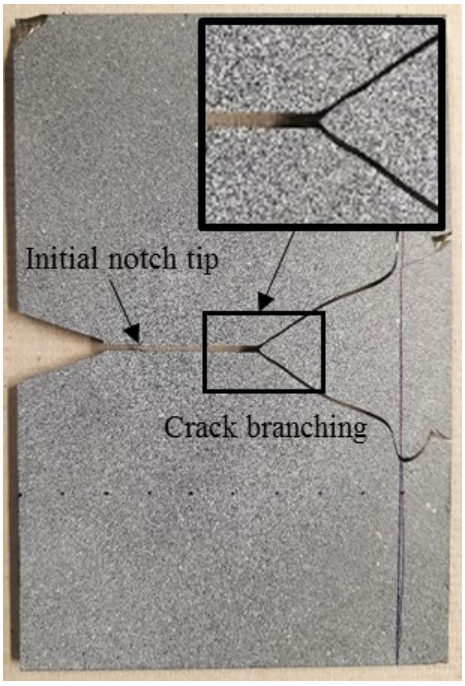

Figure 3.11: Reconstructed fractured specimen used in DIC experiment.

3.3.3 Stress intensity factor histories

Despite the challenges of locating the crack tip from the displacement field measurements, for completeness the mode-I stress intensity factors were evaluated from the data around the crack tip in conjunction with the elasto-dynamic asymptotic equations [49] and over-deterministic least-squares analysis. For a dynamically propagating crack, the crack opening displacements are given by,

$$u_y = \sum_{n=1}^{N} \frac{\left(K_I^d\right)_n B_I(c)}{2\mu}\sqrt{\frac{2}{\pi}}(n+1)\left\{-\beta_1 r_1^{n/2}\sin\frac{n}{2}\theta_1 + \frac{h(n)}{\beta_2} r_2^{n/2}\sin\frac{n}{2}\theta_2\right\} + \sum_{n=1}^{N} \frac{\left(K_{II}^d\right)_n B_{II}(c)}{2\mu}\sqrt{\frac{2}{\pi}}(n+1)\left\{\beta_1 r_1^{n/2}\cos\frac{n}{2}\theta_1 + \frac{h(\overline{n})}{\beta_2} r_2^{n/2}\cos\frac{n}{2}\theta_2\right\}, \tag{3.4}$$

where $r_m = \sqrt{X^2 + \beta_m Y^2}, \theta_m = \tan^{-1}\left(\frac{\beta_m Y}{X}\right), m = 1,2$

$$\beta_1=\sqrt{1-\left(\frac{c}{C_L}\right)^2},\ \beta_2=\sqrt{1-\left(\frac{c}{C_S}\right)^2}$$

$$C_L=\sqrt{\frac{(\kappa+1)\mu}{(\kappa-1)\rho}},\ C_S=\sqrt{\frac{\mu}{\rho}},\ \kappa=\frac{3-\nu}{1+\nu}\ for\ plane\ stress$$

$$h(n)=\begin{cases}\dfrac{2\beta_1\beta_2}{1+\beta_2^2}\ for\ odd\ n\\ \dfrac{1+\beta_2^2}{2}\ for\ even\ n\end{cases}$$

and $h(\overline{n})\ =\ h(n+1)$

$$B_I(c)\ =\ \frac{\left(1+\beta_2^2\right)}{D},\ B_{II}(c)\ =\ \frac{2\beta_2}{D},\ D=4\beta_1\beta_2-\left(1+\beta_2^2\right)^2.$$

In the above, (x, y) and (r, θ) are the Cartesian and polar coordinates instantaneously aligned with the current crack tip, respectively, c is crack velocity, C_L and C_S are longitudinal and shear wave speeds of the material, μ is shear modulus and υ is Poisson's ratio. Again $(K_I)_{n=1}$ and $(K_{II})_{n=1}$ are the mode-I and mode-II dynamic SIF, respectively. Figure 3.12 shows SIFs evaluated from the data around the crack tip in the region $0.5\le(r/B)\le1.5$ with an angular extent of $-150°\le\theta\le150°$ [125] and over-deterministic least-squares error minimization analyses. Similar to the velocity plot, the SIF data are extremely noisy due to an inaccurate crack tip location compounded by large errors in crack velocity. The mode-I SIF values increased to ~1.8±0.4 MPa√m until crack initiation before dropping due to the local unloading upon crack initiation. After crack branching, mode-I SIFs varied randomly without following any reasonable trend until the end of the observation window. The mode-II SIFs evaluated simultaneously are not included here simply due to the difficulty in comprehending very large errors.

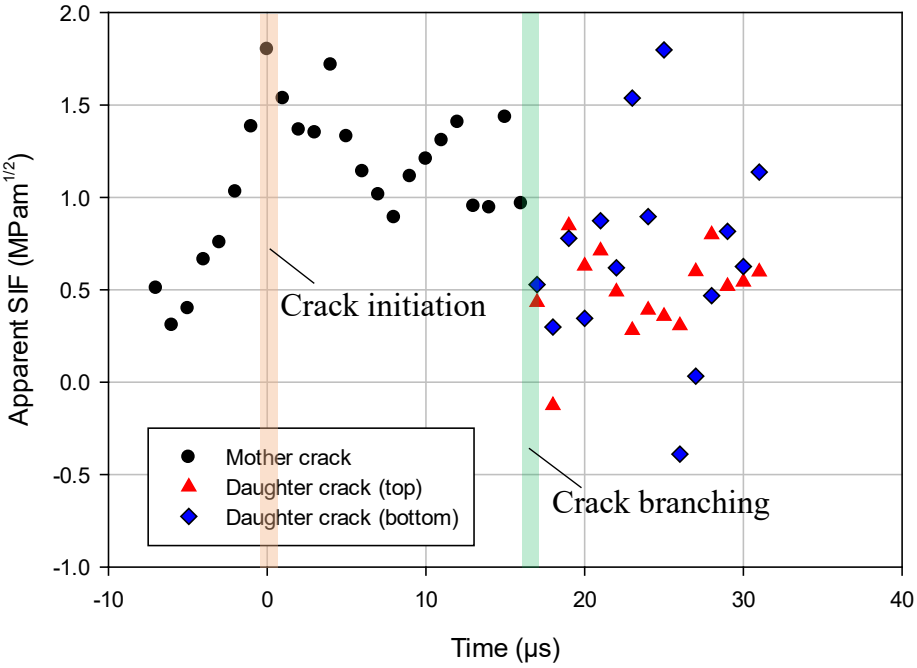

Figure 3.12: Apparent mode-I stress intensity factor histories extracted from DIC. (Time, $t = 0$ corresponds to crack initiation at the original notch-tip.)

3.4 Digital gradient sensing

3.4.1 Experimental details

A third but a relatively new method developed here at Auburn, Digital Gradient Sensing or DGS, was used next to visualize and quantify crack initiation, growth and branching phenomena and comparatively evaluate the measurements with the previous two methods. A schematic representation of the working principle for transmission-mode DGS [53] technique is shown in Figure 2.3. As in the photoelasticity and DIC counterparts, experiments were performed using a modified Hopkinson pressure bar or a long-bar impactor, see Figure 3.13. Again, the crack initiation, growth and branching were recorded using ultrahigh-speed photography for a loading pulse duration of ~120 μs. When the striker impacted the long-bar, a trigger pulse was generated

to initiate the camera to capture speckle images off the target plane through the specimen. Simultaneously, the high-speed camera triggered a pair of xenon high-energy flash lamps. A delay generator was also used in the trigger circuit as the stress wave had to propagate along length of the long-bar before loading the specimen. In these experiments, a delay of 320 μs was used. Again, a Kirana-05M ultrahigh-speed digital camera operating at 1 million frames per second with 924×768 pixels spatial resolution (10-bit gray scale images) recorded 180 full resolution images. The camera was situated at a distance of 3.86 m in front of the specimen, whereas the speckle target was at a distance of 1.0 m behind specimen. A Nikkor 400 mm focal length, $F^{\#}2.8$ lens along with a focal length doubler and adjustable bellows were used to record speckles on the target plate. After focusing on the speckles, the aperture was reduced to $F^{\#}16$ to enhance depth of focus and a good exposure. A 110×92 mm^2 region on the target corresponding to approx. 88×65 mm^2 ROI on the specimen (based on pin-hole approx.) was photographed. Besides monitoring the contact stresses on the crack flanks, the ROI covered crack initiation, propagation and branching events, all in a single experiment.

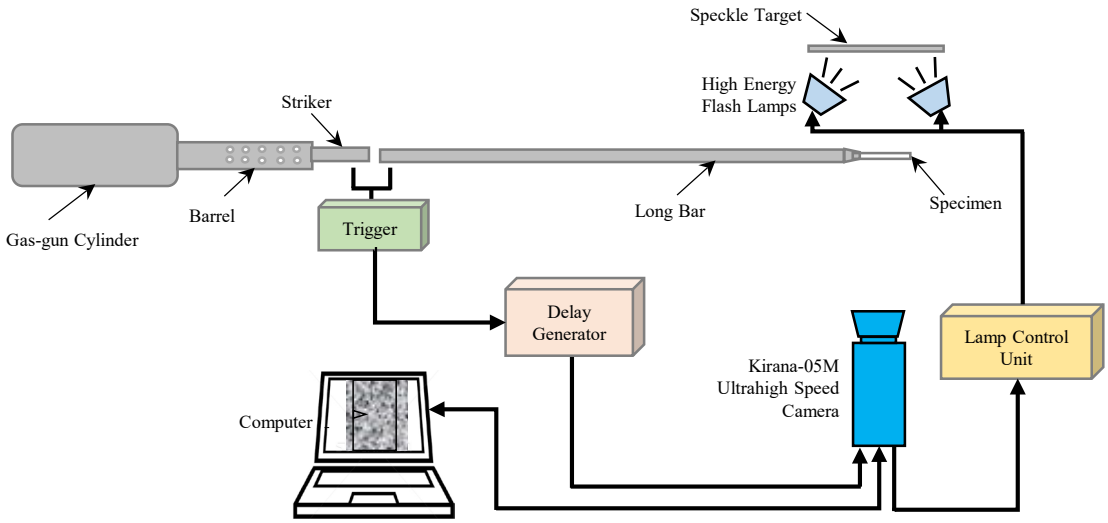

Figure 3.13: The schematic of experimental setup for transmission DGS measurements.

3.4.2 Crack length and velocity histories

Two representative speckle images recorded, one in the undeformed/reference and the other in the deformed states of specimen is shown in Figure 3.14. These speckle images are provided for completeness even though they are not visually informative. That is, the speckles or deformations around the crack tip are not readily visible except localized regions of distorted speckles in the specklegram in the deformed state when observed carefully relative to the undeformed counterpart.

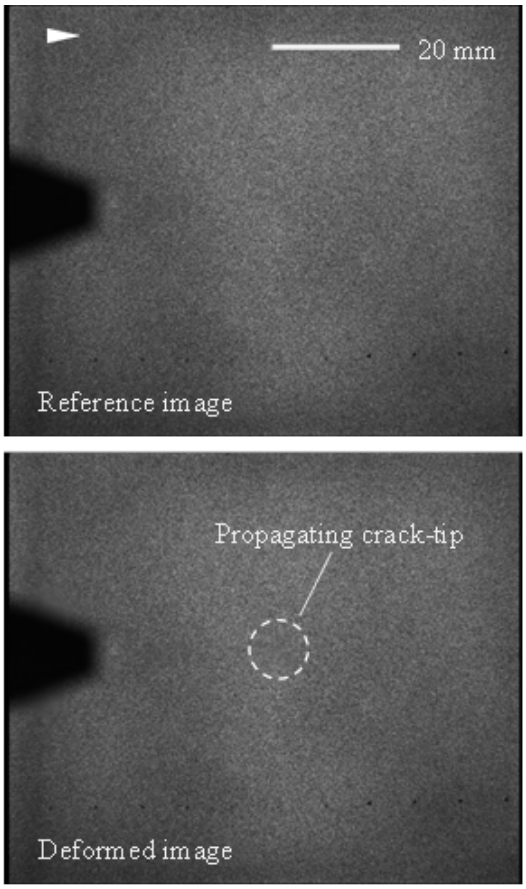

Figure 3.14: Speckle images from DGS in the undeformed (top) and deformed (bottom) states for propagating crack tip recorded by camera through the soda-lime glass specimen

This is because the camera is focused on the target instead of the specimen. However, the resulting angular deflections of light rays and hence deformations become apparent after correlating the images in the reference/undeformed and deformed states. A photograph of the

fractured specimen from this experiment is shown in Figure 3.15. After initiation at the original notch-tip, the crack propagated as a mode-I mother crack and subsequently branched into two mixed-mode daughter cracks at approx. 26 mm from the initial tip. The branched cracks maintained global symmetry relative to the mother crack as shown in the inset in Figure 3.15. Finally, when the two daughter cracks approached the specimen edge, the crack paths were visibly disturbed due to the loss of in-plane constraint.

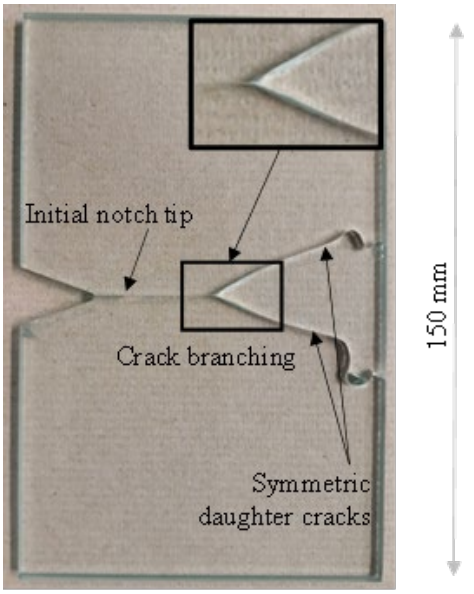

Figure 3.15: Reassembled fractured soda-lime glass specimen used in DGS experiment.

The angular deflection contours for ϕ_x and ϕ_y in two orthogonal directions (with respect to mode-I propagating mother crack) along with the resultant values of angular deflections $\phi_r \left(=\sqrt{\phi_x^2+\phi_y^2}\right)$ at select time instants are shown in Figure 3.16 as contours even though the data are available as rectangular arrays. A video animation encompassing the evolution of contact stress induced deformation of the two V-notch flanks, crack initiation, growth and branching events is available in the supplementary materials section of Ref [18]. The ϕ_x contours are symmetric about the crack growth direction whereas ϕ_y contours are antisymmetric for the mode-I mother crack. Once branching occurs, however, both sets of contours become asymmetric relative to the mixed-

mode daughter cracks. The first column in the figure corresponds to mode-I crack propagation of the mother crack (before branching) at time t = 9 μs whereas the second column represents mixed-mode crack propagation of the two daughter cracks (after branching) at time t = 29 μs. Again, the timestamps are with respect to crack initiation at the original notch-tip, t = 0. Evidently, locating the crack tip from these DGS contours is quite obvious when compared to the displacement fields from DIC (Figure 3.9), discussed earlier. This is due to the singular nature of the stress gradient fields [58] obtained from DGS. That is, the contours representing each of the measured fields have a lobed structure converging to the crack tip, marked in Figure 3.16. (and the supplementary material [18]) by a solid white dot, making it relatively easy to locate from any of the three fields at each time instant. In this work, ϕ_r was used to locate the crack tip and track the crack path by a series of successive white dots. That is, as can be seen from Figure 3.16., once the deformation contours are plotted, the instantaneous crack tip position becomes self-evident as the location where the contour maps form a closed lobe encircling the crack tip in the ϕ_r field. The measured apparent crack length and velocity histories are shown in Figure 3.18 (a) and (b), respectively. The crack length increased monotonically until the end of the observation window. And, a distinct kink in the crack length history can be noted just before the crack branching phase over t = 18-21 μs. Subsequently, the crack length increased steadily. The crack tip locations of the two mixed-mode daughter cracks were such that the instantaneous crack lengths were also in good agreement with each other indicating that the two daughter cracks grew symmetrically relative to the mode-I mother crack's growth direction. These observations are akin to the ones from the photoelastic experiment. Furthermore, despite the usage of speckles in DGS for quantifying angular deflections of light rays, the measured crack length history is relatively smooth with minimum experimental noise. This is unlike the results seen in the last section using DIC (Figure 3.10). Subsequently, the

crack length history was processed using Bezier curves as described earlier to extract the apparent crack velocity (V) using the backward difference method. The result is shown in Figure 3.17(b). The crack propagated steadily to ~1530 m/s over a ~4 μs period.

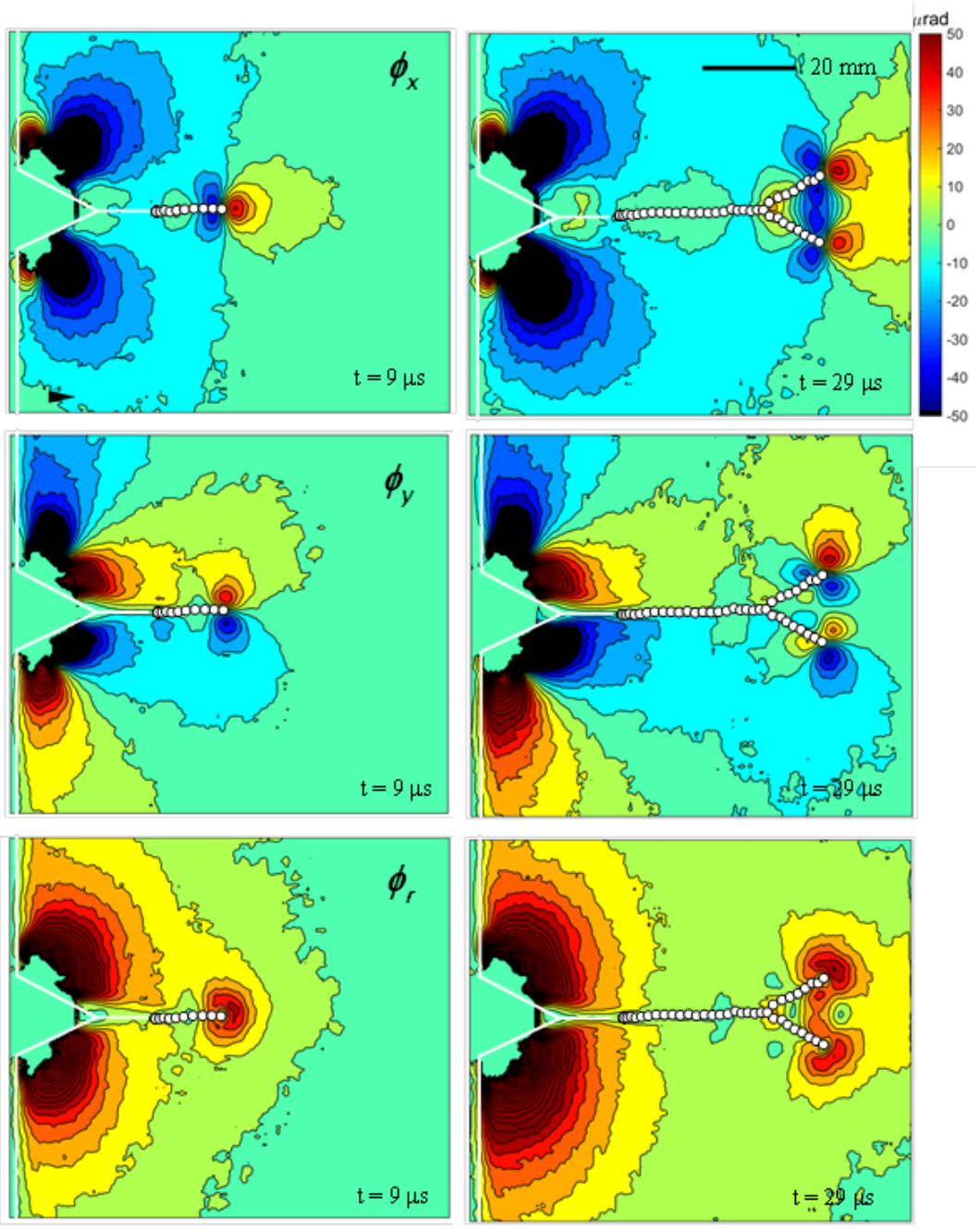

Figure 3.16: Angular deflection contours in soda-lime glass subjected to dynamic loading. The arrowhead (in the top left image) shows crack growth direction. White markers indicate crack tip locations in the previous frames. (Time, t = 0 corresponds to crack initiation at the original notch-tip.)

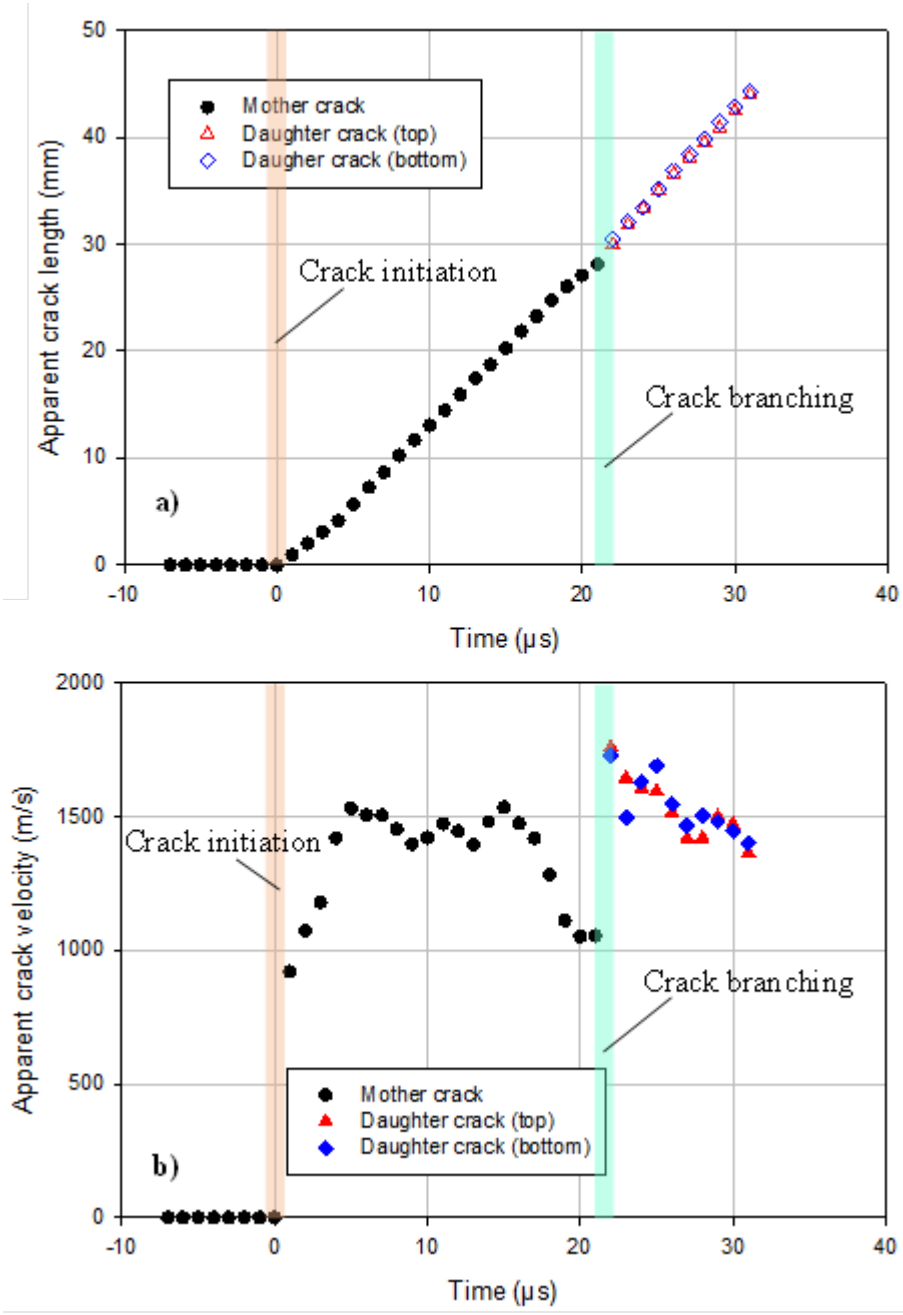

Figure 3.17: Apparent crack length (top) and velocity (bottom) histories from DGS. (Time, t =0 corresponds to crack initiation at the original notch-tip.)

Furthermore, the crack maintained an average velocity of 1400-1550 m/s in the pre-branching phase, consistent with the one reported in [19]. As the crack entered the branching phase between t = 18-21 μs, the apparent crack velocity gradually reduced to values between 1250 to 1050 m/s. This is again, similar to the observation made in the photoelastic experiment.

Subsequently, the crack branched into two mixed-mode daughter cracks, both of which almost instantaneously accelerated to ~1700 m/s. Subsequently, the two daughter cracks decelerated back to ~1500 m/s until the end of the observation window.

3.4.3 Stress intensity factor histories

Using the two orthogonal angular deflection fields in the global *x*, *y* coordinates, the instantaneous crack tip fields in the local coordinates (x', y') (x' coinciding with the instantaneous crack growth direction) for a moving crack were obtained by performing coordinate transformation:

$$\phi_{x'}(t) = \phi_x(t)\cos\theta(t) + \phi_y(t)\sin\theta(t) \tag{3.5}$$

The mode-I and mode-II SIFs were then evaluated by analyzing the data around the crack tip in conjunction with the asymptotic equations [128] using over-deterministic least-squares approach:

$$\phi_{x'} = C_\sigma B \left[\begin{array}{l} -\frac{1}{2} r_I^{-\frac{3}{2}} \left\{ f(V;C_L;C_S) A_1(t) \cos\left(\frac{3\theta_I}{2}\right) + g(V;C_L;C_S) D_1(t) \sin\left(-\frac{3\theta_I}{2}\right) \right\} \\ +\sum_{N=2}^{\infty} \left\{ A_N(t)\left(\frac{N}{2}-1\right) r_I^{\left(\frac{N}{2}-2\right)} \cos\left(\left(\frac{N}{2}-2\right)\theta_I\right) + D_N(t)\left(\frac{N}{2}-1\right) r_I^{\left(\frac{N}{2}-2\right)} \sin\left(\left(\frac{N}{2}-2\right)\theta_I\right) \right\} \end{array} \right] \tag{3.6}$$

In the above, *f* and g are functions of instantaneous crack velocity *V*, and (r_I, θ_I) denote the local crack tip polar coordinates obtained by contracting the local coordinates (x', y') as, $r_I = \sqrt{(x')^2 + \alpha_L^2 (y')^2}$ and $\theta_I = \tan^{-1}\left(\frac{\alpha_L y'}{x'}\right)$ in the crack growth direction. The coefficients $A_I(t)$ and $D_I(t)$ in the asymptotic series are related to the mode-I and mode-II SIFs, respectively, as $K_I^d(t) = A_1(t)\sqrt{\frac{\pi}{2}}$ and $K_{II}^d(t) = D_1(t)\sqrt{\frac{\pi}{2}}$. The functions *f* and *g* are,

$f(V;C_L,C_S)=\left(\frac{1+\nu}{1-\nu}\right)\frac{\left(1+\alpha_S^2\right)\left(1-\alpha_L^2\right)}{4\alpha_S\alpha_L-\left(1+\alpha_S^2\right)^2}$ and $g(V;C_L,C_S)=\left(\frac{1+\nu}{1-\nu}\right)\frac{2\alpha_S\left(1-\alpha_L^2\right)}{4\alpha_S\alpha_L-\left(1+\alpha_S^2\right)^2}$ where

$\alpha_L=\sqrt{1-\frac{\rho(1-\nu)}{2\mu}V^2}$ and $\alpha_S=\sqrt{1-\frac{\rho}{\mu}V^2}$ for plane stress, μ and ρ are shear modulus and mass density, respectively. For analysis purposes, the data near the crack tip in the region $0.5\le r/B\le 1.5$ with an angular extent of $-150^\circ\le\theta_l\le 150^\circ$ was considered. The least-squares analysis was performed choosing four (N=4) terms in the stress field. In Eq. (3.6), C_σ is the elasto-optical constant for SLG, and B is the initial thickness.

The SIF histories measured by DGS from crack initiation to branching are shown in Figure 3.18. Here t = 0 corresponds to crack initiation at the original notch-tip. The mode-I SIFs increased steadily to ~0.75 MPa√m until crack initiation as shown in Figure 3.18. Upon crack initiation, the SIFs dropped noticeably over ~2 μs to ~0.6 MPa√m due to unloading before increasing for the next ~8 μs to ~1.06 MPa√m rapidly. After branching, the mode-I SIF decreased quickly, followed by a steady growth for the next ~4 μs. The mode-II SIF values were relatively small when compared to the mode-I counterparts until branching occurred. (The non-zero mode-II SIF values in the pre-initiation period provide estimates of error in the least-squares data analysis.) The magnitude of the mode-II SIFs of the two daughter cracks increased immediately after the crack branching event, followed by a steady drop over the next ~4 μs. Finally, the daughter cracks continued to grow in a mixed-mode fashion with nearly constant mode-I and mode-II SIFs until the end of the observation window.

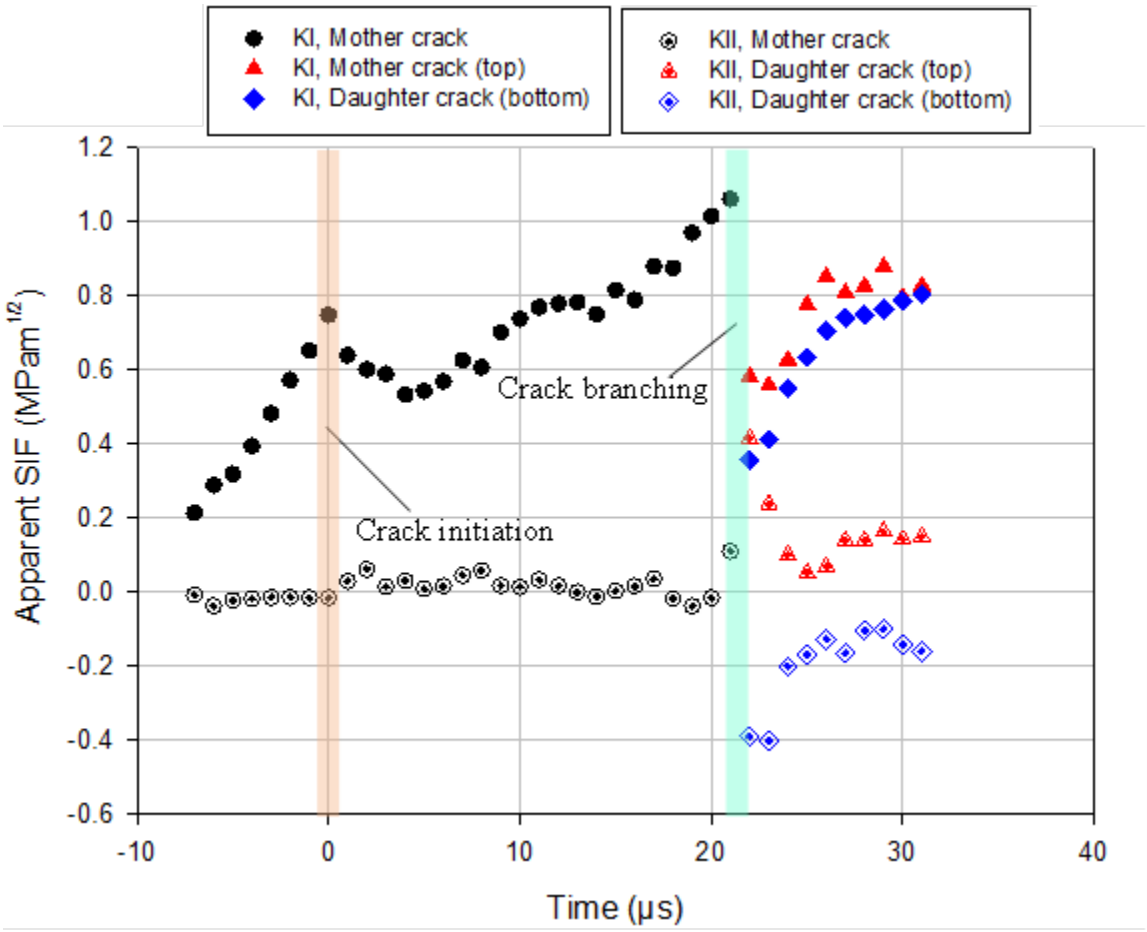

Figure 3.18: Apparent stress intensity factor histories from DGS. (Time, $t = 0$ corresponds to crack initiation at the original notch-tip)

3.4.4 Contact force history measurements

The contact force histories imposed on the V-notch flanks of the specimen by the long-bar were evaluated again via DGS measurements by using them in conjunction with the solution for line-load on an edge of a planar elastic solid. By assuming the functional form of the Flamant's solution [117] to hold under dynamic conditions, the normal forces acting on the specimen were expressed in terms of measured angular deflections of light rays as,

$$\phi_r = \sqrt{\phi_x^2 + \phi_y^2} = C_\sigma B \frac{2F(t)}{\pi B r^2} \tag{3.7}$$

where, C_σ is elasto-optic constant of SLG and B is specimen thickness. The normal force F at each time instant on the upper and lower flanks was evaluated using Eq. (3.5) and an over-deterministic least-square-analysis for the data in the region $0.75 \le r/B \le 1.75$ where r is the radial distance from the loading point. The analysis assumed a normal contact and neglected frictional effects. Thus obtained normal forces for the upper and lower flanks and the average normal force history is shown in Figure 3.19. As evident from the plots, the upper flank experienced contact forces slightly before the lower flank due to experimental asymmetry in this experiment, well captured by DGS. Yet, the individual force histories show the 'ramp-up, plateau, ramp-down' pattern, similar to the one observed in the photoelastic experiment (see, Figure 3.6).

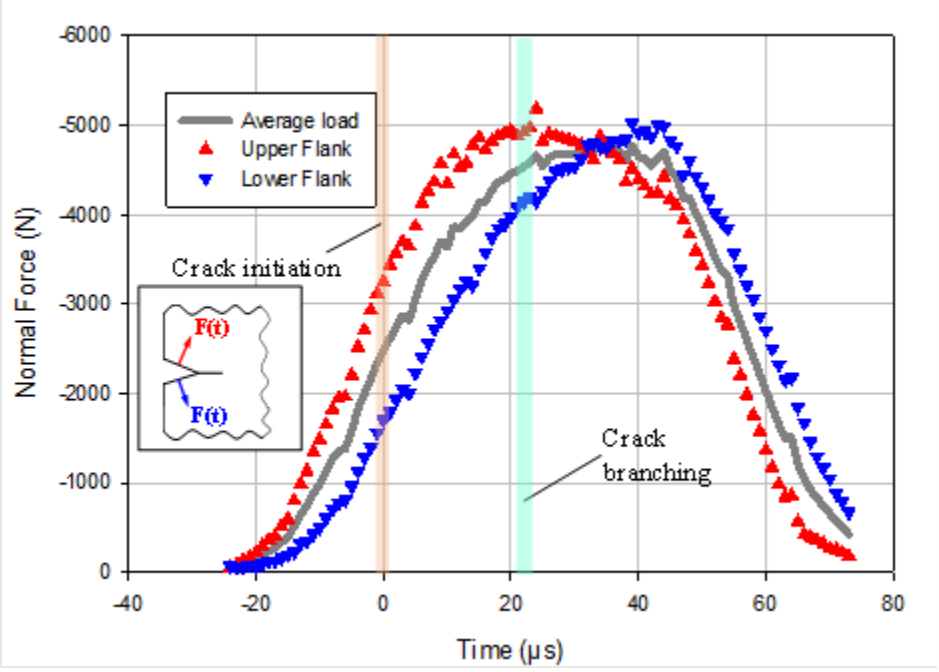

Figure 3.19: Contact force histories measured from DGS. (Time, $t = 0$ corresponds to crack initiation at the original notch-tip)

More importantly, the magnitudes of stresses evaluated from DGS and photoelasticity are very similar in terms of the peak force (~500 N) values even though they are two nominally identical but different experiments. The loading rate based on the average force history in the ramp-up

phase is ~142 MN/s, again rather close to the value in the photoelastic experiment. These confirm that DGS measurements could be used not only to map the crack tip fields but the impact load history as well with high fidelity.

3.5 Comparison of photoelasticity, DIC and DGS methods for SLG fracture

One analog and two digital full-field optical methods - photoelasticity, DIC and DGS - were implemented to visualize and quantify macroscale dynamic fracture of soda-lime glass (SLG), a rather challenging material for photomechanics investigation. The outcomes based on three nominally identical but different experiments provide new insights into the capabilities of these methods for investigating such low-toughness and high-stiffness glasses and ceramics. The results could also guide the selection and implementation of these methods at suitable length scales in the near term or spur enhancements to the methods in the long term. Conventional photoelasticity results show that insufficient birefringence of SLG along with its low fracture toughness precludes the method from being able to extract stress intensity factors via crack tip mechanical field measurements. It, however, can provide precise location of the instantaneous crack tip as well as features corresponding to contact stresses due to Rayleigh wave propagation (stitch marks in Figure 3.4) along the crack flanks with a hairline separation. The standard 2-D DIC methodology is also unsuitable in terms of its ability to both locate the instantaneous crack tip (directly from the non-singular deformation fields) and extract stress intensity factors accurately using displacements evaluated close to the measurement limit during high-speed crack growth in SLG. The singular strain fields are equally ineffective since numerical differentiation of noisy displacements further exaggerate errors that exist in the measurements. The DGS methodology, on the other hand, is rather effective in studying this challenging material system since it incorporates both elasto-optic effects and signal (speckle shift) amplification using an

'optical lever.' The measured DGS quantities being proportional to in-plane stress gradients and singular near a crack tip, locating the instantaneous crack tip from the data is easier. The extracted SIFs are equally reliable in terms of magnitude as well as trend during the fracture event.

Regarding the underlying mechanics of fracture of SLG, results from both photoelasticity and DGS consistently show a decreasing apparent crack velocity from a relatively steady value of ~1500 m/s (approx. $0.48C_R$) in the so-called mirror and mist phases of growth [78] to ~1000 m/s prior to macroscale crack branching event signaling the crack entering the hackle phase (or random microscale branch formations on the crack surfaces). As noted in the literature [129], hackle formations are a precursor to the ensuing crack branching event. Interestingly, despite the measured velocity trends, the apparent SIFs from DGS monotonically increase over the mirror to mist to hackle zones suggesting the likelihood of a critical SIF for branching to occur. Considering the monotonic increase of the apparent mode-I SIF from 0.6 MPa√m after crack initiation from the initial notch-tip to ~1.1 MPa√m prior to branching, a twofold increase of SIF as in previous works, is evident.

Chapter 4. Dynamic mixed-mode fracture

In this chapter, mixed-mode dynamic fracture of SLG under stress wave loading using the full-field optical method DGS is discussed. The goal is to obtain mixed-mode fracture characteristics including variation of the effective critical stress intensity factor at crack initiation as a function of mode-mixity. To attain a wide range of mode-mixities, a simple eccentric reverse impact loading configuration of an edge cracked plate is proposed. The modified Hopkinson pressure bar apparatus and ultrahigh-speed photography are employed to subject SLG specimens to inertial loading.

4.1 Experimental details

Multiple rectangular SLG specimens of 50 mm × 100 mm dimension, shown schematically in Figure 4.1, were extracted from a large 5.7 mm thick sheet. Subsequently, a 12 mm long notch was cut into each specimen using a 150 μm thick diamond impregnated circular saw.

a)

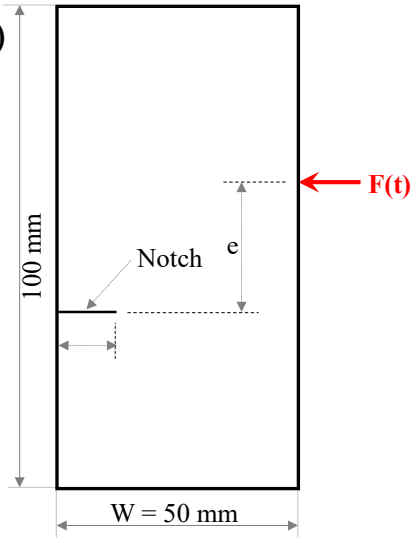

b)

Variants	Eccentricity, e, mm	Eccentricity ratio, e/W
1	0	0
2	6	0.12
3	12	0.24
4	18	0.36
5	24	0.48
6	30	0.60

Figure 4.1: Specimen geometry details (a), different configuration with corresponding eccentricity values (b). (Plate thickness = 5.7 mm; initial notch length, a = 12 mm).

The mixed-mode fracture specimen geometry and loading configurations were conceived by performing elasto-dynamic explicit simulations using ABAQUS structural analysis software (Abaqus/CAE 2016). To obtain various mode-mixities different configurations were considered by changing eccentricity ratio, *e/W* as tabulated in Figure 4.1(b). The simulations consisted of a 3D discretized model of the long-bar in contact with cracked specimen having a 12 mm long and 150 µm wide edge notch subjected to single point impact. The particle velocity corresponding to the intended impact velocity of the striker used in the actual experiments was used as input for all the eccentricity ratios. The 3D geometry of the long-bar (50 mm long, 25.4 mm diameter steel cylinder) and specimen developed for an eccentricity ratio of $e/W = 0.6$ is shown in Figure 4.2. To minimize the computational resources, shorter length of the long-bar (50 mm length) was used in FE modeling. The planar SLG specimen (150 mm × 100 mm × 5.7 mm) was modeled with 10 noded quadratic tetrahedron elements, C3D10M. The model consisted of 165,000 elements and 245,000 nodes and the initial notch was refined well (to capture shear and normal stress histories accurately) using a 20 µm length element at the notch-tip location, as shown in Figure 4.3(a).

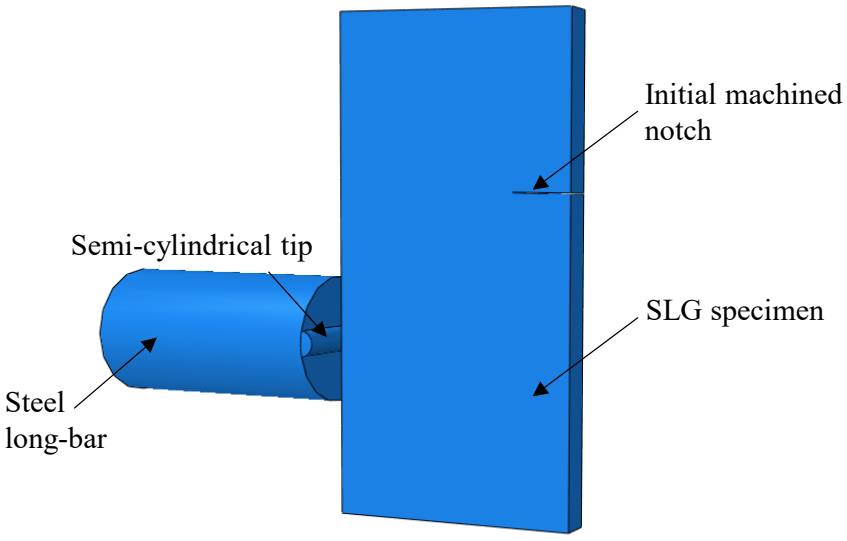

Figure 4.2: Geometry of long-bar and specimen used in 3D FEA for $e/W = 0.6$ case

Similarly, the long-bar was also modeled with 10-node quadratic tetrahedron elements, C3D10M, using 113,000 elements and 159,000 nodes (see Figure 4.3(b)) and refined the mesh on the long-bar end with a semi-cylindrical tip impart line loading. Figure 4.4 shows the particle velocity history used in the simulations for an intended striker velocity of 5.3 m/s. The particle velocity profile during plateau region (~2.7 m/s) attained was approximately 50% of striker velocity (~5.3 m/s) used during impact. A frictionless general contact was defined between the long-bar tip and the specimen.

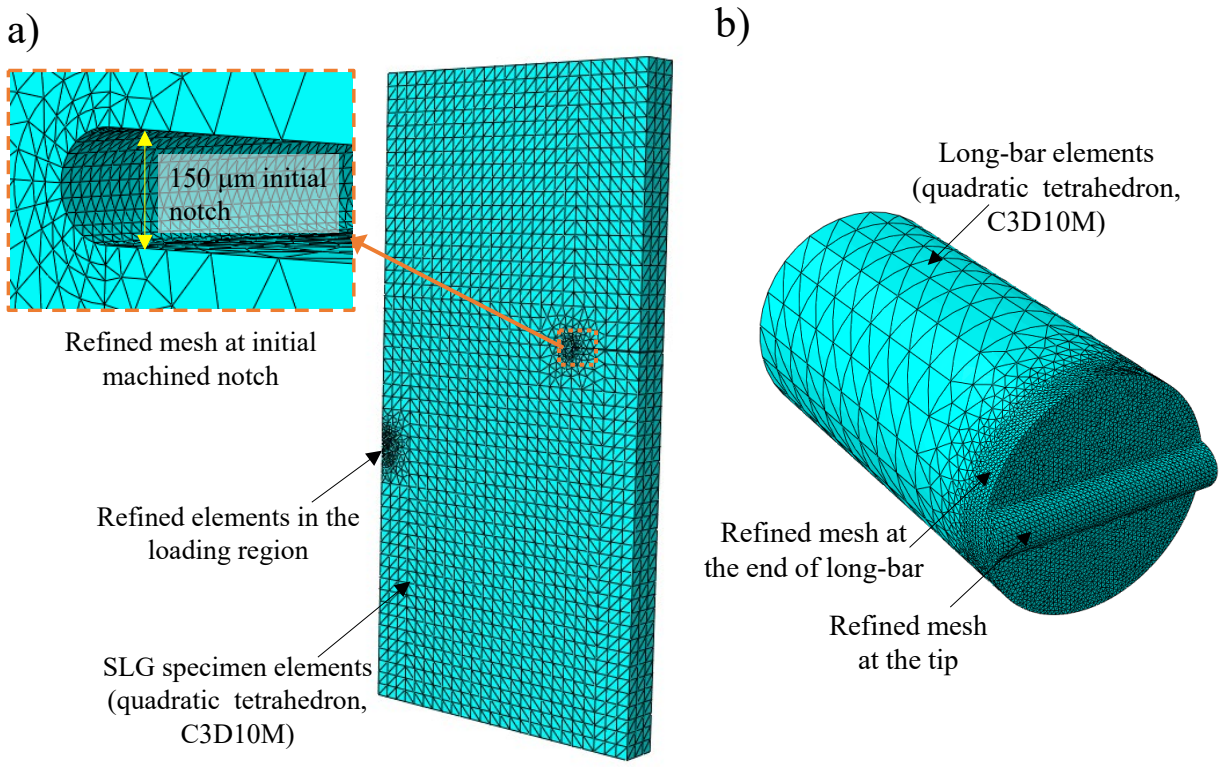

Figure 4.3: 3D FEA mesh of (a) SLG specimen along with refined initial notch for $e/W = 0.6$ case, (b) steel specimen along with refined tip.

Figure 4.5 shows the resulting instantaneous von Mises stress field in the specimen at a time instant of 47 µs after impact, as the stress waves reflected multiple times from the specimen boundaries and the machined notch. Further, notch-tip also experiences significant load by this time instant, as observed from the particle velocity profile shown in. Figure 4.4.

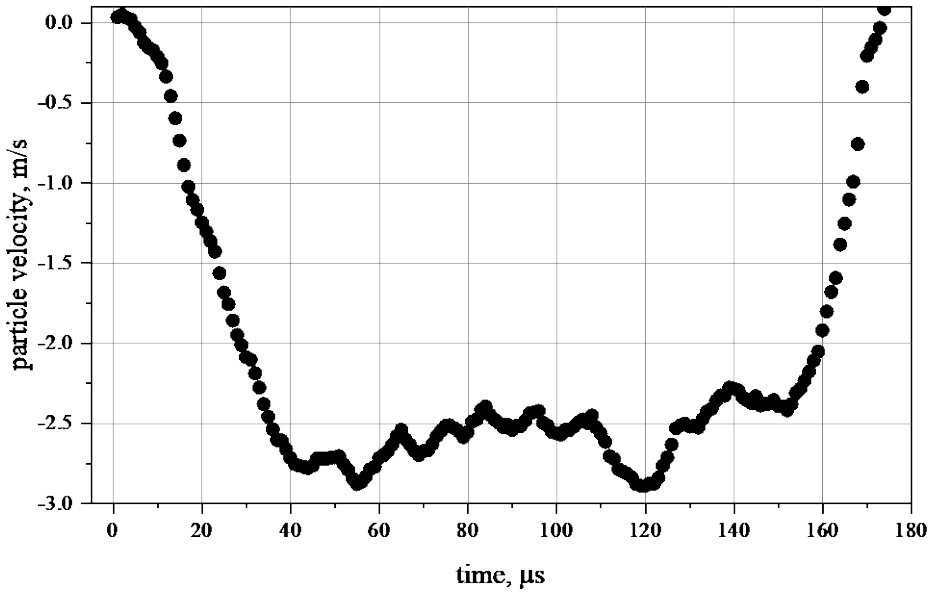

Figure 4.4: Particle velocity as input to finite element model of SLG specimen subjected eccentric loading

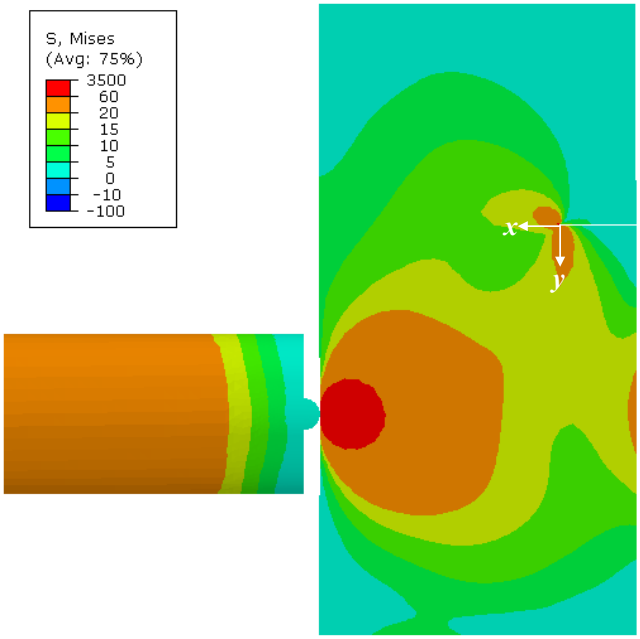

Figure 4.5: Instantaneous Von Mises stress distribution in the SLG single edge notch specimen subjected to eccentric loading for $e/W = 0.6$ case

In-plane normal stress, σ_{yy}, and shear stress, σ_{xy}, ahead of the notch at a location (r = 1 mm, θ = 0°) were extracted for different specimen configurations of e/W = 0, 0.36 and 0.6. Figure 4.6(a) and (b) shows shear stress, σ_{xy} and normal stress, σ_{yy} histories for eccentricity ratio, e/W = 0.36 and 0.6 cases respectively. The shear stress, σ_{xy} clearly dominates the normal stress, σ_{yy} in the initial stages of impact. Further, the normal stress magnitude was close to zero for a longer period of time in higher eccentricity case (e/W = 0.6), in comparison to e/W = 0.36. Before the normal stress starts increasing, presence of the higher shear stress fields results in dominating mode-II crack initiation. This clearly suggests the feasibility of this geometry to generate a wide range of mode-mixities at crack initiation. To generate various mode-mixities at crack initiation, different offset distances (or eccentricity, e) between the loading and notch axes were employed while maintaining a constant notch length in all geometries. Six geometric variants producing pure mode-I to dominant mode-II fracture at crack initiation were considered. Specifically, the specimens had eccentricities of e = 0, 6, 12, 18, 24, 30 mm relative to the loading axis and a constant notch length of 12 mm. Some relevant mechanical and physical properties of soda-lime glass are listed in Table 3.1. A general contact was defined to transfer line loading from the long-bar semi-cylindrical tip and the specimen surface.

4.2 Opto-mechanical setup

In this work, the vision-based full-field optical method - DGS - was used to study dynamic fracture in SLG under mixed-mode loading conditions. Details about the working principle of DGS method are provided in Chapter 2. To study mixed-mode dynamic fracture, the specimen was loaded eccentrically and it was placed on a soft putty strip along the top and bottom edges, as shown in Figure 4.7. This created geometric symmetry in terms of acoustic impedance while

providing nearly free-free boundary conditions along those edges. The experimental setup was as same as in dynamic fracture study detailed in Section 3.4, except the striker velocity used in these experiments was ~5.3 m/s. The magnification factor (or, the scale factor) of the recorded images was 118 μm/pixel on the target plane (94 μm/pixel on the specimen plane).

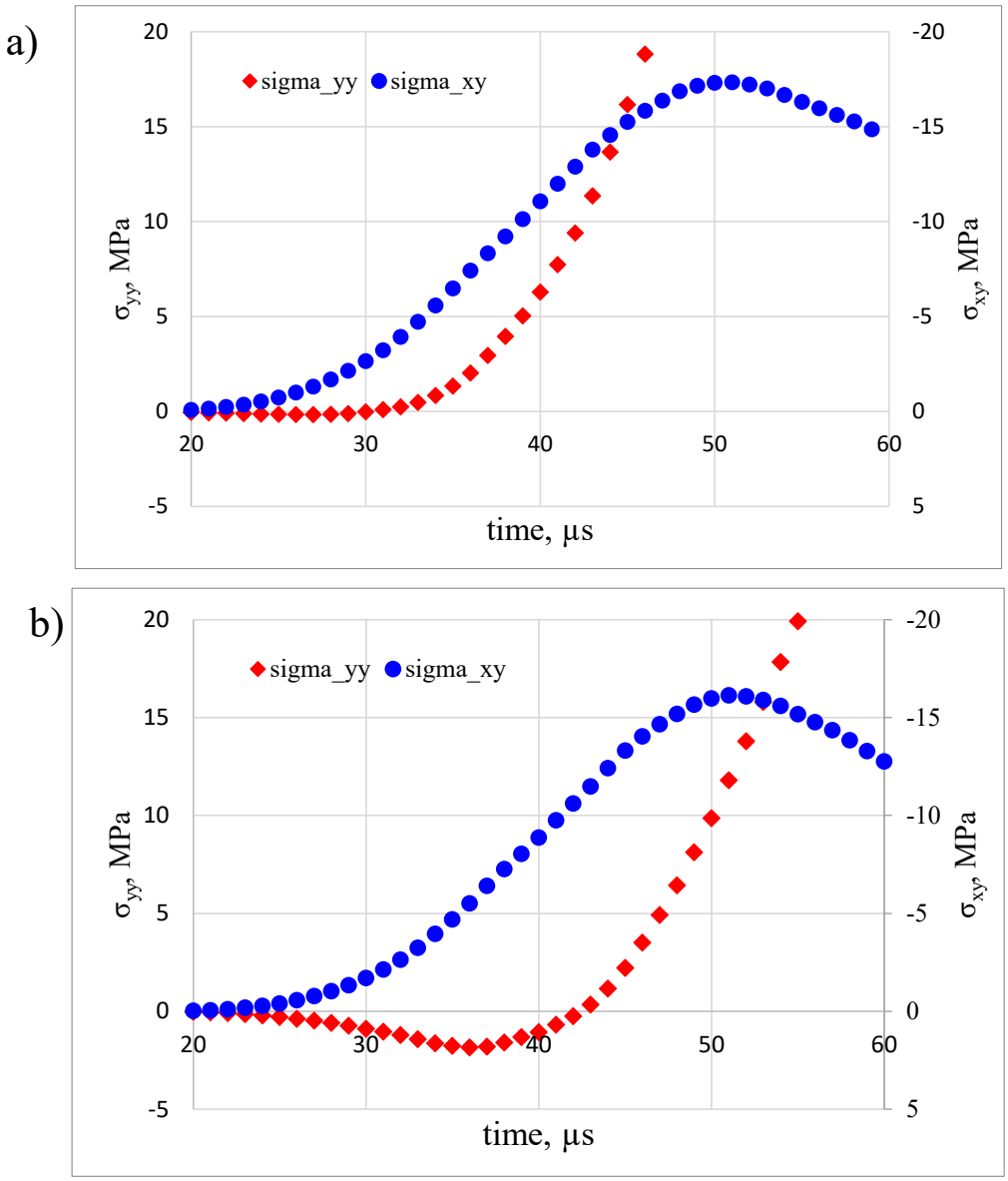

Figure 4.6: normal stress, σ_{yy} and shear stress, σ_{xy} histories for (a) eccentricity ratios, e/W = 0.36 and (b) e/W = 0.6 cases.

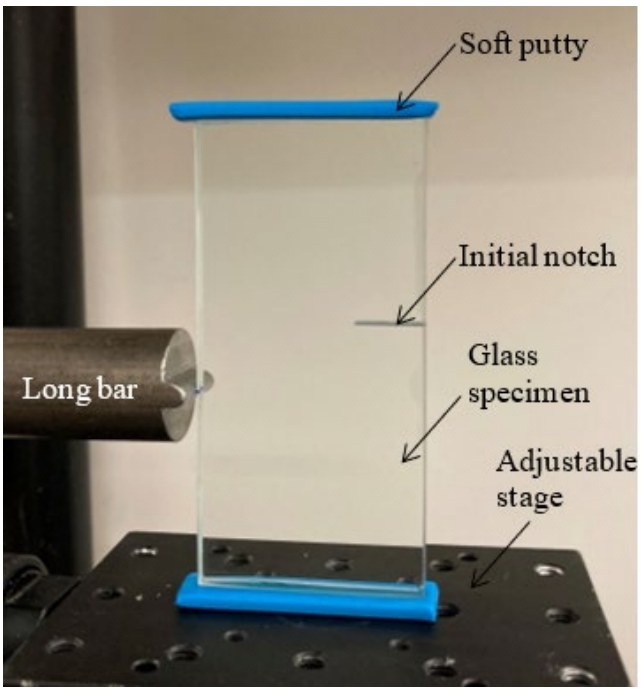

Figure 4.7: Soda-lime glass specimen subjected to dynamic reverse Impact loading. (*For clarity*, *the speckle target is not shown in the photograph*)

4.3 Stress gradient measurements

Figure 4.8 shows a pair of recorded speckle images off the target through the specimen at time instants t = -37 μs and 0, respectively; the former is in the reference/undeformed state and the latter corresponds to the crack initiation instant. The specimen edges, initial notch and crack tip location are highlighted in Figure 4.8. The speckle fields themselves are not very informative except for grey scale smearing near locations of significant deformations near the loading point and the crack tip upon careful examination. Upon correlating the speckle fields from the reference and deformed states, however, the mechanical fields become vividly evident. The angular deflections of light rays ϕ_x and ϕ_y in the two orthogonal directions (with respect to the initial notch) at select time instants for select geometries are shown in Figure 4.9 and Figure 4.10 as contour maps. They show morphological differences in the resulting mechanical fields obtained from different specimen geometries. The instantaneous contour maps were obtained by

segmenting each recorded speckle image in the reference and deformed states into 30 × 30 pixels size sub-images.

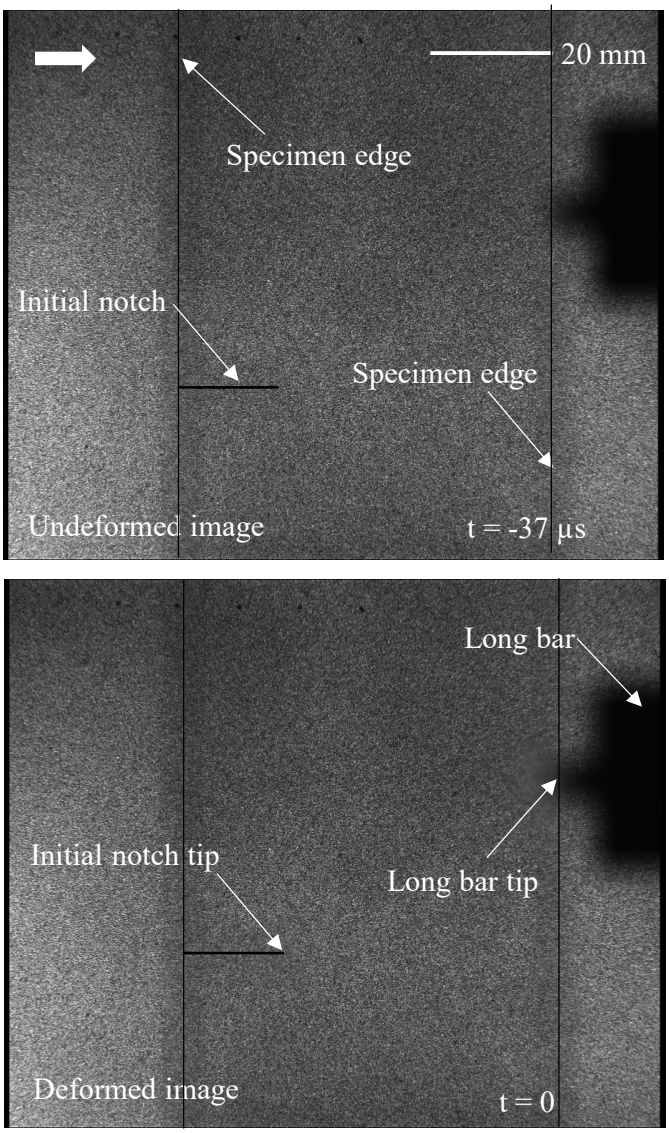

Figure 4.8: Speckle images from in the undeformed (top) and deformed (bottom) states recorded by ultrahigh-speed camera. (The heavy arrow represents crack growth direction towards the load.)

The location of a sub-image in the deformed state was determined relative to its position in the reference state by performing a gray scale correlation using a commercial image analysis software ARAMIS® (GOM mbH, Braunschwelg, Germany). A sub-image overlap of 5 pixels was used during analysis to balance computational effort and noise in the results. Once the location of

a sub-image in the deformed state was identified, the local speckle shifts were quantified at the center of each sub-image. This resulted in two pseudo speckle shift data arrays of 146 × 132 size corresponding to the horizontal and vertical directions, respectively, at each time instant. These were subsequently converted into angles ϕ_x and ϕ_y by dividing the speckle shifts by the separation distance between the specimen and target planes in the optical setup.

The specimen edges along with the initial notch are highlighted in Figure 4.9. Here, the timestamps are with respect to the instant when the crack initiated ($t = 0$) at the initial tip. The first column in Figure 4.9 represents ϕ_x contours before crack initiation at a time instant, t = -3 μs, for three select eccentricity ratios. The second column shows contour maps at crack initiation or at t = 0 and the last column represents contour plots during crack propagation. The first row represents pure mode-I loading variant, where ϕ_x contours are symmetric relative to the dominant mode-I crack path. The second row represents ϕ_x contours with an eccentricity ratio of e/W = 0.24 and the contours are asymmetric about the initial notch. The ϕ_x contours in the last row represents mode-II dominant loading case with an eccentricity ratio of e/W = 0.48. In this case, due to the higher mode-mixity, the shape of ϕ_x contours appear to have rotated significantly relative to the one in the first row.

In Figure 4.10, ϕ_y contours at select time instants for the corresponding three different eccentricity ratios are plotted. Again, the first row depicts ϕ_y contours of pure mode-I condition; hence the contour shapes are anti-symmetric with respect to the initial notch. With an increase in the eccentricity ratio to e/W = 0.24, the ϕ_y contours become asymmetric as the crack tip in this case is subjected to mixed-mode loading.

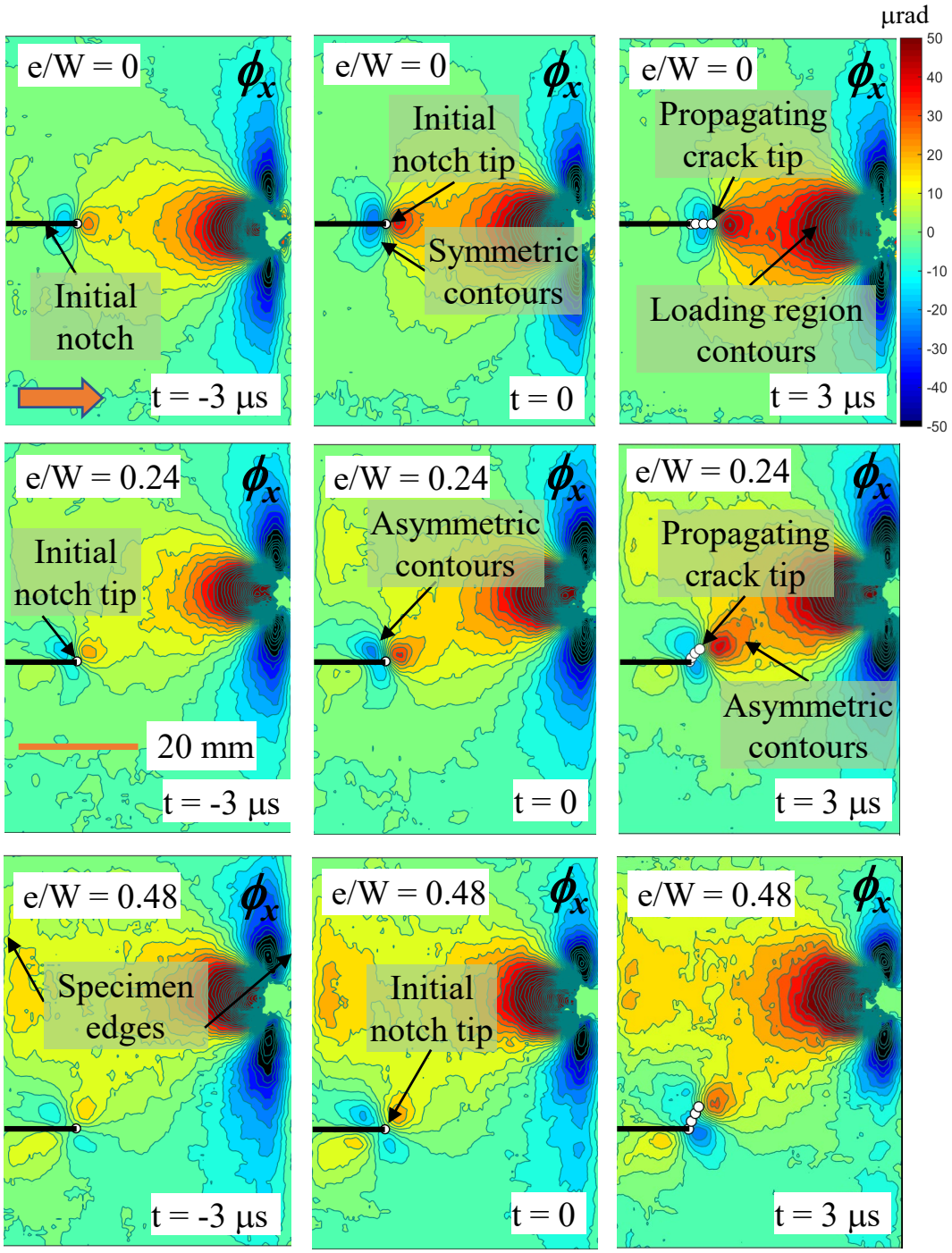

Figure 4.9: Contours of angular deflection of light rays (contour increment = 5×10^{-6} rad) in *x*-*z* plane in soda-lime glass plate at select time instants. The arrow head in the top left shows crack growth direction. (Time, $t = 0$ corresponds to crack initiation at initial notch tip.)

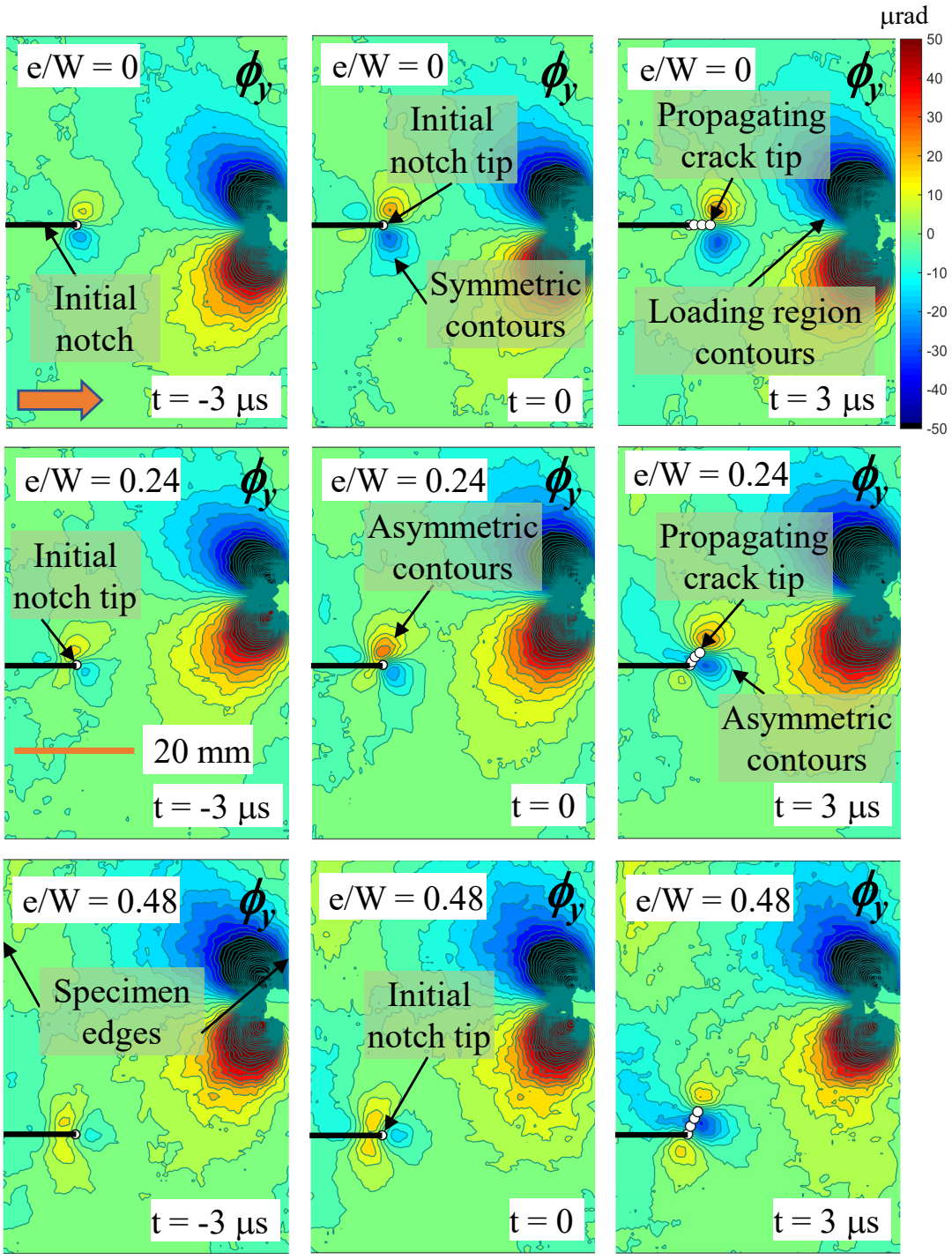

Figure 4.10: Contours of angular deflection of light rays (contour increment = 5×10^{-6} rad) in *y-z* plane in soda-lime glass plate at select time instants. The arrowhead in the top left shows crack growth direction. (Time, $t = 0$ corresponds to crack initiation at initial notch tip.)

At a higher eccentricity ratio of e/W = 0.48, the crack tip experiences a dominant mode-II loading, and hence the ϕ_y contours appear to have rotated significantly relative to the mode-I counterparts. It is noteworthy that from these two sets of angular deflection contours, locating the crack tip is relatively straight forward due to the singular nature of the mechanical fields [18]. That is, the contours representing each of the measured fields have a lobed structure that converges to the crack tip, marked in Figure 4.9 and Figure 4.10 by a solid white dot/circle, making it relatively easy to locate it at each time instant. Any uncertainty can be further resolved by considering contours of resultant angular deflection, $\sqrt{\phi_x^2 + \phi_y^2}$, which produce closed contours encircling the instantaneous crack tip and easy to identify [16].

4.4 Stress intensity factor histories

The procedure for extracting the stress intensity factor histories from the angular deflections $\phi_{x'}$ around the crack tip in conjunction with the asymptotic expressions [103] using an over-deterministic least-squares error minimization approach are similar to the description in section 3.4.3. The angular deflection contours ϕ_x and $\phi_{x'}$ in both global and local coordinates 8 μs after crack initiation is shown in Figure 4.11. As to be expected, the ϕ_x contours are asymmetric about the crack tip location whereas the $\phi_{x'}$ contours are more symmetric with respect to instantaneous crack tip propagation direction, x', suggesting crack growth under locally dominant mode-I conditions. For analysis purposes, the data near the crack tip in the region $0.35 \le r/B \le 1.35$ with an angular extent of $-150° \le \theta \le 150°$ was considered. The mode-I SIF, K_I , of the specimen with a zero-eccentricity ratio (e/W ratio*)* increased steadily from nearly zero value to ~ 0.72 MPa√m over ~ 15 μs period. The fracture toughness obtained under mode-I loading

condition is similar to the values obtained from the previous studies [16, 18]. After initiation, the mode-I SIF, K_I, is nearly constant for about 2 μs and increased again until the end of the observation window. The SIF histories are shown only for 5 μs after crack initiation since the crack tip fields start interacting with those in the loading region significantly after that. Meanwhile, the corresponding instantaneous mode-II SIF values, K_{II}, expectedly remained low. With post-initiation growth expected to occur under dominant mode-I conditions locally, one could view the mode-II SIF values to represent error estimates from the least-square error minimization method adopted here. Next, with an eccentricity ratio of $e/W = 0.12$, the K_I values increased steadily until initiation, similar to $e/W = 0$ case.

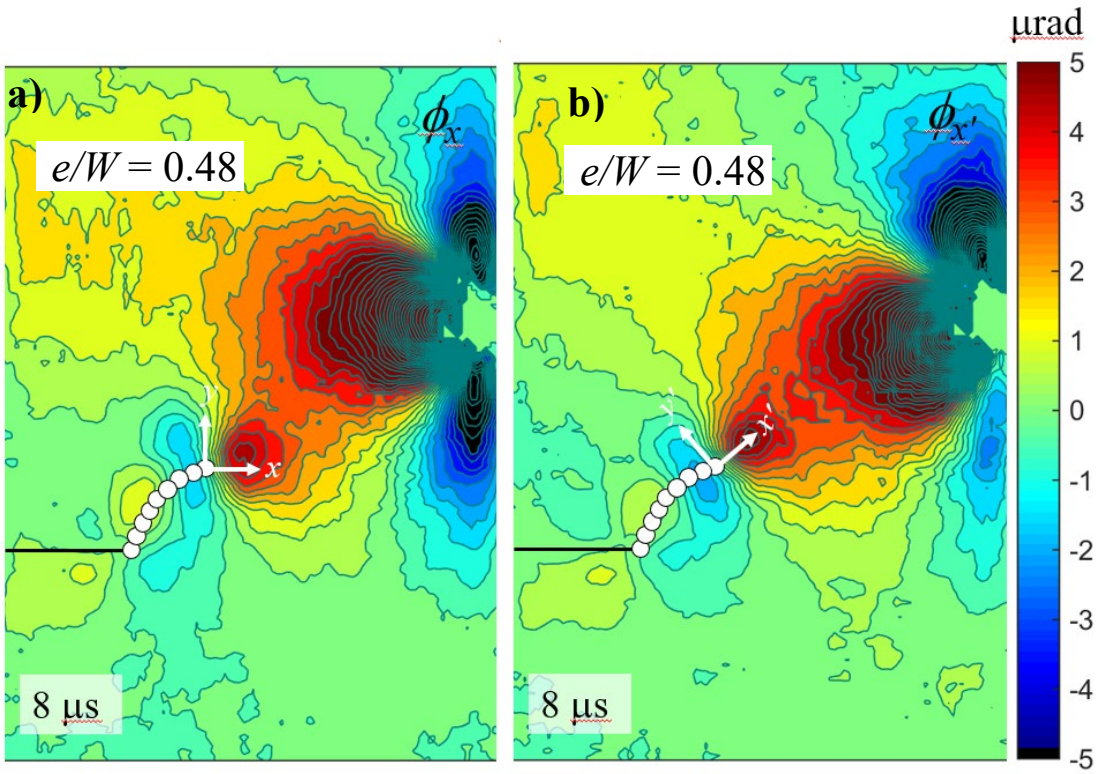

Figure 4.11: Contours of angular deflections of light rays (contour increment = 5×10^{-6} rad) in (a) global coordinates (x-z plane) and (b) local coordinates (x'-z plane) at select time instant during kinked crack growth for $e/W = 0.48$ configuration. The white markers represent crack tip locations at the current and previous time instants.

a)

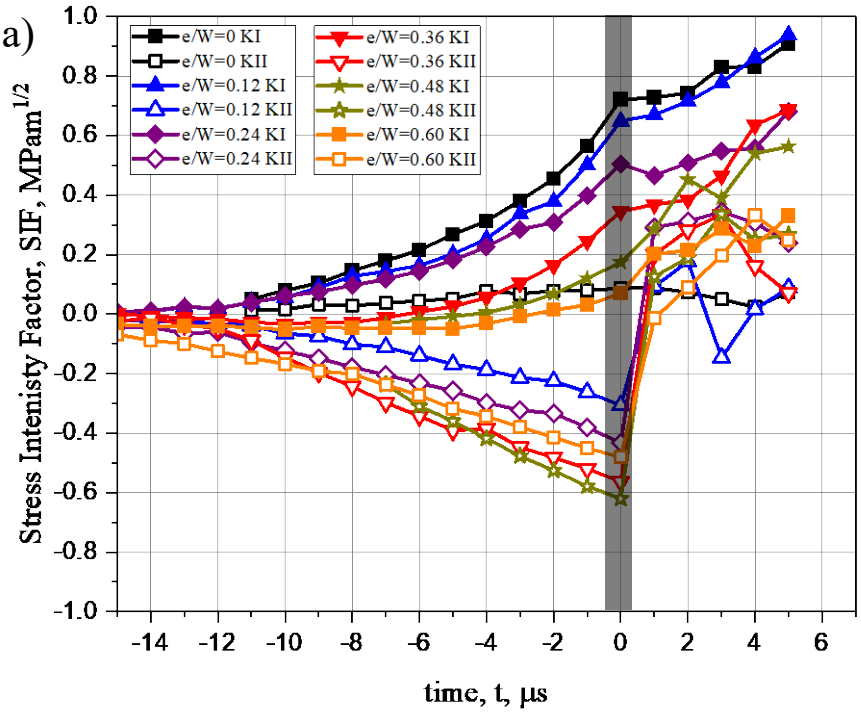
e/W=0 KI
e/W=0 KII
e/W=0.12 KI
e/W=0.12 KII
e/W=0.24 KI
e/W=0.24 KII
e/W=0.36 KI
e/W=0.36 KII
e/W=0.48 KI
e/W=0.48 KII
e/W=0.60 KI
e/W=0.60 KII
Stress Intenisty Factor, SIF, MPam^1/2
time, t, μs

b)

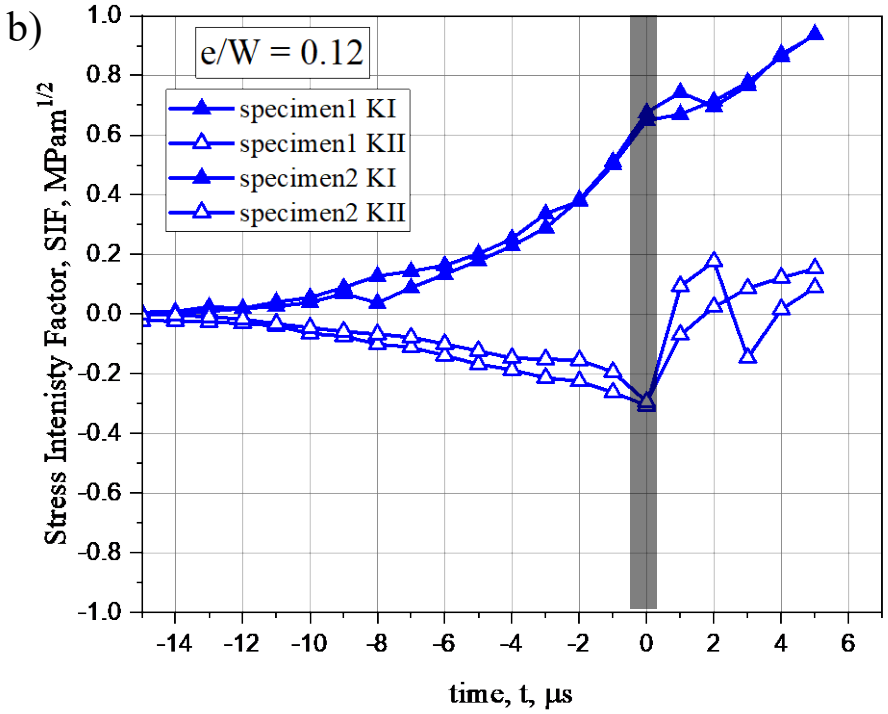
e/W = 0.12
specimen1 KI
specimen1 KII
specimen2 KI
specimen2 KII
Stress Intenisty Factor, SIF, MPam^1/2
time, t, μs

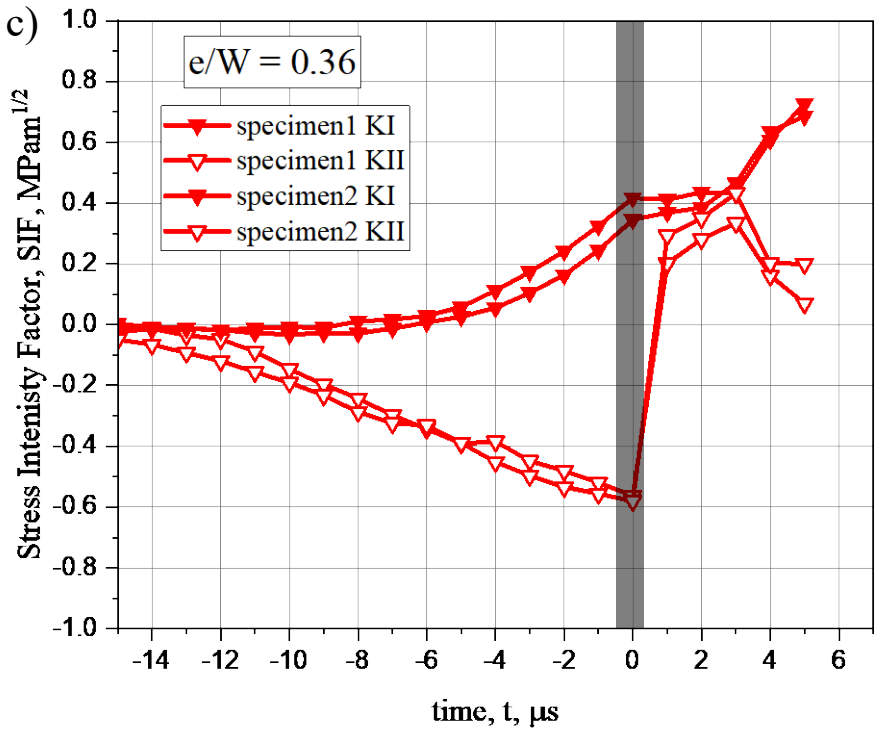

Figure 4.12: Stress intensity factor histories (a) for selected experiments from all mixed-mode configurations, (b) repeatability experiments from eccentricity ratio, $e/W = 0.12$ case and (c) repeatability experiments from eccentricity ratio, $e/W = 0.36$ case of soda-lime glass specimens subjected to dynamic loading. (Time, $t = 0$ corresponds to crack initiation at initial notch tip.)

However, the K_I values tracked below the latter case until initiation and the fracture toughness at initiation, K_{Icr}, was ~ 0.65 MPa√m in this specimen. After initiation, the mode-I SIF dropped and continued to increase, similar to the trend observed in $e/W = 0$ case. The mode-II SIF, K_{II}, for $e/W = 0.12$ variant also increased steadily in *magnitude* and reached a value of ~ -0.31 MPa√m at initiation. Once the crack initiated, the negative mode-II SIF values flipped to positive values and transiently fluctuated for ~ 3 μs before reducing to ~ 0.09 MPa√m at 5 μs. With a further increase in the eccentricity ratio, the mode-I SIF values decreased. The critical mode-I SIFs for $e/W = 0.24$, 0.36, 0.48 and 0.60 were ~ 0.50 MPa√m, 0.35 MPa√m, 0.17 MPa√m, and 0.07 MPa√m,

respectively, and the post initiation mode-I SIF values also show similar trends observed in e/W = 0 and 0.12 cases. It is noteworthy that the magnitude of mode-II SIF increased until e/W = 0.48 case and decreased for e/W = 0.60 case. The corresponding mode-II values were ~ -0.33 MPa√m, -0.48 MPa√m, -0.52 MPa√m, and -0.41 MPa√m. In the post initiation phase, the mode-II SIF values flipped to positive values and fluctuated for a few microseconds due to the transients before reducing to small values. In each case from e/W = 0 to 0.60, two to four experiments were conducted to ensure repeatability. Figure 4.12(b) and (c) show SIF histories for multiple e/W = 0.12 and 0.36 cases; reasonably good repeatability and data trends are seen given the challenging brittle material system being investigated.

4.5 Fracture envelope for SLG

The measurements described above were compiled into plots of critical effective SIF ($\left(K_{eff}\right)_{cr} = \sqrt{K_{Icr}^2 + K_{IIcr}^2}$) and critical mode-mixity ($\psi_{cr} = \left|\tan^{-1}\left(\frac{K_{Icr}}{K_{IIcr}}\right)\right|$) at crack initiation in Figure 4.13(a) and (b) as a function of e/W, the specimen dependent geometric parameter. The $\left(K_{eff}\right)_{cr}$ values are nearly constant for e/W ratios up to 0.36 with a decreasing trend seen at higher values of e/W namely, 0.48 and 0.6. The ψ_{cr} values on the other hand show a monotonically increasing trend over the entire e/W range examined. Using these two plots and by eliminating the geometric parameter e/W, a mixed-mode fracture characteristic plot for SLG was generated and is shown in Figure 4.13(c). It suggests that the critical fracture toughness evaluated as $\left(K_{eff}\right)_{cr}$ of SLG is generally independent of mode-mixity at crack initiation until a mode-mixity of ~ 65°.

a)

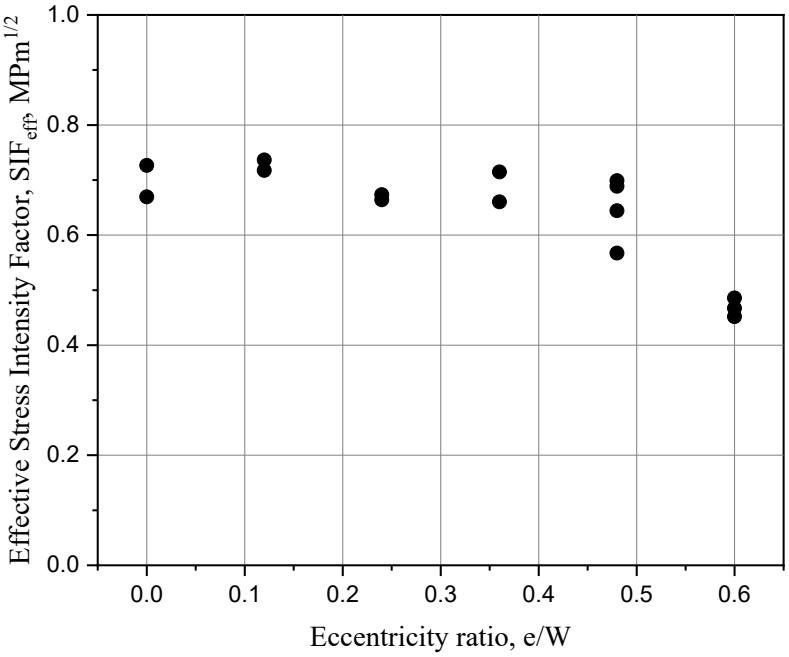
Effective Stress Intensity Factor, SIF_{eff}, $MPm^{1/2}$
1.0
0.8
0.6
0.4
0.2
0.0
0.0
0.1
0.2
0.3
0.4
0.5
0.6
Eccentricity ratio, e/W

b)

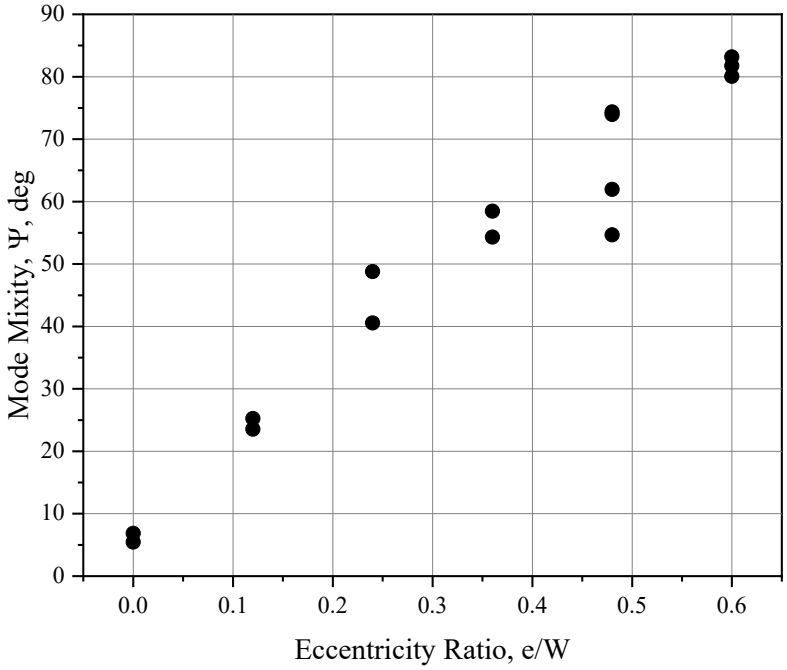
Mode Mixity, Ψ, deg
90
80
70
60
50
40
30
20
10
0
0.0
0.1
0.2
0.3
0.4
0.5
0.6
Eccentricity Ratio, e/W

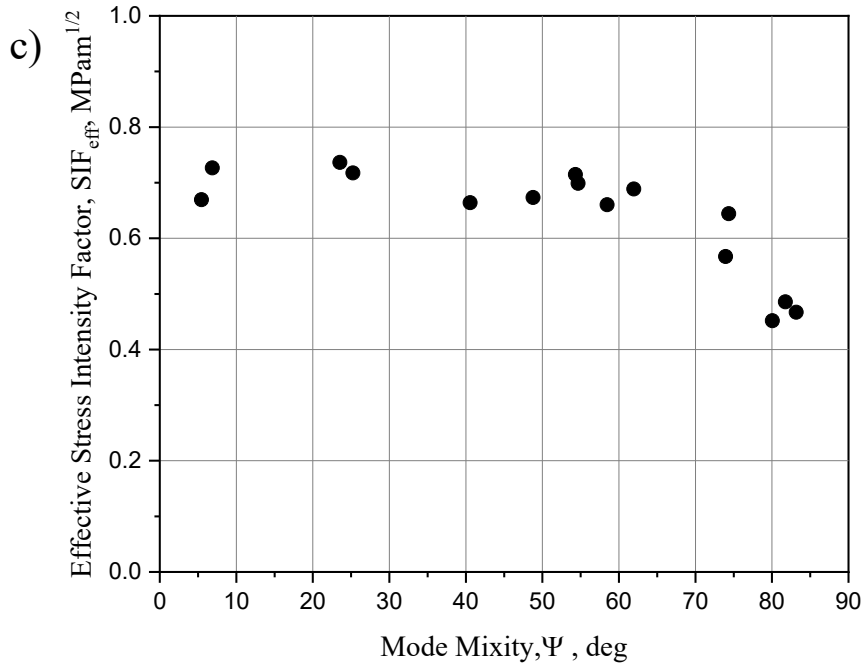

Figure 4.13: Compilation of measured fracture parameters for SLG from different mixed-mode fracture experiments: (a) Dependence of effective critical stress intensity factor on eccentricity, (b) Dependence of mode-mixity on eccentricity and (c) Variation of effective critical stress intensity factors with mode-mixity.

Beyond that and up to a mixity of 85° achieved in the current work, there is a visible drop in the $\left(K_{eff}\right)_{cr}$ value to ~0.45 MPa√m and an extrapolated value of ~ 0.35 MPa√m at ψ_{cr} of 90° or the pure mode-II condition. This is somewhat counter to the mixed-mode fracture behaviors of ceramics such as alumina and zirconia [130] and soft stones reported in the literature. It is likely attributed to the amorphous nature of SLG. That said, there are reports in the literature where a drop in the strength of borosilicate glass and soda-lime glass with increasing shear in shear-compression tests [131, 132] is observed. Furthermore, Johnston et. al [133] and Mirsayar et. al [134, 135] have reported a reduction in the fracture toughness of Johnstone, Neyriz and Harsin

marble rock materials at higher mode-mixities, suggesting consistency of the present observation with those reports.

A fracture envelope was also generated using the critical mode-I and mode-II SIF values, K_{Icr} and K_{IIcr}, obtained using the methodology detailed previously. The resulting plot is shown in Figure 4.14 using solid symbols.

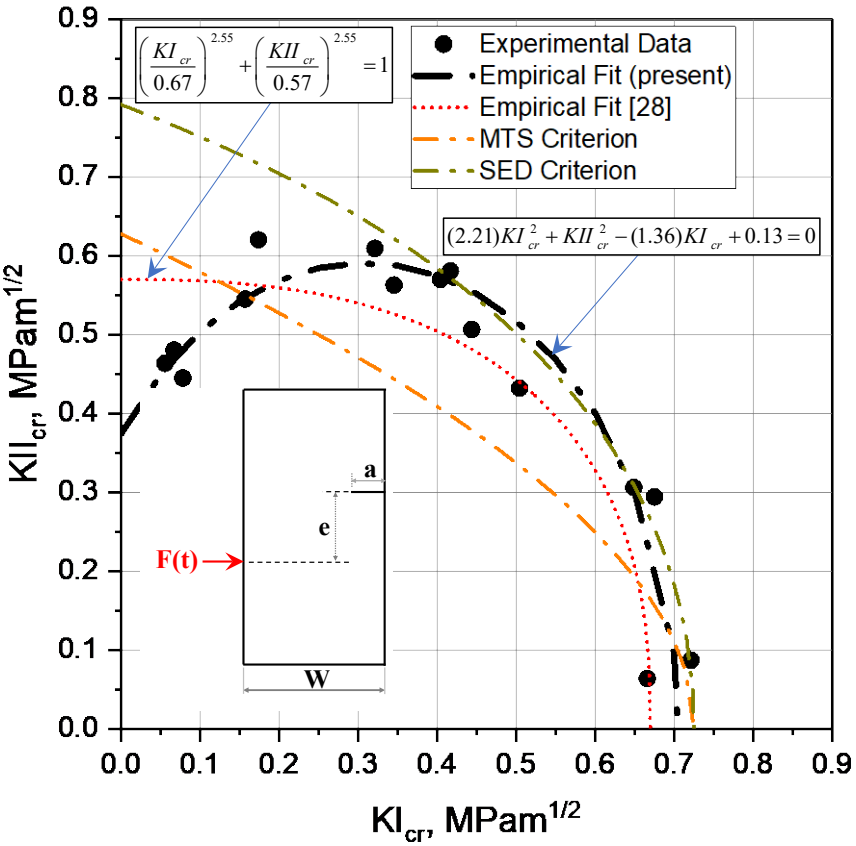

Figure 4.14: Mixed-mode fracture envelopes for soda-lime glass.

The fracture envelope was compared with two popular mixed-mode crack propagation criteria for brittle materials. First, the Maximum Tangential Stress (MTS) criterion [136, 137] was considered. As per the MTS criterion, crack should grow in a direction perpendicular to the

maximum hoop stress, $\sigma_{\theta\theta}$, at the crack tip when the hoop stress reaches a critical value. It is governed by,

$$K_I \cos^3\frac{\theta_{cr}}{2} - \frac{3}{2}K_{II}\cos\frac{\theta_{cr}}{2}\sin\theta_{cr} = K_{Icr} \tag{4.1}$$

where θ_{cr} is the crack kink angle. Next, the Strain Energy Density (SED) criterion [137] was also used to compare it with the experimental results. As per the SED criterion, crack should propagate in a direction of minimum SED, $S(\theta)$ given by,

$$S(\theta) = \left(\frac{1}{\pi}\right)\left(g_{11}K_I^2 + 2g_{12}K_I K_{II} + g_{22}K_{II}^2\right) \tag{4.2}$$

where $\begin{Bmatrix} g_{11} \\ g_{12} \\ g_{22} \end{Bmatrix} = \left(\frac{1}{16\mu}\right)\begin{bmatrix} (1+\cos\theta_{cr})(\eta-\cos\theta_{cr}) \\ 2\cos\theta_{cr} - (\eta-1) \\ (\eta+1)(1-\cos\theta_{cr}) + (1+\cos\theta_{cr})(3\cos\theta_{cr}-1) \end{bmatrix}$,

μ = shear modulus, $\eta = \frac{3-\upsilon}{1+\upsilon}$ for plane stress, and propagate when minimum SED reaches a critical value $S_{cr}(\theta)$. Evidently, both MTS and SED criteria are not very representative of the measured data at higher mode-mixities with the latter following the trend better than the former. It is also worth noting that an empirical curve of the type,

$$\left(\frac{K_{Icr}}{0.67}\right)^{2.55} + \left(\frac{K_{Icr}}{0.57}\right)^{2.55} = 1 \tag{4.3}$$

has been shown to fit the soft stone (Johnstone) data better in Ref. [133]. The resulting empirical fit is also shown in Figure 4.14. Again, the agreement between the fit and the data is not good particularly at higher mode-mixities. Accordingly, a different empirical fit of the type,

$$(2.21)K_{Icr}^2 + K_{IIcr}^2 - (1.36)K_{Icr} + 0.13 = 0 \tag{4.4}$$

was considered. It fits the experimental data well over the entire range of mixities with critical values for pure mode-I and mode-II conditions as 0.71 and 0.37 MPa√m, respectively.

Next, the kink angles from failed specimens were also measured from fractured specimens and compared directly with the ones from MTS and SED criteria. Figure 4.15 shows magnified views of fractured specimens with increasing eccentricity. For better visual clarity, only lower part of the fractured specimens is shown.

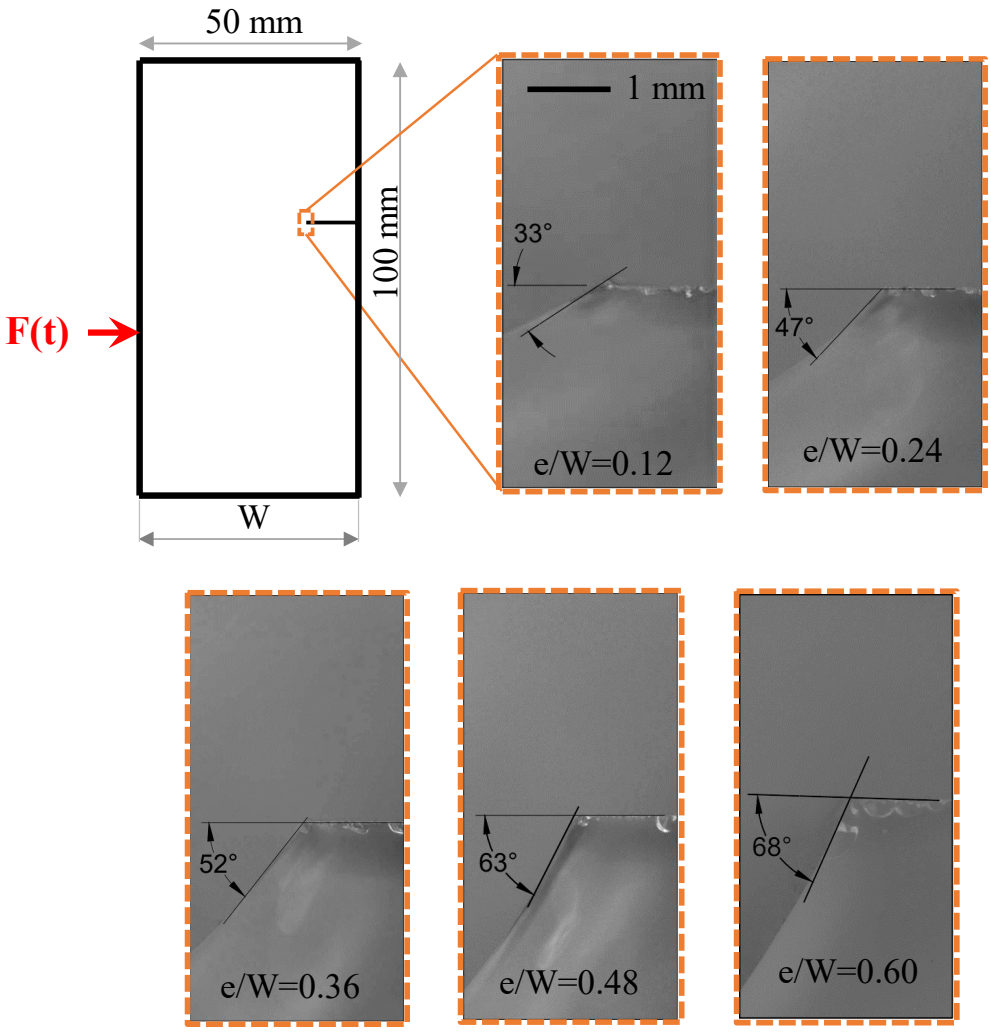

Figure 4.15: Measured kink angles obtained from soda-lime glass from different dynamic fracture experiments. Measurement accuracy is ±2°.

The measured kink angle from mixed-mode experiments were 33°, 47°, 52°, 63° and 68° for eccentricity ratios, *e/W*, of 0.12, 0.24, 0.36, 0.48 and 0.60, respectively, with a ±2° measurement accuracy. The kink angles from MTS criterion were evaluated using,

$$K_I\left[-\sin\frac{\theta_{cr}}{2}-\sin\frac{3\theta_{cr}}{2}\right]+K_{II}\left[-\cos\frac{\theta_{cr}}{2}-3\cos\frac{3\theta_{cr}}{2}\right]=0$$
$$K_I\left[-\cos\frac{\theta_{cr}}{2}-3\cos\frac{3\theta_{cr}}{2}\right]+K_{II}\left[\sin\frac{\theta_{cr}}{2}+9\sin\frac{3\theta_{cr}}{2}\right]<0 \quad (4.5)$$

using measured critical SIFs at crack initiation (Figure 4.14). The results are compared with the ones measured from the fractured specimens in Table 4.1. The kink angles from the MTS criterion for eccentricity ratios of e/W = 0, 0.12, 0.24, 0.36, 0.48 and 0.60 was 11°, 39°, 51°, 59°, 65° and 68°, respectively, and are in reasonably good agreement but for the mode-I case which produced a small yet distinct kink while initiating from the notch tip.

Table 4.1 – Measured kink angles from experiments along with MTS and SED criteria predicted angles. (Measurement accuracy is ± 2°)

Eccentricity ratio, e/W	**Measured Kink Angle, deg**	**MTS criterion, α, deg**	**SED criterion, β, deg**
0	5	11	9
0.12	33	39	33
0.24	47	51	44
0.36	52	59	56
0.48	63	65	67
0.60	68	68	72

The SED criterion was also used for estimating crack kink angles by satisfying the following equations:

$$\left[2\cos\theta_{cr}-(\eta-1)\right]\sin\theta_{cr}K_I^2+2\left[2\cos 2\theta_{cr}-(\eta-1)\cos\theta_{cr}\right]K_IK_{II}+\left[(\eta-1-6\cos\theta_{cr})\sin\theta_{cr}\right]K_{II}^2=0 \quad (4.6)$$

$$[2\cos(2\theta_{cr})-(\eta-1)\cos\theta_{cr}]K_I^2+2[(\eta-1)\sin\theta_{cr}-4\sin(2\theta_{cr})]K_I K_{II}+\left[(\eta-1)\cos\theta_{cr}-6\cos(2\theta_{cr})\right]K_{II}^2>0$$

where η a function of Poisson's ratio (assumed to be = 2.28 for SLG and plane stress condition). The resulting kink angles are also tabulated in Table 4.1. The kink angles obtained from the SED criterion for eccentricity ratio of *e/W* = 0, 0.12, 0.24, 0.36, 0.48 and 0.60 was 9°, 33°, 44°, 56°, 67° and 72°, respectively, again in reasonable agreement with the measurements. Thus, both MTS and SED criteria show a reasonably good match with the kink angles of fractured specimens.

Chapter 5. Cascading crack bifurcations: Quantification of pre-cursors

In this chapter, details on a full-field optical investigation of dynamic crack branching phenomenon in SLG using test geometries capable of producing single and cascading bifurcations when subjected to stress wave loading is presented. The linear elastic frame mechanics (LEFM)-based precursors extracted from optical measurements leading up to branching in SLG are identified. The suggested precursors are based on crack velocity, stress intensity factors, higher order coefficients of the asymptotic crack tip fields and non-dimensional parameters based on a combination of these quantities. Fracture surface roughness and other features are also separately quantified via high resolution post-mortem examination to corroborate with the optically measured quantities.

5.1 Experimental details

Transparent SLG plates used to study dynamic mode-I crack branching were commercially procured. Specimens were cut from a single large 5.7 mm thick plate into samples of two different dimensions: (a) 150 mm length, and 100 mm width, and (b) 150 mm length, and 150 mm width. A symmetric 40° V-notch was introduced at the mid-span of each specimen type along the 150 mm edge, as shown in Figure 5.1. The apex of the V-notch was extended by 8 mm using a 0.3 mm thick diamond impregnated circular saw. Mechanical and physical properties of SLG relevant to this work are listed in Table 3.1. Transmission-mode Digital Gradient Sensing (DGS) technique [54] was used in this work to visualize and quantify crack tip fields associated with crack initiation, growth, and branching phenomena. The working principle of DGS method is described in Chapter

2 and the experimental setup is detailed in section 3.4. The loading phase, crack initiation[2], mode-I crack growth leading to mixed-mode branching were all recorded using the ultrahigh-speed camera for a loading pulse duration of ~120 μs in the 100 mm × 150 mm specimen geometry. In the 150 mm × 150 mm specimen geometry, however, the temporal window of interest covered mode-I crack growth, and first and subsequent crack branching events but not crack initiation.

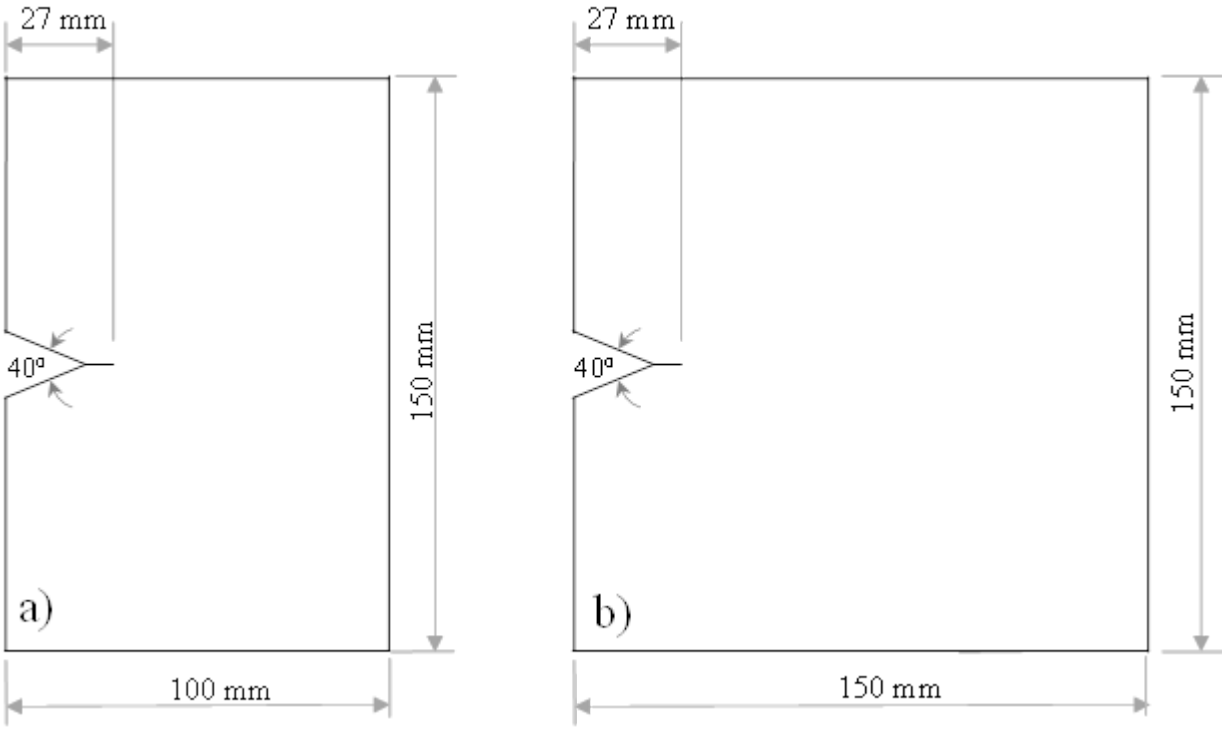

Figure 5.1: Two soda-lime glass specimen geometries (a) and (b) with extended V-notch. (Plate thickness = 5.7 mm).

A 110 × 92 mm^2 region on the target corresponding to approx. 88×65 mm^2 on the specimen, was photographed. Besides monitoring the contact stress evolution on the crack flanks [18], the ROI covered crack initiation, mode-I crack propagation of the mother crack leading to two mixed-

[2] Based on the load history on notch flanks reported in [18] for this experiment, it takes ~25 μsec after the start of the compressive notch flank loading to initiate the crack in the 100 mm wide sample. This corresponds to the reflected, tensile (longitudinal) waves to reach the notch tip.

mode daughter crack/branch formation in the first geometry (100 mm × 150 mm specimen). In the second geometry (150 mm × 150 mm specimen), the size of the ROI was maintained the same but was advanced into the middle of the specimen to be able to capture some of the mode-I mother crack growth before branching, first mixed-mode daughter crack branch formation and then the evolution of *a pair* of cascading mixed-mode granddaughter cracks and their growth.

5.2 Crack length and velocity histories

100 mm × 150 mm specimen: Experimental details and crack length and velocity histories and stress intensity factor histories up to crack branching are already provided in section 3.4. The current section is primarily focused on crack branching, hence only a few important details are provided here to avoid repetition. A photograph of the fractured specimen from this experiment is shown in Figure 5.2, After initiating from the notch-tip, the crack propagated as a mode-I mother crack and subsequently bifurcated into two dominant mixed-mode daughter cracks at a distance of approx. 25 mm from the initial tip. The branched cracks maintained global symmetry relative to the mother crack with an angle of ~50^{o} between them, see Figure 5.2. Finally, when the two daughter cracks approached the specimen edge, the crack paths became unstable resulting in waviness due to the loss of in-plane constraint.

The angular deflections of light rays, ϕ_x and ϕ_y, in two orthogonal directions (with respect to mode-I propagating mother crack) along with the resultant values of angular deflections $\phi_r \left(=\sqrt{\phi_x^2+\phi_y^2}\right)$ at select time instants, are shown in Figure 5.3 as contour maps. Using 2% of the scale factor (= 123 μm/pixel) as the limit of 2-D DIC method's capability for detecting speckle shifts accurately, the lowest angular deflections of light rays measurable is ~2.5×10^{-6} radians.

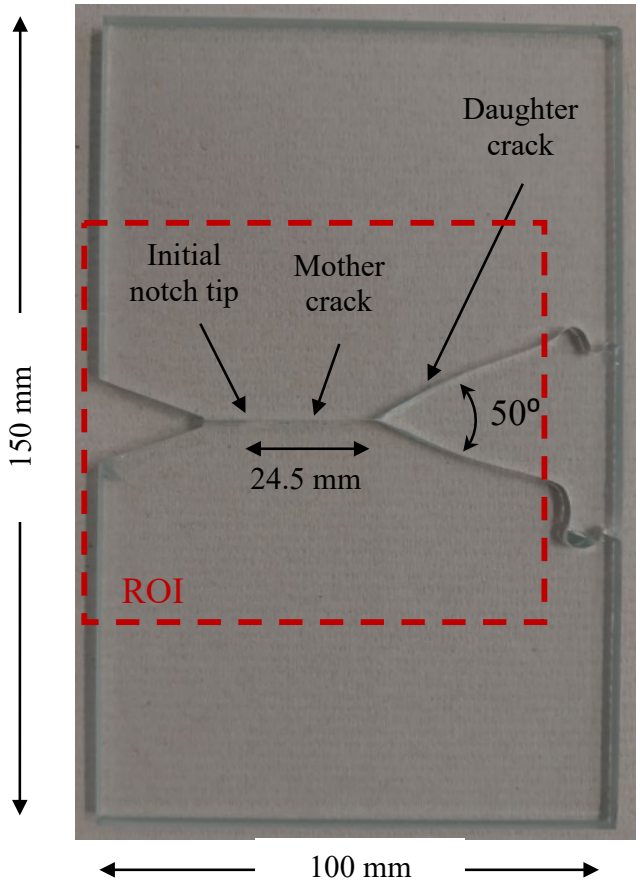

Figure 5.2: Photograph of the reconstructed fractured soda-lime glass specimen with a single crack branching event.

The first column in Figure 5.3 corresponds to mode-I crack propagation of the mother crack (before branching) at time τ = -13 μs whereas the second column represents mixed-mode crack propagation of the two daughter cracks (after branching) at time τ = 7 μs. Here, *the timestamps are with respect to the time instant when crack branching occurred or* τ = 0. A video animation encompassing the evolution of stress gradients along the two V-notch flanks[3], and near the crack tip at initiation, during growth and branching events are available in the Ref. [16]. In this work, ϕ_r contours are used to locate the crack tip and track the crack path. The characteristics of angular

[3] The stress gradient contours adjacent to the two V-notch flanks suggest that the contact between the long-bar and the specimen has resulted in a (compressive) line-load acting at about 5 mm from the left edge of the specimen. Details on estimated load history from these contours is reported in Ref. [18].

deflection contours and its ability in locating precise crack tip location at different stages including crack initiation, crack propagation and crack branching are provided in section 3.4. To assess the error associated with instantaneous crack tip position, stress gradient contours are plotted at each time step in three different increments (4, 8, 12 micro-radians) and the crack tip is identified. The scatter in the crack tip location in these three measurements is then used to estimate the likely error in the instantaneous crack velocity.

The apparent crack length and velocity histories are shown in Figure 5.4(a) and (b), respectively, including the error bars. The crack length increased monotonically until the end of the observation window. A subtle kink in the crack length history between τ = -4 to -1 μs can be seen before crack branching. Subsequently, the crack length increased steadily. The crack tip locations of the two mixed-mode daughter cracks were such that the instantaneous crack lengths overlapped with each other as the two daughter cracks grew symmetrically relative to the mode-I mother crack. The crack length histories were smoothed using Bezier curves [116] and then the apparent crack velocity (V) histories were extracted using the backward difference method, see Figure 5.4(b). The crack accelerated to ~1530 m/s over ~4 μs duration following initiation. Subsequently, the crack maintained an average velocity of 1400-1550 m/s in the pre-branching phase, consistent with those reported in Refs. [18, 19, 87, 138]. As the crack entered the branching phase between τ = -4 to -1 μs, the apparent crack velocity gradually reduced, to values between 1250 to 1050 m/s. This dip in the crack speed prior to the crack branching event stands out as a potential precursor of impending crack bifurcation. Soon after this dip, the crack branched into two angled mixed-mode daughter cracks, both accelerated to ~1700 m/s almost instantaneously[4].

[4] The velocity data for ~3 μs soon after branching is more ambiguous relative to the pre-branching counterparts. The maximum error in crack velocity was 80-90 m/s with most data showing a scatter in the 50 m/s range.

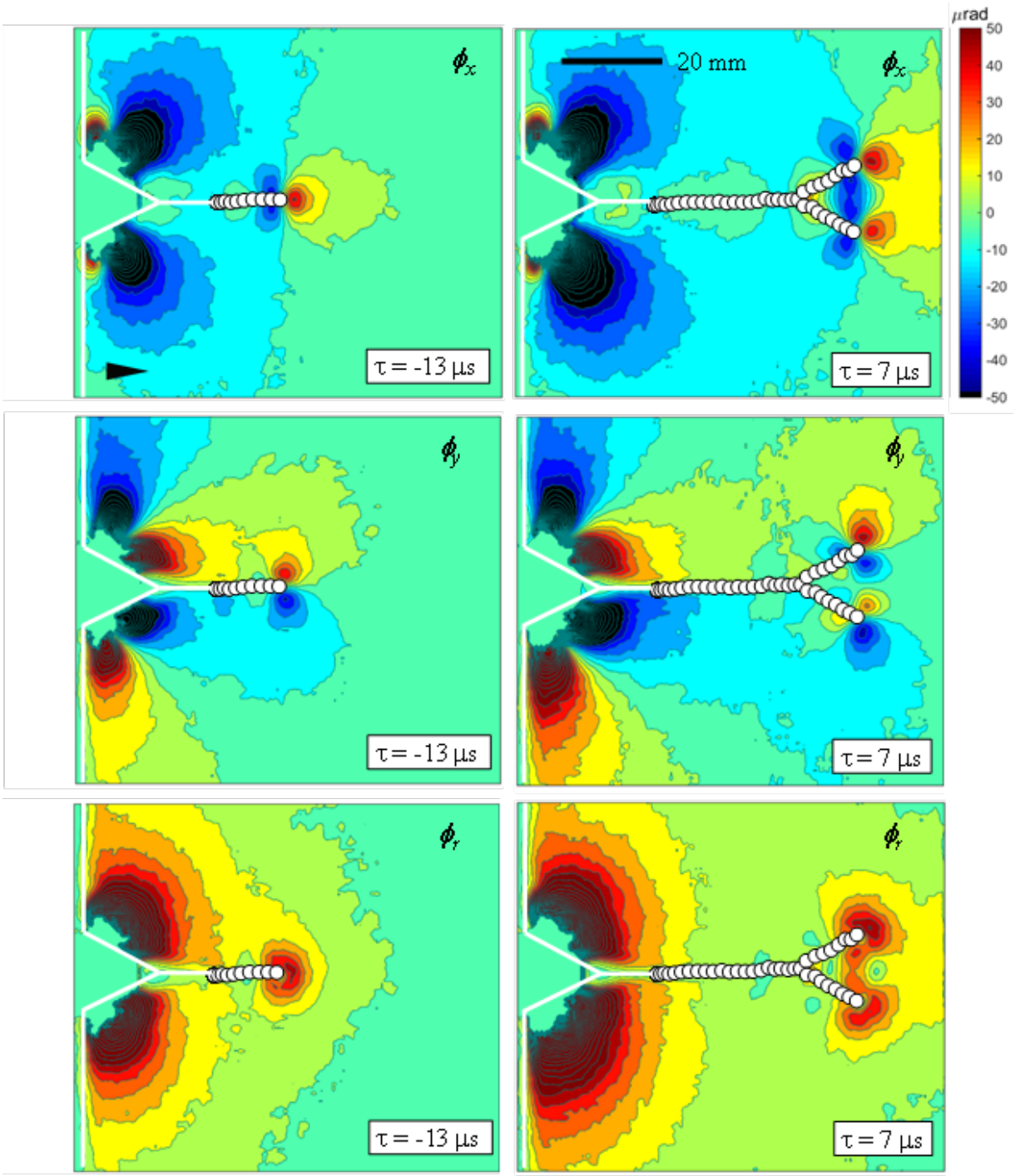

Figure 5.3: Contours of angular deflections of light rays (contour increment = 8×10^{-6} rad) in 100 mm × 150 mm soda-lime glass plate. The arrowhead (in the top left image) shows crack growth direction. White markers indicate crack tip locations in the previous frames. (Time, τ = 0 corresponds to crack branching of the mother crack.)

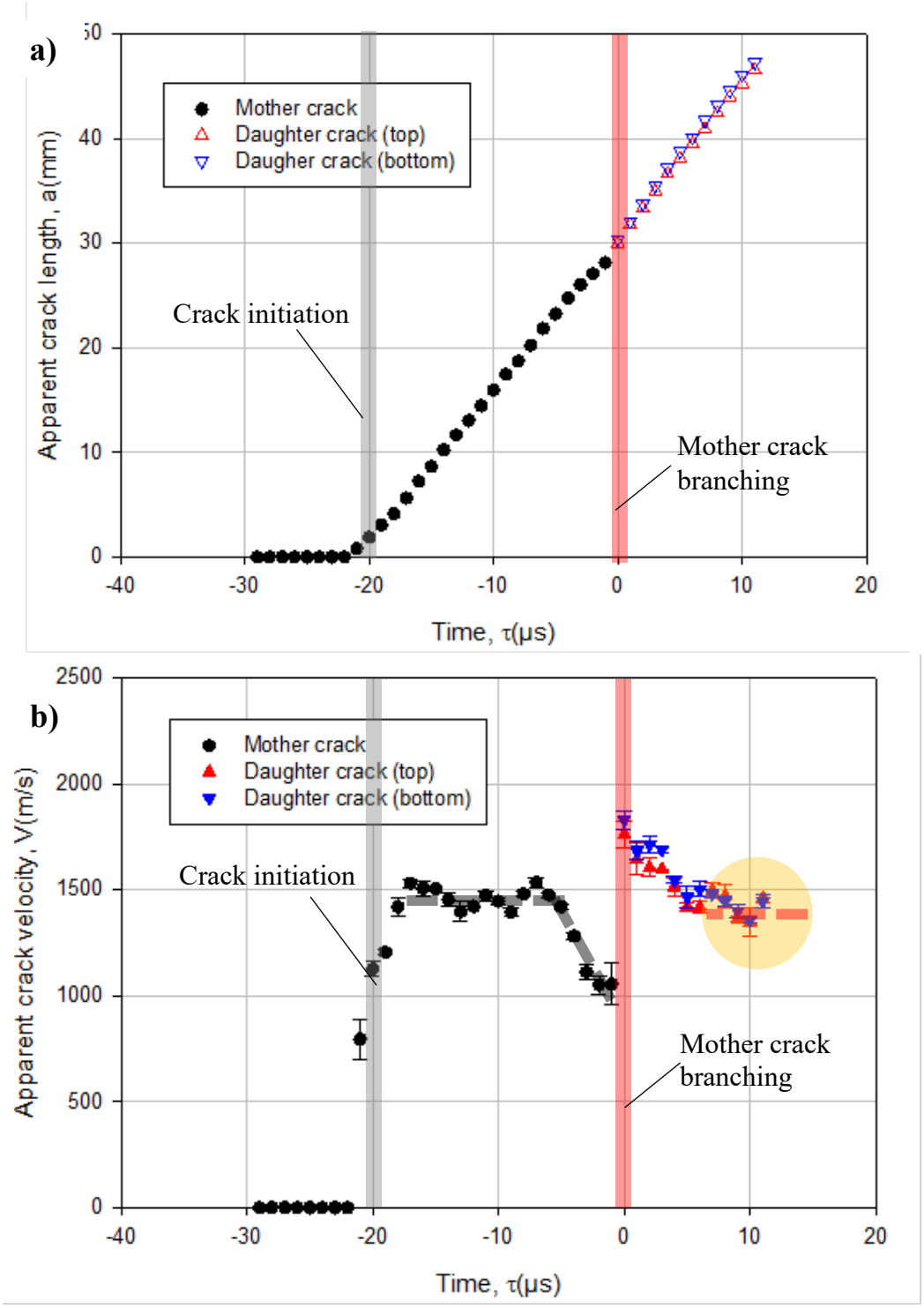

Figure 5.4: Apparent crack length (top) and crack velocity (bottom) histories for 100 mm × 150 mm soda-lime glass plate. (Time, $\tau = 0$ corresponds to mother crack branching event; the heavy broken lines highlight manually overlaid data trends.)

The two daughter cracks subsequently decelerated back to ~1500 m/s until the end of the observation window and no further crack velocity reduction similar to the mother crack was seen. These trends have been highlighted in the plots using thick broken lines or shaded circles superposed on instantaneous values[5].

150 mm × 150 mm specimen: A photograph of the fractured specimen from the experiment is shown in Figure 5.5.

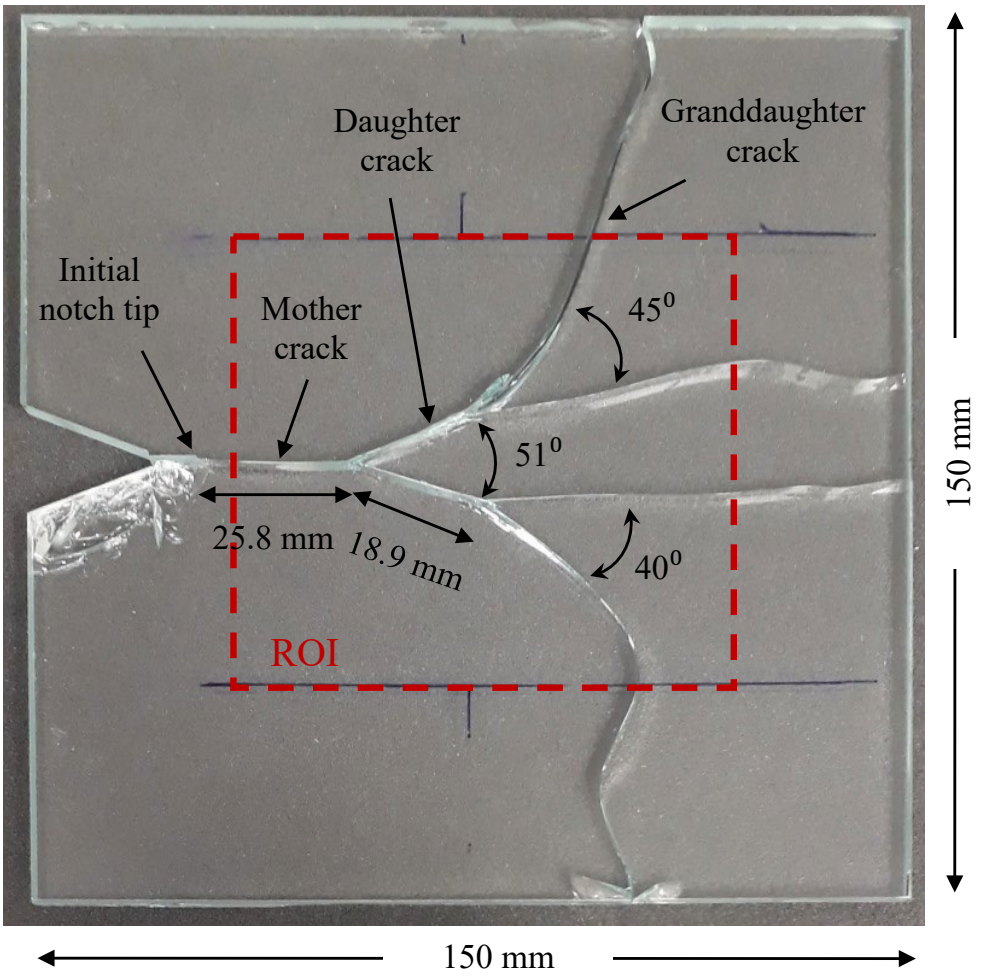

Figure 5.5: Photograph of the reconstructed fractured soda-lime glass specimen with cascading crack bifurcations.

[5] Note that some liberty has been exercised while highlighting these trends for interpretation purposes.

Evidently, after initiating at the original notch-tip *located outside the ROI*, the mother crack first propagated as a nominally mode-I crack and subsequently branched into two mixed-mode daughter cracks at a distance of approx. 26 mm from the initial tip. The daughter cracks maintained global symmetry relative to the mother crack, with an angle of ~51° between them, as evident in Figure 5.5. A similar crack branching pattern with somewhat lower degree of symmetry and angular separations was seen in another experiment as shown in Figure 5.6.

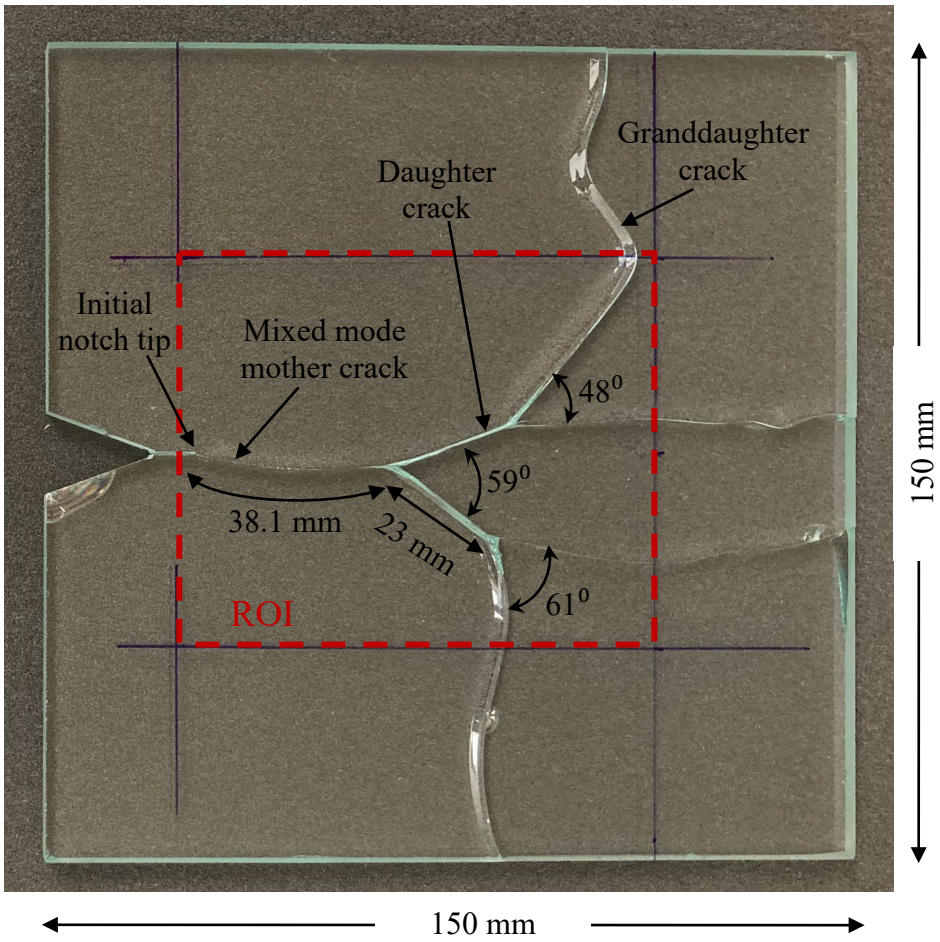

Figure 5.6: Photograph of the reconstructed fractured soda-lime glass specimen from the repeatability experiment with cascading crack bifurcations.

These features are similar to the 100 mm × 150 mm specimen even though the specimen geometry is different. Both the daughter cracks, after propagating over a distance of approx. 20 mm, branched/bifurcated again and produced two dominant granddaughter cracks each, resulting

in four simultaneously propagating crack tips in the ROI. These granddaughter cracks were somewhat less symmetric relative to the daughter cracks when compared to the daughter cracks relative to the mother crack. Yet, given the unavoidable loading/setup asymmetries and local material anomalies, the overall symmetry achieved in terms of the crack branch formations is rather noteworthy. In order to ascertain the repeatability of this test, additional tests on 150 mm × 150 mm_geometry were carried out and the resulting fractured specimen is shown in Figure 5.6. The ROI in this experiment covers all the major eventes from crack initation, propagation and cascading crack birfurcations of mother and daughter cracks.

The angular deflections of light rays, ϕ_x and ϕ_y, in the two orthogonal directions (with respect to mode-I propagating mother crack) at three select time instants, are shown in Figure 5.7 as contour maps. (The image analysis parameters are same as the ones discussed previously.) The first row in the figure shows mode-I crack propagation of the mother crack (before branching) at a time instant τ = -5 μs whereas the second row corresponds to mixed-mode propagation of the two daughter cracks (subsequent to the first branching event) at τ = 9 μs. The last row corresponds to mixed-mode propagation of all four granddaughter cracks (after the second branching event) at τ = 25 μs. (*Note that* τ *= 0 corresponds to the first crack branching event.*) The solid white dots are again superposed on the stress gradient contours to represent the location of crack tips at the current and prior time instants to help visualize the histories during the fracture event. A video animation of the entire fracture evolution including mode-I crack growth and the two crack branching events resulting in two daughter cracks and four granddaughter cracks is available in the *supplementary materials section from* Ref. [16].

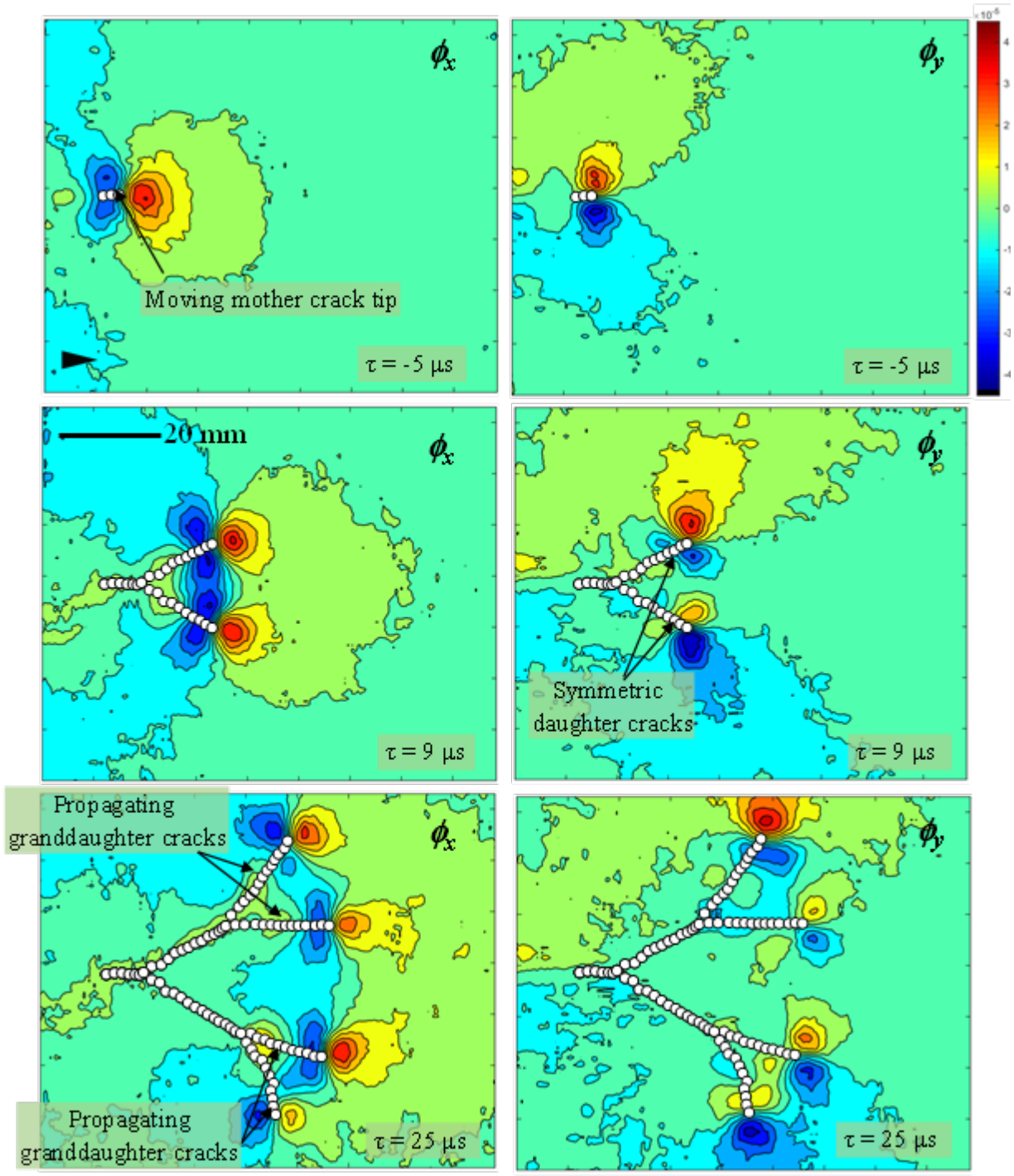

Figure 5.7: Angular deflection contours (contour interval = 7×10^{-6} rad) in 150 mm × 150 mm soda-lime glass plate. The arrowhead (in the top left image) shows crack growth direction. White markers indicate crack tip locations in the previous frames. (Time, τ = 0 corresponds to crack branching event.)

Again, the ϕ_x contours are symmetric relative to the mother crack path whereas ϕ_y contours are antisymmetric. The two daughter as well as the four granddaughter crack tip fields are all asymmetric relative to the mother crack. As in the 100 mm × 150 mm specimen, contours of ϕ_r (not shown for brevity) were plotted at each time instant and used to locate the crack tip and track the crack path by a series of successive white dots. The angular deflection contours for the repeatability experiment is shown in Figure 5.8. Again, the angular deflection contours shown similar features as observed in primary specimen (from 150 mm × 150 mm specimen) and in 100 mm × 150 mm specimen. A video animation of angular deflection contours (starting from crack initiation, mode-I crack propagation, cascading crack bifurcation and mixed-mode crack propagation of daughter and granddaughter cracks) for the repeatability test also available in the *supplementary materials section from* Ref. [16].

The apparent crack velocity histories for are shown in Figure 5.9. As the propagating mother crack entered the observation window (solid black circles), the crack was already slowing down from around 1500 m/s to ~1000 m/s (over ~6 μs), prior to branching. This behavior is consistent with that seen in the 100 mm × 150 mm geometry (see, Figure 5.4(b)). Once the crack branched first (at τ = 0), the velocities of the two daughter cracks (solid blue and red triangles, upright triangles for the upper branch, inverted triangles for the lower branch) jump to ~1900 m/s but rapidly decelerate to ~1500 m/s and continue propagating at this speed for the next 4 to 5 μs. Subsequently, a second slowing trend, again from ~1500 m/s to ~1000 m/s over the next 6-7 μs, for both the daughter cracks is evident. (The lower branch traveled at a higher velocity relative to the upper branch, possibly due to experimental anomalies.) The reduction in the crack speed prior to the second pair of crack branching events is consistent with that for the mother crack and can be identified again as a precursor of branching event.

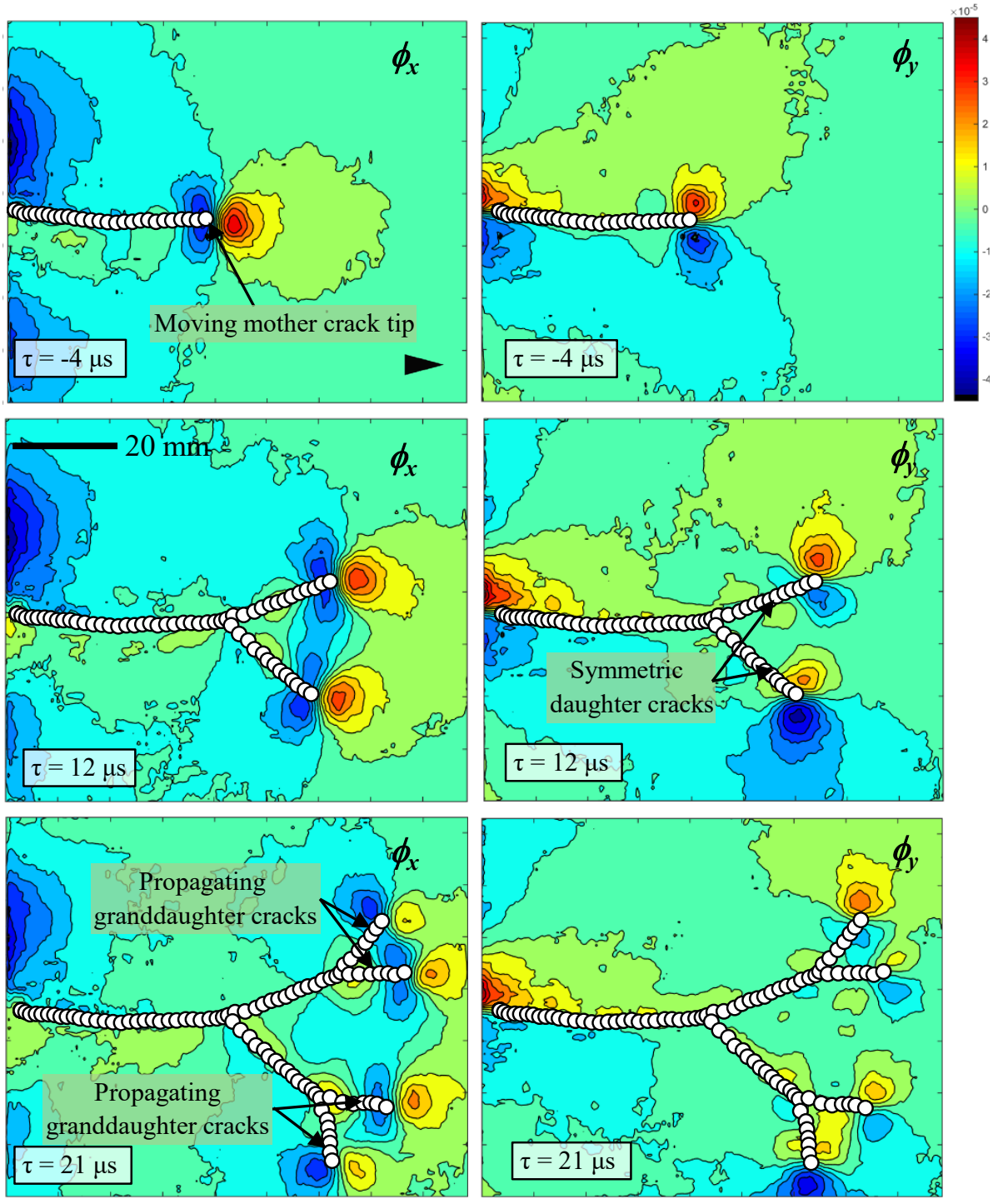

Figure 5.8: Angular deflection contours from the repeatability experiment (contour interval = 7×10^{-6} rad) in 150 mm × 150 mm soda-lime glass plate at different time instants. The arrowhead (in the top left image) shows crack growth direction. Circular markers indicate crack tip locations in the previous frames. (τ = 0 corresponds to crack branching event.)

The second branching event occurred between 13-15 μs; the upper branch bifurcated first followed by the lower branch a couple of microseconds later. Once branching occurred, each granddaughter crack accelerated to ~2000 m/s, again consistent with the first branching event at $\tau = 0$.

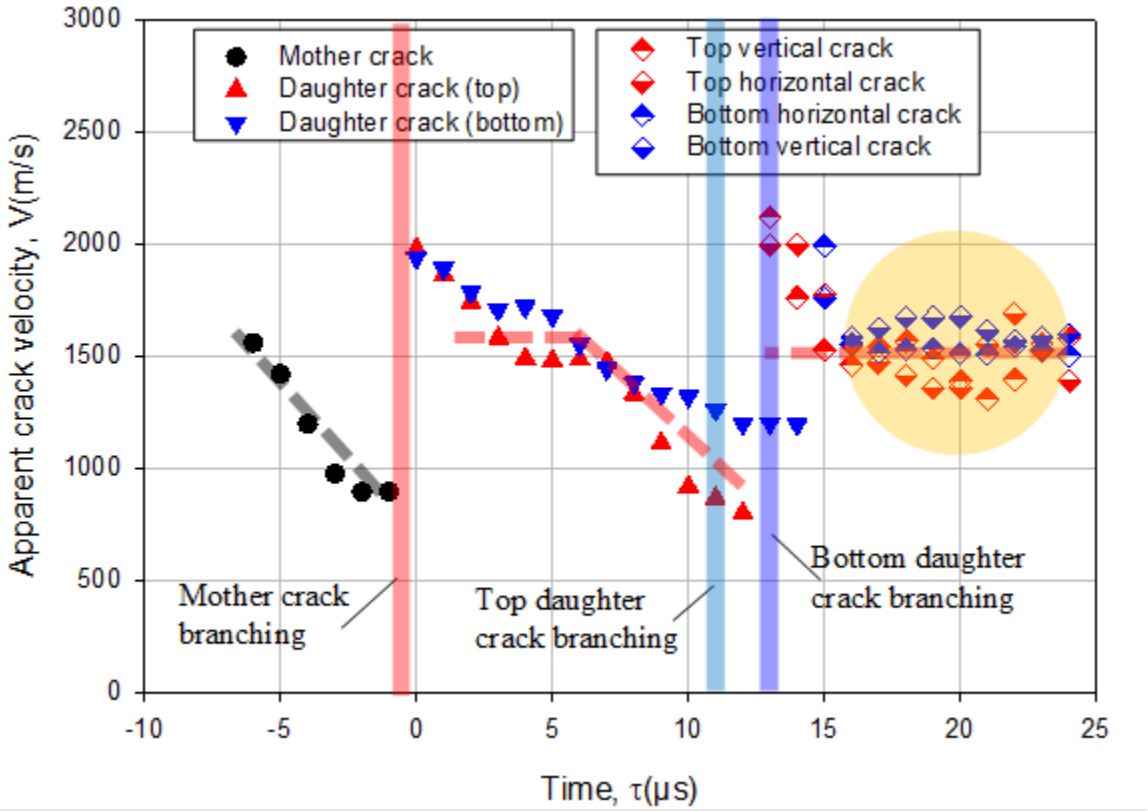

Figure 5.9: Apparent/macroscale crack velocity histories from 150 mm × 150 mm soda-lime glass plate. (Time, $\tau = 0$ corresponds to mother crack branching event; the heavy broken lines highlight approx. data trends.)

A gradual deceleration of granddaughter cracks to a steady 1500 m/s is evident for the rest of the observation window without further slowing down. Accordingly, based on the characteristics noted during the previous three branching events, no further branching should occur and this pattern indeed holds true. That is, from the photograph of the fractured specimen, it is clear that no further branching occurred outside the observation window. Again, note that

approximate data trends are highlighted using heavy broken lines superposed on instantaneous data obtained from DGS. The crack velocity results for the repeatability test are shown in Figure 5.10. The results generally followed the trends described above except at crack initiation from the initial notch due to loading asymmetries. That is, crack velocities dropped prior to mother and daughter cracks branching, as observed in single (100 mm × 150 mm soda-lime glass plate) and cascading branching (150 mm × 150 mm soda-lime glass plate) experiments.

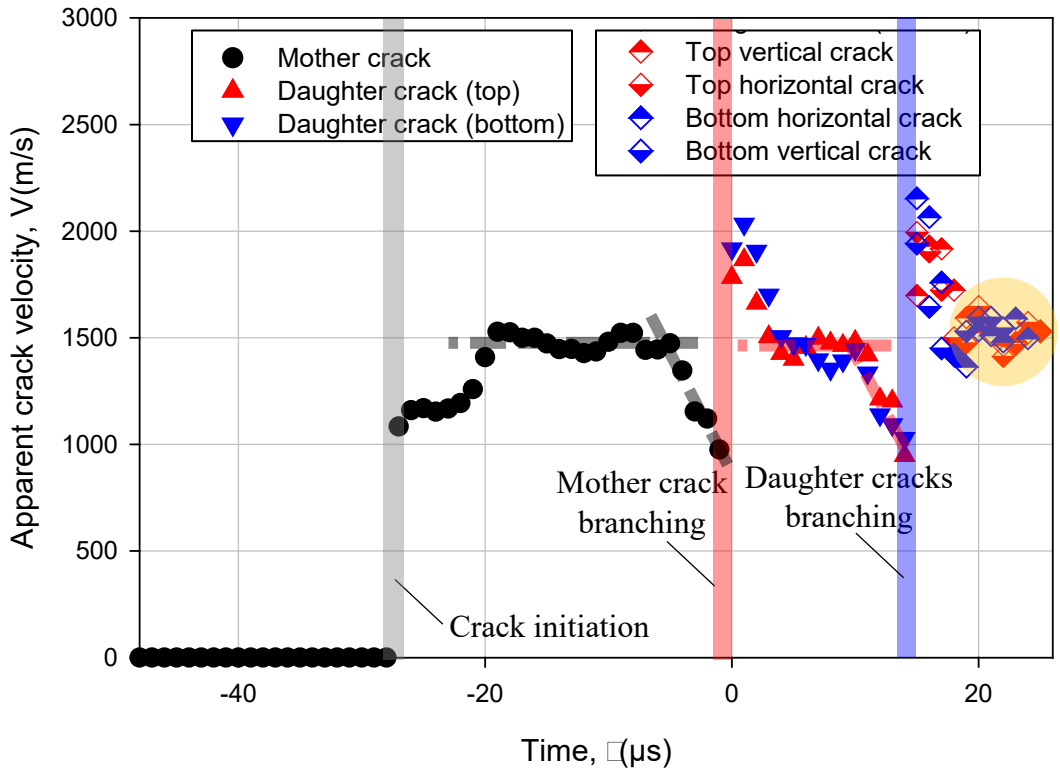

Figure 5.10: Apparent/macroscale crack velocity histories from repeatability experiment for 150 mm × 150 mm soda-lime glass plate. (τ = 0 corresponds to mother crack branching event; thick broken lines and shaded zones are manually overlaid to highlight/suggest data trends.)

5.3 Stress intensity factor histories

Section 3.4.3 provides detailed steps used for extracting stress intensity factor histories under stress wave loading. The results extracted using that approach are discussed next.

100 mm × 150 mm specimen: The SIF histories extracted from DGS data before crack initiation until branching to post-branching phases of fracture are shown in Figure 5.11(a). Here $\tau = 0$ again corresponds to the mother crack branching event. The mode-I SIF, K_I, (solid black symbols) increased steadily to ~0.75 MPa√m until the crack initiated. Upon crack initiation at the original notch-tip, K_I dropped noticeably for ~2 μs to a value of ~0.6 MPa√m ($=\left(K_I\right)_i$) due to unloading. Subsequently, it nearly doubled over the next ~8 μs to ~1.1 MPa√m before branching into two daughter cracks. During the same time period, the mode-II SIF, K_{II}, (open black symbols) values were approx. zero within the accuracy of the SIF extraction scheme used. After branching[6], the magnitudes of K_I decreased (red solid upright triangle for the upper branch, blue solid downward triangle for the lower branch) while K_{II} (red open upright triangle for the upper branch, blue open downward triangle for the lower branch) increased almost instantaneously for each of the mixed-mode daughter cracks. As to be expected, the signs of K_{II} were different for the two daughter cracks in the post-branching regime. The magnitude of both SIFs attained relatively steady values during mixed-mode crack growth over the next 10 μs. The K_{II} values were relatively small when compared to K_I counterparts as the cracks approached a steady growth phase. In Figure 5.11(b), the two SIF histories are combined as the effective SIF, K_{eff} ($=\sqrt{K_I^2 + K_{II}^2}$), histories[7]. In the pre- and post-crack initiation phases, K_{eff} trends are approx. same as the ones for K_I in Figure

[6] The SIF data for ~3 μs after branching event is more ambiguous relative to pre-branching counterparts.

[7] The effective SIF, $K_{eff}^d = \sqrt{G^d E} = \sqrt{A_1 K_I^2 + A_2 K_{II}^2}$ where G^d is the energy release rate and A_1 and A_2 are functions of instantaneous crack speed [143]. In these experiments, K_{eff}^d was found to be 1.04-1.06 times the corresponding K_{eff}.

5.11(a). That is, K_{eff} values increase continuously from approx. ~0.6 to ~1.15 MPa√m or the $\left(K_I\right)_i$ value approx. doubled during mode-I crack growth phase and then branched at $\tau = 0$. This doubling of K_{eff} could be added into the basket of plausible crack branching precursors along with the crack speed reduction noted earlier. After crack branching and a noticeable drop in K_{eff} values associated with the branching event, a relatively steady value of 0.85 MPa√m is attained by each of the two daughter cracks. These steady values being lower than $2\left(K_I\right)_i$ seen when the mother crack branched, no further crack branching from neither of these two daughter cracks occurred in this geometry.

<u>150 mm × 150 mm specimen:</u> The histories of the effective SIF, K_{eff}, for the mother crack (solid black circles), the two daughter cracks (red solid upright and blue inverted triangles for the upper and lower branches, respectively) and all four granddaughter cracks (half-filled diamonds, red for the top pair and blue for the bottom pair of granddaughter cracks; the upper and lower half-fill correspond to the respective branches) are plotted in Figure 5.12 over the window of observation. As in the 100 mm × 150 mm specimen, the increasing trend in K_{eff} to approx. 1.3 MPa√m in the pre-branching phase of the mother crack is evident. Soon after the crack bifurcated, values of K_{eff} each of the two daughter cracks dropped over 2-3 μs period to approx. 0.6 MPa√m. This value matches well with the one after crack initiation $\left(K_I\right)_i$ in the 100 mm × 150 mm geometry. Subsequently, the values increase to ~1.15 MPa√m for the upper branch and 1.25 MPa√m for the lower branch. These values are approx. twice the post-branching value of ~0.6 MPa√m and also

close to the value ($\left(K_I\right)_i$) for the mode-I mother crack when it branched at $\tau = 0$ in the smaller size specimen.

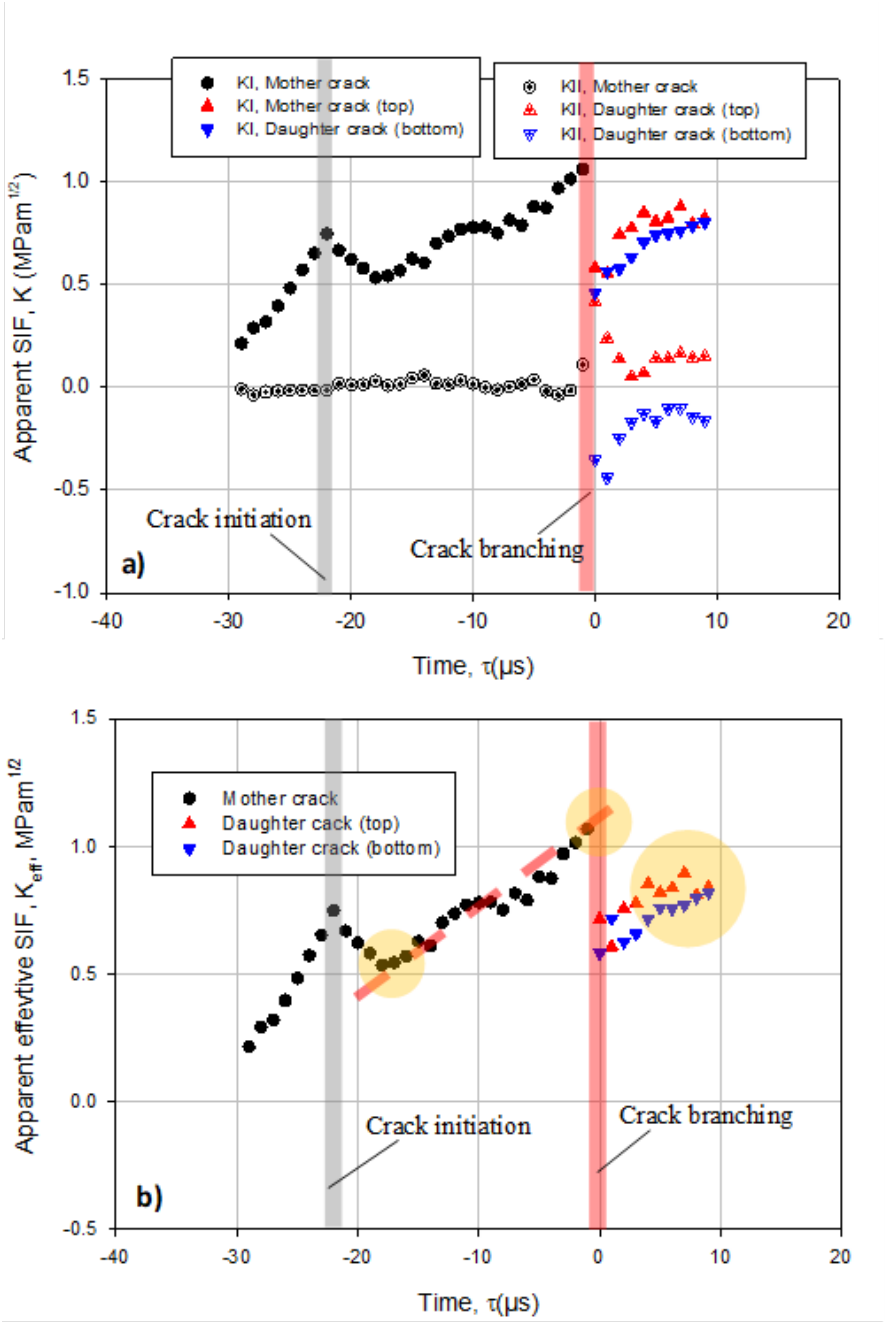

Figure 5.11: Stress intensity factor (SIF) histories for 100 mm × 150 mm soda-lime glass plate: (a) Apparent K_I and K_{II}, (b) Effective SIF, $K_{eff} = \sqrt{K_I^2 + K_{II}^2}$. (Time, $\tau = 0$ corresponds to mother crack branching event; the heavy broken lines highlight approx. data trends.)

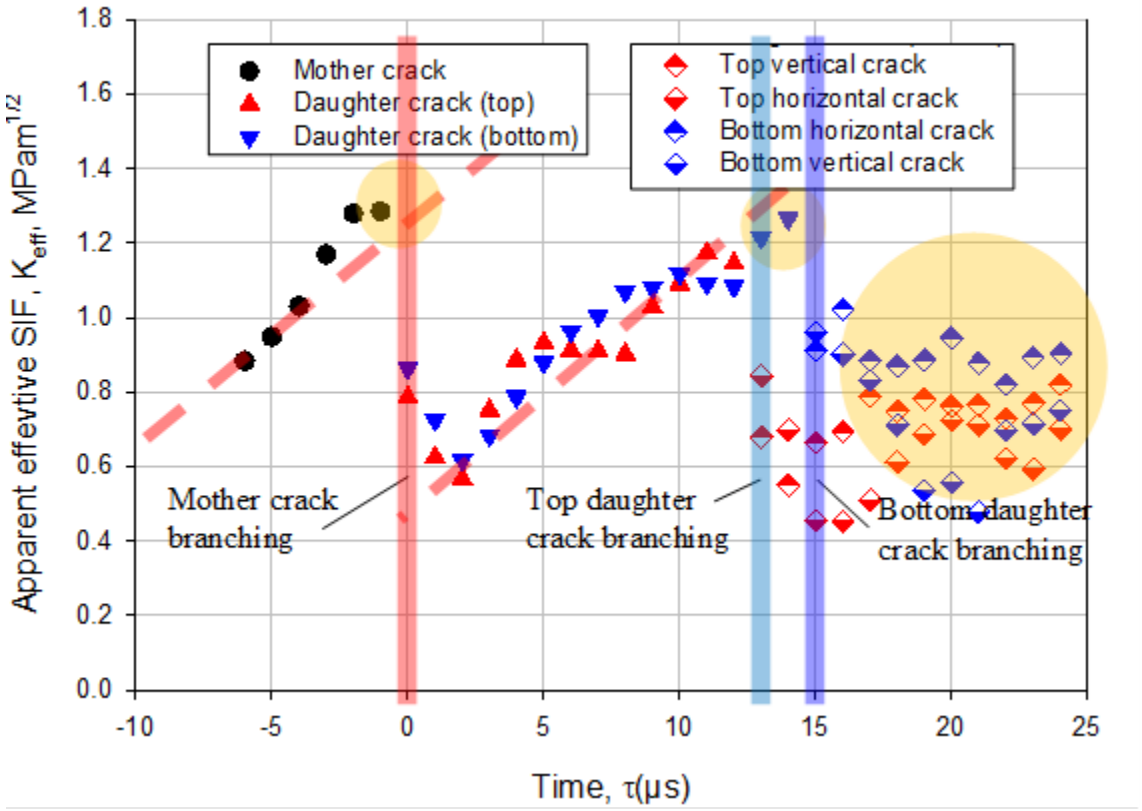

Figure 5.12: Effective stress intensity factor ($K_{eff} = \sqrt{K_I^2 + K_{II}^2}$) histories for 150 mm × 150 mm soda-lime glass plate (Time, $\tau = 0$ corresponds to mother crack branching event; the heavy broken lines highlight approx. data trends.)

Again, K_{eff} attaining a value of approx. twice $\left(K_I\right)_i$ is similar to the crack branching precursor observed in the 100 mm × 150 mm geometry. The upper branch, however, bifurcated first followed by the lower branch, ~2 μs later. The drop in K_{eff} for each of the resulting four granddaughter cracks is evident but with more scatter, ranging between 0.5-0.9 MPa√m, attributed to progressively increasing asymmetries in crack paths resulting in slightly different stress wave emanations and reflections from the newly formed crack faces and free edges of the specimen.

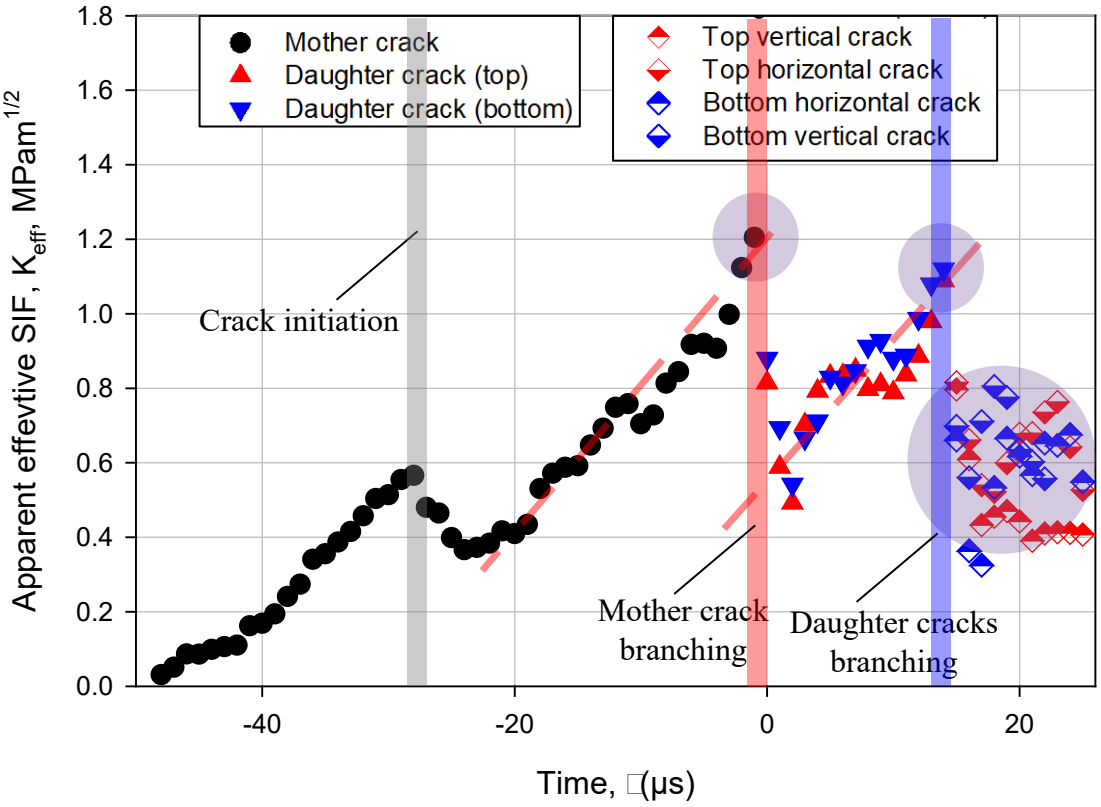

Figure 5.13: Effective stress intensity factor ($K_{eff} = \sqrt{K_I^2 + K_{II}^2}$) histories from repeatability experiments for 150 mm × 150 mm soda-lime glass plate (Time, $\tau = 0$ corresponds to mother crack branching event; the heavy broken lines highlight approx. data trends.)

Such data scatter and asymmetries are expected to increase further if additional bifurcation events were to occur. However, in this geometry, no further branching of any of the granddaughter cracks occurred. This is consistent with the fact that K_{eff} values for the granddaughter cracks never increased to values above $2\left(K_I\right)_i$ seen after crack initiation.

The effective SIF histories for the repeatability test is shown in Figure 5.13. Again, K_{eff} values of mother and daughter cracks reached twice the value at initiation ($2\left(K_I\right)_i$) prior to crack

branching and it is observed in a single specimen. These results show good repeatability of the trends noted in earlier single and cascading crack branching experiments.

5.4 Histories of higher order coefficients

In addition to the histories of SIFs, coefficients of higher order terms (HOT)[8] in the asymptotic stress field (see, Eq. (3.6)) namely, A_3, D_3 were also extracted during the least-squares analysis of stress gradients described earlier. These HOT coefficients account for the finite specimen geometry and loading configuration under quasi-static conditions and a similar interpretation under dynamic conditions is reasonable. It should be noted that the asymptotic expressions for the fields under consideration are devoid of the coefficients of r^0 term and hence the so-called *T*-stress suggested in the literature [139-141] to cause (a) curving of crack path during quasi-static growth and (b) branching of crack during dynamic events are not available in DGS measurements. Accordingly, the next dominant coefficients in the field, namely the coefficients of the $r^{1/2}$ term, A_3 and D_3 associated with the symmetric and antisymmetric parts of the asymptotic expansion, respectively, were extracted and examined.

For the 100 mm × 150 mm specimen, histories of A_3, D_3 and $A_{eff}\left(=\sqrt{A_3^2+D_3^2}\right)$ are plotted in Figure 5.14(a) and (b). *Being coefficients of the HOT of the asymptotic field, higher degree of noise is to be expected.* Before crack initiation, the *magnitude* of the coefficient of the symmetric part or $|A_3|$ increases monotonically up to initiation (solid back circles) from the notch-tip to approximately 230 MPa/√m but drops slightly to 210 MPa/√m following initiation and then remains nearly constant over the next 10 μs of mode-I mother crack growth.

[8] In order to obtain similar coefficients of higher order terms (HOT) as that of Atluri and Kobyashi [111] stress field expressions, divide the coefficient A_N or D_N with the respective term *N*.

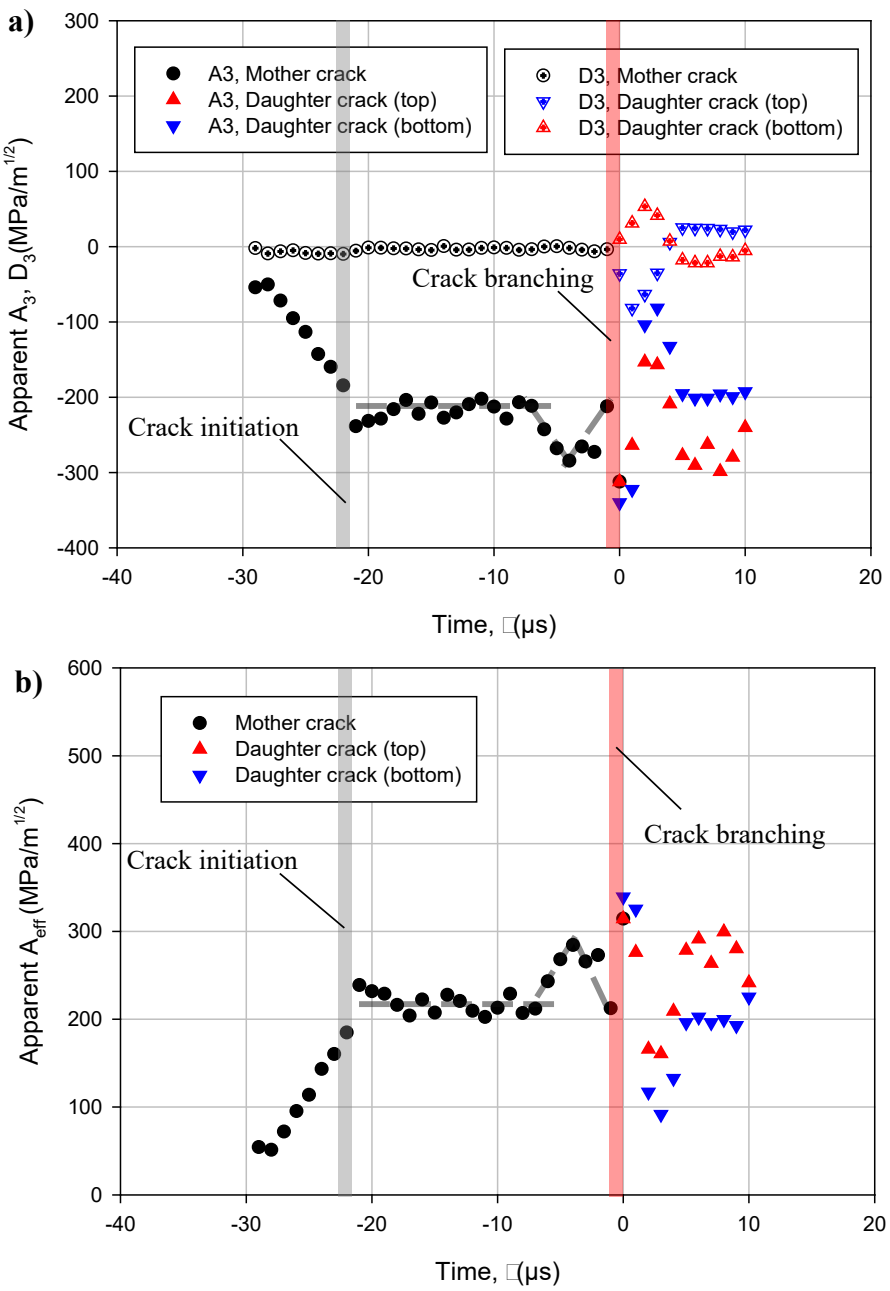

Figure 5.14: Higher order term histories for 100 mm × 150 mm soda-lime glass plate: (a) A_3 and D_3, (b) $A_{eff} = \sqrt{A_3^2 + D_3^2}$ (Time, $\tau = 0$ corresponds to mother crack branching event; the heavy broken lines highlight approx. data trends.)

At approximately 6 μs prior to the observed crack branching event (at $\tau = 0$), the *magnitude* of A_3 begins to increase to 280-290 MPa/√m before dropping to ~ 210 MPa/√m. This results in a

noticeable 'V' shaped kink in the data trend, highlighted by the heavy broken gray line superposed on the solid symbols in the plot. During this period leading up to crack branching, the values of the coefficient D_3 (open black symbols) are nearly zero. After the transients associated with crack branch formation[9] have diminished, the mixed-mode daughter cracks attain nearly constant values (solid upright red and downward blue symbols) of -200 and -220 MPa/√m for the rest of the observation window whereas D_3 values (open upright red and downward blue symbols) attain small negative and positive values, respectively. The A_{eff} trends in Figure 5.14(b) are approximately same as the ones for $|A_3|$ in the pre- and post-crack initiation regimes. That is, A_{eff} increased monotonically until crack initiation (solid back circles) to ~200 MPa/√m. Upon crack initiation, A_{eff} values decreased slightly from 240 MPa/√m to 215 MPa/√m and continued to be nearly constant for ~10 μs. In pre-branching phase (at $\tau \sim$ -6 μs) a noticeable spike or an inverted V-shaped kink is evident in the A_{eff} histories. Interestingly, the increasing trend in the *magnitude* of A_{eff} prior to crack branching event as well as the 'V' shaped kink stands out as a precursor to the impending crack branching event. After the transients associated with the crack branching event diminish, the A_{eff} values don't show any noticeable features that standout and no further macroscale crack branching was observed from neither of the two daughter cracks.

In Figure 5.15(a), histories of A_3, D_3 for the 150 mm × 150 mm specimen are plotted. Remembering that the ROI in this geometry was chosen to primarily capture the post-branching behavior, only limited amount of propagation of the mother crack towards its first branching event was monitored at the beginning of the time window.

[9] The HOT data for ~3 μs after each branching event is relatively more ambiguous when compared to pre-branching counterparts.

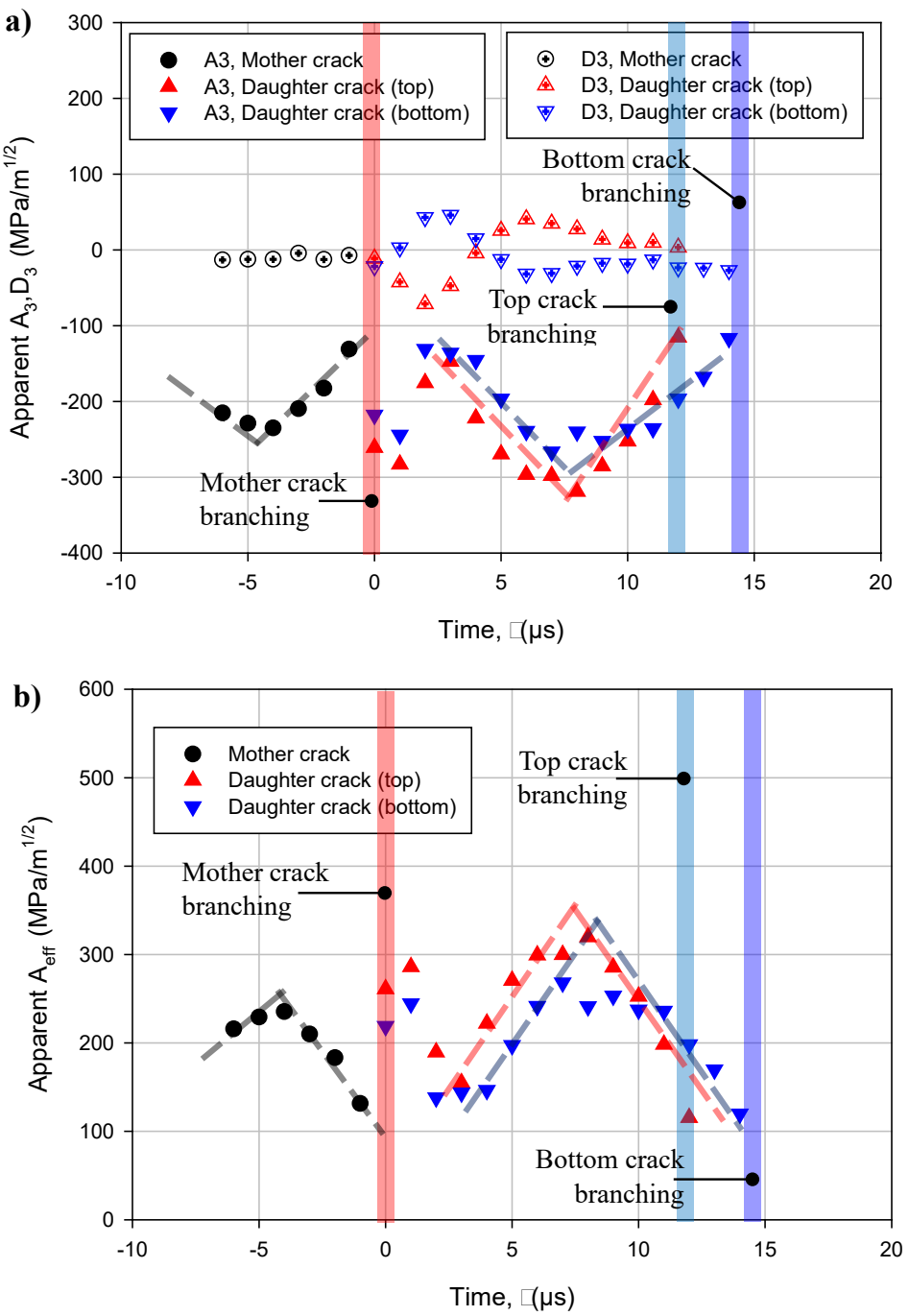

Figure 5.15: Higher order term histories for 150 mm × 150 mm soda-lime glass plate: (a) A_3 and D_3, (b) $A_{eff} = \sqrt{A_3^2 + D_3^2}$ (Time, $\tau = 0$ corresponds to mother crack branching event; the heavy broken lines highlight approx. data trends.)

The solid black symbols for the mother crack show the previously noted 'V' shaped kink highlighted by the broken gray trend line prior to the branching event of the mother crack. Once

the transients due to branching of the mode-I mother crack diminish, the values of $|A_3|$ for both the daughter cracks show an increasing trend, from 100 to 250 MPa/√m for the lower branch and 150 to 320 MPa/√m for the upper branch. Once again, the data for both the mixed-mode daughter cracks show the previously noted 'V' shaped signature in the history (highlighted by the broken red and blue trend lines) before producing a set of two granddaughter crack pairs at 12 and 14 μs. The histories of D_3 for each of these cracks (open blue and red symbols) in the ROI do not show anything distinct *before* the branching event. In Figure 5.15(b), A_3 and D_3 histories are combined as $A_{eff}\left(=\sqrt{A_3^2+D_3^2}\right)$. As the magnitude of D_3 are small relative to that for A_3, the A_{eff} histories are similar to that of $|A_3|$. That is, A_{eff} histories show a distinct spike or inverted V-shaped kink (again highlighted by the broken red and blue trend lines) before the mother crack branches as well as the two grand-daughter cracks branch. Again, these trends seem consistent not only with that for the mother crack prior to its branching event but also the one observed in the 100 mm × 150 mm geometry. The data trends, however, are noticeably different from the one in Figure 5.15. As mother crack initiated in this test as a mixed-mode crack at the notch-tip that eventually followed a dominant mode-I path before branching. Yet, the V-shaped kink features prior to branching are still evident.) The A_3, D_3 and A_{eff} histories for the repeatability test are shown in Figure 5.16. Again, a distinct V-shaped kink data trends are observed for mother and daughter cracks in pre-branching phase depicting similar trends observed in the single and cascading branching experiments. In light of the above observations, one could surmise that the increasing trend in the *magnitude* of A_{eff} as well as the 'V' shaped kink in the data trends for each of the four branching events in the two different geometries standout as potential precursors of the bifurcation event.

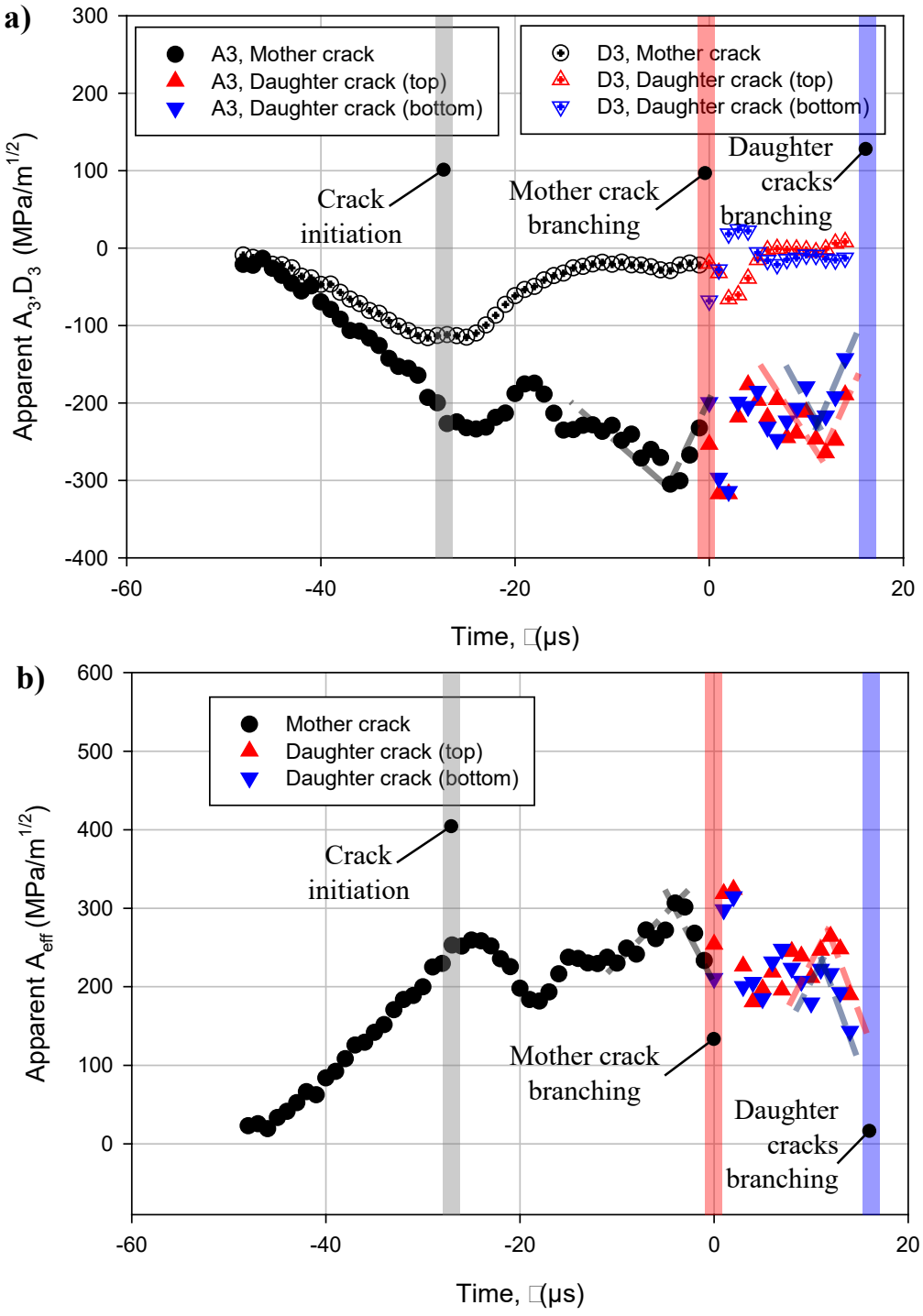

Figure 5.16: Higher order term histories from repeatability experiment for 150 mm × 150 mm soda-lime glass plate: (a) A_3 and D_3, (b) $A_{eff} = \sqrt{A_3^2 + D_3^2}$ (Time, $\tau = 0$ corresponds to mother crack branching event; the heavy broken lines highlight approx. data trends.)

5.5 Discussion

The crack growth results presented above from two different SLG specimen geometries subjected to nominally identical loading present several unique features prior to crack bifurcation. The optically measured fracture parameters and resulting data trends leading up to single and triple crack bifurcations seen in these two geometries, apparent (or macroscale) crack speed V, apparent effective SIF K_{eff}, and higher order coefficient, A_{eff}, all exhibit distinct signatures/features. The apparent crack velocity (V) prior to crack branch formation in each of the instances dropped from a relatively steady value of ~1500 m/s to ~1000 m/s. This feature was seen consistently in each of the four crack bifurcation events in the two mode-I and two mixed-mode cracks, and hence qualifies to be considered a macroscale precursor of bifurcation event. A monotonic increase of the effective SIF (K_{eff}) and more importantly the doubling of its value, from $\left(K_I\right)_i$ of ~0.6 MPa√m to ~1.2 MPa√m for SLG, was also observed consistently prior to each of the crack bifurcation events and is a second precursor of branching. Lastly, the higher order coefficient A_{eff} extracted prior to each of the branching events consistently showed roughly an 'inverted V' shaped kink in the data trend for all four bifurcation events. The change in the slope of A_{eff} prior to each of the branching events stands out as another precursor.

Based on the above three different crack branching precursors identified via direct optical measurements, a combined non-dimensional crack bifurcation parameter, $\hat{K} = \left[\left(\frac{K_{eff}}{A_{eff}\left(W-a\right)}\right)\left(\frac{C_L}{V}\right)\right]$ was also formulated. Here, C_L is the longitudinal wave speed in SLG, a is instantaneous crack length, W is the width of the specimen in the crack growth direction and

$A_{eff} = \sqrt{A_3^2 + D_3^2}$. The histories of $\hat{K}$ are plotted for both the specimen geometries and repeatability experiment are shown in Figure 5.17 and Figure 5.18 respectively.

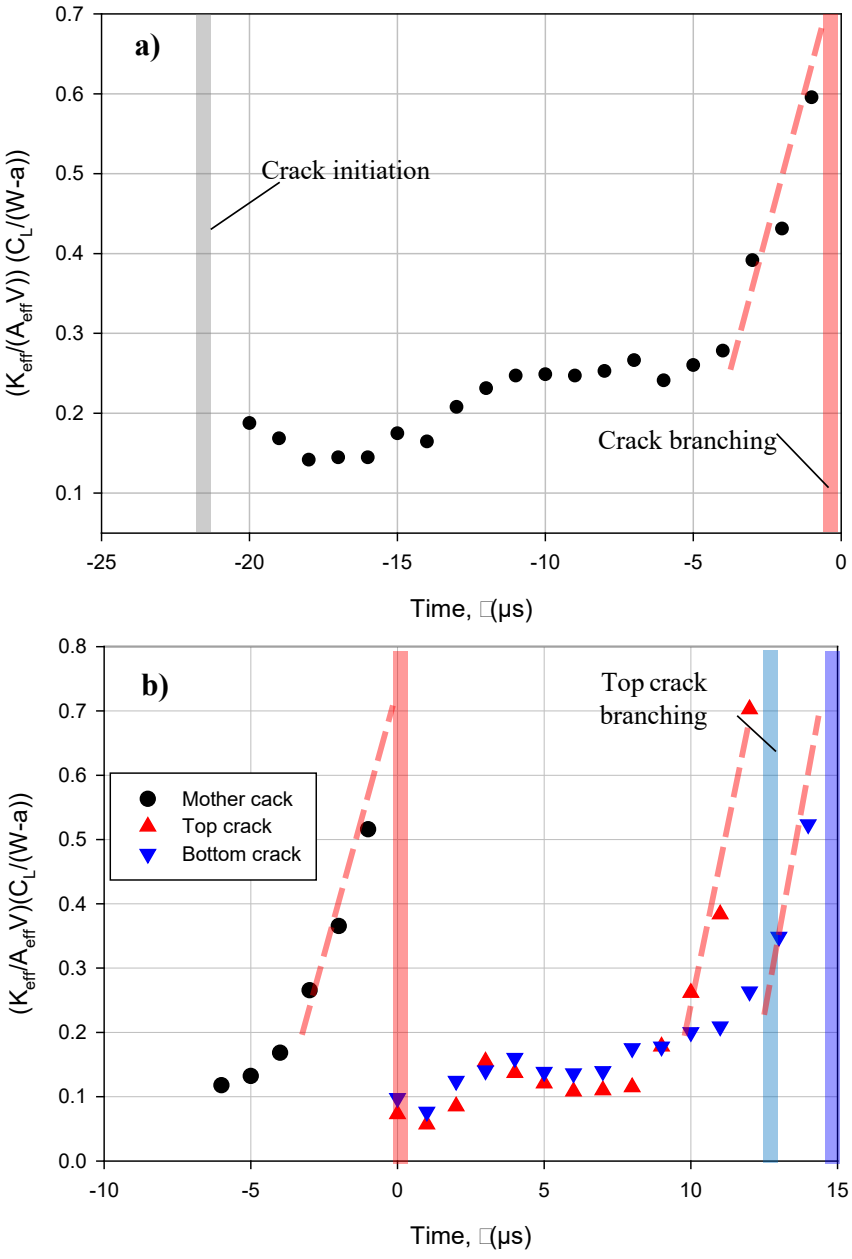

Figure 5.17: Histories of non-dimensional parameter, $\hat{K} = \left(\frac{K_{eff}}{A_{eff}V}\right)\left(\frac{C_L}{W-a}\right)$ from repeatability experiment for 150 mm × 150 mm soda-lime glass plates. ($\tau = 0$ corresponds to mother crack branching event; thick broken lines are manually overlaid to highlight/suggest data trends.)

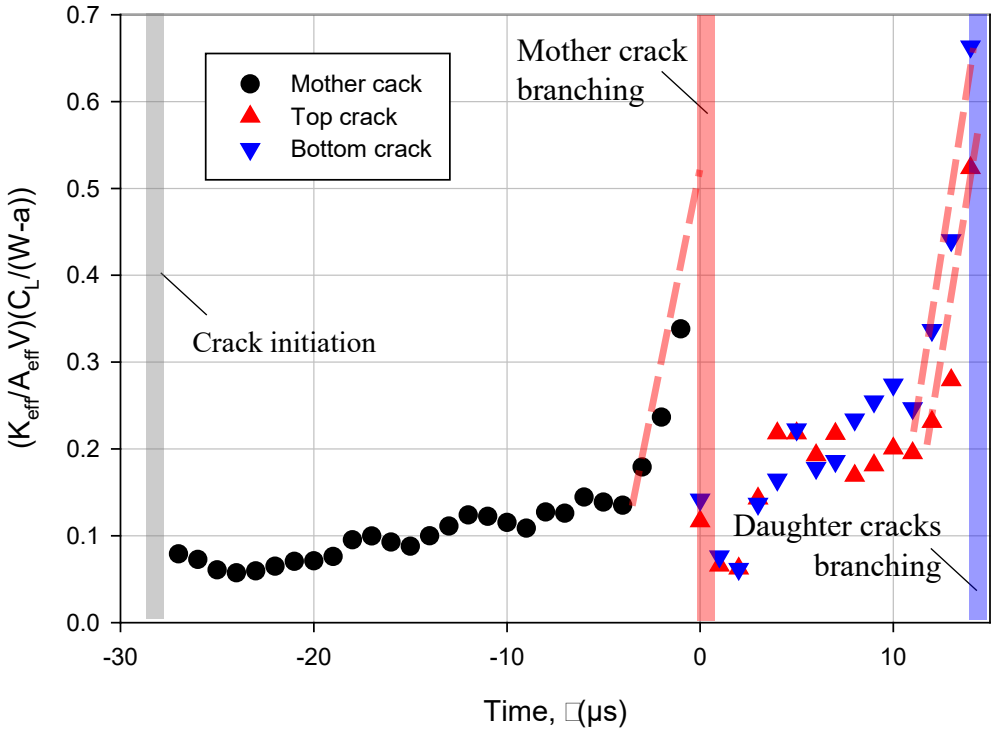

Figure 5.18: Histories of non-dimensional parameter, $\hat{K} = \left(\frac{K_{eff}}{A_{eff}V}\right)\left(\frac{C_L}{W-a}\right)$ from repeatability experiment for 150 mm × 150 mm soda-lime glass plates. ($\tau = 0$ corresponds to mother crack branching event; thick broken lines are manually overlaid to highlight/suggest data trends.)

Based on the data trends, a sharp rise in the *magnitude* of $\hat{K}$ prior to branching event is consistently evident and also serves as a LEFM-based precursor of crack bifurcation. A 3 to 4 fold increase in the magnitude of $\hat{K}$ at branching is notable in each of these plots. The universality of the parameter, however, needs to be further tested by investigating similar behaviors in other amorphous brittle materials to fully understand its physical meaning. Furthermore, *it should also be noted that these precursors are limited to the impending crack bifurcation but they do not indicate the direction of the daughter and granddaughter cracks.* Therefore, additional work, possibly by considering the so-called *T*-stress (or, σ_{0x} in the experimental mechanics community) in addition to the precursors identified in this work, is necessary as well.

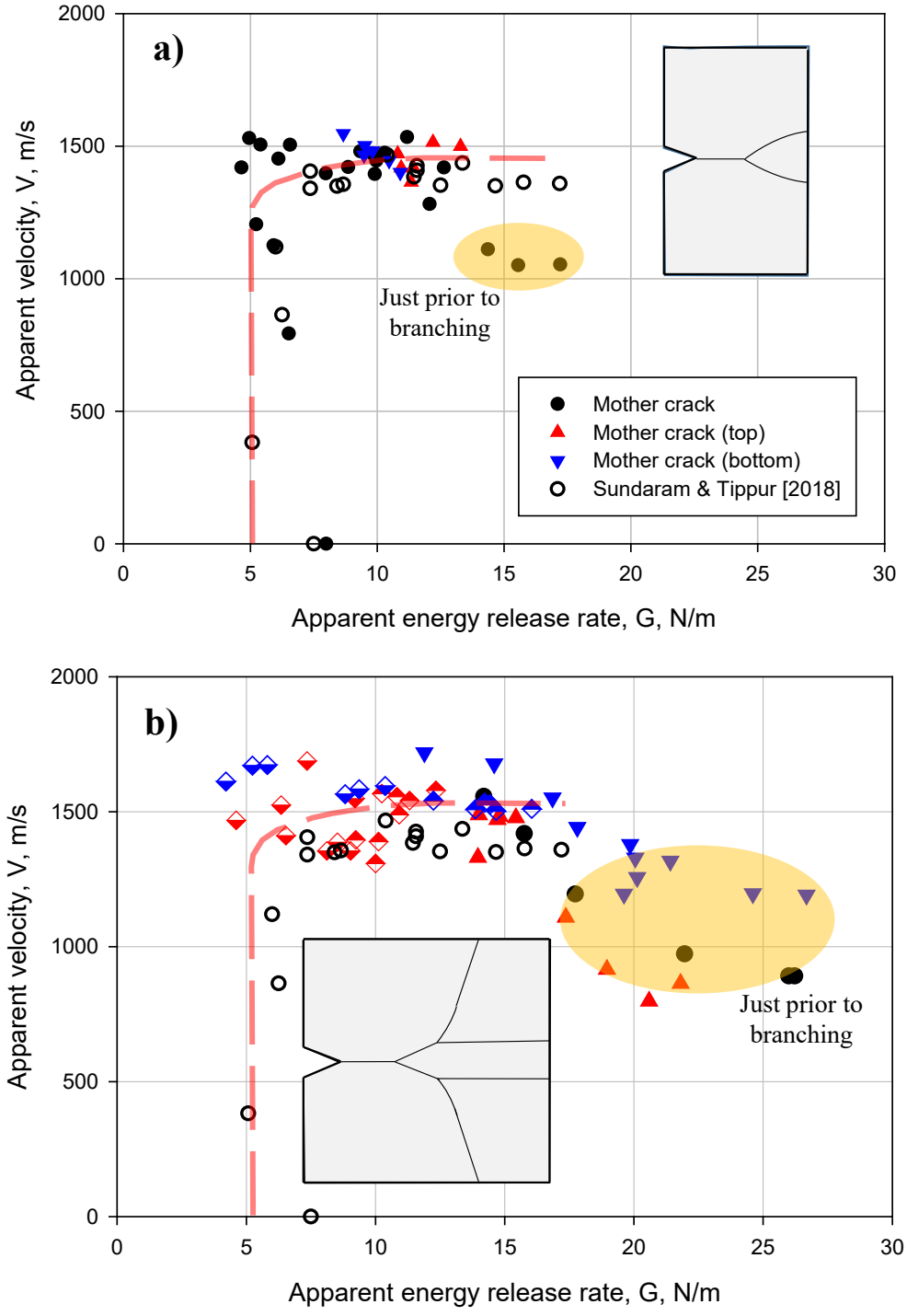

Figure 5.19: Variation of apparent energy release rate (G) with apparent crack velocity (V) from DGS for (a) 100 mm × 150 mm and (b) 150 mm × 150 mm soda-lime glass plates. (The heavy broken lines and shaded zones are manually overlaid to suggest data trends.)

The relationship between instantaneous energy release rate G^d and crack velocity V in both these geometries were also assessed by computing the former using $G^d E = A_1 K_I^2 + A_2 K_{II}^2$ for plane stress conditions where E is the elastic modulus of SLG and A_1, A_2 are velocity dependent functions [142]. The results are shown in for the two specimen geometries and repeatability experiment are shown in Figure 5.19(a),(b) and Figure 5.20 respectively. The data from Sundaram and Tippur's [19] work (open symbols) are also superimposed on the current ones. Given the potential experimental errors involved in both the measured quantities of these graphs, the agreement is rather good. The overall trend line of the data is also suggested and the cluster of data points corresponding to just prior to branching seem to be outliers to the overall G-V trend.

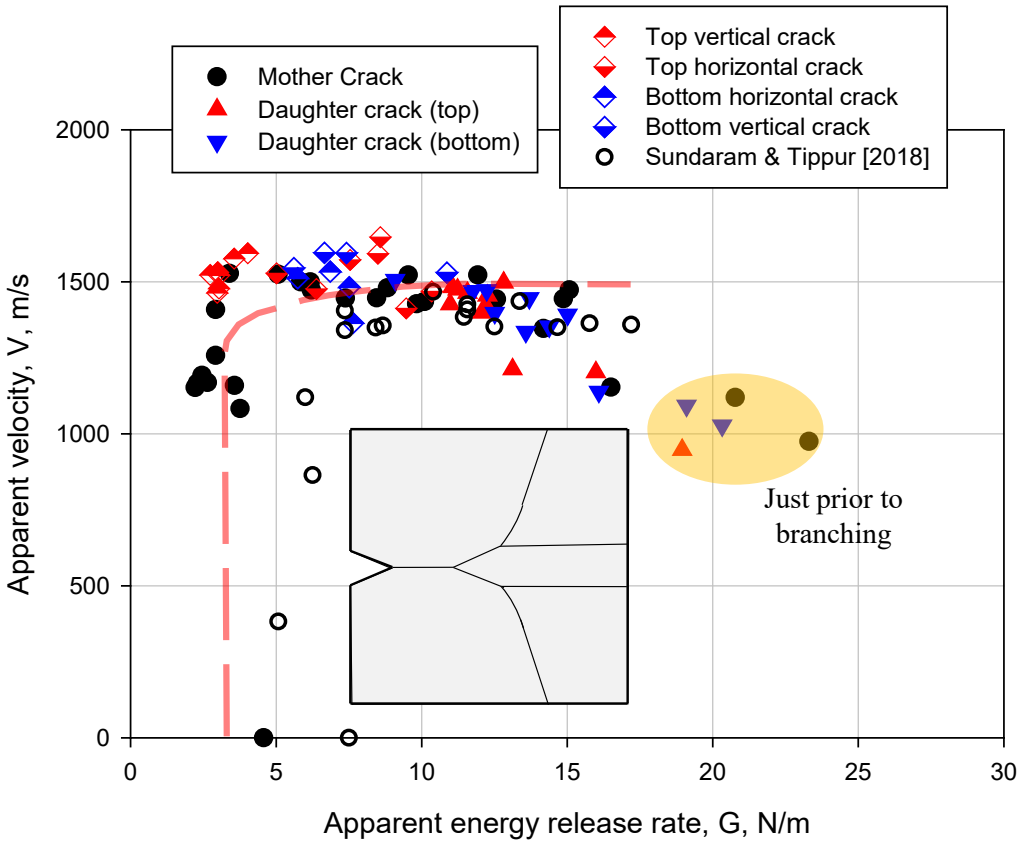

Figure 5.20: Dependence of energy release rate (G) and crack velocity (V) from repeatability experiment for 150 mm × 150 mm soda-lime glass plates. (The heavy broken line and shared region are manually overlaid to show the trend line.)

Linking the macroscale optical measurements with microscale fracture surface features could be a way forward for understanding crack branching better. Accordingly, an attempt to link LEFM-based parameters to the fracture surface features extracted via post-mortem fractography was carried out. First, a Keyence digital microscope (VHX-6000, resolution 1 μm) was used to examine the surface features by photographing the fractured surfaces in different regions, starting from the initial notch front zone to where the crack branched macroscopically. A digitally stitched, pseudo-colored image of the same for the 100 mm × 150 mm sample is shown in Figure 5.21[10]. As reported in several previous dynamic crack growth investigations on in amorphous brittle polymers and glasses, the 'mirror-mist-hackle' zones are evident in this image [19, 78]. Similar features were also observed in 150 mm × 150 mm sample prior to and after each of the three branching events and are not shown here for brevity. The accuracy of the digital microscope, however, was found insufficient to capture detailed surface features and quantify the roughness in the mirror region and early stages of the mist region. Hence, an optical profilometer (Bruker Contour Elite K 3D, resolution 10 nm) was used for further analysis of the 100 mm × 150 mm specimen surface. Fractography of discrete locations along the centerline of the fracture surface over approximately 0.63 × 0.47 mm region in 1 mm steps, from the initial notch front to where the crack branched (or, the hackle region), was undertaken. A few select pseudo-colored images corresponding to the mirror, mist, and hackle zones of those measurements are shown in Figure 5.22. (Note that the surface profile scales are different in each of these images due to vast differences in scales.) In the mirror and mist regions (Figure 5.22(a), (b)), periodic and curved striations representing the so-called Wallner lines, caused by the interference of stress waves emanating from the growing crack with those reflected off the free specimen surfaces, are evident.

[10] The region very close to the initial notch front is excluded from the image; the arrow mark indicates the crack growth direction.

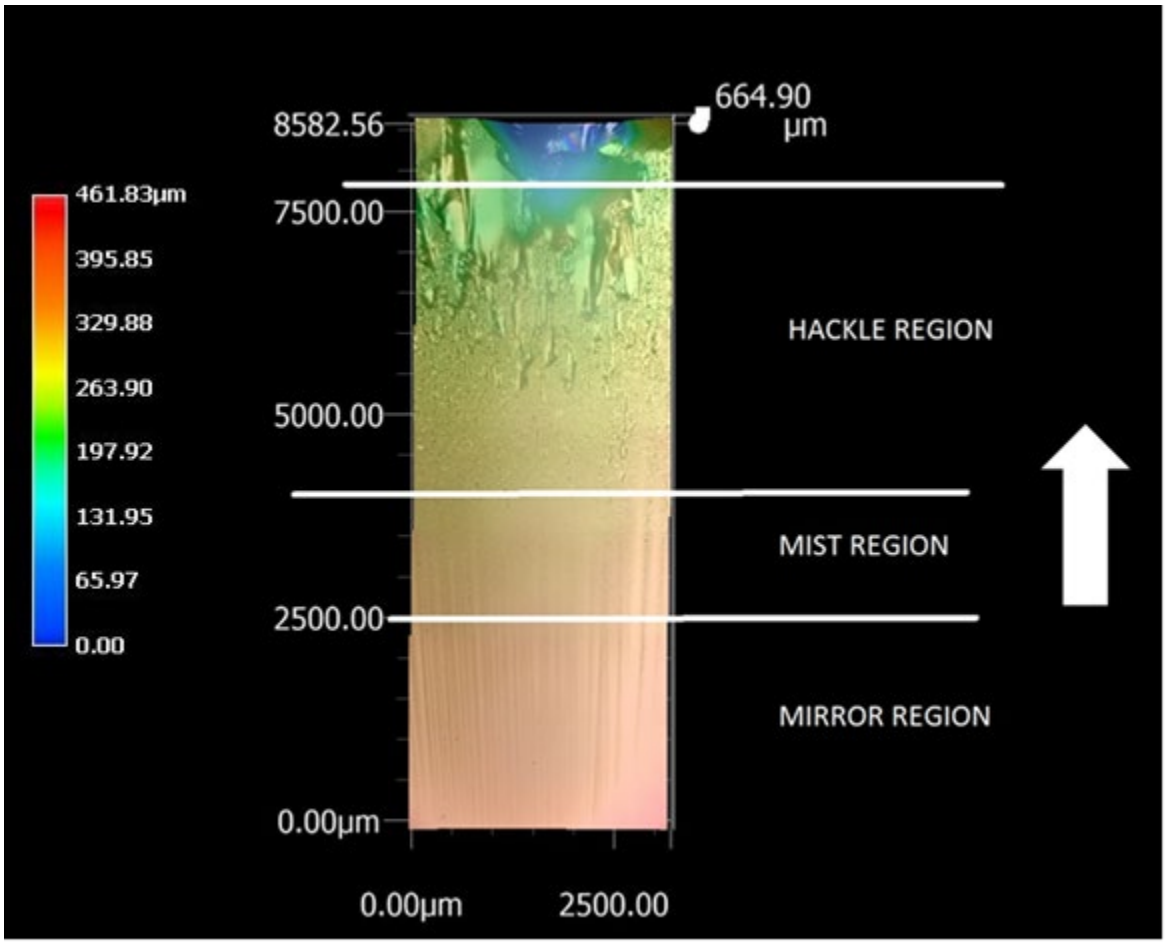

Figure 5.21: Digitally stitched image of fractured surface for 100 mm × 150 mm and soda-lime glass plates. (The white arrow indicates crack growth direction.)

Apart from this, the surface is relatively featureless when compared to quasi-brittle polymers [78] which commonly show conic marks attributed to material inhomogeneities and defects. The Wallner lines become less discernable when the crack enters the mist and hackle zones (Figure 5.22(c), (d)) where there is significantly higher surface roughness relative to the mirror region. A plot of the surface roughness (averaged over 0.63 mm × 0.47 mm) along the crack path where the crack branches in the specimen is plotted in Figure 5.23: (a) Variation of surface roughness (R_a) at different distances from the initial crack front and (b) Variation of (R_a) with crack velocity for 100 mm × 150 mm specimen. (The lack of any correlation between surface roughness

and crack speed is noticeable.)(a). A roughness value of R_a ~0.25 μm soon after crack initiation from the notch drops to 30-80 nm range until the crack grows by approx. 20 mm.

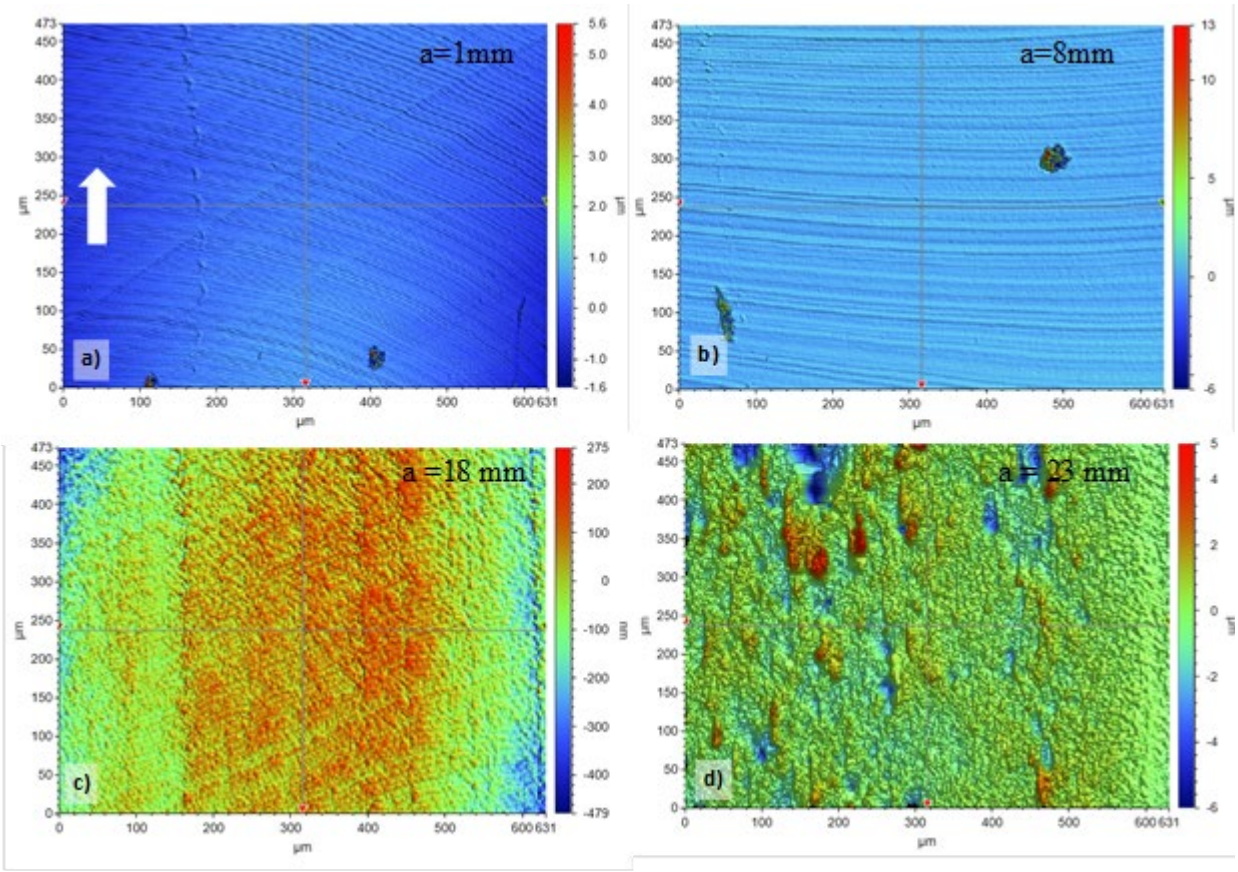

Figure 5.22: Images of the fractured surface at different distances from the initial notch front obtained from optical profilometer for 100 mm × 150 mm. (The arrow indicates crack growth direction.)

Next, a steep rise in R_a to 3-4 μm is evident as the crack enters the 'hackle' phase. The trend line for R_a extrapolates to ~6 μm at crack branching. It is worth noting that Sundaram and Tippur [19], who used a coarser contact-type surface profiler, also noted a similar value of roughness in the hackle region prior to branching. Figure 5.23: (a) Variation of surface roughness (R_a) at different distances from the initial crack front and (b) Variation of (R_a) with crack velocity for 100 mm × 150 mm specimen. (The lack of any correlation between surface roughness and crack speed is noticeable.)(b) shows variation of R_a as a function of crack velocity.

Note that the number of data points is different in this plot relative to Figure 5.23: (a) Variation of surface roughness (R_a) at different distances from the initial crack front and (b) Variation of (R_a) with crack velocity for 100 mm × 150 mm specimen. (The lack of any correlation between surface roughness and crack speed is noticeable.)(a) since velocity data was obtained from optical measurements and not from fractography. Evidently, there is no obvious correlation between the two measurements in Figure 5.23: (a) Variation of surface roughness (R_a) at different distances from the initial crack front and (b) Variation of (R_a) with crack velocity for 100 mm × 150 mm specimen. (The lack of any correlation between surface roughness and crack speed is noticeable.)(b). This is unlike a few other investigations on dynamic fracture of quasi-brittle polymers [143-145].

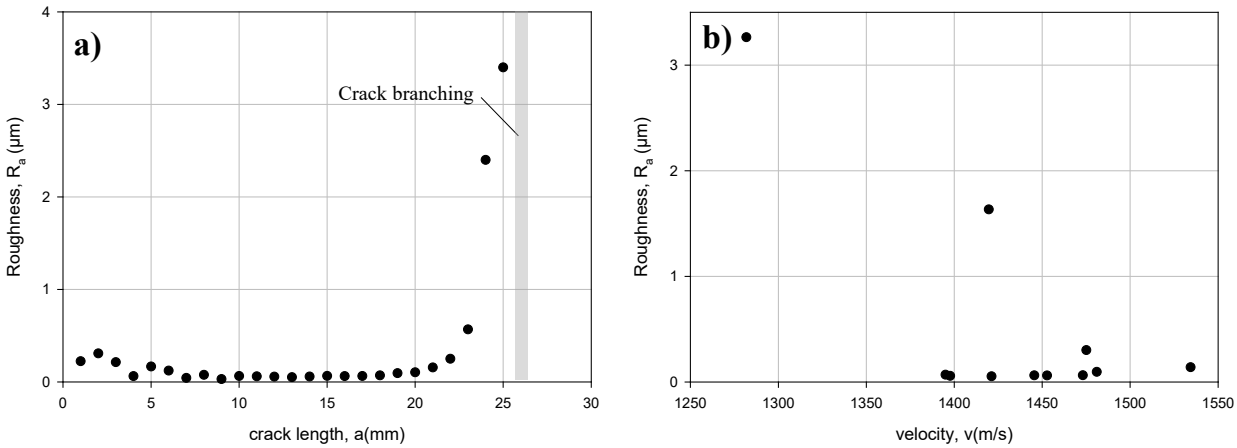

Figure 5.23: (a) Variation of surface roughness (R_a) at different distances from the initial crack front and (b) Variation of (R_a) with crack velocity for 100 mm × 150 mm specimen. (The lack of any correlation between surface roughness and crack speed is noticeable.)

The measured roughness obtained from fractography was examined relative to the corresponding (effective) stress intensity factors in Figure 5.24. Note that log(R_a) is plotted with K_{eff} in light of the power-law type variation evident in Figure 5.24. An approximately linear variation of log(R_a) with K_{eff} is evident.

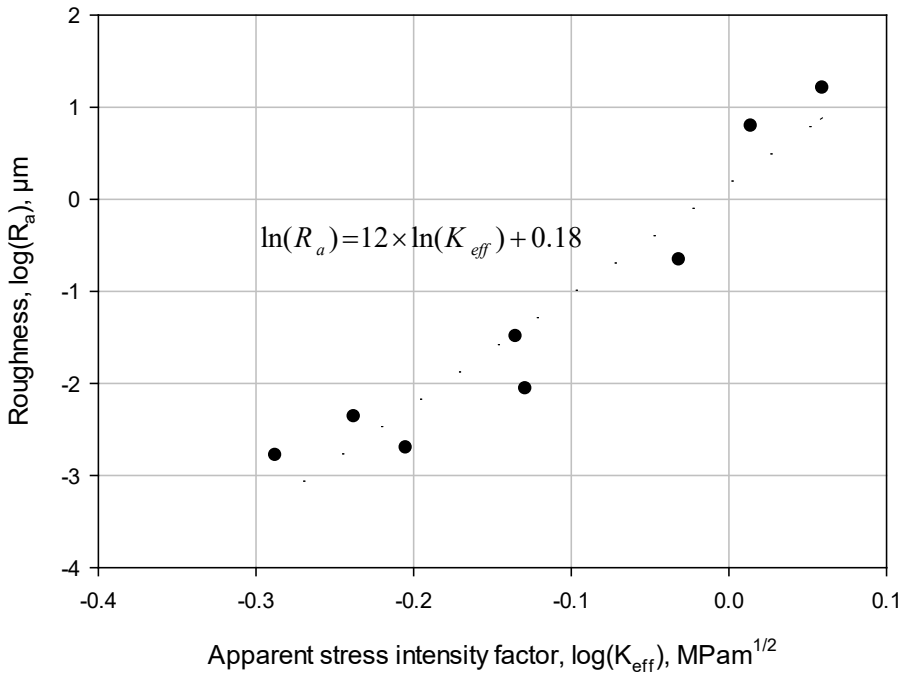

Figure 5.24: Variation (linear fit) of surface roughness, log(R_a) with apparent effective stress intensity factor, K_{eff} for 100 mm × 150 mm soda-lime glass plate.

Chapter 6. Crack initiation and slow growth in a self-healed plate

In this chapter, crack initiation and quasi-static (slow) crack growth from a self-healed crack in an SLG plate is investigated. A wedge-splitting test geometry (WST) is adopted along with displacement-controlled loading to accomplish the task. Full-field optical method of DGS is employed to visualize and quantify fracture parameters. A companion finite element analysis is also carried to evaluate features of self-healed crack not evident to experimental results.

6.1 Specimen preparation

SLG specimens were machined from a 5.7 mm thick, commercially procured sheet into the Wedge Splitting Test (WST) specimens illustrated in Figure 6.1. WST geometry is commonly used to assess fracture characteristics of ceramic, geo and cementitious materials. A 10 mm long notch was cut into the specimen using a 300 μm thick diamond impregnated circular-saw.

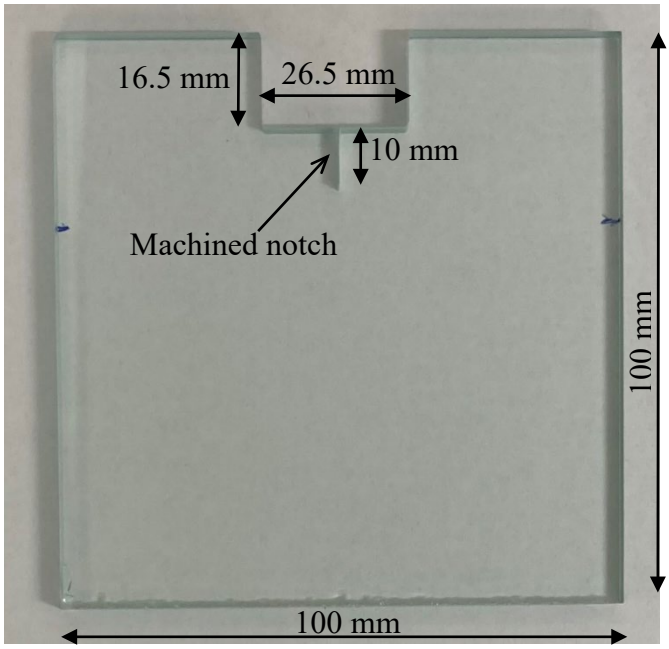

Figure 6.1: Wedge Splitting Test (WST) soda-lime glass specimen geometry with machined notch. (Plate thickness = 5.7 mm; notch length 10 mm).

To generate a natural crack in the specimen, a steel wedge was tapped into the machined notch using a rubber mallet while the specimen was resting on its opposite edge on a table-top. This resulted in a natural crack from the initial notch-tip. Once, the natural mode-I crack was generated, the wedge was retracted and the specimen was rested under laboratory conditions for a few hours before testing. In the interim, the natural crack self-healed, as evident in Figure 6.2 [146].

6.2 Experimental details

As demonstrated in the earlier chapters, the full-field vision-based method Digital Gradient Sensing (DGS) when used in light transmission-mode is highly effective in mapping stress gradient fields near stress concentrations [16, 18, 19, 54]. Though DGS has been used in the previous chapters for studying fast fracture events in SLG, its applicability to slow and subcritical crack growth is unknown and yet to be demonstrated. The extremely small deformations during subcritical crack growth makes it a rather challenging to quantify as crack growth is known to occur at much lower values of stress intensity factors relative to the fracture toughness of SLG. DGS technique [54] was attempted in this work to visualize and quantify crack tip fields associated with crack initiation and growth of a self-healed crack and subsequent initiation at the natural crack tip followed by slow crack growth phenomena. Working principle of DGS technique has been discussed in Chapter 2.

A Point Grey Grasshopper3 digital camera with 2048 × 2048 pixels sensor and 18-108 mm focal length zoom lens was used to record speckles on the target plane, through the specimen, at 5 fps. The target plane was located behind the specimen plane at a distance of ~0.6 m and the camera was at ~0.9 m ahead of the specimen plane. A Point Grey Grasshopper3 digital camera with 2048 × 2048 pixels sensor and 18-108 mm focal length zoom lens was used to record speckles on the

target plane, through the specimen, at 5 fps. The target plane was located behind the specimen plane at a distance of ~0.6 m and the camera was at ~0.9 m ahead of the specimen plane.

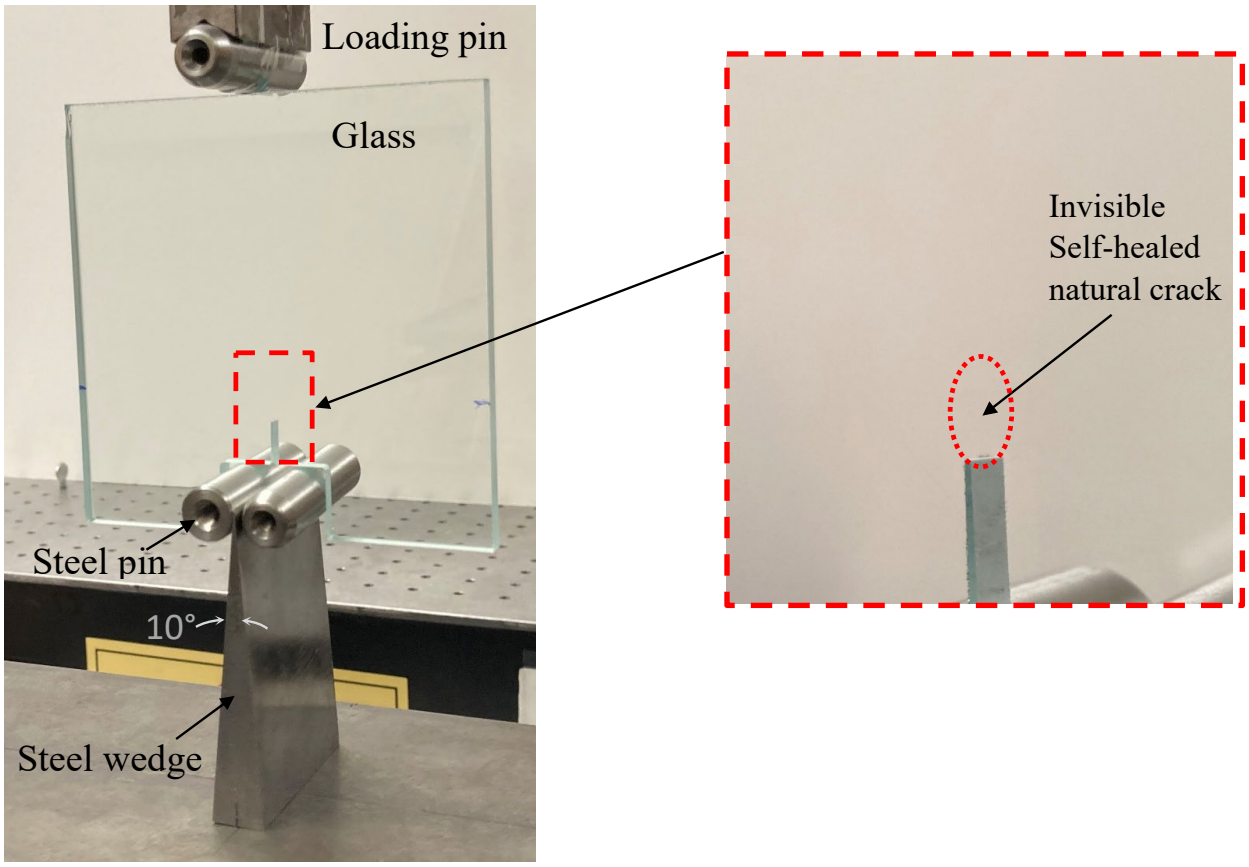

Figure 6.2: WST (Wedge Splitting Test) specimen loading configuration. Notice the lack of evidence of the healed-crack emanating from the notch-tip.

The ROI in this experiment covered all the events including initiation and growth of the self-healed crack as well as the natural crack. A 141 × 141 mm^2 region covered by random speckles on the target, corresponding to approx. 84 × 84 mm^2 on the specimen, was photographed. The resulting magnification factor (or, the scale factor) of these images was 69 μm/pixel. Assuming a speckle shift sensitivity of approx. 1% of the magnification factor, an angular deflection accuracy of about 10 μrad was expected.

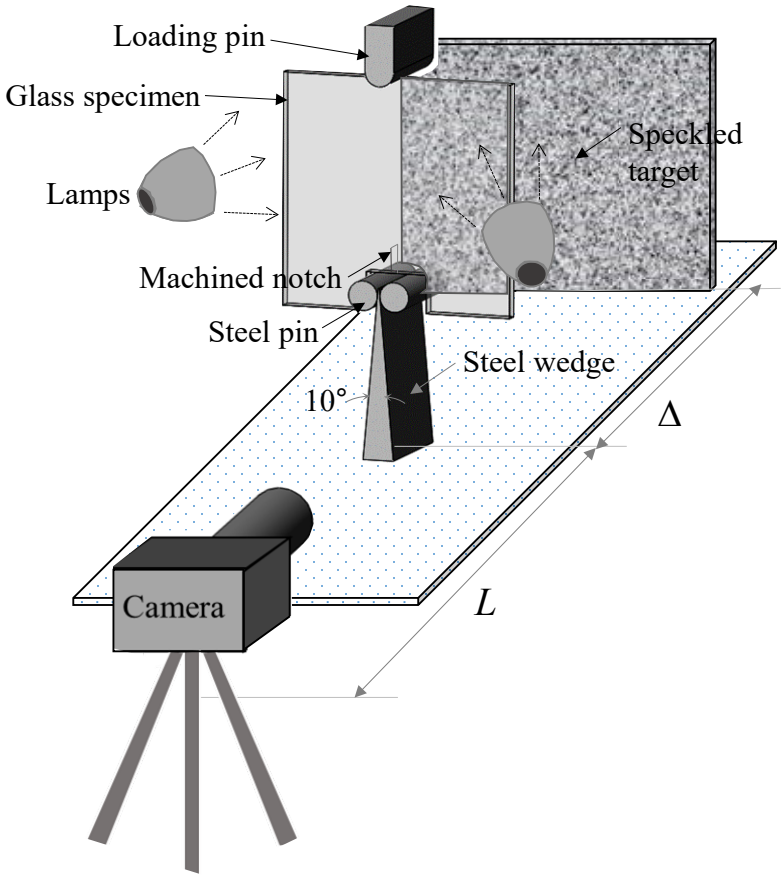

Figure 6.3: Schematic of DGS experimental setup with WST specimen geometry.

The load-displacement plot recorded by the load-cell of the testing machine is shown in Figure 6.4(a). The load increased monotonically until crack initiation. (The initial loading phase was nonlinear due to the backlash in the loading screw and friction at multiple contact pairs, Figure 6.4a).) Once the healed crack initiated at ~92 N, the load dropped instantaneously to ~71 N. Subsequently, the load increased linearly to a value of ~88 N until initiation of the natural hairline crack that had previously healed. Later, a slow crack growth in the specimen resulted in a more gradual reduction of load, as highlighted in Figure 6.4(a). (Figure 6.4(a) also shows the recorded load histories with horizontal axis as time, *t*, on top of the chart.) As expected, both the load-displacement plot and the load history show similar trends due to the constant loading rate used

during the test. For analyzing the optical data, images and hence load/deflection data at every 2 second intervals were considered to reduce the amount of post-processing of full-field optical data. Accordingly, the load-displacement plot corresponding to the reduced data set is shown in Figure 6.4b).

6.3 Stress gradient measurements

A speckle image in the early stages of loading of the specimen with the self-healed crack is shown in Figure 6.5. The specimen edge, initial notch, healed crack region and natural crack tip location are all identified in the figure. A photograph of the fractured specimen from this experiment is also shown in Figure 6.6. During the experiment, the crack initiated from the self-healed notch-tip after it opened suddenly while loading at a constant rate. Subsequently, the crack initiated at the original hairline crack tip, produced during wedge insertion step, and it propagated slowly in a mode-I condition.

The angular deflections of light rays, ϕ_x and ϕ_y, in two orthogonal directions (with respect to the propagating mode-I mother crack) at select time instants, are shown in Figure 6.7 as contour maps. These contour maps were obtained by segmenting the target plane speckle images in the reference and deformed states of the specimen, recorded at different time instants, into 60 × 60 pixel sub-images. An overlap of 10 pixels was used during digital image correlation operation. This resulted in data arrays of pseudo speckle shifts corresponding to horizontal and vertical directions, δ_x and δ_y, respectively. Each of these arrays were 178 × 198 in size. These were subsequently converted into ϕ_x and ϕ_y fields by dividing speckle shifts by the gap Δ between the specimen and target planes in the optical setup. The first column in Figure 6.7 represents contours of ϕ_x and ϕ_y for the initial notch-tip (before the self-healed crack opened) at time t = -

32 s whereas the second column correspond to the natural crack tip fields (after the healed crack opened) at time t = -20 s. Here, *the timestamps are with respect to the instant when the crack initiated at the natural crack tip due to wedge insertion, identified as* $t = 0$.

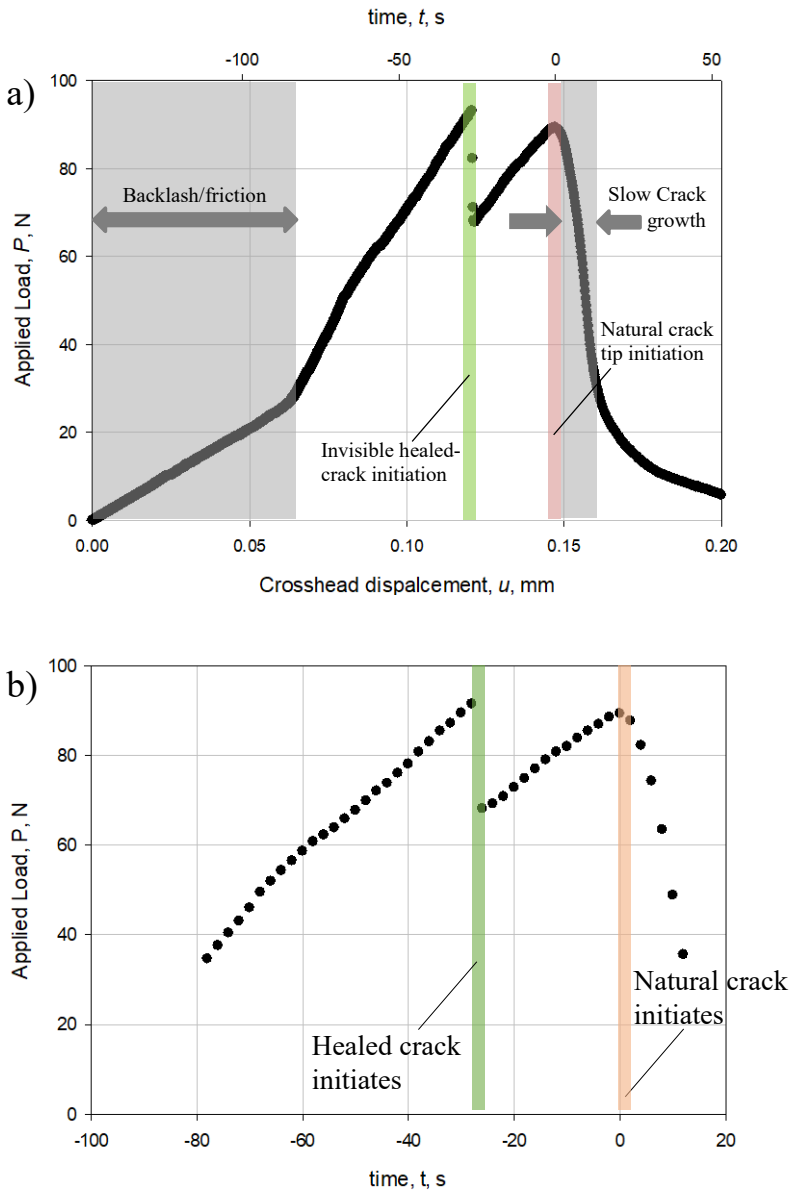

Figure 6.4: Far-field measurements: (a) Load-displacement record from the testing machine and (b) Load history corresponding to fracture parameters evaluated using DGS (data at every 2 s time step was considered, Time, $t = 0$ corresponds to crack initiation at natural crack tip).

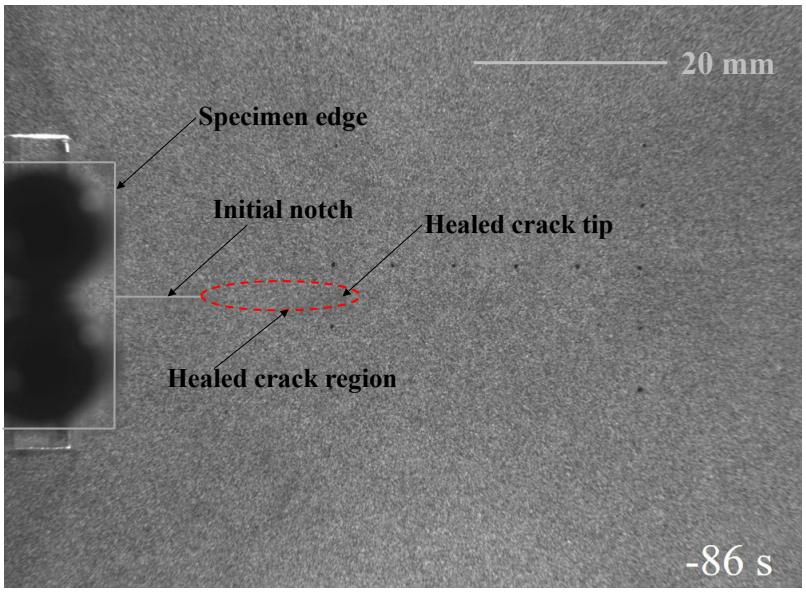

Figure 6.5: Far-field measurements: (a) Load-displacement record from the testing machine and (b) Load history corresponding to fracture parameters evaluated using DGS (data at every 2 s time step was considered, Time, $t = 0$ corresponds to crack initiation at natural crack tip).

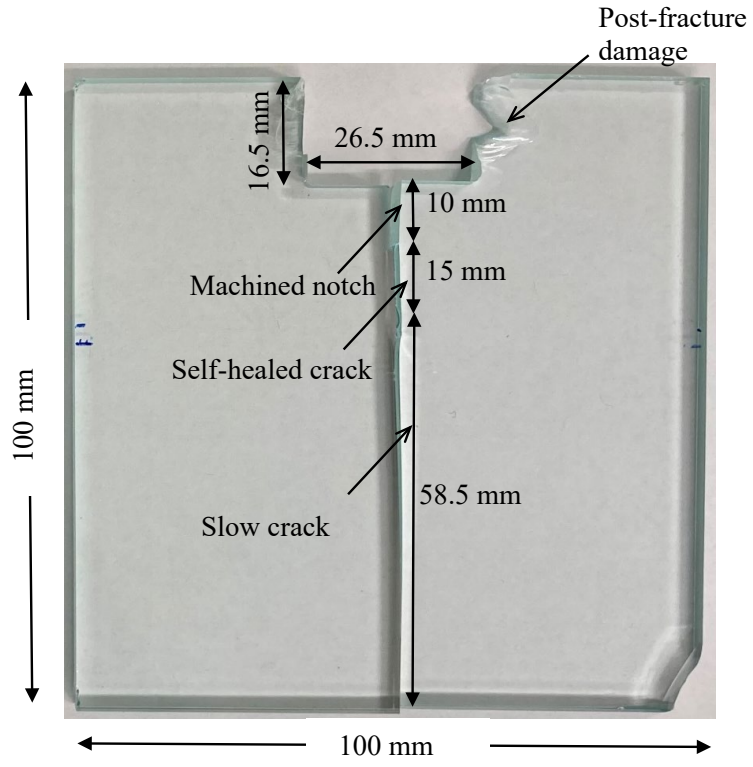

Figure 6.6: Photograph of fractured WST specimen. (Visible damage to edges are due to collision of fractured pieces with equipment in the post-fracture phase).

6.4 Stress intensity factor histories

The mode-I SIFs were then evaluated by analyzing the angular deflections ϕ_x around the crack tip in conjunction with the asymptotic equation [103] using an over-deterministic least-squares error minimization approach using the asymptotic stress gradient field expression,

$$\phi_x = C_\sigma B \frac{\partial\left(\sigma_x + \sigma_y\right)}{\partial x} = C_\sigma B \left[-\frac{1}{2} r^{-\frac{3}{2}} \left\{ A_1 \cos\left(\frac{3\theta}{2}\right) \right\} + \sum_{N=2}^{\infty} \left(\frac{N}{2} - 1\right) r^{\left(\frac{N}{2}-2\right)} \left\{ A_N \cos\left(\left(\frac{N}{2} - 2\right)\theta\right) \right\} \right] \quad (6.1)$$

In the above, (r, θ) denote the local crack tip polar coordinates, and $r = \sqrt{x^2 + y^2}$ and $\theta = \tan^{-1}\left(\frac{y}{x}\right)$ in the crack growth direction. The coefficient A_1 in the asymptotic series are related to the mode-I SIF, as $K_I = A_1\sqrt{\frac{\pi}{2}}$. The crack travelled with an average velocity of 2×10^{-3} m/s during slow crack growth phase. For analysis purposes, the data near the crack tip region with an angular extent of $-150° \le \theta \le 150°$ but different radial extents was considered. The least-squares analysis was performed with four (N = 3) terms in the asymptotic stress field expressions and was guided by previous works [94, 95]. In Eq. (6.1), C_σ is the elasto-optical constant for SLG, and B is the nominal plate thickness.

The SIF histories extracted from DGS data starting at the instant the healed crack initiated and then propagated slowly are shown in Figure 6.8. Again, here t = 0 corresponds to crack initiation at the natural crack tip produced after the wedge insertion into the notch. The mode-I SIF, K_I, (solid black symbols) increased steadily from much lower values to ~0.37 MPa√m when the self-healed crack initiated. This is accompanied by an abrupt jump in the stress intensity factor to ~0.5 MPa√m as the crack length suddenly increased from its shorter self-healed state to longer hairline crack state. Subsequently, the stress intensity factors for the natural crack increased almost

linearly for the next 22 seconds until the crack initiated at the natural tip and grew slowly afterwards. During slow crack growth, the stress intensity factors are nearly constant, as indicated by the trend line. Interestingly, the DGS method is able to estimate the fracture toughness of the pre-crack even when the angular deflections are very small, approx. 10 to 20 μrad. The results are, however, relatively noisy due to the fact that the experiments were conducted without any vibration and thermal isolation of the optical setup.

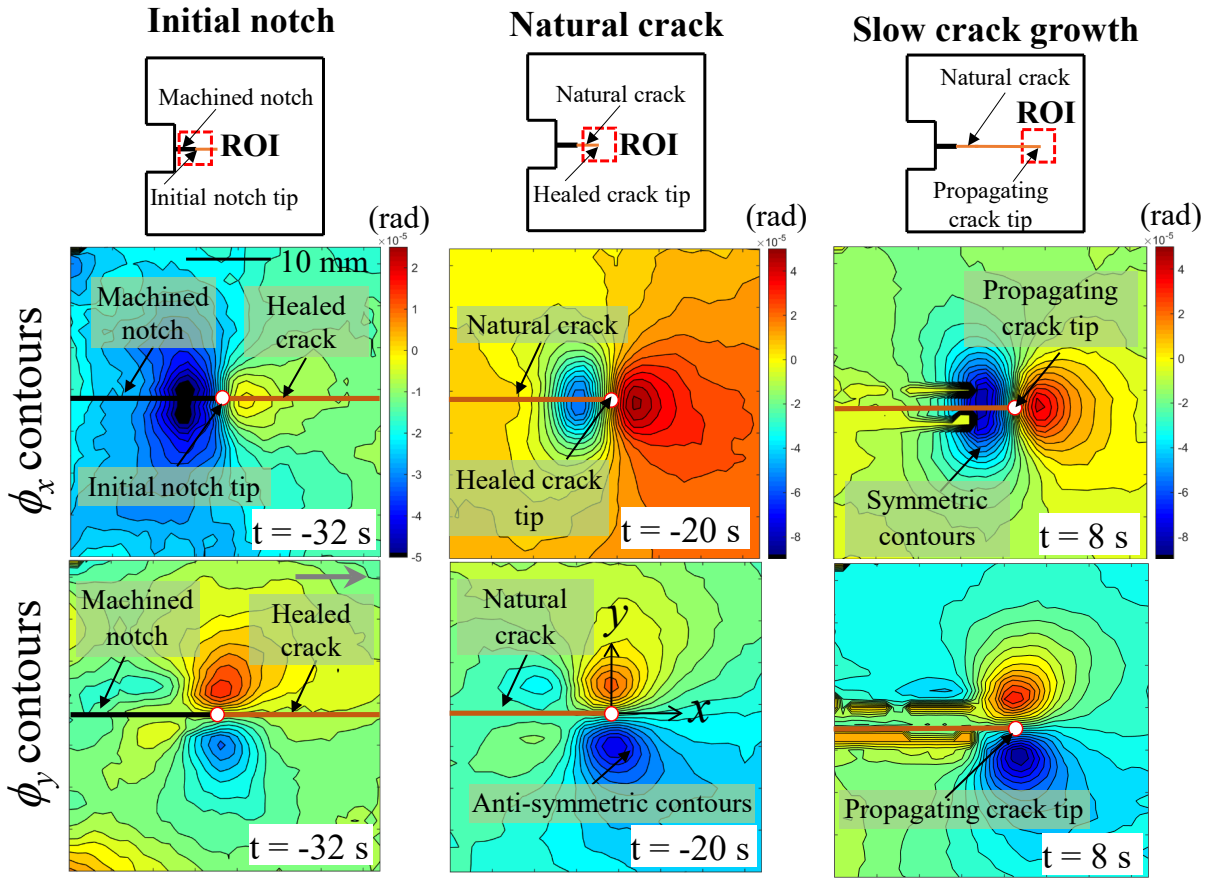

Figure 6.7: Contours of angular deflections of light rays (contour increment = 5×10^{-6} rad) in WST soda-lime glass plate with a self-healed crack measured using DGS. The arrowhead (in the bottom left image) shows crack growth direction.

In addition to SIF history, the energy release rate, $G = K_I^2 / E$, was also evaluated and is shown in Figure 6.9. The energy release rate increased until the healed crack initiated at ~2 J/m^2.

Subsequently, G increased instantaneously (to approx. 3 J/m^2) due to the sudden opening of the self-healed crack. Afterwards, G increased to ~7 J/m^2 when it initiated at the natural crack tip. Later, the crack continued to propagate in a mode-I fashion until the end of observation window with approximately the same value at initiation, as suggested by gray trend line.

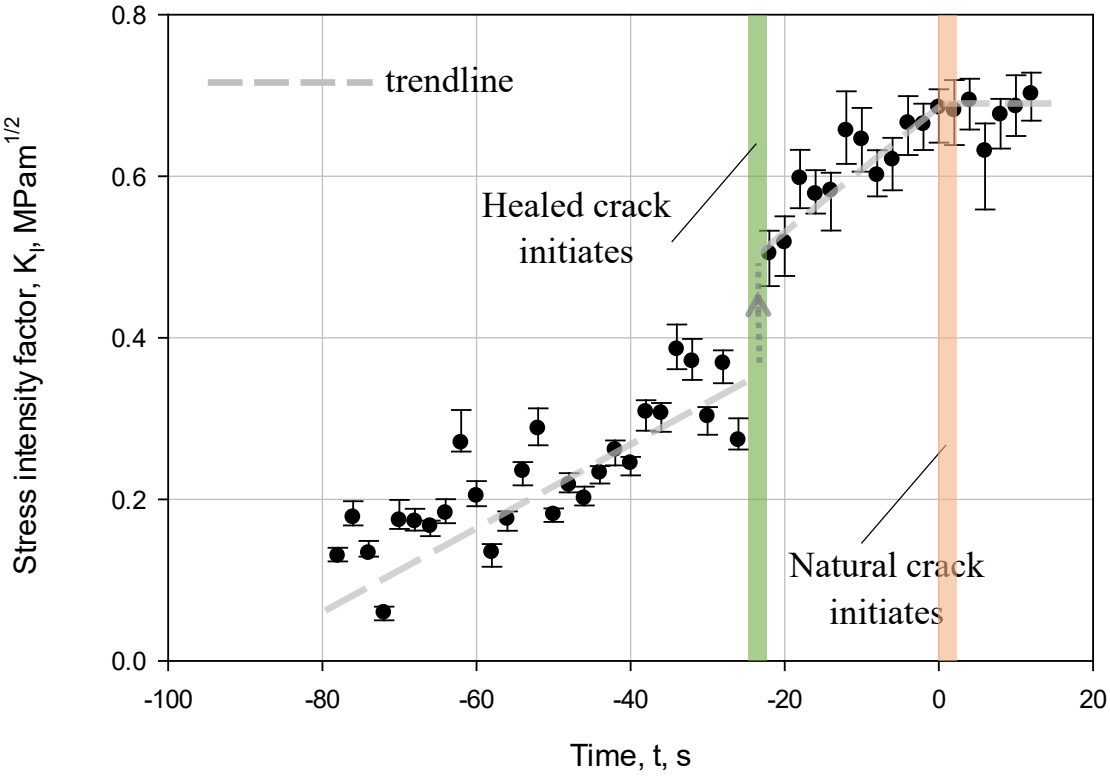

Figure 6.8: Stress intensity factor history for WST soda-lime glass specimen with a self-healed crack. (Time, t = 0 corresponds to crack initiation at natural crack tip.)

6.5 Finite element model

A complementary finite element analysis was carried out for evaluating the fracture parameters at crack initiation and during slow crack growth. Components of WST assembly included the SLG specimen, steel pins and the wedge. The components like steel pins and the wedge (Young's modulus, E = 200 GPa) cannot be treated as rigid when compared to the stiffness

of the specimen since SLG is also a relatively stiff material (E = 70 GPa) and has a high configurational stiffness in the WST geometry. Hence, upon loading, the strain energy gets stored in the steel pins and wedge as well the SLG specimen. To capture proper loading on the specimen in the setup as precisely as possible, the WST assembly was modeled for finite element analysis using Abaqus (Simulia, Rhode Island, USA) for performing a companion evaluation. Figure 6.10(a) shows the 2-D geometric model. Due to symmetry, only one half of the model was considered. Figure 6.10(b) shows the corresponding discretized model for FEA along with the symmetry boundary conditions. To implement self-healed crack, a total of 73 spring elements of type SPRING1 were used. These elements were connected from node (on the crack surface) to the ground and oriented normal to the crack flank. Interfaces between wedge and steel pins, SLG specimen and steel pins were modeled using contact pairs as shown in inset of Figure 6.10(b). Since the steel pins are relatively stiff compared to specimen, pins were modeled as the master surface and specimen as the slave surface. All the master and slave surfaces were represented in red and magenta colors, respectively, as depicted in inset of Figure 6.10(b). And, surface-to-surface contact was used to simulate all steel to steel, steel to SLG contact pairs with a coefficient friction of 0.1. To achieve convergence, finite displacements (0.01 mm on the pin and 0.05 mm on wedge) were imposed. Abaqus/CAE software was used by employing quadratic plane stress elements (CPS8R) for the soda-lime glass specimen, steel pins and the wedge. In total the model consisted of 31000 elements and 93000 nodes. Experimentally measured crosshead displacements at each time instant were imposed at the top loading point of the specimen. The bottom edge of the wedge was fully constrained and symmetric boundary conditions were applied on the line-of-symmetry of the specimen and wedge. The computed in-plane displacement field, u_y around the crack tip under plane-stress condition was expressed using the asymptotic equation,

$$u_y = \sum_{N=1}^{\infty} \frac{1}{2\mu} A_N r^{N/2} \left\{ \left(\frac{3-\upsilon}{1+\upsilon} \right) \sin\frac{N}{2}\theta + \frac{N}{2}\sin\left(\frac{N}{2} - 2 \right)\theta - \left(\frac{N}{2} + (-1)^N \right) \sin\frac{N}{2}\theta \right\} \quad (6.2)$$

In the above, (r,θ) denote the local crack tip polar coordinates, and $r = \sqrt{x^2 + y^2}$ and $\theta = \tan^{-1}\left(\frac{y}{x}\right)$ in the crack growth direction. The coefficient A_1 in the asymptotic series are related to the mode-I SIF as, $K_I = A_1\sqrt{2\pi}$. For analysis, the data near the crack tip in the region $0.25 \le r/B \le 1.5$ behind the crack tip were considered. Using the first 3 terms ($N = 3$) behind the crack tip $(\theta = \pi)$, Eq. (6.2) is simplified as,

$$Eu_y(r, \theta = \pi) = 4\left(\frac{K_I}{\sqrt{2\pi}} \right) r^{\frac{1}{2}} - 4r^{\frac{3}{2}} A_3 \quad (6.3)$$

The overdeterminstic least-squares analysis was performed on Eq. (6.3) to evaluate mode-I stress intensity factor, K_I. In Eq. (6.3), E is the modulus of elasticity of SLG.

To simulate self-healed crack in the specimen, spring elements (see, Figure 6.10(b)) were used by assuming normal contact. The potential reduction in stiffness across the crack flanks due to self-healing was simulated by varying the elastic modulus of those spring elements. Furthermore, the stiffness of those springs were assumed to be uniform but varied from 100% to 40% of virgin SLG to simulate varying degrees of healing. Each case was simulated separately for the same applied far-field loading up to when the self-healed crack initiated in the experiments. The distribution of dominant stress σ_{yy} is shown in Figure 6.10(c) as a representative case. The stress contours for the virgin material (100% E) appears to be greater when compared to the self-healed crack whose elastic modulus was chosen to be 60% of the virgin material. This indicates that the specimen experiences higher stress if the stiffness of self-healed crack is equal to that of the virgin material. The results for stress intensity factors are shown in Figure 6.11(a). The mode-I stress intensity factor, K_I, increased monotonically in each case. Evidently, the rate of increase in

K_I is noticeably affected by the choice of the stiffness of the crack flank contact elements. Upon overlaying each of these data sets on experimental counterparts, it was concluded that the simulation corresponding to approx. 60% of the virgin material modulus matched the experimental ones quite well. Thus, a 40% reduction in the elastic modulus due to self-healing appears to have occurred in the present case.

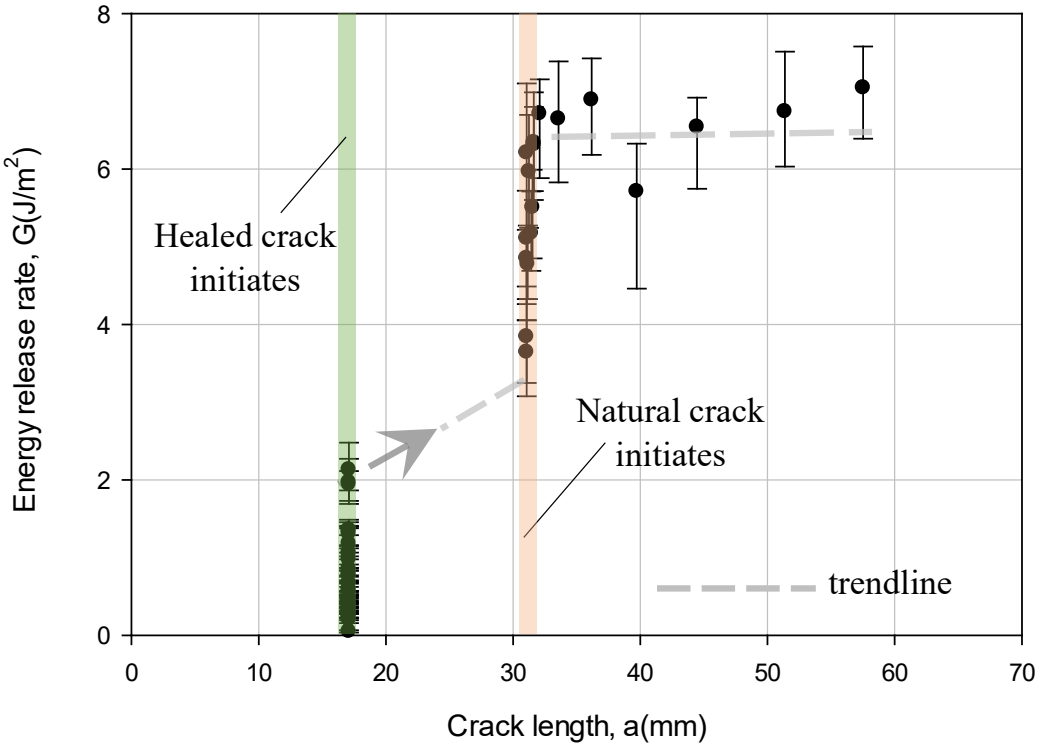

Figure 6.9: Crack growth resistance behavior of self-healed crack in soda-lime glass.

Subsequently, the K_I values increased suddenly as in the experimental counterparts due to a jump in the crack length as the self-healed crack opened instantaneously. After initiation of the self-healed crack, the values increased again monotonically until the natural crack tip initiated. The K_I value at the natural crack tip was ~0.7 MPa√m, close to the experimental counterpart. Once the crack initiated, it propagated and reduced to ~ 0.65 MPa√m by the end of the observation window. The K_I values from experiments and simulation show a good agreement.

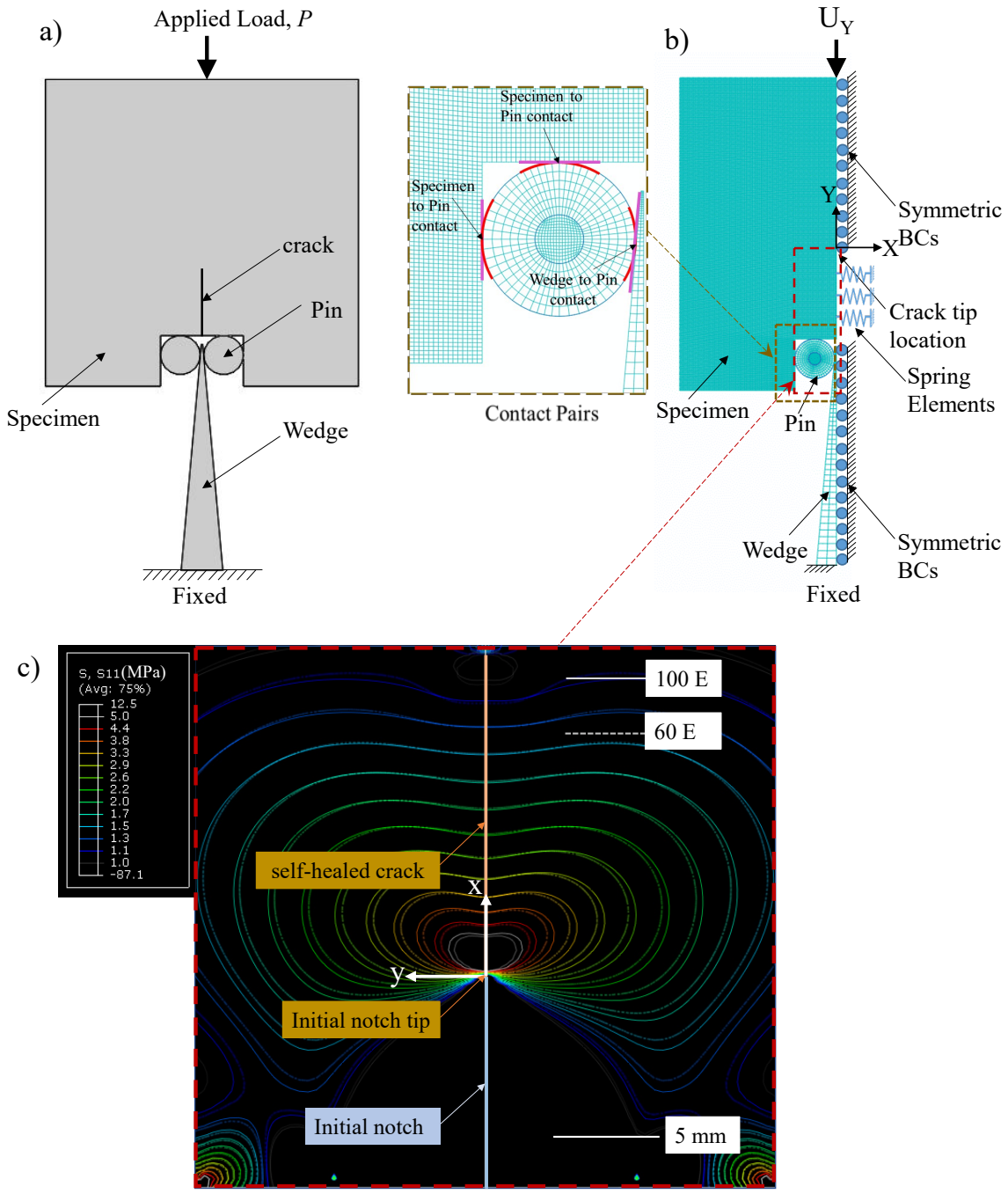

Figure 6.10: Numerical model details for simulating the WST geometry: (a) 2-D geometry and (b) 2-D Finite Element Model with (c) σ_{yy} stress distribution at self-healed crack region (specimen alone was shown in inset)

6.6 Discussion

The crack initiation and slow crack growth characteristics of soda-lime glass containing a self-healed crack show that the mode-I stress intensity factors, K_I, of the self-healed crack increase until initiation at ~0.37 MPa√m under laboratory conditions. This value of fracture toughness of the self-healed crack measured here is far below that of virgin SLG, by a factor of nearly two. Thus, it should be a concern for the mechanical integrity of load bearing structures involving SLG due to the possibility of invisible self-healed cracks. These general observations and fracture parameter quantifications are rather consistent with prior works in the literature made using far field load/deflection measurements instead of full-field optical evaluations undertaken here. Wiederhorn and Townsend [94] studied slow crack growth in double cantilever beam specimens subjected to bending. They have reported an even lower critical stress intensity factor of ~0.17 MPa√m (20% of the value relative to the virgin material) and the corresponding fracture energy of ~0.2 ± 0.2 J/m^2. Michalske et al., [95] investigated self-healing of cracks in soda-lime glass using double-cleavage drilled-hole compression (DCDC) specimen. The strain energy release rate for reopening of the healed cracks was obtained as ~1.7 ± 0.2 J/m^2 (and the critical K_I ~0.34 ± 0.02 MPa√m).

This being an optical study of fracture characteristics of SLG in the presence of self-healed cracks, it is necessary to examine the results in the context of potential measurement errors. As DGS quantifies angular deflection of light rays that are proportional to two orthogonal stress gradients, there are potential sources of measurement errors including those due to crack tip location and quantification of extremely small angular deflections of the order of 10 μrad. Due to the singular nature of these stress gradients at the crack tip, the contours converge, as shown in the left column of Figure 6.7, to the crack tip. Hence, identification of the crack tip is relatively straight

forward and shown to be accurate to < 200 μm of positional error [19]. Furthermore, DGS is able to quantify them in the whole field even though the angular deflections of light rays caused by the stress-state around the crack tip are very small. Figure 6.8 shows experimental scatter in the stress intensity factor history of self-healed crack. The data before the initiation of the self-healed crack when the angular deflections of the light rays are relatively small when compared to those at later stages is worth examining more carefully. Noting that these experiments were conducted under nominal conditions in a lab situated on top floor of a four-story building without vibration isolation and in open circulating air. Thus, structural vibrations and thermal/air currents during experimentation contribute towards perturbation of lights rays and experimental scatter in the data. Hence, to ensure that the reported data trends are indeed reliable, two successive images, both in the undeformed state of the specimen, were correlated with each other and the resulting 'angular deflections' ϕ_x and ϕ_y are plotted in Figure 6.12(a) and (b). These angular deflections values are considered along three neighboring vertical lines at 31.50 mm, 31.91 mm and 32.32 mm relative to the loading point on the WST geometry. It can be observed that, these values fluctuate in the range of 10 μrad instead of being zero expected under ideal conditions of no mechanical vibrations and thermal perturbations in the optical paths. Similar plots of ϕ_x and ϕ_y are shown Figure 6.13(a) and (b) but along three neighboring horizontal lines located at 8.80 mm, 9.21 mm and 9.62 mm relative to the initial notch. Despite a few local peaks, the scatter in the data is well within 5 μrad. Hence, it is reasonable to conclude that a 10 μrad measurement accuracy from the optical setup and post-processing method used for measurements.

Another source of experimental scatter is associated with the evaluation of K_I from data in the *vicinity* of the crack tip at different radial extents. Different data zones, $0.35 \le r/B \le 1.1$,

$0.3 \le r/B \le 1.2$, $0.35 \le r/B \le 1.1$, $0.3 \le r/B \le 1.3$, $0.3 \le r/B \le 1.2$, $0.3 \le r/B \le 1.5$, and $0.25 \le r/B \le 1.5$, $0.3 \le r/B \le 1.3$ were used separately during least-squares analyses.

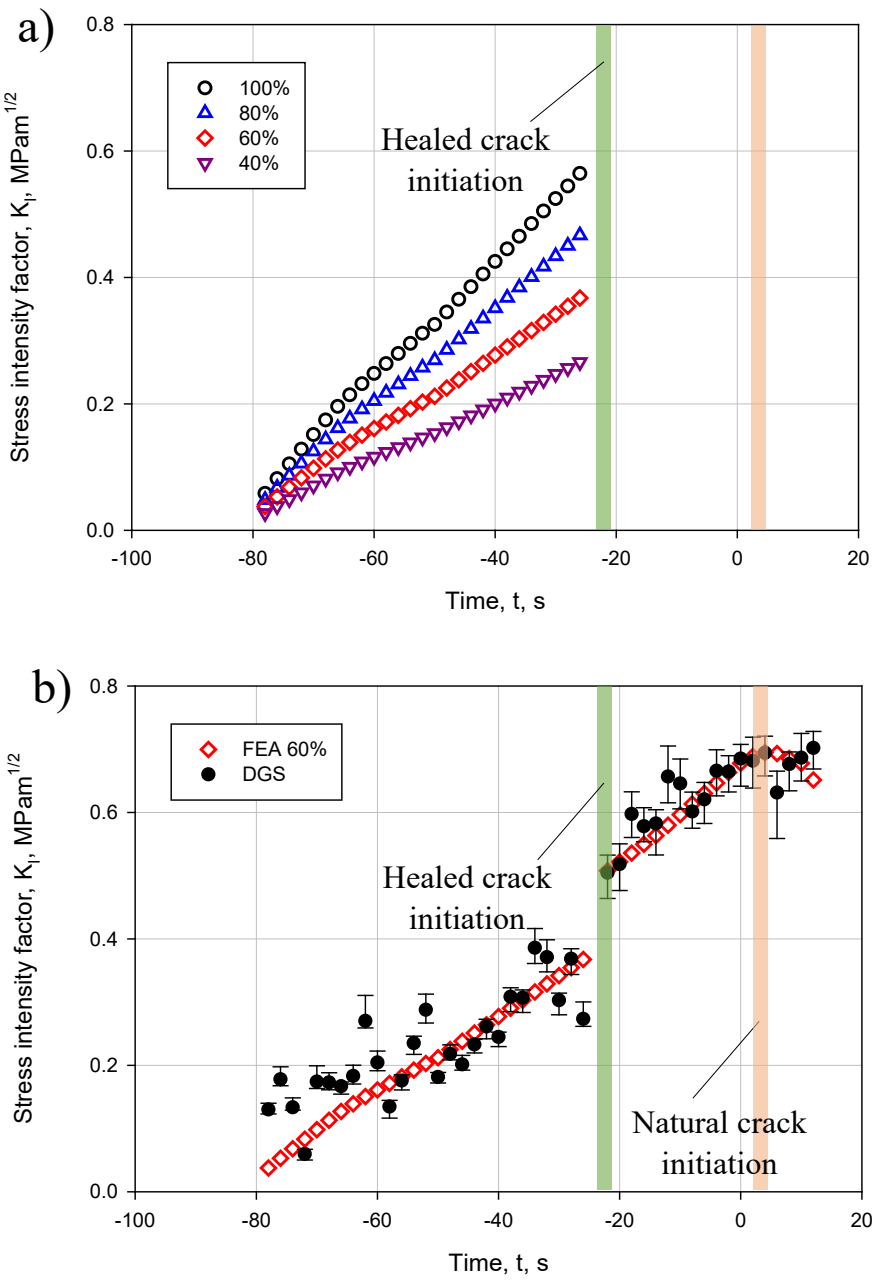

Figure 6.11: Stress intensity factor histories from FEA: (a) SIF histories for different crack flank stiffness up to healed crack initiation, (b) SIF histories along with DGS experimental results for 60% stiffness. (Time, $t = 0$ corresponds to crack initiation at natural crack tip.)

The inner limit was to avoid data influenced by triaxial deformations whereas the outer limit was to prevent excessive far-field effects that influence the outcome due to the limited number of terms employed in the asymptotic stress field expression. The stress intensity factors were evaluated from all these regions separately and averaged. The scatter in the results are shown in Figure 6.8 using error bars.

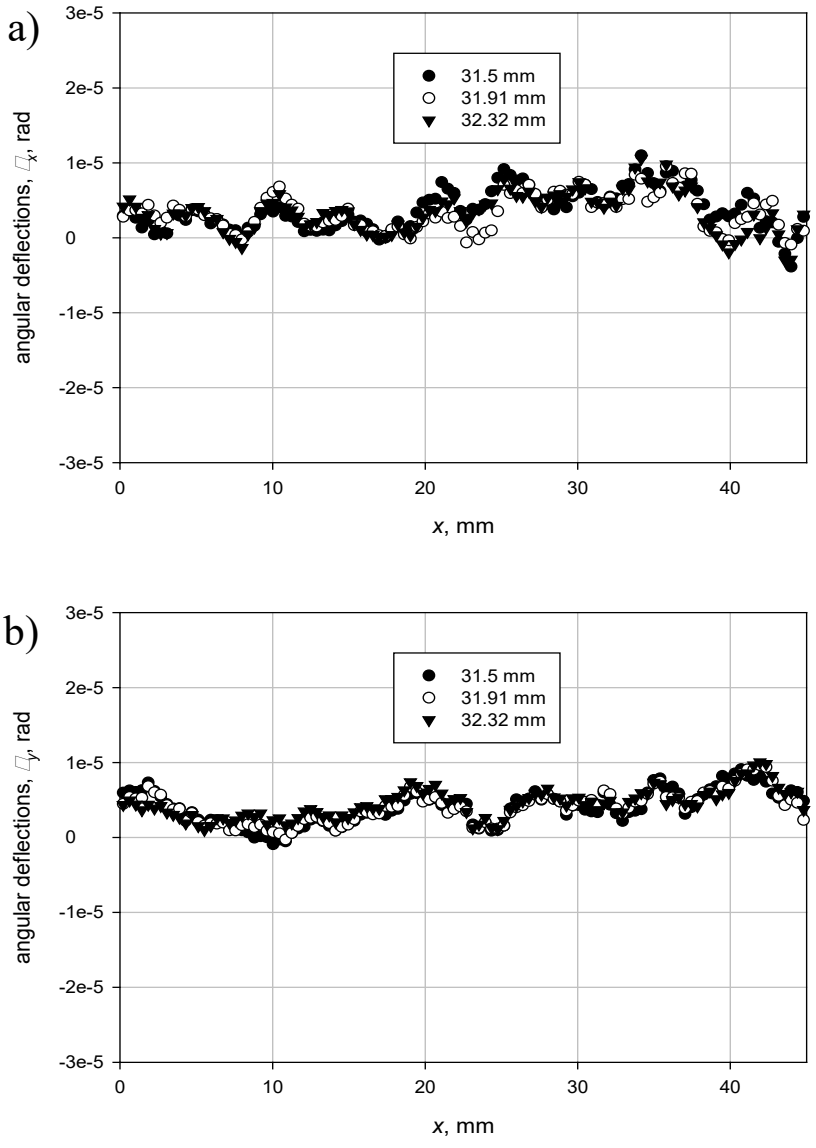

Figure 6.12: Error assessment of angular deflections along three neighboring locations; (a) ϕ_x and (b) ϕ_y. (x = 0 corresponds to the upper loading point on WST geometry.)

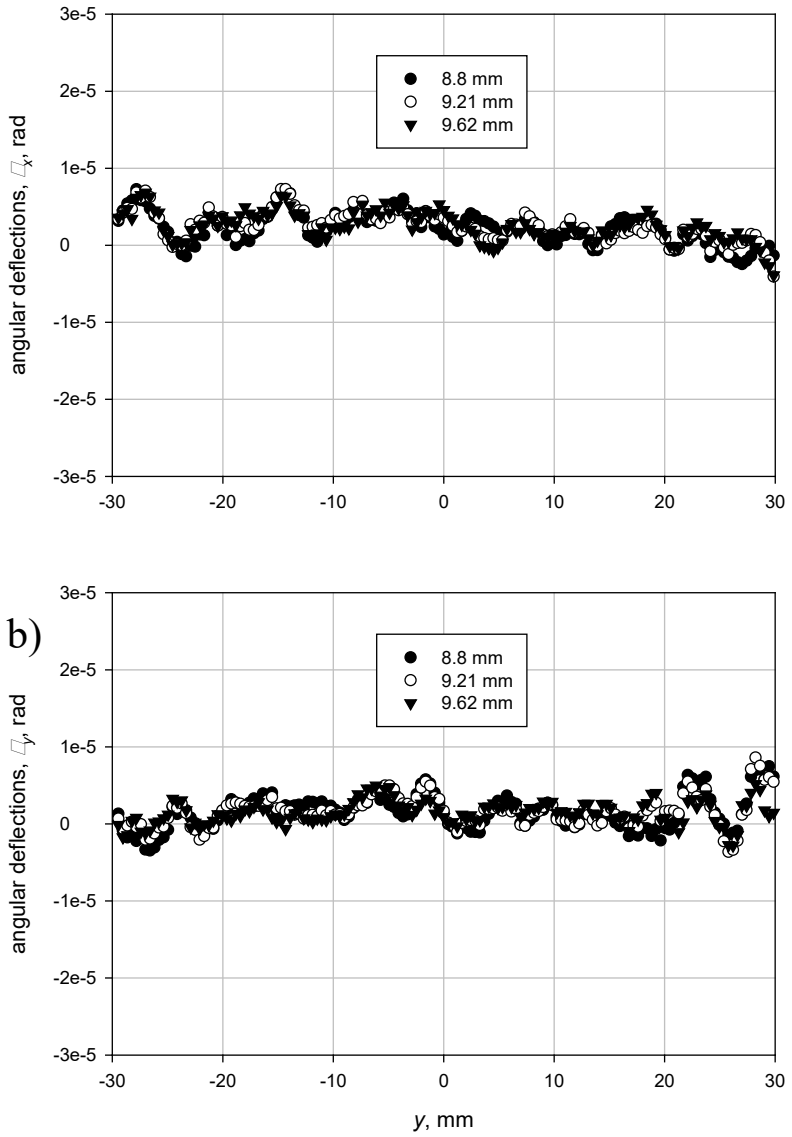

Figure 6.13: Error assessment of angular deflections along three neighboring locations; (a) ϕ_x and (b) ϕ_y. (y = 0 corresponds to initial notch position.)

The resulting fracture toughness of the self-healed crack tip was 0.37 ± 0.03 MPa√m (energy release rate of ~1.8 J/m^2), far below the 0.7 MPa√m for the virgin material. These suggest the robustness of the measurements presented in this work.

Chapter 7. Conclusions

In this dissertation, the feasibility of using full-field optical methods to investigate fracture mechanics of soda-lime glass (SLG) under both quasi-static and dynamic loading conditions for directly measuring crack fields was investigated. Fractures occurring at crack speeds in the $< 10^{-3}$ to $> 10^{3}$ m/sec range were studied. In the first part, the issue of implementing full-field optical methods to study dynamic crack initiation, growth and branching events in this high-stiffness and low-toughness material was addressed. Three different methods - photoelasticity, 2-D DIC and DGS - were all implemented for mapping mechanical fields in specimens subjected to stress wave loading. The major outcomes of this research are as follows:

- Photoelastic recordings allowed precise visualization and quantification of crack length history and reliable velocity history. The stress intensity factor histories, however, could not be evaluated due to the lack of well-formed crack tip fringes. Hence photoelastic method is suitable to test velocity based criteria of crack growth and branching in SLG. However, criteria pertaining SIFs and/or energy release rate cannot be verified.
- 2-D DIC did not allow direct visualization of the crack tip at different time instants. The identification of the crack tip via dominant displacement fields did not fare any better. The former being a non-singular kinematic quantity, the uncertainty in locating the crack tip was prohibitively high. These resulted in unrealistic instantaneous velocities and stress intensity factors both in terms of trends and magnitudes. Thus it was concluded that crack velocity and stress intensity factor histories cannot be correctly quantified using DIC.
- DGS, though relies on principles of 2-D DIC to quantify speckle shifts, measures quantities that are proportional to in-plane stress gradients in the whole field. This feature permitted visualization and quantification of crack length and crack velocity histories with high precision

due to the singular nature of the resulting mechanical fields. The measured values were also in close agreement with the photoelastic counterparts. Furthermore, the dynamic fracture characteristics such as instantaneous stress intensity factors including crack initiation and growth toughness values were measured with good precision. Thus, both velocity, stress intensity factor and and/or energy release rate criteria can be readily verified using DGS.

- Finally, the profile, magnitude and duration of normal force histories acting on the V-notch flanks of the specimen measured using photoelasticity and DGS corroborated well with each other in two nominally identical but different experiments. Thus, the speckle-based digital method - DGS - fares well relative to the well-established analog photoelastic method.

In the second part of the dissertation, an optical investigation of mixed-mode dynamic fracture behavior of soda-lime glass was undertaken. A simple reverse impact specimen geometry with a constant crack length but subjected to eccentric loading was introduced to create mode-mixities from mode-I to nearly mode-II condition at crack initiation. The impact loading was achieved using a long-bar loading apparatus and crack tip mechanical fields were mapped in real-time by employing the Digital Gradient Sensing (DGS) method along with ultrahigh-speed photography. The stress gradients in two mutually perpendicular in-plane direction were visualized and quantified by measuring angular deflections of light rays from the early stages of loading to crack initiation and subsequent crack propagation. From the time-resolved measurements, mode-I and mode-II SIF histories were extracted by performing over-deterministic least-squares minimization of optical data along with prevailing asymptotic description of the crack tip fields. A monotonic increase in mode-mixity at crack initiation with load-line eccentricity is observed. Using the critical stress intensity factors at crack initiation, a fracture envelope was generated for SLG. The relationship between the effective critical stress intensity factors, $\left(K_{eff}\right)_{cr}$, and critical

mode-mixity, ψ_{cr}, was obtained as a fracture characteristic of the material. The $\left(K_{eff}\right)_{cr}$ values remain nearly constant until a mode-mixity of ~65° and then rapidly decreases until ~85°, the maximum mixity achieved in this work. This behavior seems analogous to decreased material strength of borosilicate glass as shear stress increases, reported in the literature. The kink angles at crack initiation were measured directly from the fractured specimens. The predicted kink angles for MTS and SED criteria were also quantified separately using measured critical stress intensity factors. Reasonably good agreement of measured kink angles with MTS and SED predictions are observed. However, the fracture envelope based on neither of these popular criteria for brittle materials match well with measurements at higher mode-mixities. An empirical quadratic fit of data seems to follow the measured trends well. The resulting critical SIF values of ~0.71 MPa√m and ~0.37 MPa√m, respectively, for mode-I and -II states are obtained.

In the third part of dissertation, full-field quantitative visualization of time-resolved stress gradients near dynamically growing cracks in soda-lime glass plates of two different geometries subjected to nominally identical symmetric stress wave loading was undertaken using the Digital Gradient Sensing (DGS) technique. The first geometry produced a single crack bifurcation event; a dynamically propagating mode-I mother crack branched into two globally symmetric mixed-mode daughter cracks. The second geometry produced three cascading crack bifurcation events; a dynamically growing mode-I mother crack bifurcated into two globally symmetric mixed-mode daughter cracks, each of which bifurcated again into two granddaughter cracks subsequently. The optical measurements were utilized to quantify fracture parameter histories during various fracture events. Subsequently, LEFM-based precursors prior to each of the bifurcation events were identified. They included crack velocities (V), effective stress intensity factors (K_{eff}), higher order coefficients (A_{eff}) of the asymptotic crack tip fields. Two additional parameters based on these

three measured quantities namely, $\hat{\sigma}$ and $\hat{K}$, were also formulated. Fracture surface roughness and other fractographic features were also separately quantified via high resolution post-mortem study and examined relative to the optical measurements. The main results of this work can be summarized for soda-lime glass as follows:

- A drop in the macroscale (apparent) crack velocity V from a steady value of ~1500 m/s to ~ 1000 m/s was observed consistently when crack branching was imminent in both single and cascading branch formation geometries.
- The cracks bifurcated when K_{eff} reached approximately twice the value at initiation (~0.6 MPa√m) in both the single and cascading branch formation geometries.
- The cracks bifurcated after the higher order coefficient of the asymptotic field A_{eff} showed a distinct kink in the data trend.
- Energy release rates showed strong dependence with crack speeds in all experiments. Due to the drop in the crack speed prior to each bifurcation event, the G-V trends contain a cluster of data points just before crack bifurcation.
- A non-dimensional parameter $\hat{K}$, formulated using measured V, K_{eff}, and A_{eff}, consistently showed a steep raise prior to each crack bifurcation.
- The surface roughness showed the mirror-mist-hackle features but without conic marks seen in quasi-brittle polymers.
- The fracture surface roughness (R_a) was quantified in each of mirror-mist-hackle zones and a power-law type variation was observed with K_{eff} and $\hat{\sigma}$. A linear relationship between $\log(R_a)$ and K_{eff} was obtained.

- The crack bifurcation angles based on measured parameters is, however, lacking in this investigation. Evaluation of the *T*-stress from measurements is a possible way to address this shortcoming via additional experiments and numerical simulation of the reported experiments.

In the last part of the dissertation, a somewhat obscure yet important issue of quasi-static fracture mechanics of soda-lime glass (SLG) with a self-healed crack was studied. The full-field optical method of digital gradient sensing or DGS was used to investigate the problem of crack initiation and slow growth from a self-healed crack in a SLG coupon. A WST specimen geometry with a pre-cut notch was adopted for experimentation. A mode-I natural hairline crack was generated by tapping a wedge into the notch that self-healed subsequently under ambient conditions upon retracting the wedge. The WST specimen with a self-healed crack was reloaded afterwards in a testing machine in a displacement controlled mode while monitoring the crack tip region to quantify mechanical fields using DGS. DGS was able to quantify extremely small angular deflections of light rays, of the order of 10 μrad, due to the crack tip state of stress under quasi-static conditions without optical or mechanical isolation of the setup. Two orthogonal stress gradients, one parallel and the other perpendicular to the crack, were quantified in the entire region of interest. By performing least-squares analysis of the measured quantities, in conjunction with expressions for asymptotic stress gradient fields, the stress intensity factors and energy release rates at various stages of fracture were evaluated.

The experimental results indicate that the self-healed crack initiated at a critical stress intensity factor of ~0.37 MPa√m and fracture toughness of 1.8 J/m^2. These values are far below that for the virgin SLG of ~0.7 MPa√m and ~6.5 J/m^2, respectively, when the crack initiated from the natural hairline crack. This in turn suggests that structural design involving SLG needs to consider substantial degradation of fracture toughness in the presence of undetected self-healed

cracks. A companion finite element analysis of the WST geometry with far-field displacements imposed on the specimen as boundary condition was also undertaken to supplement measurements. The self-healed crack was simulated using reduced contact stiffness across the healed crack flanks. The results show that a uniform 40% degradation of spring stiffness along the crack flanks was able to mimic the experimental trends well.

7.1 Future work

In the current research work, static and dynamic fracture of SLG was investigated using full-field optical methods. During this study crack branching was investigated in single and cascading crack branching experiments and precursors were identified in both configurations. However, a robust dynamic crack growth direction criterion suitable for highly brittle materials needs to be attempted in the future. Furthermore, the effect of *T*-stress on the crack growth direction needs to be investigated to understand the intricacies involved in crack branching phenomenon.

The effect of atmospheric and/or operating conditions including temperature, humidity on SLG on crack growth needs to be investigated using full-field optical method DGS as it is relatively easy to find the crack tip location and also sensitive enough to capture micro-level angular deflection contours under low tensile failure strains around the dynamically propagating crack tip.

Currently, DGS method is limited to study planar solids and it can be extended to study non-planar solids as well, by keeping the specimen in a refractive index matching fluid. This method also can be used for non-destructive testing of phase objects to visualize and quantify defects and flaws.

DGS method can be easily extended to investigate highly brittle materials (due to its robust crack-tip location identification capabilities and sensitivity for capturing sub-micron level crack-

tip field displacements) including ceramics where a ultrahigh-speed imaging of 5 Mfps capability may be required due to high crack velocities and low tensile strains around the crack-tip. For this purpose, an experimental setup using backlit speckles along with pulsed laser was developed and DGS method successfully captured angular deflection contours even at such ultrahigh-speed (5Mfps).

References

1. Grujicic, M., Bell, W.C., and Pandurangan, B., *Design and material selection guidelines and strategies for transparent armor systems.* Materials & Design, 2012. 34: p. 808-819.
2. Salem, J.A., *Transparent armor ceramics as spacecraft windows.* Journal of the American Ceramic Society, 2013. 96(1): p. 281-289.
3. McCauley, J.W., Strassburger, E., Patel, P., Paliwal, B., and Ramesh, K.T., *Experimental observations on dynamic response of selected transparent armor materials.* Experimental Mechanics, 2013. 53(1): p. 3-29.
4. Le Bourhis, E., *Glass: mechanics and technology*. 2014: John Wiley & Sons.
5. Rice, P. and Dutton, H., *Structural glass*. 1995: Taylor & Francis.
6. Jelle, B.P., *Solar radiation glazing factors for window panes, glass structures and electrochromic windows in buildings—Measurement and calculation.* Solar Energy Materials and Solar Cells, 2013. 116: p. 291-323.
7. Leslie, M., *Space Tourism Begins to Take Off*. 2022, Elsevier.
8. Ryan, C.M., Harris, D.C., Wright, J.C., Stanley, A.M., and Choi, S.R., *Slow crack growth in multispectral zinc sulfide for use in aircraft window design.* Optical Engineering, 2022. 61(4): p. 047103.
9. Goldstein, M.J., *Private Space Travel*. 2017: Space Discovery Guides.
10. Nichols, R.T. and Sowers, R.M., *Laminated materials, glass.* Kirk-Othmer Encyclopedia of Chemical Technology, 2000: p. 1-17.
11. Musgraves, J.D., Hu, J., and Calvez, L., *Springer handbook of glass*. 2019: Springer.
12. Albrecht, U.-V., von Jan, U., Kuebler, J., Zoeller, C., Lacher, M., Muensterer, O.J., Ettinger, M., Klintschar, M., and Hagemeier, L., *Google Glass for documentation of medical findings: evaluation in forensic medicine.* Journal of medical Internet research, 2014. 16(2): p. e3225.
13. Vallero, D.A., *34 - Control of Stationary Sources*, in *Fundamentals of Air Pollution (Fourth Edition)*, D.A. Vallero, Editor. 2008, Academic Press: Burlington. p. 852-885.
14. Synowicki, R.A., Johs, B.D., and Martin, A.C., *Optical properties of soda-lime float glass from spectroscopic ellipsometry.* Thin Solid Films, 2011. 519(9): p. 2907-2913.
15. Dally, J.W., Riley, W.F., and Kobayashi, A.S., *Experimental stress analysis.* 1978.
16. Dondeti, S. and Tippur, H.V., *Cascading Crack Bifurcations in Soda-Lime Glass: Quantification of Fracture Mechanics-Based Precursors Using Digital Gradient Sensing.* International Journal of Solids and Structures, 2021: p. 111252.DOI: https://doi.org/10.1016/j.ijsolstr.2021.111252.
17. Döll, W., *Investigations of the crack branching energy.* International Journal of Fracture, 1975. 11(1): p. 184-186.
18. Dondeti, S. and Tippur, H.V., *A Comparative Study of Dynamic Fracture of Soda-Lime Glass Using Photoelasticity, Digital Image Correlation and Digital Gradient Sensing Techniques.* Experimental Mechanics, 2020. 60(2): p. 217-233.DOI: https://doi.org/10.1007/s11340-019-00549-5.
19. Sundaram, B.M. and Tippur, H.V., *Dynamic fracture of soda-lime glass: A full-field optical investigation of crack initiation, propagation and branching.* Journal of the Mechanics and Physics of Solids, 2018. 120: p. 132-153.DOI: https://doi.org/10.1016/j.jmps.2018.04.010.
20. Shin, J. and Nam, K., *Groove formation in glass substrate by a UV nanosecond laser.* Applied Sciences, 2020. 10(3): p. 987.

21. Rubin, M., *Optical properties of soda lime silica glasses.* Solar energy materials, 1985. 12(4): p. 275-288.
22. Varshneya, A.K., *Fundamentals of inorganic glasses*. 2013: Elsevier.
23. Dally, J.W., *Dynamic photoelastic studies of fracture.* Experimental Mechanics, 1979. 19(10): p. 349-361.
24. Dally, J.W., *An introduction to dynamic photoelasticity.* Experimental Mechanics, 1980. 20(12): p. 409-416.
25. Bradley, W.B. and Kobayashi, A.S., *An investigation of propagating cracks by dynamic photoelasticity.* Experimental Mechanics, 1970. 10(3): p. 106-113.
26. Shukla, A., Jain, N., and Chona, R., *A review of dynamic fracture studies in functionally graded materials.* Strain, 2007. 43(2): p. 76-95.
27. Ramulu, M., Kobayashi, A.S., and Kang, B.S.-J. *Dynamic crack branching—a photoelastic evaluation*. in *Fracture Mechanics: Fifteenth Symposium*. 1984. ASTM International.
28. Tippur, H.V., Krishnaswamy, S., and Rosakis, A.J., *A coherent gradient sensor for crack tip deformation measurements: analysis and experimental results.* International Journal of Fracture Mechanics, 1991. 48(3): p. 193-204.
29. Krishnaswamy, S., Tippur, H.V., and Rosakis, A.J., *Measurement of transient crack-tip deformation fields using the method of coherent gradient sensing.* Journal of the Mechanics and Physics of Solids, 1992. 40(2): p. 339-372.
30. Tippur, H.V., Krishnaswamy, S., and Rosakis, A.J., *Optical mapping of crack tip deformations using the methods of transmission and reflection coherent gradient sensing: a study of crack tip K-dominance.* International Journal of Fracture, 1991. 52(2): p. 91-117.
31. Conner, R.D., Rosakis, A.J., Johnson, W.L., and Owen, D.M., *Fracture toughness determination for a beryllium-bearing bulk metallic glass.* Scripta Materialia, 1997. 37(9): p. 1373-1378.
32. Bedsole, R. and Tippur, H.V., *Dynamic fracture characterization of small specimens: a study of loading rate effects on acrylic and acrylic bone cement.* Journal of engineering materials and technology, 2013. 135(3).
33. Isaac, J.P., Dondeti, S., and Tippur, H.V., *Crack initiation and growth in additively printed ABS: Effect of print architecture studied using dic.* Additive Manufacturing, 2020: p. 101536.
34. Owens, A.T. and Tippur, H.V., *Measurement of mixed-mode fracture characteristics of an epoxy-based adhesive using a hybrid digital image correlation (DIC) and finite elements (FE) approach.* Optics and Lasers in Engineering, 2021. 140: p. 106544.
35. Isaac, J.P., Dondeti, S., and Tippur, H.V., *Fracture behavior of additively printed ABS: Effects of print architecture and loading rate.* International Journal of Solids and Structures, 2021. 212: p. 80-95.
36. Peters, W.H., Ranson, W.F., Kalthoff, J.F., and Winkler, S.R., *A study of dynamic near-crack-tip fracture parameters by digital image analysis.* Le Journal de Physique Colloques, 1985. 46(C5): p. C5-631-C5-638.
37. Pasumarthy, R.K.A. and Tippur, H.V., *Mechanical and optical characterization of a tissue surrogate polymer gel.* Polymer Testing, 2016. 55: p. 219-229.
38. Isaac, J.P., Lee, S., Thompson, S., Saharan, A., Shamsaei, N., and Tippur, H.V., *Role of Build Orientation on Quasi-Static and Dynamic Fracture Responses of Additively Manufactured AlF357 and AlSi10Mg Alloys.* Additive Manufacturing, 2022: p. 103080.

39. Weeks, J.S., Gandhi, V., and Ravichandran, G., *Shock compression behavior of stainless steel 316L octet-truss lattice structures.* International Journal of Impact Engineering, 2022. 169: p. 104324.
40. Sharafisafa, M. and Shen, L., *Experimental investigation of dynamic fracture patterns of 3D printed rock-like material under impact with digital image correlation.* Rock Mechanics and Rock Engineering, 2020. 53(8): p. 3589-3607.
41. Zhang, Q.B. and Zhao, J., *Quasi-static and dynamic fracture behaviour of rock materials: phenomena and mechanisms.* International Journal of Fracture, 2014. 189(1): p. 1-32.
42. Wu, W., Zhu, J.B., and Zhao, J., *Dynamic response of a rock fracture filled with viscoelastic materials.* Engineering Geology, 2013. 160: p. 1-7.
43. Bedsole, R.W., Bogert, P.B., and Tippur, H.V., *An experimental investigation of interlaminar and intralaminar dynamic fracture of CFRPs: Effect of matrix modification using carbon nanotubes.* Composite Structures, 2015. 132: p. 1043-1055.
44. Kushvaha, V. and Tippur, H., *Effect of filler shape, volume fraction and loading rate on dynamic fracture behavior of glass-filled epoxy.* Composites Part B: Engineering, 2014. 64: p. 126-137.
45. Jajam, K.C., Rahman, M.M., Hosur, M.V., and Tippur, H.V., *Fracture behavior of epoxy nanocomposites modified with polyol diluent and amino-functionalized multi-walled carbon nanotubes: A loading rate study.* Composites Part A: Applied Science and Manufacturing, 2014. 59: p. 57-69.
46. Miao, C., Du, H., Zhang, X., and Tippur, H.V., *Dynamic crack initiation and growth in cellulose nanopaper.* Cellulose, 2022. 29(1): p. 557-569.
47. Jajam, K.C., Bird, S.A., Auad, M.L., and Tippur, H.V., *Tensile, fracture and impact behavior of transparent Interpenetrating Polymer Networks with polyurethane-poly (methyl methacrylate).* Polymer Testing, 2013. 32(5): p. 889-900.
48. Sharafisafa, M., Aliabadian, Z., and Shen, L., *Crack initiation and failure development in bimrocks using digital image correlation under dynamic load.* Theoretical and Applied Fracture Mechanics, 2020. 109: p. 102688.
49. Kirugulige, M.S. and Tippur, H.V., *Measurement of fracture parameters for a mixed-mode crack driven by stress waves using image correlation technique and high-speed digital photography.* Strain, 2009. 45(2): p. 108-122.
50. Lee, D., Tippur, H., Kirugulige, M., and Bogert, P., *Experimental study of dynamic crack growth in unidirectional graphite/epoxy composites using digital image correlation method and high-speed photography.* Journal of composite materials, 2009. 43(19): p. 2081-2108.
51. Makki, E.A., Parrikar, P.N., and Shukla, A., *Response of coated laminated glass panels subjected to combined blast and temperature loadings.* Journal of Dynamic Behavior of Materials, 2015. 1(4): p. 409-422.
52. Aliabadian, Z., Sharafisafa, M., Tahmasebinia, F., and Shen, L., *Experimental and numerical investigations on crack development in 3D printed rock-like specimens with pre-existing flaws.* Engineering Fracture Mechanics, 2021. 241: p. 107396.
53. Periasamy, C. and Tippur, H.V., *Full-field digital gradient sensing method for evaluating stress gradients in transparent solids.* Applied Optics, 2012. 51(12): p. 2088-2097.DOI: https://doi.org/10.1364/AO.51.002088.

54. Periasamy, C. and Tippur, H.V., *Measurement of orthogonal stress gradients due to impact load on a transparent sheet using digital gradient sensing method.* Experimental Mechanics, 2013. 53(1): p. 97-111.
55. Jain, A.S. and Tippur, H.V., *Mapping Static and Dynamic Crack-Tip Deformations Using Reflection-Mode Digital Gradient Sensing: Applications to Mode-I and Mixed-Mode Fracture.* Journal of Dynamic Behavior of Materials, 2015. 1: p. 315-329.DOI: https://doi.org/10.1007/s40870-015-0024-4.
56. Jain, A.S. and Tippur, H.V., *Extension of reflection-mode digital gradient sensing method for visualizing and quantifying transient deformations and damage in solids.* Optics and Lasers in Engineering, 2016. 77: p. 162-174.
57. Sundaram, B.M. and Tippur, H.V., *Dynamics of crack penetration vs. branching at a weak interface: an experimental study.* Journal of the Mechanics and Physics of Solids, 2016. 96: p. 312-332.
58. Sundaram, B.M. and Tippur, H.V., *Full-field measurement of contact-point and crack-tip deformations in soda-lime glass. Part-II: Stress wave loading.* International Journal of Applied Glass Science, 2018. 9(1): p. 123-136.
59. Miao, C. and Tippur, H.V., *Measurement of sub-micron deformations and stresses at microsecond intervals in laterally impacted composite plates using digital gradient sensing.* Journal of Dynamic Behavior of Materials, 2018. 4(3): p. 336-358.
60. Miao, C. and Tippur, H.V., *Fracture behavior of carbon fiber reinforced polymer composites: an optical study of loading rate effects.* Engineering Fracture Mechanics, 2019. 207: p. 203-221.
61. Mason, J.J., Lambros, J., and Rosakis, A.J., *The use of a coherent gradient sensor in dynamic mixed-mode fracture mechanics experiments.* Journal of the Mechanics and Physics of Solids, 1992. 40(3): p. 641-661.DOI: https://doi.org/10.1016/0022-5096(92)80007-D.
62. Guo, Z.K., Kobayashi, A.S., and Hawkins, N.M., *Dynamic mixed mode fracture of concrete.* International Journal of Solids and Structures, 1995. 32(17): p. 2591-2607.DOI: https://doi.org/10.1016/0020-7683(94)00284-4.
63. Kirugulige, M.S. and Tippur, H.V., *Mixed-mode dynamic crack growth in functionally graded glass-filled epoxy.* Experimental mechanics, 2006. 46: p. 269-281.DOI: https://doi.org/10.1007/s11340-006-5863-4.
64. Kirugulige, M. and Tippur, H.V., *Mixed-Mode Dynamic Crack Growth in a Functionally Graded Particulate Composite: Experimental Measurements and Finite Element Simulations.* Journal of Applied Mechanics, 2008. 75(5).DOI: https://doi.org/10.1115/1.2932095.
65. Sundaram, B.M. and Tippur, H.V., *Dynamic mixed-mode fracture behaviors of PMMA and polycarbonate.* Engineering Fracture Mechanics, 2017. 176: p. 186-212.DOI: https://doi.org/10.1016/j.engfracmech.2017.02.029.
66. Braunagel, M.J. and Griffith, W.A., *Microstructural controls on mixed mode dynamic fracture propagation in crystalline and porous granular rocks.* Journal of Geophysical Research: Solid Earth, 2022. 127(3): p. e2021JB022528.DOI: https://doi.org/10.1029/2021JB022528.
67. Snow, T., Woolley, W., Metcalf, R.M., Rosenberg, J., Acevedo, C., and Kingstedt, O.T., *Effect of collagen damage induced by heat treatment on the mixed-mode fracture behavior*

of bovine cortical bone under elevated loading rates. International Journal of Fracture Mechanics, 2022. 233(1): p. 85-101.DOI: https://doi.org/10.1007/s10704-021-00612-0.
68. Aliha, M.R.M., Samareh-Mousavi, S.S., and Mirsayar, M.M., *Loading rate effect on mixed mode I/II brittle fracture behavior of PMMA using inclined cracked SBB specimen.* International Journal of Solids and Structures, 2021. 232: p. 111177.DOI: https://doi.org/10.1016/j.ijsolstr.2021.111177.
69. Morales, R.C., Baek, J., Sharp, D., Aderounmu, A., Wei, H., Chen, J.S., and Eliasson, V., *Mode-II Fracture Response of PMMA Under Dynamic Loading Conditions.* Journal of Dynamic Behavior of Materials, 2022. 8(1): p. 104-121.DOI: https://doi.org/10.1007/s40870-021-00320-9.
70. Aliha, M.R.M. and Bahmani, A., *Rock fracture toughness study under mixed mode I/III loading.* Rock Mechanics and Rock Engineering, 2017. 50(7): p. 1739-1751.DOI: https://doi.org/10.1007/s00603-017-1201-7.
71. Asareh, I., Yoon, Y.C., and Song, J.H., *A numerical method for dynamic fracture using the extended finite element method with non-nodal enrichment parameters.* International Journal of Impact Engineering, 2018. 121: p. 63-76.DOI: https://doi.org/10.1016/j.ijimpeng.2018.06.012.
72. Imachi, M., Tanaka, S., and Bui, T.Q., *Mixed-mode dynamic stress intensity factors evaluation using ordinary state-based peridynamics.* Theoretical and Applied Fracture Mechanics, 2018. 93: p. 97-104.DOI: https://doi.org/10.1016/j.tafmec.2017.07.008.
73. Cheng, Z., Zhang, G., Wang, Y., and Bobaru, F., *A peridynamic model for dynamic fracture in functionally graded materials.* Composite Structures, 2015. 133: p. 529-546.DOI: https://doi.org/10.1016/j.compstruct.2015.07.047.
74. Grégoire, D., Maigre, H., Réthoré, J., and Combescure, A., *Dynamic crack propagation under mixed-mode loading–comparison between experiments and X-FEM simulations.* International Journal of Solids and Structures, 2007. 44(20): p. 6517-6534.DOI: https://doi.org/10.1016/j.ijsolstr.2007.02.044.
75. Kidane, A., Chalivendra, V.B., Shukla, A., and Chona, R., *Mixed-mode dynamic crack propagation in graded materials under thermo-mechanical loading.* Engineering fracture mechanics, 2010. 77(14): p. 2864-2880.DOI: https://doi.org/10.1016/j.engfracmech.2010.07.004.
76. Ruiz, G., Pandolfi, A., and Ortiz, M., *Three-dimensional cohesive modeling of dynamic mixed-mode fracture.* International Journal for Numerical Methods in Engineering, 2001. 52(1-2): p. 97-120.DOI: https://doi.org/10.1002/nme.273.
77. Field, J.E., *Brittle fracture: its study and application.* Contemporary Physics, 1971. 12(1): p. 1-31.
78. Ravi-Chandar, K. and Knauss, W.G., *An experimental investigation into dynamic fracture: II. Microstructural aspects.* International Journal of Fracture, 1984. 26(1): p. 65-80.
79. Ravi-Chandar, K. and Knauss, W.G., *An experimental investigation into dynamic fracture: IV. On the interaction of stress waves with propagating cracks.* International Journal of Fracture, 1984. 26(3): p. 189-200.
80. Ramulu, M. and Kobayashi, A.S., *Mechanics of crack curving and branching—a dynamic fracture analysis*, in *Dynamic fracture*. 1985, Springer. p. 61-75.
81. Yoffe, E.H., *LXXV. The moving griffith crack.* The London, Edinburgh, and Dublin Philosophical Magazine and Journal of Science, 1951. 42(330): p. 739-750.

82. Congleton, J. and Fetch, N.J., *Crack-branching.* Philosophical Magazine, 1967. 16(142): p. 749-760.
83. Sharon, E., Gross, S.P., and Fineberg, J., *Local crack branching as a mechanism for instability in dynamic fracture.* Physical Review Letters, 1995. 74(25): p. 5096.
84. Xu, D., Liu, Z., Liu, X., Zeng, Q., and Zhuang, Z., *Modeling of dynamic crack branching by enhanced extended finite element method.* Computational Mechanics, 2014. 54(2): p. 489-502.
85. Bobaru, F. and Zhang, G., *Why do cracks branch? A peridynamic investigation of dynamic brittle fracture.* International Journal of Fracture, 2015. 196(1-2): p. 59-98.
86. Bieniawski, Z.T., *Fracture dynamics of rock.* International Journal of Fracture Mechanics, 1968. 4(4): p. 415-430.
87. Schardin, H., *Velocity effects in fracture.* Fracture (Edited by Averbach et al.), John Wiley, 1959.
88. Eshelby, J.D., *Energy relations and the energy-momentum tensor in continuum mechanics*, in *Fundamental contributions to the continuum theory of evolving phase interfaces in solids*. 1999. p. 82-119.
89. Xu, X.P. and Needleman, A., *NUMERICAL SIMULATIONS OF FAST CRACK-GROWTH IN BRITTLE SOLIDS.* Journal of the Mechanics and Physics of Solids, 1994. 42(9): p. 1397-&.DOI: 10.1016/0022-5096(94)90003-5.
90. Zhou, F. and Molinari, J.F., *Dynamic crack propagation with cohesive elements: a methodology to address mesh dependency.* International Journal for Numerical Methods in Engineering, 2004. 59(1): p. 1-24.
91. Zeng, Q., Motamedi, M.H., Leong, A.F.T., Daphalapurkar, N.P., Hufnagel, T.C., and Ramesh, K.T., *Validated simulations of dynamic crack propagation in single crystals using EFEM and XFEM.* International Journal of Fracture, 2019. 215(1-2): p. 49-65.
92. Karma, A. and Lobkovsky, A.E., *Unsteady crack motion and branching in a phase-field model of brittle fracture.* Physical review letters, 2004. 92(24): p. 245510.
93. Ha, Y.D. and Bobaru, F., *Studies of dynamic crack propagation and crack branching with peridynamics.* International Journal of Fracture, 2010. 162(1-2): p. 229-244.
94. Wiederhorn, S.M. and Townsend, P.R., *Crack healing in glass.* Journal of the American ceramic society, 1970. 53(9): p. 486-489.
95. Michalske, T.A. and Fuller Jr, E.R., *Closure and repropagation of healed cracks in silicate glass.* Journal of the American Ceramic Society, 1985. 68(11): p. 586-590.
96. Stavrinidis, B. and Holloway, D.G., *Crack healing in glass.* 1983. 24(1): p. 19-25.
97. Wiederhorn, S.M., *Subcritical crack growth in ceramics*, in *Fracture mechanics of ceramics*. 1974, Springer. p. 613-646.
98. Munz, D. and Fett, T., *Ceramics: mechanical properties, failure behaviour, materials selection*. Vol. 36. 1999: Springer Science & Business Media.
99. Wiederhorn, S.M., *Influence of water vapor on crack propagation in soda-lime glass.* Journal of the American Ceramic Society, 1967. 50(8): p. 407-414.
100. To, T., Célarié, F., Roux-Langlois, C., Bazin, A., Gueguen, Y., Orain, H., Le Fur, M., Burgaud, V., and Rouxel, T., *Fracture toughness, fracture energy and slow crack growth of glass as investigated by the Single-Edge Precracked Beam (SEPB) and Chevron-Notched Beam (CNB) methods.* Acta Materialia, 2018. 146: p. 1-11.

101. Ferretti, D., Rossi, M., and Royer-Carfagni, G., *An ESPI experimental study on the phenomenon of fracture in glass. Is it brittle or plastic?* Journal of the Mechanics and Physics of Solids, 2011. 59(7): p. 1338-1354.
102. Singh, B.K., Mehta, D.S., and Senthilkumaran, P., *Interferometric visualization of crack growth in glass plate.* Applied Physics B, 2019. 125(2): p. 21.
103. Sundaram, B.M. and Tippur, H.V., *Full-field measurement of contact-point and crack-tip deformations in soda-lime glass. Part-I: Quasi-static Loading.* International Journal of Applied Glass Science, 2018. 9(1): p. 114-122.DOI: https://doi.org/10.1111/ijag.12278.
104. Harmuth, H., Rieder, K., Krobath, M., and Tschegg, E., *Investigation of the nonlinear fracture behaviour of ordinary ceramic refractory materials.* Materials Science and Engineering: A, 1996. 214(1-2): p. 53-61.
105. Brühwiler, E. and Wittmann, F.H., *The wedge splitting test, a new method of performing stable fracture mechanics tests.* Engineering fracture mechanics, 1990. 35(1-3): p. 117-125.
106. Korte, S., Boel, V., De Corte, W., and De Schutter, G., *Static and fatigue fracture mechanics properties of self-compacting concrete using three-point bending tests and wedge-splitting tests.* Construction and Building Materials, 2014. 57: p. 1-8.
107. Walter, R., Østergaard, L., Olesen, J.F., and Stang, H., *Wedge splitting test for a steel–concrete interface.* Engineering fracture mechanics, 2005. 72(17): p. 2565-2583.
108. Vargas, R., Neggers, J., Canto, R.B., Rodrigues, J.A., and Hild, F., *Analysis of wedge splitting test on refractory castable via integrated DIC.* Journal of the European Ceramic Society, 2016. 36(16): p. 4309-4317.
109. Dai, Y., Gruber, D., and Harmuth, H., *Determination of the fracture behaviour of MgO-refractories using multi-cycle wedge splitting test and digital image correlation.* Journal of the European Ceramic Society, 2017. 37(15): p. 5035-5043.
110. Kobayashi, A.S., *Handbook on Experimental Mechanics*. 2 ed.: VCH.
111. Bruck, H.A., McNeill, S.R., Sutton, M.A., and Peters, W.H., *Digital image correlation using Newton-Raphson method of partial differential correction.* Experimental mechanics, 1989. 29(3): p. 261-267.
112. Chen, B. and Jungstedt, E., *Fast and large-converge-radius inverse compositional Levenberg–Marquardt algorithm for digital image correlation: principle, validation, and open-source toolbox.* Optics and Lasers in Engineering, 2022. 151: p. 106930.
113. Yoneyama, S., *Basic principle of digital image correlation for in-plane displacement and strain measurement.* Advanced Composite Materials, 2016. 25(2): p. 105-123.
114. Born, M. and Wolf, E., *Principles of optics: electromagnetic theory of propagation, interference and diffraction of light*. 2013: Elsevier.
115. Bradley, W.B. and Kobayashi, A.S., *Fracture dynamics—a photoelastic investigation.* Engineering Fracture Mechanics, 1971. 3(3): p. 317-332.DOI: https://doi.org/10.1016/0013-7944(71)90041-5.
116. Prautzsch, H., Boehm, W., and Paluszny, M., *Bézier and B-spline techniques*. 2013: Springer Science & Business Media.
117. Budynas, R.G., *Advanced strength and applied stress analysis*. 1977: McGraw-Hill Science, Engineering & Mathematics.
118. Chao, Y.J., Luo, P.F., and Kalthoff, J.F., *An experimental study of the deformation fields around a propagating crack tip.* Experimental mechanics, 1998. 38(2): p. 79-85.

119. Kirugulige, M.S., Tippur, H.V., and Denney, T.S., *Measurement of transient deformations using digital image correlation method and high-speed photography: application to dynamic fracture.* Applied optics, 2007. 46(22): p. 5083-5096.
120. Abanto-Bueno, J. and Lambros, J., *Investigation of crack growth in functionally graded materials using digital image correlation.* Engineering Fracture Mechanics, 2002. 69(14-16): p. 1695-1711.
121. Lopez-Crespo, P., Shterenlikht, A., Patterson, E.A., Yates, J.R., and Withers, P.J., *The stress intensity of mixed mode cracks determined by digital image correlation.* The Journal of Strain Analysis for Engineering Design, 2008. 43(8): p. 769-780.
122. Yoneyama, S., Morimoto, Y., and Takashi, M., *Automatic evaluation of mixed-mode stress intensity factors utilizing digital image correlation.* Strain, 2006. 42(1): p. 21-29.
123. Mathieu, F., Hild, F., and Roux, S., *Identification of a crack propagation law by digital image correlation.* International Journal of Fatigue, 2012. 36(1): p. 146-154.
124. Peters, W.H. and Ranson, W.F., *Digital imaging techniques in experimental stress analysis.* Optical engineering, 1982. 21(3): p. 427-431.
125. Yoneyama, S., Ogawa, T., and Kobayashi, Y., *Evaluating mixed-mode stress intensity factors from full-field displacement fields obtained by optical methods.* Engineering fracture mechanics, 2007. 74(9): p. 1399-1412.
126. Jin, H. and Bruck, H.A., *Pointwise digital image correlation using genetic algorithms.* Experimental Techniques, 2005. 29(1): p. 36-39.
127. Poissant, J. and Barthelat, F., *A novel "subset splitting" procedure for digital image correlation on discontinuous displacement fields.* Experimental mechanics, 2010. 50(3): p. 353-364.
128. Sundaram, B.M. and Tippur, H.V., *Dynamic crack growth normal to an interface in bi-layered materials: an experimental study using digital gradient sensing technique.* Experimental Mechanics, 2016. 56(1): p. 37-57.
129. Rose, L.R.F., *Recent theoretical and experimental results on fast brittle fracture.* International Journal of Fracture, 1976. 12(6): p. 799-813.
130. Zimmermann, E.A., Launey, M.E., Barth, H.D., and Ritchie, R.O., *Mixed-mode fracture of human cortical bone.* Biomaterials, 2009. 30(29): p. 5877-5884.DOI: https://doi.org/10.1016/j.biomaterials.2009.06.017.
131. Nie, X., Chen, W.W., Sun, X., and Templeton, D.W., *Dynamic failure of borosilicate glass under compression/shear loading experiments.* Journal of the American Ceramic Society, 2007. 90(8): p. 2556-2562.DOI: https://doi.org/10.1111/j.1551-2916.2007.01819.x.
132. Tan, S., Yao, X., Long, S., Zhang, X., and Zang, S., *Static and dynamic strength of soda-lime glass under combined compression-shear loading.* Journal of Non-Crystalline Solids, 2019. 516: p. 14-25.DOI: https://doi.org/10.1016/j.jnoncrysol.2019.04.024.
133. Lim, I.L., Johnston, I.W., Choi, S.K., and Boland, J.N., *Fracture testing of a soft rock with semi-circular specimens under three-point bending. Part 2—mixed-mode.* International Journal of Rock Mechanics and Mining Sciences & Geomechanics Abstracts, 1994. 31(3): p. 199-212.DOI: https://doi.org/10.1016/0148-9062(94)90464-2.
134. Mirsayar, M.M., Razmi, A., and Berto, F., *Tangential strain-based criteria for mixed-mode I/II fracture toughness of cement concrete.* Fatigue & Fracture of Engineering Materials & Structures, 2018. 41(1): p. 129-137.DOI: https://doi.org/10.1111/ffe.12665.

135. Mirsayar, M.M., Razmi, A., Aliha, M.R.M., and Berto, F., *EMTSN criterion for evaluating mixed mode I/II crack propagation in rock materials.* Engineering Fracture Mechanics, 2018. 190: p. 186-197.DOI: https://doi.org/10.1016/j.engfracmech.2017.12.014.
136. Erdogan, F. and Sih, G.C., *On the Crack Extension in Plates Under Plane Loading and Transverse Shear.* Journal of Basic Engineering, 1963. 85(4): p. 519-525.DOI: https://doi.org/10.1115/1.3656897.
137. Sun, C.T. and Jin, Z.H., *Chapter 5 - Mixed Mode Fracture*, in *Fracture Mechanics*, C.T. Sun and Z.H. Jin, Editors. 2012, Academic Press: Boston. p. 105-121.
138. Miao, C. and Tippur, H.V., *Dynamic Fracture of Soda-lime Glass Plates Studied using Two Modified Digital Gradient Sensing Techniques.* Engineering Fracture Mechanics, 2020: p. 107048.
139. Chao, Y.J., Liu, S., and Broviak, B.J., *Brittle fracture: variation of fracture toughness with constraint and crack curving under mode I conditions.* Experimental mechanics, 2001. 41(3): p. 232-241.
140. Ramulu, M. and Kobayashi, A.S., *Dynamic crack curving—a photoelastic evaluation.* Experimental Mechanics, 1983. 23(1): p. 1-9.
141. Cotterell, B. and Rice, J.R., *Slightly curved or kinked cracks.* International journal of fracture, 1980. 16(2): p. 155-169.
142. Ravi-Chandar, K., *Dynamic fracture*. 2004: Elsevier.
143. Arakawa, K. and Takahashi, K., *Relationships between fracture parameters and fracture surface roughness of brittle polymers.* International Journal of Fracture, 1991. 48(2): p. 103-114.
144. Hull, D., *Influence of stress intensity and crack speed on fracture surface topography: mirror to mist to macroscopic bifurcation.* Journal of materials science, 1996. 31(17): p. 4483-4492.
145. Takahashi, K., Kido, M., and Arakawa, K., *Fracture roughness evolution during mode I dynamic crack propagation in brittle materials.* International journal of fracture, 1998. 90(1-2): p. 119-131.
146. Dondeti, S. and Tippur, H.V., *Crack initiation and slow growth in soda-lime glass from a self-healed crack.* Theoretical and Applied Fracture Mechanics, 2022. 119: p. 103341.DOI: https://doi.org/10.1016/j.tafmec.2022.103341.
147. *ALON® Optical Ceramic's Key Features*. Available from: http://www.surmet.com/technology/alon-optical-ceramics/index.php.

Appendix A

A.1 Dynamic fracture of SLG bilayers

Dynamic fracture of SLG bilayer specimens made with Eastman Saflex® RB11 Clear PVB (Polyvinyl Butyral) interlayer was studied using full-field optical method DGS under stress wave loading. The experimental setup used was similar to dynamic fracture studied in monolithic SLG specimens, see section 3.4. A 5.7 mm thick SLG specimen of 100 mm × 150 mm was machined from larger sheet and a 0.38 mm thick PVB film was introduced between layer-I and layer-II. Material properties of PVB film are provided in Table A1. SLG specimen edges were smoothed on the 100 mm × 7.5 mm surface using a rotary table grinder. The laminates were prepared by bonding a stack consisting of layer-I (SLG), PVB film, layer-II (SLG), each butted against the other. This assembly was placed in an oven and heated to 130°C for 40 minutes. During processing, the oven chamber was evacuated to remove any air bubbles along the interface. After cooling, a 40° V-notch was introduced into layer-I and that notch was further extended by 8 mm as in the monolithic SLG experiments. The interface was located at a distance of 11 mm from the initial machined notch in each specimen.

Table A1 - Some relevant PVB film properties

Parameter	Value	Units
Film thickness	0.38	mm
Elastic modulus, E	1.56	MPa
Tensile strength, σ_t	27	MPa
Poisson's ratio, υ	0.5	-
Refractive index, n	1.478	-

This resulted in 38 mm and 62 mm wide layer-I and layer-II planar specimens. Three different striker velocities, V = 2.5 m/s, 4.2 m/s, 5.6 m/s were used to study the dynamic crack growth behavior and the resulting fractured bilayers, shown in Figure A1. The heavy black arrow in Figure A1 represents crack growth direction towards the PVB interface.

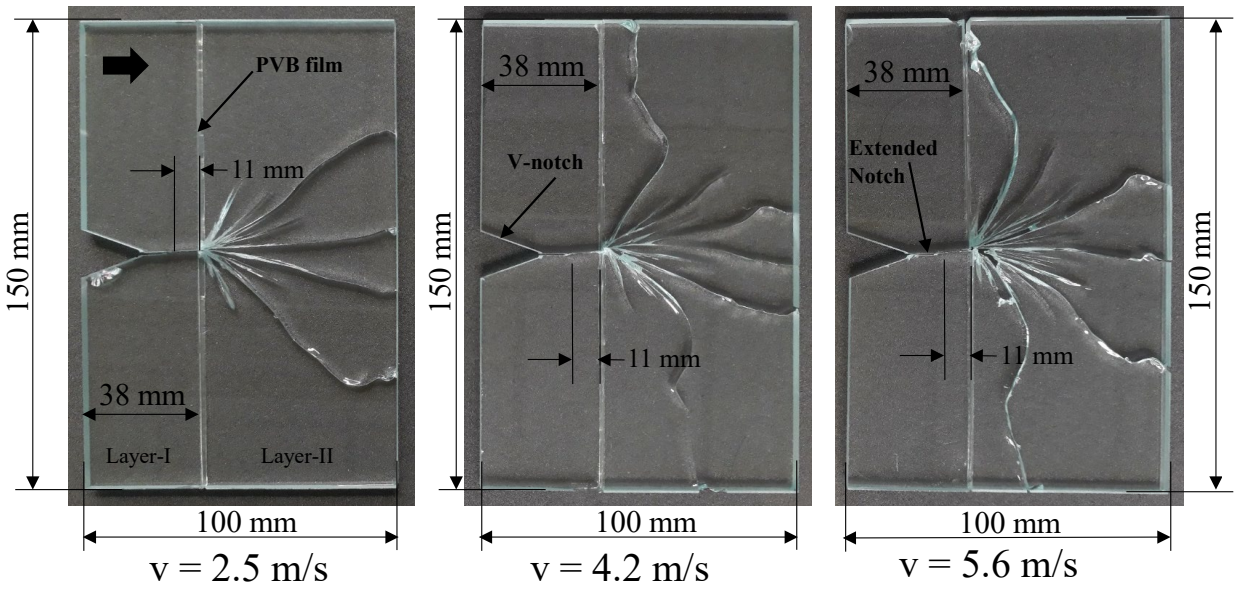

Figure A1: Fractured SLG bilayer with PVB interface subjected to striker velocities, V = 2.5 m/s, 4.2 m/s, 5.6 m/s.

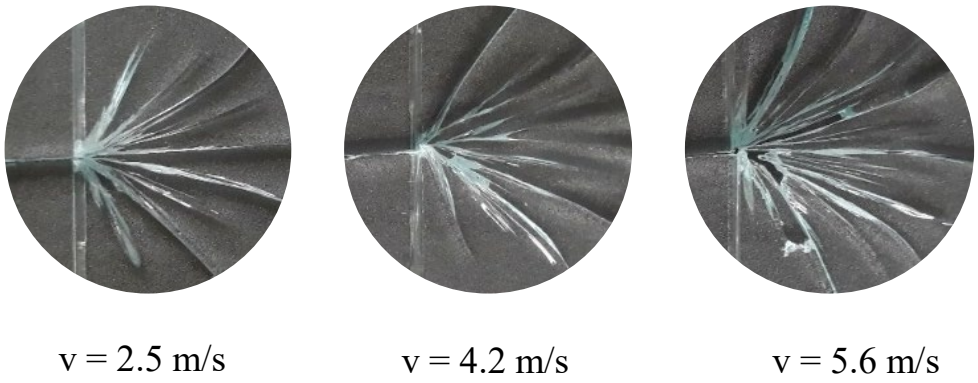

Figure A2: Palm-tree cracking pattern emanating from PVB film interface in SLG bilayer subjected to striker velocities, V = 2.5 m/s, 4.2 m/s, 5.6 m/s respectively.

Due to the dynamic load acting on the specimen, once the crack initated at the initial notch-tip, it approached the interface and then got arrested momentarily. During this arrested state, the energy accumulated at the crack tip. When the accurmulated crack tip energy at the interface was released, it produced multiple branches. Interestingly, the branched cracks resembled a symmetric palm-tree structure relative to the mother crack, as shown in Figure A2. It can be observed that the number of cracks increased with striker vlocity. The number of crack branches for striker velocities, V = 2.5 m/s, 4.2 m/s, 5.6 m/s were 9, 11 and 13, respectively. To visualize the dynamic crack tip fields, DGS was implemented along with high-speed photography and the angular deflection contours of ϕ_x and ϕ_y for all three different striker velocities were obtained after correlating speckle images.

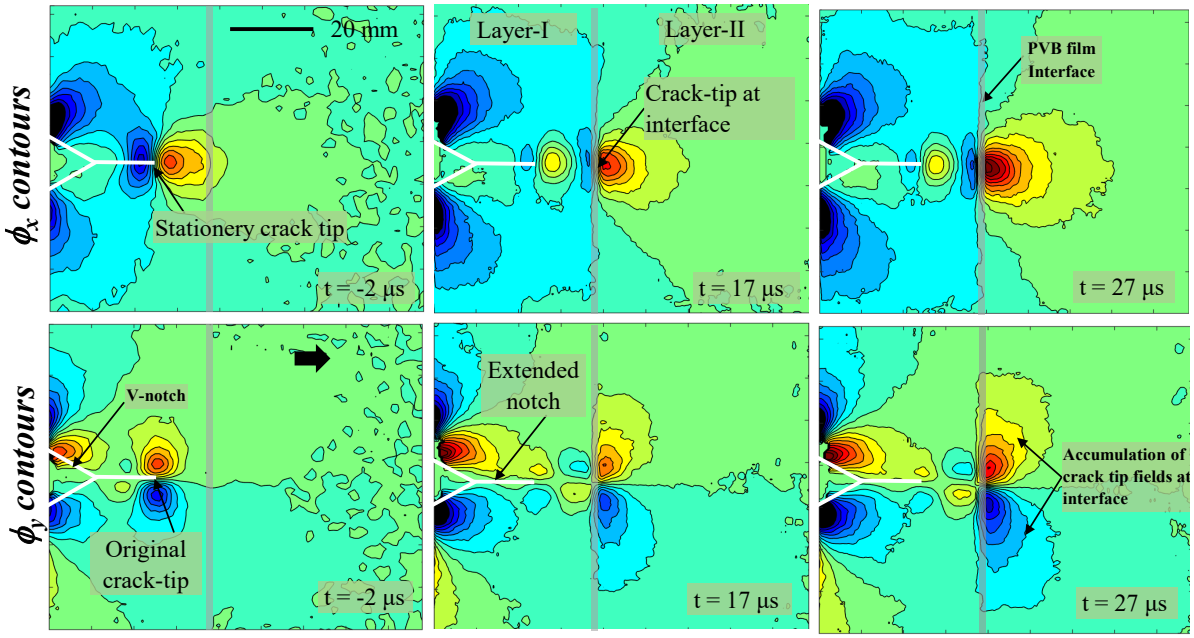

Figure A3: Angular deflection contours (contour interval = 10×10^{-6} rad) in 100 mm × 150 mm bilayer soda-lime glass plate subjected to 2.5 m/s striker velocity. The arrowhead (in the bottom left image) shows crack growth direction. (Time, t = 0 corresponds to crack initiation at the initial machined notch-tip.)

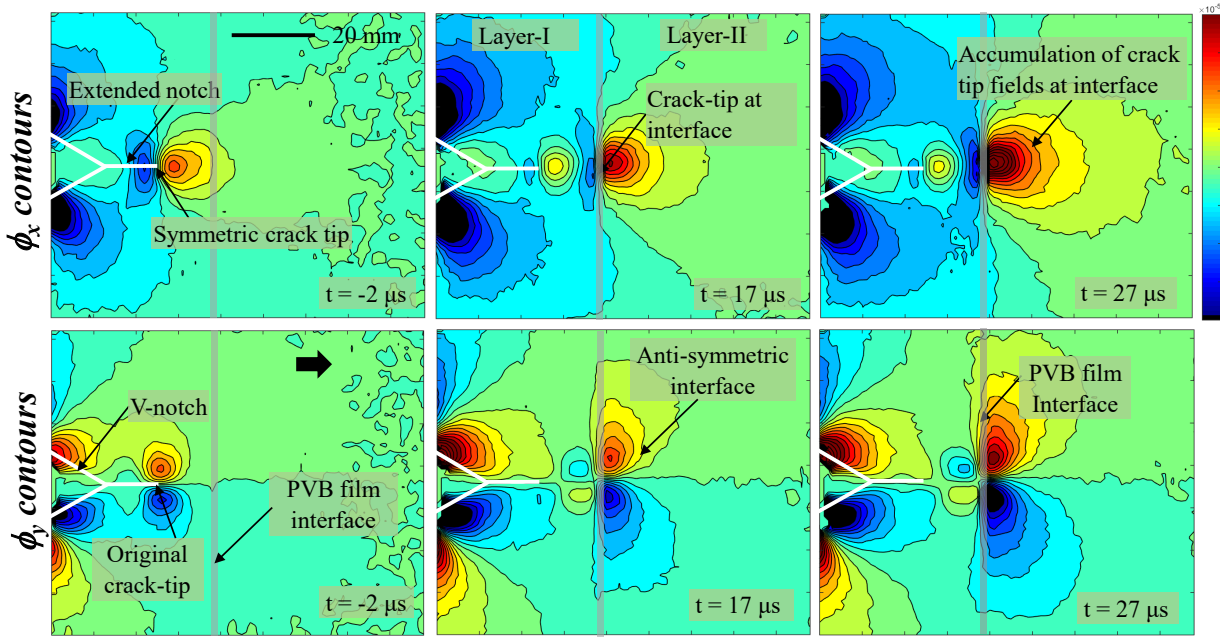

Figure A4: Angular deflection contours (contour interval = 10×10^{-6} rad) in 100 mm × 150 mm bilayer soda-lime glass plate subjected to 4.2 m/s striker velocity. The arrowhead (in the bottom left image) shows crack growth direction. (Time, t = 0 corresponds to crack initiation at the initial machined notch-tip.)

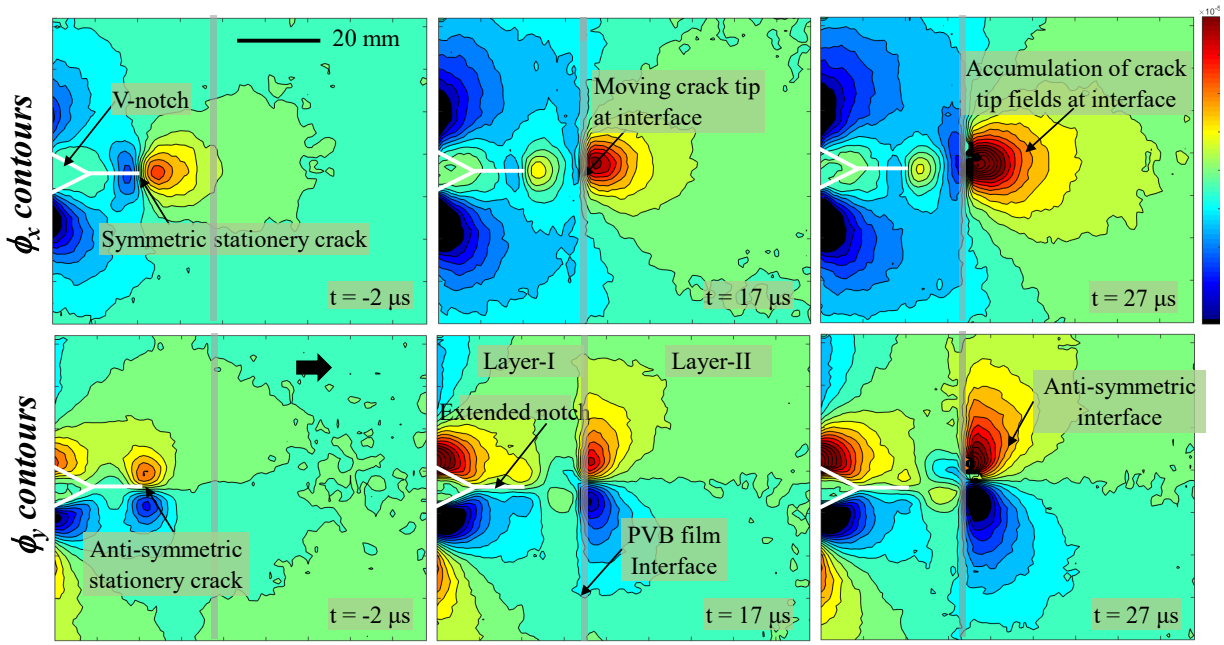

Figure A5: Angular deflection contours (contour interval = 10×10^{-6} rad) in 100 mm × 150 mm bilayer soda-lime glass plate subjected to 5.6 m/s striker velocity. The arrowhead (in the bottom left image) shows crack growth direction. (Time, t = 0 corresponds to crack initiation at the initial machined notch-tip.)

They are shown in Figure A3, Figure A4 and Figure A5. Here, time, $t = 0$ corresponds to crack initiation at the original machined notch-tip. Again, the ϕ_x and ϕ_y contours are symmetric and anti-symmetric, respectively, about the initial notch-tip prior to crack initiation, as observed in monolithic dynamic fracture experiments. With an increase in striker velocity, the number of contours also increased at the interface. Similarly, the number of cracks also increased with striker velocity as shown in Figure A2. The interface absorbed more energy with increase in striker velocity and in turn, the absorbed energy resulted in more number of cracks when it got released.

A.2 Dynamic fracture of ALON® using photoelasticity and DGS methods

Dynamic fracture of Surmet ALON® (Aluminum Oxynitride) was investigated using full-field optical method DGS and photoelasticity under dynamic loading. ALON has high strength, scratch resistance and is four times stiffer than SLG. It has excellent optical transparency and has greater potential for aerospace, space, semiconductor and defense applications [147]. A few mechanical and physical properties of ALON relevant to this work are listed in Table A2

Table A2 – Some relevant ALON properties

Property	**Value**
Density, ρ	3670 kg/m^3
Longitudinal wave speed, C_L	9543 m/s
Shear wave speed, C_S	6040 m/s
Rayleigh wave speed, C_R	5557 m/s
Elastic modulus, E	315 GPa
Poisson's ratio, υ	0.24
Tensile strength, σ_t	379 MPa
Compressive strength, σ_c	2677 MPa
Hardness (Knoop, 200g), HK	1850 (9 Mohr's scale) kg/mm^2
Coeffecient of thermal expansion	7.5×10^{-6} (30-900°C)

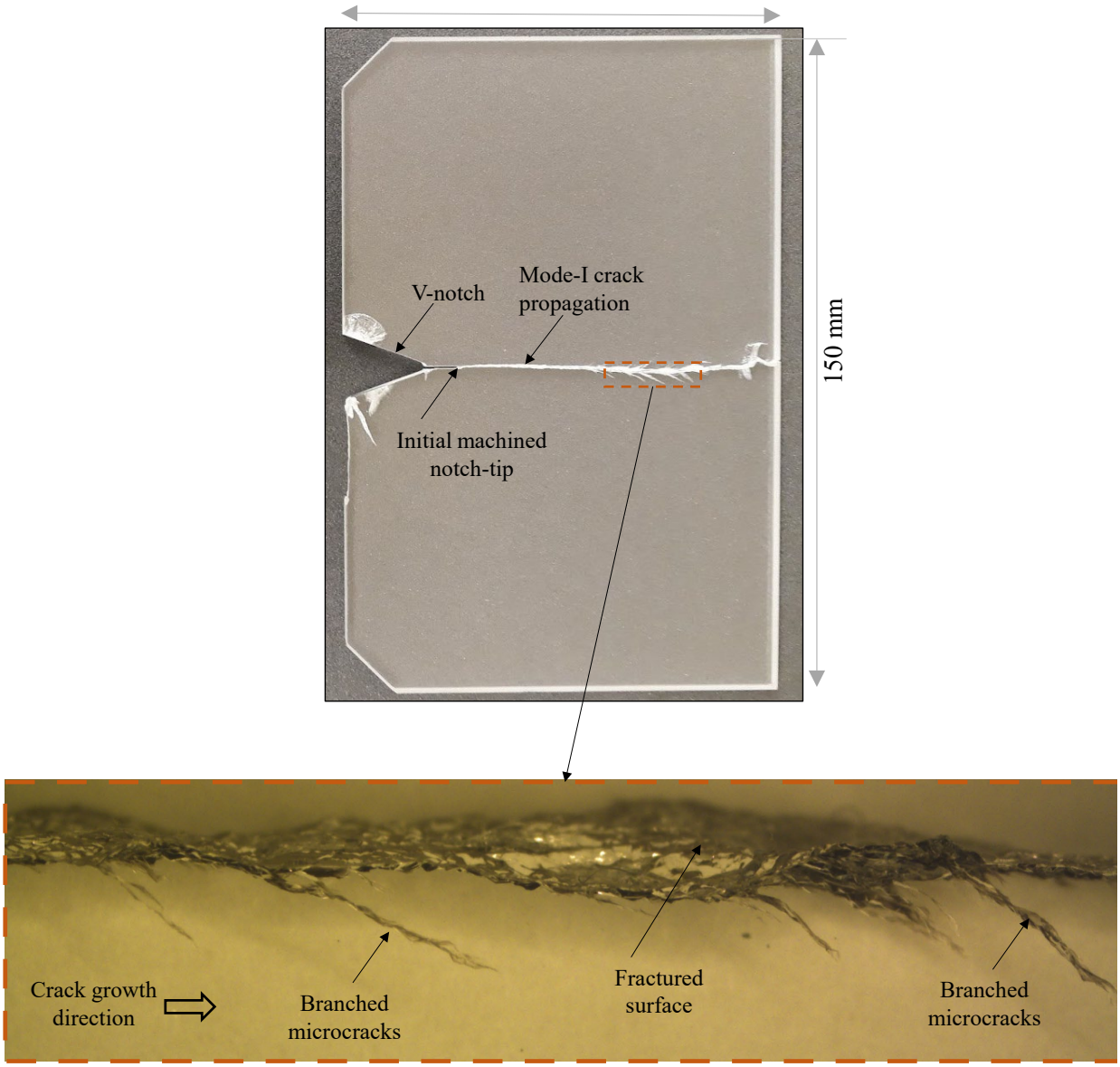

Figure A6: Re-assembled fractured ALON specimen used in DGS study along with magnified microcracks off the crack path.

A 5.6 mm thick planar ALON specimen of 100 mm × 150 mm size was machined with 40° V-notch and 8 mm notch was extended similar to the SLG specimen. The experimental setup for performing dynamic fracture tests is same as the one given in section 3.4. The resulting fractured specimen is show in Figure A6. Once the specimen subjected to stress wave loading, the crack initiated at the initial notch-tip location and propagated in a mode-I fashion and did not show

macroscale crack branching as observed in SLG counterparts. A few macroscale microbranches were observed after the crack propagated the middle of the specimen. A set of undeformed and deformed speckle image recorded by camera is also shown in Figure A7. The angular deflection contours for ϕ_x and ϕ_y did not show discernible crack tip fields due to the polycrystaline nature of ALON, but the concentrated contours at the V-notch were seen (see, Figure A8).

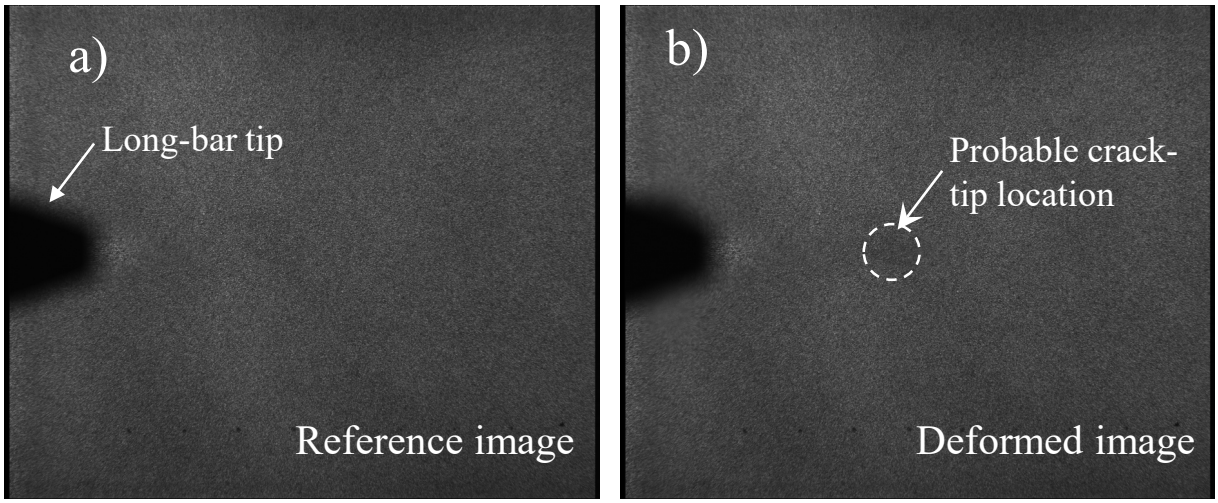

Figure A7: Speckle images recorded in ALON® using DGS method in a) reference state and b) deformed state for a dynamically propagating crack tip

Next, dynamic photoelastic experiments were conducted on ALON under nominally identical conditions used in the DGS counterpart. The re-assembled fratured specimen is shown in Figure A9. Similar tp DGS experiment, the crack intiiated from the machined notch-tip. But it propgated in a slightly mixed-mode fashion due assymetry in the loading at the v-notch flanks (see Figure A9).

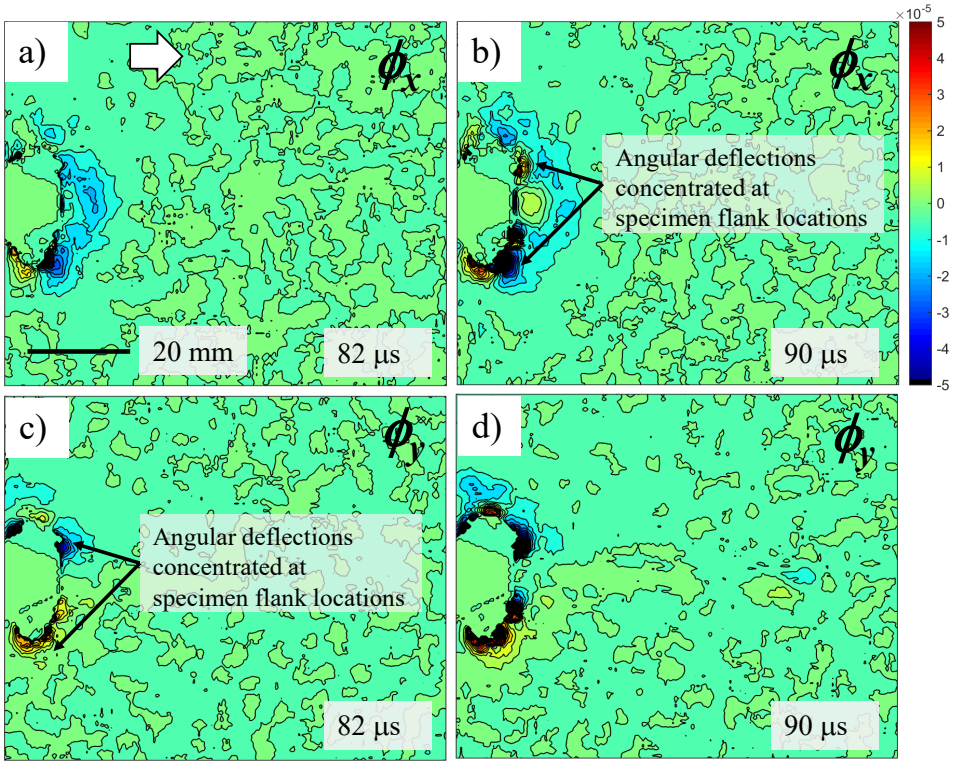

Figure A8: Angular deflection contours of light rays (contour increment = 5×10^{-6} rad) in ALON specimen subjected to dynamic loading. The arrow head in the top left image shows crack growth direction. (Time is zero for the first speckle image recorded by the camera.)

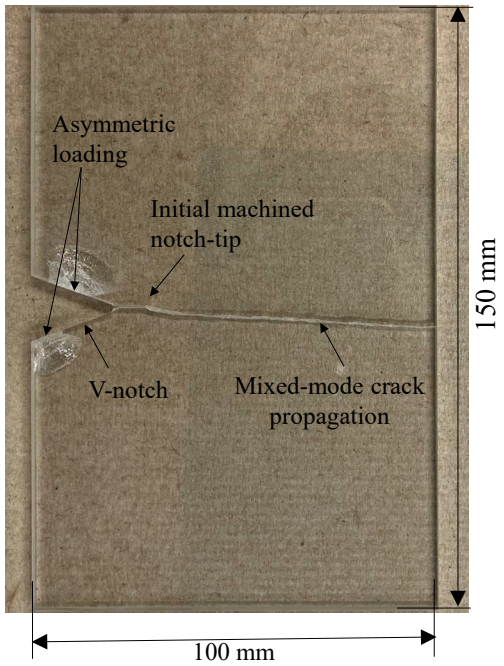

Figure A9: Re-assembled fractured ALON specimen used in photoelastic study.

Photoelasticfringes recorded by the ultrahigh-speed camera at 1 Mfps rate are shown in Figure A10.Figure A10(a) and (b) shows photoelastic fringes prior to crack initiation and at the early stages of crack intiation from the original notch-tip. Figure A10(c) and (d) correspond to the advanced stages of crack propagation.

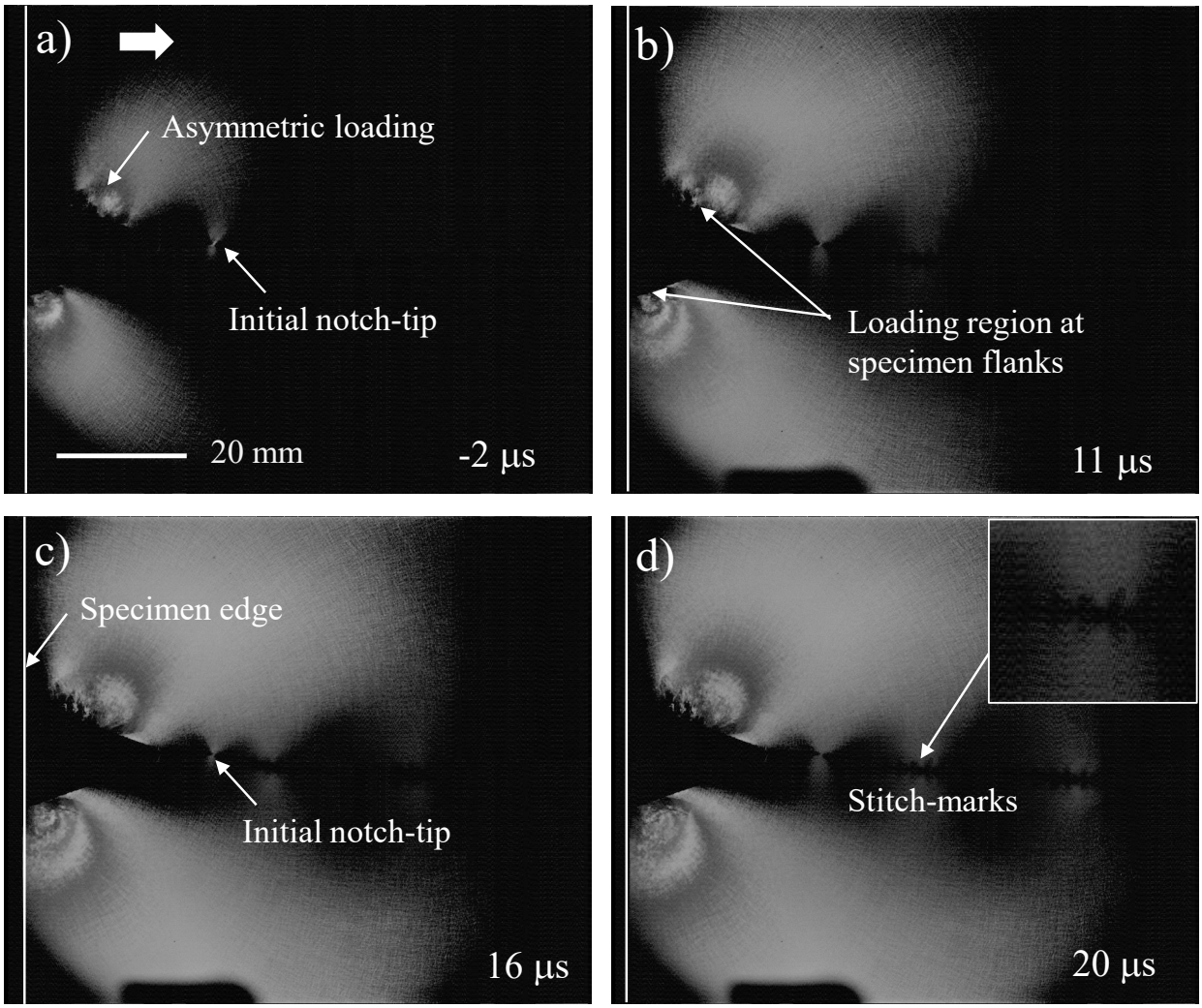

Figure A10: Photoelastic fringes in ALON specimen subjected to dynamic loading. Arrowhead in the top left image shows crack growth direction. (Time, $t = 0$ corresponds to crack initiation at the original notch-tip.)

The initial notch-tip location is readily evident from the recorded fringes. Further, stitch marks along the propagating crack flanks were also observed in ALON specimen, similar to SLG counterpart. From these dynamic photoelastic fringes, the crack tip locations were identified and

the crack velocity histories were obtained as shown in Figure A11. The crack velocity after initiation accelerated almost instantaneously to ~1500 m/s in the first microsecond. Later, the crack velocity increased gradually to ~2700 m/s towards the end of observation window, which is approx 70% faster than the max. crack speed observed in soda-lime glass.

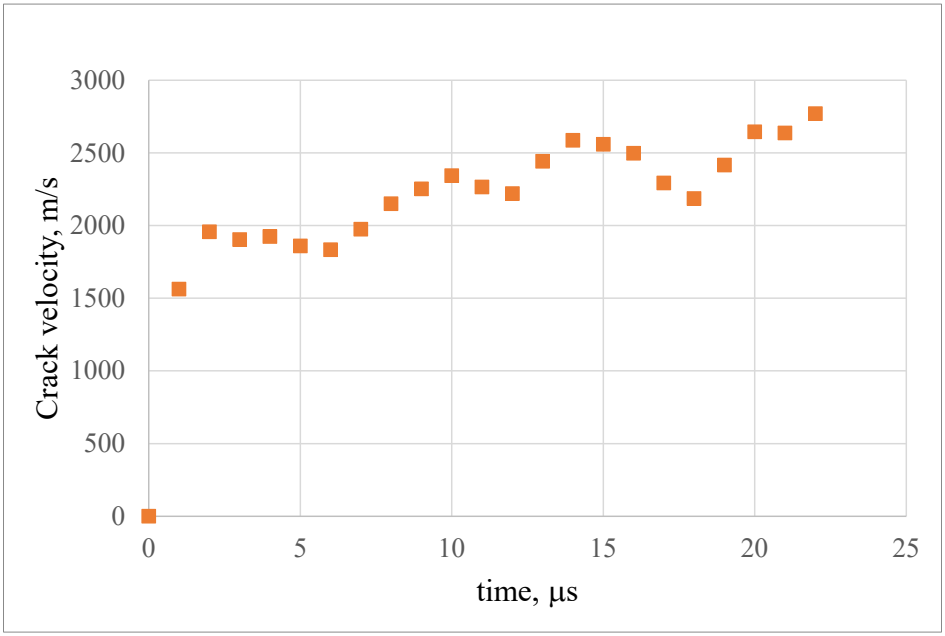

Figure A11: Apparent crack velocity history for ALON from photoelastic experiment. (Time, t = 0 corresponds to crack initiation at the original notch-tip.)

A.3 Edge-on-Impact (EOI) study on ALON® using photoelasticity and DIC methods

Subsequently, photoelastic experiments were conducted on 5.6 mm thick plate of 60 mm × 45 mm planar dimensions by applying an edge load using the long-bar. The made an areal contact at the center of the short edge of the specimen. The specimen was placed on a strip of putty to mitigate acoustic impedence issue and all the other edges were free to reflect the load except where the load was imposed. The experimental setup for performing dynamic fracture using photoelasticity is as shown in Figure A12. The striker velocity used in this experiment was ~8.2 m/s and the photoelastic fringes were captured at 1 Mfps using the ultrahigh-speed camera. The

resulting photoelastic fringes are shown in Figure A13. These results suggests that, photoelasticity can potentially be useful to study failure of ALON due to compressive loads.

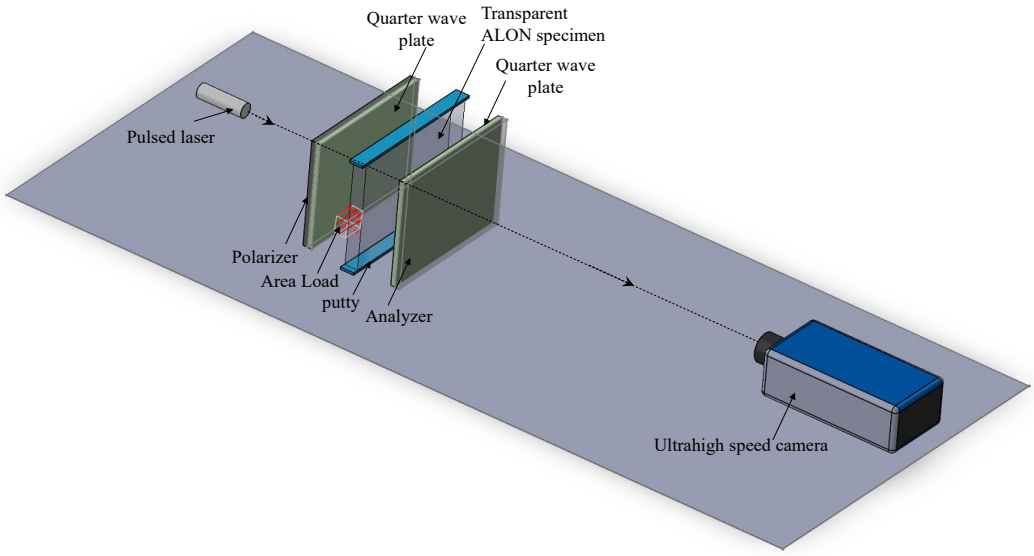

Figure A12: Schematic representation of dynamic load acting on ALON specimen using photoelasticity (dark-field circular polariscope). The load was applied using Hopkinson pressure bar making an area contact.

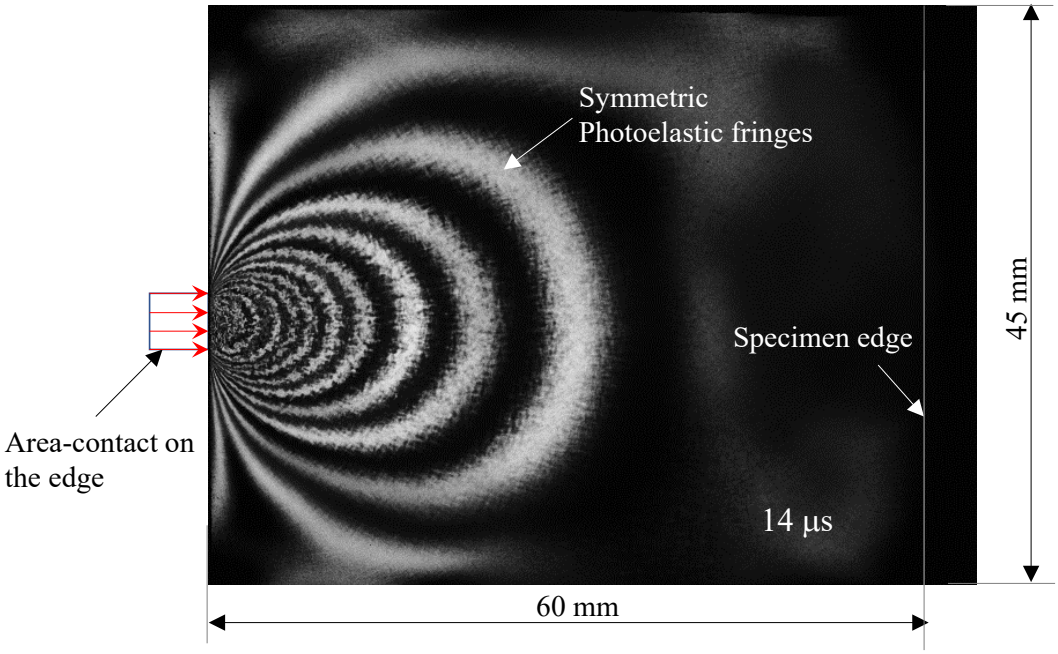

Figure A13: Photoelastic fringes in ALON specimen subjected to dynamic load at 14 µs after impact. Arrowheads (in the top left image) represents area load.

Finally DIC method was attempted to investigate dynamic fracutre in ALON. A single edge notch specimen of size 60 mm × 90 mm with a 10 mm notch was subjected to area contact using Hopkinson pressure bar. The re-assembled fractured specimen is shown in Figure A14.

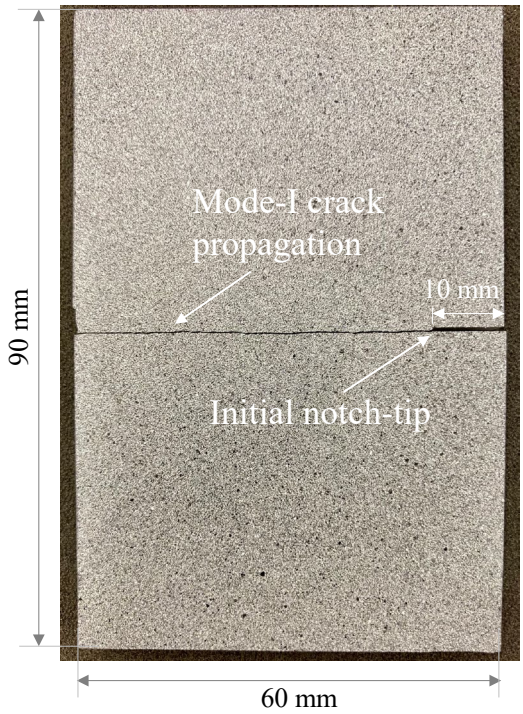

Figure A14: Re-assembled fractured ALON specimen used in DIC method.

.

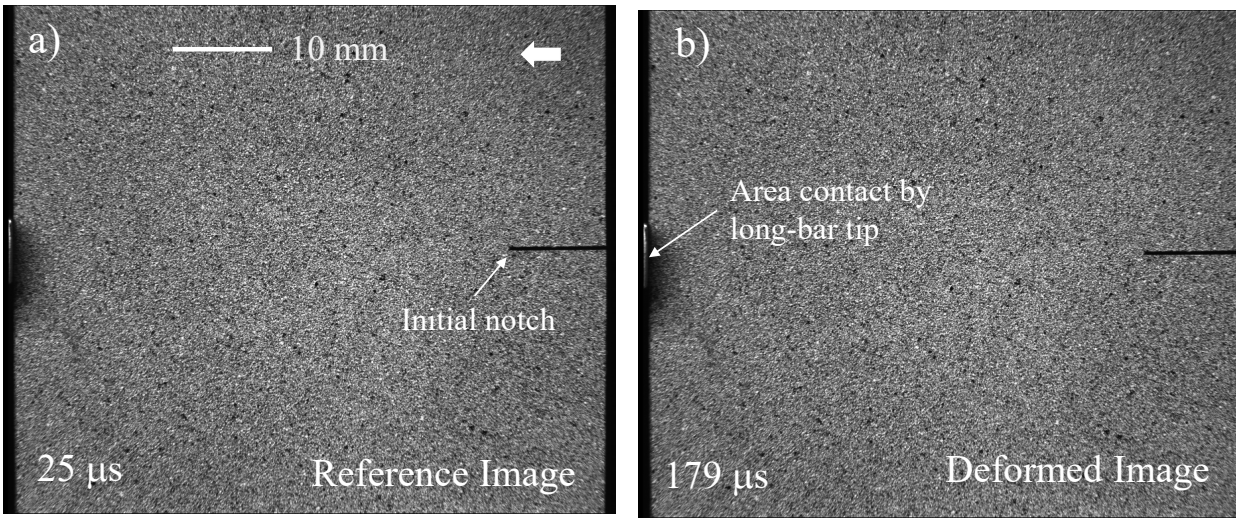

Figure A15: DIC speckle images from Edge on impact experiment subjected to area contact loading (Time is zero for the first speckle image recorded by camera.)

The Speckle images recorded and dominant displacment contours (in a direction normal to mode-I crack propagation) are shown in Figure A15 and Figure A16 respectively. The displacment contours did not show any crack tip fields, due to low tensile failure strains which is in agreement with previous studies conducted on SLG [18].

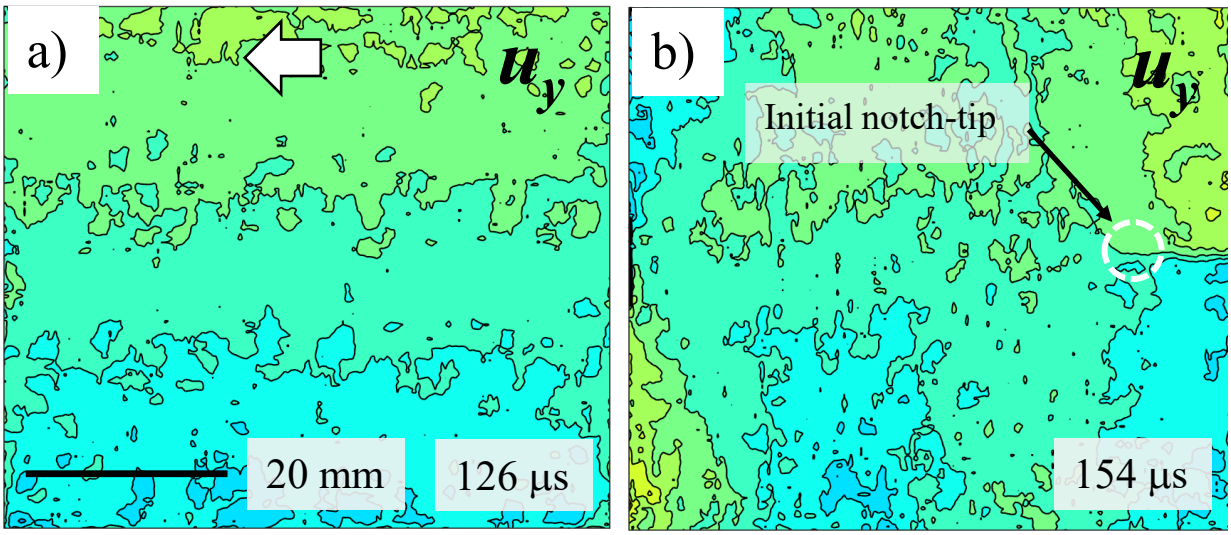

Figure A16: Displacement contours on ALON specimen surface along the vertical direction (normal to the mode-I crack propagation) from DIC at ~126 µs and ~154 µs. (Time is zero for the first speckle image recorded by camera.)

A.4 Edge-on-Impact (EOI) study on SLG using photoelasticity and DGS methods

Dynamic fracture of SLG subjected to Edge-on-Impact (EOI) loading was studied using full-filed optical methods photoelasticity and DGS. A 5.7 mm thick SLG specimens of 75 mm × 150 mm were machined from a large sheet and a line-load was dynamically applied on the longer edge (75 mm × 5.7 mm surface) of the specimen using a long-bar with a semi-cylindrical profile. First, the dynamic photoelastic experiments were conducted using the ultrahigh-speed camera. The experimental setup and optical settings used were same as the ones used in the previous photoelastic studies detailed in section 3.2. The striker velocity and ROI used in this experiment

were ~5.3 m/s and 56 mm × 47 mm, respectively. The resulting photoelastic fringes at different time instants during dynamic impact loading are shown in Figure A17.

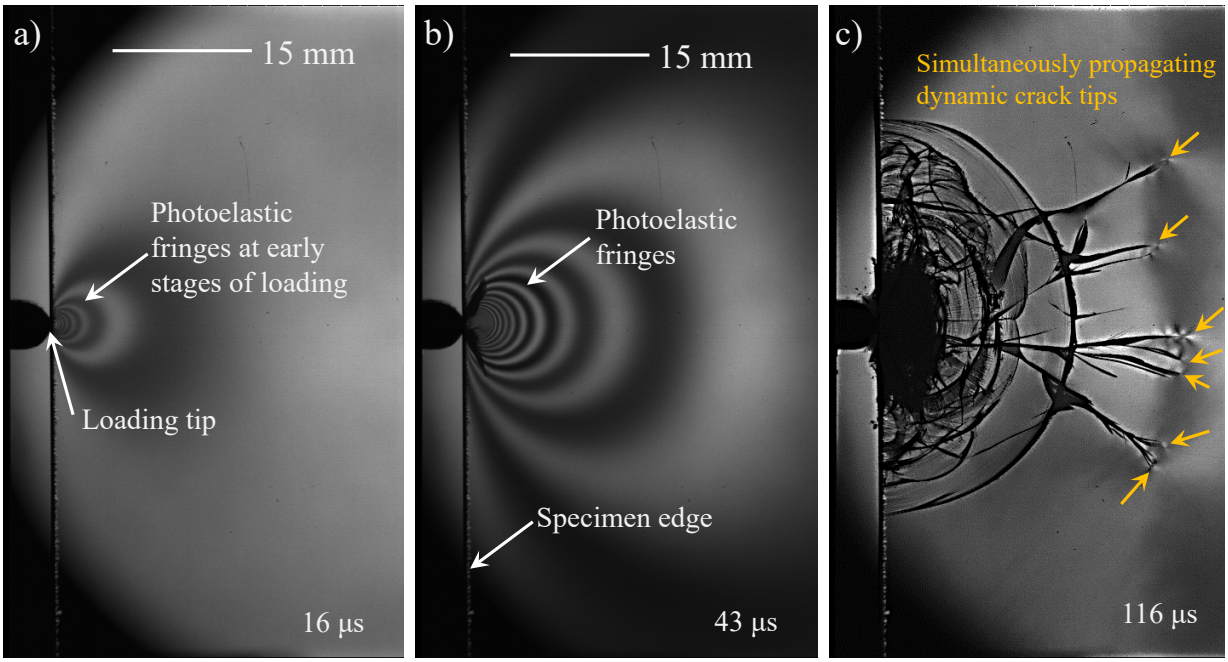

Figure A17: Photoelastic fringes in SLG specimen subjected to dynamic line loading at (a) initial stages of loading, (b) relatively higher loads with well-developed fringes and (c) post damage stage where multiple simultaneously propagating dynamic crack tips were observed. Time zero corresponds to the start of specimen loading. (As above images are cropped for better visualization, the image dimensions are different from ROI used in the experiment)

Figure A17(a) shows photoelastic fringes at the early stages (at 16 µs) of loading. Figure A17(b) depicts well-developed fringes at a later time instant (at 43 µs). Due to the imposed line load, a region of severe stress concentration occurs. Once the specimen was loaded further (at 116 µs), the material underwent crushing and fragmentation with multiple radial and circumferential cracks due to stress concentration. Figure A17(c) shows simultaneously propagating dynamic crack tips in radial direction and the crack tip locations are pointed using colored arrows. A continuous interaction of stress fields between these crack tips also can be seen in the Figure A17(c).

To evaluate the normal forces acting on the SLG specimen, the functional form of Flamant's closed form solution [117] was used in conjunction with the stress-optic law. The procedure for evaluating the normal forces is already explained in section 3.2 and the resulting normal force history is shown in Figure A18.

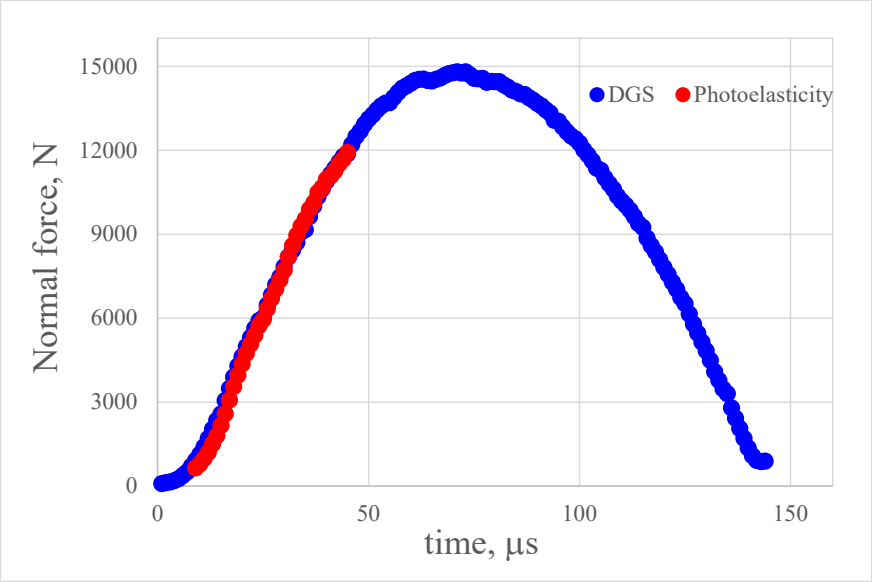

Figure A18: Contact force histories from edge on impact line loading on SLG specimen determined using dynamic photoelasticity and DGS methods.

Next, the normal forces acting on the SLG specimen were investigated using full-field optical method DGS using the same geometry and loading conditions as in photoelastic experiments. The opto-mechanical setup employed in DGS method is already described section 3.4. After correlating the speckle images, the resulting angular deflections of the light rays ϕ_x and ϕ_y at different time instants of specimen loading are shown in Figure A19 and Figure A20, respectively. The angular deflection contours ϕ_x symmetric with respect to the loading point and the angular deflection contours ϕ_y are anti-symmetric as expected for a specimen subjected to line loading [53].

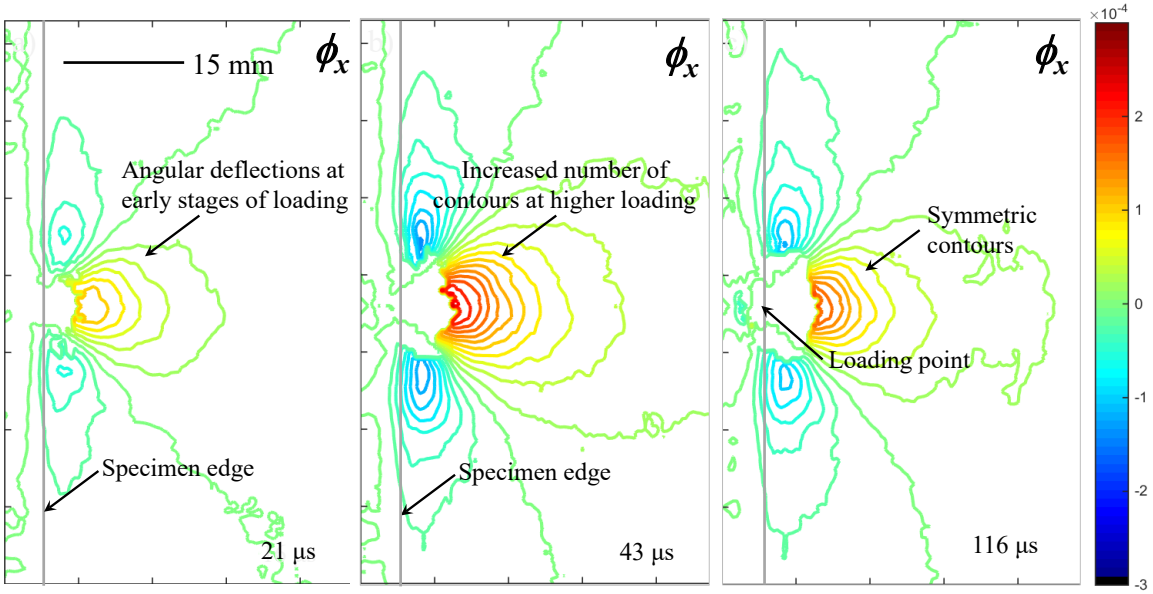

Figure A19: Contours of angular deflections of light rays (contour increment = 20×10^{-6} rad) in SLG specimen subjected to dynamic line loading at (a) initial stages of loading, (b) relatively higher loads with well-developed contours and (c) unloading stage with decreasing contours where simultaneously propagating dynamic crack tips were observed. Time zero corresponds to the specimen loading initiation. (Contours in the above images are cropped for better visualization, the image dimensions are different from ROI used in the experiment)

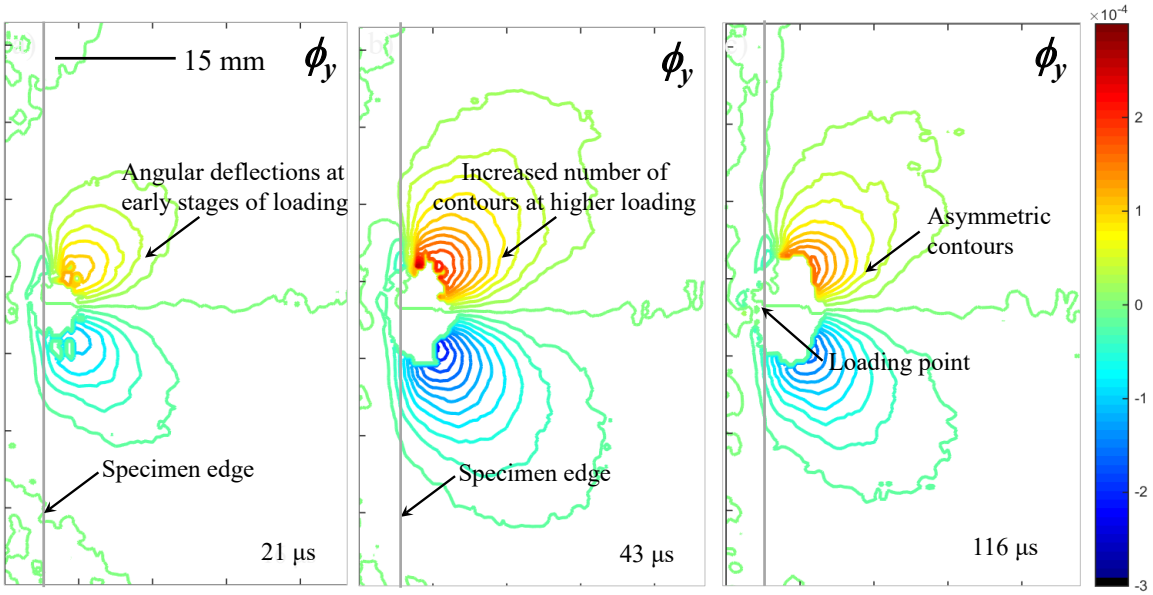

Figure A20: Contours of angular deflections of light rays (contour increment = 20×10^{-6} rad) in SLG specimen subjected to dynamic line loading at (a) initial stages of loading, (b) relatively higher loads with well-developed contours and (c) unloading stage with decreasing contours where simultaneously propagating dynamic crack tips were observed. Time zero corresponds to the specimen loading initiation. (Contours above are cropped for better visualization, the image dimensions are different from ROI used in the experiment)

The normal forces acting on the specimen at each time instant were evaluated by performing over-deterministic least-squares analysis for the data in the region $1.5 \le r / B \le 2.5$ and the resulting normal force histories are shown in Figure A18 along with the photoelastic experimental results. The normal forces determined from the DGS method has a duration of ~ 150 μs with a peak load of 15000 N. The normal force histories measured from the DGS method are compared with the photoelastic data with good success.